

DETRITAL ZIRCON AGES AND PROVENANCE OF THE TRIASSIC (?)  
CARPHOLITE-BEARING METACONGLOMERATES IN THE SOUTHERN  
MENDERES MASSIF

A THESIS SUBMITTED TO  
THE GRADUATE SCHOOL OF NATURAL AND APPLIED SCIENCES  
OF  
MIDDLE EAST TECHNICAL UNIVERSITY

BY

ZEHRA DEVECI

IN PARTIAL FULFILLMENT OF THE REQUIREMENTS  
FOR  
THE DEGREE OF MASTER OF SCIENCE  
IN  
THE DEPARTMENT OF GEOLOGICAL ENGINEERING

SEPTEMBER 2013



Approval of the thesis

**DETRITAL ZIRCON AGES AND PROVENANCE OF THE TRIASSIC (?)  
CARPHOLITE-BEARING METACONGLOMERATES IN THE SOUTHERN  
MENDERES MASSIF**

submitted by **ZEHRA DEVECİ** in partial fulfillment of the requirements for the degree of **Master of Science in Geological Engineering Department, Middle East Technical University** by,

Prof. Dr. Canan Özgen  
Dean, Graduate School of **Natural and Applied Sciences** \_\_\_\_\_

Prof. Dr. M. Erdin Bozkurt  
Head of Department, **Geological Engineering** \_\_\_\_\_

Prof. Dr. M. Erdin Bozkurt  
Supervisor, **Geological Engineering Dept., METU** \_\_\_\_\_

**Examining Committee Members:**

Prof. Dr. Kadir Dirik  
Geological Engineering Dept., Hacettepe Un. \_\_\_\_\_

Prof. Dr. Erdin Bozkurt  
Geological Engineering Dept., METU \_\_\_\_\_

Prof. Dr. Nurettin Kaymakçı  
Geological Engineering Dept., METU \_\_\_\_\_

Assoc. Prof. Dr. Bora Rojay  
Geological Engineering Dept., METU \_\_\_\_\_

Asist. Prof. Dr. A. Arda Özacar  
Geological Engineering Dept., METU \_\_\_\_\_

**Date:** September 4, 2013

**I hereby declare that all information in this document has been obtained and presented in accordance with academic rules and ethical conduct. I also declare that, as required by these rules and conduct, I have fully cited and referenced all material and results that are not original to this work.**

Name, Last name: Zehra Deveci

Signature:

## ABSTRACT

### DETRITAL ZIRCON AGES AND PROVENANCE OF THE TRIASSIC (?) CARPHOLITE-BEARING METACONGLOMERATES IN THE SOUTHERN MENDERES MASSIF

Deveci, Zehra

M.Sc., Department of Geological Engineering

Supervisor: Prof. Dr. Erdin Bozkurt

September 2013, 156 pages

The recent documentation of HP relics (carphiolite-bearing metaconglomerates) from the Kurudere area (Selimiye-Milas, Muğla) was one of the most important discoveries in the southern Menderes Massif. The metaconglomerates form the lowest most lithologies of the so-called marble unit and lie structurally above the schists with a proposed thrust fault. The metaconglomerates occur at two distinct horizons, each of which shows opposing sense of shearing in an overturned anticlinal structure. U–Pb–Hf zircon analyses of detrital zircons (450 grains) were performed by using Laser ablation induced couple mass spectrometry method (LA-ICPMS). The youngest grain is Asselian (earliest Permian) in age ( $298\pm 5$  Ma, conc. 104%) while a Mezoarchean zircon grain ( $3020\pm 16$  Ma; conc. 101%) forms the oldest. The youngest zircon grain is therefore consistent with previous contention that the metaconglomerate is late Triassic in age. The dominance of Ordovician to Cryogenian (Neoproterozoic) zircons and lack of Mesoproterozoic (1.1–1.7 Ga) zircons suggest Pan-African terranes (the northern Gondwana provenance) as the main source area.  $\epsilon_{\text{Hf}}$  values of 144 zircon grains indicate both reworking of an old crust and a juvenile crustal source. The detrital zircon populations and  $\epsilon_{\text{Hf}}$  values are very distinct from those reported in the southern Menderes metasediments and show pronounced similarities with that of Cycladic rocks. It is therefore concluded that the Kurudere HP metaconglomerates and possibly the overlying marbles in the southern Menderes Massif may belong to the Cycladic blueschist units. The occurrence of north-vergent overturned fold and associated kinematics suggest tectonic emplacement of the Cycladic unit above the Menderes sequence sometime after Eocene but before late Oligocene.

**Key Words:** southern Menderes Massif, Cyclades, metaconglomerate, detrital zircon, U-Pb-Hf isotopes, laser ablation induced couple mass spectrometry method (LA-ICPMS).

## ÖZ

### GÜNEY MENDERES MASİFİ'NDEKİ TRİYAS YAŞLI (?) KARFOLİTLİ METAÇAKILTAŞLARININ KIRINTILI ZİRKON YAŞLARI VE KÖKENİ

Deveci, Zehra

Yüksek Lisans, Jeoloji Mühendisliği Bölümü

Tez Danışmanı: Prof. Dr. Erdin Bozkurt

Eylül 2013, 156 Sayfa

Kurudere köyü (Selimiye-Milas, Muğla) yakın civarında yüzeyleyen metasedimanlarda (karfolitli metaçakıltaş) YB metamorfizması kalıntılarının tanımlanmış olması güney Menderes Masifi'nde son zamanlarda yapılan en önemli keşiflerden birisidir. Metaçakıltaş, 'mermer örtüsü' olarak tanımlanan birimin en alt seviyesini oluştururken yapısal olarak, muhtemelen bindirme fayı, şist birimlerini üzerler. Bölgede metaçakıltaş iki farklı seviye ile temsil edilirken, kuzeye devrik yatık kıvrım içinde herbir düzey zıt yönlerde hareket veren yapısal elemanlarla süslenmiştir; bu durumda metaçakıltaş düzeyleri kıvrımın kanatlarını temsil ederler. Kırintılı zirkonlardan (450 adet) U-Pb-Hf zirkon analizleri, Lazer Aşındırılmalı-Endüktif Eşleşmiş Plazma Kütle Spektrometre (LA-ICPMS) yöntemi ile yapılmıştır. En genç tanenin Aseliyen (Erken Permiyen) ( $298 \pm 5$  Ma, uym. 104%), en yaşlı tanenin ise Mezoarkeen ( $3020 \pm 16$  Ma; uym. 101%) yaşta olduğu belirlenmiştir. En genç tanenin yaşı, daha önce birim için öngörülen geç Triyas yaşını desteklemektedir. Ordovisiyen-Orta Neoproterozoik yaş aralığındaki zirkon tanelerinin baskınlığı ve Mezoproterozoik (1.1-1.7 Ga) zamandaki boşluk, ana kaynak olarak Pan-Afrikan kökene işaret etmektedir. Yüzkırkdört adet zirkondan ölçülen  $\epsilon_{\text{Hf}}$  değerleri, tanelerin hem ilksel hem de taşınmış kabuksal kaynağa ait olduğunu göstermektedir. Metaçakıltaş biriminin kırintılı zirkon popülasyonu ve  $\epsilon_{\text{Hf}}$  değerleri literatürde ifade edilen ve güney Menderes metasedimanlarına ait değerlerden farklıdır ve Kiklatlarla benzerlik göstermektedir. Buna dayanarak, güney Menderes Masifi'ndeki Kurudere YB metaçakıltaşlarının ve üzerindeki mermer serinin Kiklatlara ait olabileceği sonucuna varılmıştır. Kuzeye devrik kıvrımın varlığı ve ilgili kinematik belirteçleri, Kiklatlara ait kaya topluluklarının Eosen-Geç Oligosen zaman diliminde Menderes serisinin üzerine tektonik olarak yerleşmesi olarak yorumlanabilir.

**Anahtar Kelimeler:** güney Menderes Masifi, Kiklatlar, metaçakıltaşları, kırintılı zirkon, U-Pb-Hf izotopları, Lazer Aşındırılmalı-Endüktif Eşleşmiş Plazma Kütle Spektrometre (LA-ICPMS) yöntemi

To My Father

## ACKNOWLEDGEMENT

I would like to express gratitude to Prof. Dr. Erdin Bozkurt for his endless supports and encouragement to this study not only as a supervisor but also as a teacher and a father. I have learnt much more from his enthusiasm and open heart side about science.

I also thank to Dr. Axel Gerdes for guidance in Geochronology and Radiogenic Isotope Laboratory, Institute of Geoscience, Goethe University of Frankfurt. And of course I appreciate to Linda Marko for helping in the laboratory, her endless patient and memorable friendship.

I ought to thank Orhan Karaman during the preparation of thin sections and his company and endless support during fieldwork.

Many thanks to Mustafa Kaplan and Bülent Tokay for their companionship in the field.

I would also like to give my special thanks to my father Memiş Deveci and my sister, Şule Gürboğa for valuable encouragement. I shouldn't forget my niece, Bilge Gürboğa. Thanks God that I have a family like you.

I would like to thank my friends especially Emrah Aral for supporting and enduring me.

This thesis was supported by TÜBİTAK grant 110Y069. Thanks are also due to TÜBİTAK for their generosity and scholarship (within the frame of 1001 project) for two years.

## TABLE OF CONTENTS

ABSTRACT.....	v
ÖZ .....	vi
ACKNOWLEDGEMENT .....	viii
TABLE OF CONTENTS.....	ix
LIST OF TABLES .....	xi
LIST OF FIGURES .....	xii
1 INTRODUCTION.....	1
1.1 DEFINITION OF PROBLEM: DETRITAL ZIRCON DATING.....	1
1.2 PURPOSE AND SCOPE.....	4
1.3 LOCATION OF THE STUDY AREA.....	6
1.4 METHODS OF STUDY .....	9
1.5 GEOLOGICAL OVERVIEW OF SOUTHERN MENDERES MASSIF .....	10
1.6 PREVIOUS STUDIES: THE KURUDERE HP-LT ROCKS .....	16
2 DESCRIPTION OF UNITS .....	25
2.1 INTRODUCTION .....	25
2.2 ROCK UNITS .....	25
2.2.1 METACONGLOMERATES .....	27
2.2.2 METAPELITIC ROCKS .....	34
2.2.3 QUARTZ VEINS.....	39
3 U-Pb GEOCHRONOLOGY AND Hf ISOTOPE DATA.....	43
3.1 INTRODUCTION.....	43
3.2 MATERIAL .....	44
3.3 MINERAL SEPARATION .....	44
3.4 METHOD.....	45
3.4.1 FEATURES OF ZIRCON AND ISOTOPIC SYSTEMS .....	46
3.4.1.1 U-Pb SYSTEMS.....	47
3.4.1.2 Hf ISOTOPE .....	47
3.4.1.3 U-Pb-Hf COMBINATION FOR ZIRCON .....	48
3.4.2 INTERPRETATION OF CL IMAGES .....	49
3.4.3 ANALYTICAL PROCESS.....	50
3.5 RESULTS.....	51
4 STRUCTURAL GEOLOGY .....	65
4.1 INTRODUCTION.....	65
4.2 STRUCTURAL FEATURES.....	65
4.2.1 FOLIATION AND LINEATION .....	65
4.2.2 CRENULATION CLEAVAGE.....	70
4.2.3 FOLDS .....	74
4.3 KINEMATIC INDICATORS.....	76
5 DISCUSSION .....	83

5.1	AGE OF THE METACONGLOMERATES.....	83
5.2	ORIGIN OF THE METACONGLOMERATE .....	83
5.2.1	CYCLADIC MASSIF .....	83
5.2.2	SOUTHERN MENDERES MASSIF.....	85
5.2.3	COMPARISON OF CYCLADES AND SOUTHERN MENDERES MASSIF.....	86
5.3	PROVENANCE OF KURUDERE METACONGLOMERATES .....	87
5.4	INTERPRETATION OF STRUCTURAL DATA .....	91
6	CONCLUSIONS .....	95
7	REFERENCES .....	97
	APPENDICES .....	115
	APPENDIX A.....	115
	PROCESS OF MINERAL SEPARATION.....	115
	CRUSHING .....	115
	WILFLEY TABLE .....	116
	HEAVY LIQUID .....	117
	MAGNETIC SEPARATION.....	118
	HAND PICKING .....	119
	EPOXY, POLISHING AND CATHODOLUMINESCENCE IMAGES .....	119
	APPENDIX B.....	121
	LIST OF U-Pb AND Hf DATA .....	121

## LIST OF TABLES

### TABLES

Table 1.1 Age data from the southern Menderes Massif (courtesy of Erdin Bozkurt).....	2
Table 3.1. List of samples from Kurudere metaconglomerates. ....	44
Table B.1 The list of U-Pb measurements. ....	122
Table B.2 List of $\epsilon_{\text{Hf}}$ values of different zircon grains. ....	147

## LIST OF FIGURES

### FIGURES

Figure 1.1 Gneissic core and overlying schist and Lycian Nappes, dash line indicates Cyclades-Menderes Thrust, K– Kurudere Village (Whitney et al., 2008; kinematic hinge is from Iredale, 2005 in Whitney et al., 2008). .....	5
Figure 1.2. Tectonic map of the Aegean and Anatolian region showing the locations of Menderes and Cycladic massifs (from Jolivet et al., 2012). Black lines– main active structures; thick violet or blue lines– main sutures zones; thin blue lines– main thrusts in the Hellenides; NCDS– North Cycladic Detachment, SD– Simav Detachment; AIW– Almyropotamos window; BD– Bey Daglari; CB– Cycladic Basement; CBBT–Cycladic Basement basal thrust; CBS– Cycladic Blueschists; CHSZ– Central Hellenic Shear Zone; CR– Corinth Rift; CRMC– Central Rhodope Metamorphic Complex; GT– Gavrovo–Tripolitza Nappe; KD– Kazdag dome; KeD– Kerdylion Detachment; KKD– Kesebir–Kardamos dome; KT– Kefhalonia Transform Fault; LN– Lycian Nappes; LNBT– Lycian Nappes Basal Thrust; MCC– Metamorphic Core Complex; MG– Menderes Grabens; NAT– North Aegean Trough; NCDS– North Cycladic Detachment System; NSZ– Nestos Shear Zone; OIW– Olympos Window; OsW– Ossa Window; OSZ– Ören Shear Zone; Pel. – Peloponnese; ÖU– Ören Unit; PQN– Phyllite–Quartzite Nappe; SiD– Simav Detachment; SRCC– South Rhodope Core Complex; StD– Strymon Detachment; WCDS– West Cycladic Detachment System; ZD– Zaroukla Detachment.....	6
Figure 1.3 Simplified geological map of the Menderes Massif and subdivision into the submassifs (modified from Candan et al., 2000). .....	7
Figure 1.4 Geological map of the Bafa Lake-Selimiye area in the southern Menderes Massif (from Başarı 1970). Courtesy of Erdin Bozkurt. ....	8
Figure 1.5 Location map showing topographic features of the study area.....	9
Figure 1.6 Simplified geological map of the Southern Menderes Massif (from Bozkurt, 2007). .....	14
Figure 1.7 Simplified stratigraphic section of the southern Menderes Massif (from Rimmelé et al., 2003a). .....	16
Figure 1.8 Geological map of the southern Menderes Massif showing the location and distribution of HP assemblages (from Rimmelé et al., 2003a). .....	18
Figure 1.9 View of the accretionary complex during the Eocene showing the structural position of the main HP units in Western Anatolia (from Rimmelé et al., 2003a). ....	19
Figure 1.10 Geological map of the Karaburun Ridge (from Whitney et al., 2008). ....	21
Figure 2.1 Geological map of Kurudere HP metamorphic rocks.....	26
Figure 2.2 A view from thin ridges formed by metaconglomerates. ....	27

Figure 2.3 A view from the metaconglomerates. Please note abundance of holes left behind by the weatering and removal of quartz pebbles. ....	28
Figure 2.4 Views from the metaconglomerates. (a) There is grain size variation within the same bed where pebble-rich and pebble-poor domains seem to alternate. (b) The lateral passages between pebbly and sandy levels are also common. (c, d) In almost everywhere larger quartz pebbles are deformed, flatenned and elongated in the plane of foliation. In such cases, foliation is pronounced and penetrative. (e, f) In other cases, large quartz pebbles resist deformation and appear as large porphyroclasts within a fine grained matrix foliation, thus giving the rock an augen structure. Note in (f) how relatively smaller pebbles are flatenned and elongated and define the matrix foliation. Also, matrix foliation abust against the large quartz pebble. ....	29
Figure 2.5 A view from the metaconglomerate. Note the difference in the degree and intensity of deformation between relatively larger and smaller quartz pebbles. Also note that one of the larger pebbles defines $\sigma$ -geometry, which is consistent with a top-to-the-left sense of shearing. Foliation is penetrative and well developed; elongated and flattened quartz pebbles in the foliation plane are evident. ....	30
Figure 2.6 Photomicrograph from matrix of the metaconglomerate. Note domainal structure of the rock, defined by quartz- and mica-rich domains. There are also textural differences in the quartz domains. Fine-grained equant quartz grains (to the left) define a ribbon structure where long axis of elongate quartz grains define a foliation paralleling that of white mica foliation. Larger quartz grains are characteristic with their patchy and undulose extinction and define well-developed triple junctions (TJ) among the grains; this indicates the role of recovery process. Otherwise, quartz grains tend to show regular and straight boundaries with local embayments. Mica-rich domain (Mca) defines a penetrative foliation and also forms the boundary between quartz-rich domains. ....	31
Figure 2.7 Photomicrographs from the metaconglomerate. (a–d) Microscopic (crossed polars) view of kyanite (Ky) and quartz (Qtz). Note that kyanite in (a) tends to show parallelism with the foliation in the rock. Quartz grains in both microphotograph are larger crystals and show undulatory extinction. Note also triple-grain boundary among grains in lower left corner of (d). (b, c) BSE images of kyanite and quartz. ....	32
Figure 2.8 Photomicrograph (crossed polars) of a coarse kyanite (Ky) together with quartz (Qtz) and phengite (Ph) in matrix of the metaconglomerate.....	33
Figure 2.9 Rutile, as an accessory mineral, was determined by using SEM Jeol JSM-6490 electron microscopy and INCA software.....	33
Figure 2.10 Field view illustrating lateral passages between metaconglomerate and metapelites. ....	34
Figure 2.11 (a) Field view from coarse (cm-scale) chlorite grains in metapelites. Note how they overgrow the main foliation in the rock and gives the rock a characteristic appearance, spotted texture. (b) The coarse chlorite occurs as high relief, strongly pleochrioc (from pale light blue to dark blue) mineral under microscope (plane light	

view). (c) Parallely and lamelley extincted from light green, light blue to dark purple chlorite in crossed polars microscopic view is characteristic.....	36
Figure 2.12 Photomicrographs (plane light) of post-tectonic chlorite (Chl) porphyroblasts overprinting older matrix foliation (f). Note random orientation of large porphyroblasts in (a) with respect to the main foliation. Note also how inclusions in the porphyroblasts are parallel to, and pass into, the matrix foliation.....	36
Figure 2.13 Microscopic view of carpholite (Car) crystals in infolded metapelite.....	37
Figure 2.14 Views of metapelites exposed in the area between Çileklik Hill and Lomburt Hill (see Figure 2.1 for location): (a) quartz pebbles in the metapelite; (b) boudinaged quartz veins within fine-grained metapelitic unit; (c) folded in reddish metapelitic unit.....	38
Figure 2.15 A view from a large flattened quartz pebble in the metapelites. Note that the pebble is large enough to appear as a thin layer within pelites. ....	38
Figure 2.16 A close-up view of a quartz vein is within the metapelitic rocks. Pen is about 13-cm long. ....	39
Figure 2.17 Views from deformed and folded quartz veins. Note S-shape geometry of the vein (a) and thickening in the hinge zone (b) of folds.....	39
Figure 2.18. Views from the quartz veins in the Kurudere area: (a, b) monominerallic milky quartz veins within the metaconglomerate unit; (c) kyanite-quartz vein; note blue kyanite blades with random orientation; (d) a quartz vein characterized by dense magnesiocarpholite fibers; (e) a deformed/folded milky quartz vein. ....	40
Figure 2.19 A field view from fibrous magnesiocarpholite (Car) in a quartz vein (Qtz). ....	41
Figure 2.20 A view from kyanite-bearing quartz vein in folded black metapelitic unit. Coordinates: 35555015E/ 4139481N. Pencil is about 13-cm long. ....	42
Figure 3.1 Simplified scheme of a mass spectrometer (from Gross, H.J., 2010).....	45
Figure 3.2 CL images showing different zone structure of zircons which may occur in the same sample (Sample 331): (1) disrupted zoned texture, convolute zonation in an idiomorphic crystal; (2, 3) relatively U-less core and U-rich rim with oscillatory zoning; (4, 5) sector zoned inherited core with U-rich oscillatory zoned rim; (6) sector zonation of a grain; (7) perfect, bright oscillatory zoning; (8) xenomorphic grain with metamorphic rim; (9) disturbed oscillatory zoning in idiomorphic crystal; (10) idiomorphic crystal with oscillatory zonation; (11) U-poor core and U-rich rim in xenomorphic crystal; (12) composite zircon –inherited core and magmatic growth; (13, 14) partly preserved zonation and recrystallization; (15) xenomorphic grain with inherited core and rim without zonation (featureless) (from samples 331, 332, 333, 333B).....	49
Figure 3.3 CL images and ablated spots for measuring U-Pb and Hf isotope ratio. Red circles shows location of spots. ....	50
Figure 3.4 U-Pb concordia diagram of detrital zircon ages from sample 331. ....	53
Figure 3.5 Probability/density plot of detrital zircons from sample 331.....	53
Figure 3.6 CL images of analyzed detrital zircons in sample 331. ....	54

Figure 3.7 U-Pb concordia diagram of detrital zircon ages from sample 332. ....	55
Figure 3.8 Probability/density plot of detrital zircons from sample 332. ....	55
Figure 3.9 CL images of detrital zircons picked from sample 332. ....	56
Figure 3.10 U-Pb concordia diagram of detrital zircon ages from sample 333. ....	57
Figure 3.11 Probability/density plots of detrital zircons from sample 333. ....	57
Figure 3.12 CL images of analysed detrital zircons belong to sample 333. ....	58
Figure 3.13 U-Pb concordia diagram of detrital zircon ages from sample 333B and the youngest zircon grain with U-rich core and U-poor rim. ....	59
Figure 3.14 Probability/density plot of detrital zircons from sample 333B. ....	59
Figure 3.15 CL images of analysed detrital zircons picked from sample 333B. ....	60
Figure 3.16 Probability/density plot of all processed detrital zircon grains. ....	61
Figure 3.17 U-Pb-Hf plot of detrital zircons younger than 1000 Ma. ....	61
Figure 3.18 U-Pb-Hf plot of concordant detrital zircon grains older than 1000 Ma. ....	62
Figure 3.19 U-Pb-Hf plot of all concordant zircon grains. ....	62
Figure 4.1. (a, b) Field appearances of foliation in the metaconglomerates. Note that it is pronounced and penetrative in the fine-grained parts and is defined by the preferred parallel alignment of micas and quartz grains. Larger quartz pebbles are either flattened in the plane of foliation or stand out as resistant porphyroclasts, giving the rock an augen structure (f– foliation). (c) Where deformation is intense, many quartz pebbles are flattened and elongated; together with micas and fine quartz grains; flattened grains define the main foliation in the rock. (d) Field view of the foliation in the metapelitic rocks. Pencil is about 13-cm long. ....	66
Figure 4.2 S-dipping foliation at microscopic scale where it is defined by the preferred parallel alignment of mica minerals and long axis of quartz ribbons. Note the dominal structure defined by alternating quartz- and mica-rich domains. Note also texture and size of quartz grains in quartz-domains as well. ....	67
Figure 4.3 Views from metapelites in the area between Çileklik Hill and Lomburt Hill (see Figure 2.1 for location): (a) quartz pebbles (indicated by blue circles) in metapelites, (b) small-scale fold in a reddish metapelitic unit, (c) boudinaged quartz veins in fine-grained metapelitic unit. Note how quartz veins are disrupted and isolated within the metapelites in (c). Pencil is about 13-cm long. ....	68
Figure 4.4 Stereonet pole plots of (a) south-dipping foliation and (b) almost N–S-trending mineral stretching lineation in the Kurudere area (Rockworks16). ....	69
Figure 4.5 (a) Field view and (b) photomicrograph of crenulation cleavage in metapelites. S <sub>1</sub> – older foliation, S <sub>2</sub> – crenulation cleavage. ....	71
Figure 4.6 A view from shear cleavage developed in the metapelites. Note milimetric-scale displacement along discrete cleavages. ....	71
Figure 4.7 Stereonet pole plots of (a) hinge line of crenulation in metapelites, and (b) hinge line of folds (fold axis) in the metaconglomerates (Rockworks16). ....	72
Figure 4.8 Mechanism of a symmetrical crenulation foliation S <sub>2</sub> by buckling S <sub>1</sub> . (a) Initial foliation S <sub>1</sub> parallel to the direction of maximum shortening. (b) Shortening	

generates symmetrical crenulation by buckling or (c) chevron style of crenulation (from Twiss and Moores, 2007).....	73
Figure 4.9 Production of asymmetrical crenulation foliation $S_2$ by buckling of $S_1$ . a) Initial foliation $S_1$ is at a low angle to the direction of maximum shortening. b) Asymmetric crenulation is occurred by buckling of $S_1$ . $S_1$ has rotated to a low angle with the crenulation axial surface and defines the short limb of the crenulation. Hinges may be sharp or rounded (Twiss and Moores, 2007).....	73
Figure 4.10 Folded thin, fine-grained dark metapelitic unit within the metaconglomerates, Karaburun Ridge. ....	74
Figure 4.11 General views from mesoscales folds in the metaconglomerates. (a, b) Folds are obvious where metaconglomerates contain thick dark layers of more sandy levels; in such cases the geometry of the wrinkles and the hinge lines of the folds are obvious for inspection; (c) an overturned intrafolial fold with its axes almost parallel to the foliation; (d) where quartz veins are present, folds become more pronounced; (e, f) Z- and S-geometries are common; in these photographs they indicate top-to-the-north and top-to-the-south sense of shear respectively; (g, h) flattened quartz pebbles in folded structures. ....	76
Figure 4.12 Views of kinematic indicators from northern side of study area: (a, e) Mesofolds in the metaconglomerates; the folds are obvious where metapelites intercalations occur. (b) Microscopic view of quartz grain oriented oblique to the main foliation in the rock. The long axis of quartz grain defines the S-foliation whereas the matrix foliation, C surfaces; (c) Mesoscale en-échelon folds in the metaconglomerate; (d) Poorly-developed $\sigma$ -geometry defined by a large quartz porphyroclasts and dynamically recrystallized mantle around it. Note that the quartz is dynamically recrystallized into smaller subgrains. The undulose extinction of new grains is evident. Note also thin blade of white mica defining the S-foliation in the rock. The stair-stepping geometry defined by larger grain and deformed mantle is evident. The C-S fabric development in (b) and (d) forms overwhelming evidence for movement sense. The asymmetry and shape of the folds are considered to suggest sense of shear. All of these meso- and micro-structures are consistent in indicating a top-to-the-south sense of shear. Thin sections are cut parallel to the mineral stretching lineation and perpendicular to the main foliation in the sample. ....	79
Figure 4.13 Top-to-the-north kinematic indicators in Çileklik hill in the south of the study area. (a–d) $\sigma$ -type quartz porphyroclasts and pebbles embedded within a fine-grained matrix of quartz, white mica and chlorite. Note how matrix foliation wraps around porphyroclasts and deformed pebbles. In all, the stair-stepping geometry of recrystallized and/or elongated tails is pronounced. (e) Microscopic view of a quartz pebble. The quartz grain is dynamically recrystallized into subgrains, each of which show characteristic undulose extinction. The boundaries of subgrains are irregular/serrated and indicates that grain-boundary migration is an important deformation mechanism subsequent to subgrain formation. Deformation band formation and kinking are also characteristic. The long axis of the porphyroclast	

defines the S-foliation whereas matrix foliation of white mica and fine-grained quartz represent the C-foliation. ....	81
Figure 5.1 Published detrital zircon ages from the Cyclades Massif (Keay et al., 2001; Keay and Lister, 2002).....	85
Figure 5.2 Published probability-density plots of detrital zircon from Southern Menderes Massif schists (from Zlatkin et al., 2013).....	89
Figure 5.3 Bimodal distribution of detrital zircon ages between 550 and 650 Ma that symbolize two distinct stages of during Pan-African Orogeny. ....	90
Figure 5.4. $\epsilon_{\text{Hf}}$ values southern Menderes Massif (Zlatkin et al., 2013).....	91
Figure 5.5 Schematic cross-section across the study are and interpretation of kinematic data.....	93
Figure A.1 A view of a roller crushed in the crushing laboratory of the Department of Geological Engineering in Dokuz Eylül University.....	114
Figure A. 2 Wilfley table with water and manually adjusted. Light and heavy minerals separation is seen. ....	117
Figure A.3 The heavy liquid bromoform and sample are mixed in a glass; then wait for sometime until the heavier and heaviest minerals are separated according to their relative density with respect to the density of the liquid. Then the mixture is run through separating funnel. ....	118
Figure A.4 View of a magnetic separator in Geochronology and Radiogenic Isotope Laboratory, Institute of Geoscience, Göethe University of Frankfurt. ....	119
Figure A. 5 View of a binocular microscope. ....	119
Figure A.6 View of mounted and polished zircon grains ready for cathodoluminescence imaging. ....	120
Figure A.7 Cathodoluminescence images of detrital zircons from Kurudere metaconglomerates (sample 331).....	120



# CHAPTER 1

## INTRODUCTION

### 1.1 DEFINITION OF PROBLEM: DETRITAL ZIRCON DATING

Detrital minerals in sedimentary rocks have been the subject of quantitative methods for last century with the rising of analytical opportunities. Notedly, zircon has kept its popularity for a long time because of its resistance at the Earth's surface; it is therefore prominently preferred to interpret the provenance, age and history of a sedimentary deposits. Detrital zircon analysis uses age of the zircon to determine provenance of, and develop a geological history of, sedimentary units and their source areas. Ideally, the analyzed sample would completely represent a full story of geological history because zircons may include evidence for all possible provenances and their relationships to each other (cf. Fedo et al., 2003).

Although detrital zircon geochronology is an important tool to date the minimum age of sediments and to test their provenance, such a study, in modern terms, was not carried out the in Menderes Massif yet. Most of the existing geochronologic works in the southern Menderes Massif is concentrated on the age of metagranitic rocks and cooling history of the massif (Table 1.1). There are three attempts of detrital zircon geochronology on the metasediments of the southern Menderes Massif: (1) Candan et al. (2011a) dated, using the  $^{207}\text{Pb}/^{206}\text{Pb}$  single-zircon evaporation technique, eleven detrital zircon grains from muscovite schists, which yielded scattered ages between 642 Ma and 3239 Ma, with a major cluster at ca. 640–670 Ma. The age of these sediments are considered to constrain between 642 and 550 Ma (Ediacaran); (2) Later, Koralay et al. (2012) also dated eleven detrital zircon grains from garnet schists;  $^{207}\text{Pb}/^{206}\text{Pb}$  single-zircon evaporation ages range from  $2482\pm 6$  to  $610\pm 5$  Ma. They constrain the age of sedimentation between 600 Ma and 550 Ma ((Ediacaran). More recently, Zlatkin et al. (2013) date two samples, using LA-ICP-MS, from the cover sediments immediately above the core orthogneisses in Kaletepe area. The first sample is from Gökçay conglomerates; 47 concordant zircon grains yielded ages between  $584\pm 9$  and  $3043\pm 27$  Ma. The other sample comes from quartzitic unit above; the age of 90 detrital zircon grains range from  $533\pm 14$  Ma to  $2927\pm 11$  Ma. These authors also accepted previous contentions and suggested Ediacaran ages for the lowest representatives of the cover schists. Variable  $\epsilon\text{Hf}$  (t) values from the two samples are

interpreted to suggest : (i) significant crustal reworking of 620–720 Ma zircon juvenile magmatic zircons, (ii) Pan-African remobilization and mixing of Neoproterozoic-aged detrital zircons.

As is seen from above two works, there are only for samples dated by using detrital zircon geochronology from the whole southern Menderes Massif. In addition to all, except the Zlatkin et al. (2013) paper, the other two employed only eleven grains from two samples each. Whereas to obtain a reasonable and statistically sound age population from a sediments several ten's of grains should be dated (around 100 zircon grains) and this is impossible by using evaporation technique because it is really very expensive technique; no one can effort to pay for it and most of the zircon grains have metamorphic rims which is given mix age with evaporation technique. LA-ICP-MS U-Pb technique is a new, relatively cheap, widely accepted and used method in dating detrital zircons from (meta)sediments.

The above-mentioned published detrital zircon ages are only from the lowest representatives of the cover schists and there are no other similar work on the whole schist unit and the overlying marble cover. The whole southern Menderes metasediments are several hundreds' of metres thick and about 150 detrital zircon grains mean nothing in describing and discussing age and provenance of the metasediments. There is an urgent need for a detrital zircon geochronology employing several tens' of samples along several measured sections. Off a particular relevance to present research, it is aimed at taking advantage of LA-ICP-MS U-Pb method in dating detrital zircons from HP metaconglomerates of the southern Menderes Massif. This is crucial because the origin of these kyanite+magnesiocarpholite-bearing metaconglomerates is highly debated (see next sections) and bears in the better understanding of evolution of the Southern Menderes Massif.

Table 1.1 Age data from the southern Menderes Massif (courtesy of Erdin Bozkurt).

Lithology	Age (Ma)	Method	References
orthogneisses	490 ± 90 – 529	Rb-Sr whole rock	Satir and Friedrichsen, 1986
	2555 – 1740	<sup>207</sup> Pb- <sup>206</sup> Pb single zircon evaporation	Reischmann et al., 1991
	546.4±0.8 and 546.0±1.6 (mean 546±1.2)		Hetzel and Reischmann, 1996
	521 ± 8.0 – 572 ± 7.0 (mean c. 550)		Loos and Reischmann, 1999
	547.2 ± 1.0		Gessner et al., 2001b
	530.9±5.3		Koralay et al., 2007
	552.1±2.4 – 545.6±2.7		Dora et al., 2005 <sup>1</sup>

<sup>1</sup> from Koralay et al., 2012

	549±26		
	541±14 – 566±9	U-Pb SIMS zircon	Gessner et al., 2004
	43.4±1.3 and 37.9±0.4	Ar-Ar muscovite	Hetzel and Reischmann, 1996
	32.1±0.5	Ar-Ar white mica	Gessner et al., 2001a
	27.88±1.52 and 24.69±0.90	zircon fission track	Ring et al., 2003
	24.68±2.19 – 15.12±1.09 (concentrate around 22–21)	apatite fission track	
	571±9 – 437±28 <sup>2</sup> (mean 501±18)	Th-Pb monazite	Catlos and Çemen, 2005
	mean 42±5 and one grain 33.1±0.7 <sup>3</sup>		
Metasediments	40.0±1.8 and 34.5±1.4	<sup>40</sup> Ar- <sup>39</sup> Ar muscovite	Hetzel and Reischmann, 1996
	2094±2 – 526±7	<sup>207</sup> Pb- <sup>206</sup> Pb single zircon evaporation	Loos and Reischmann, 1999
metasediments and orthogneisses	502±10 and 471±8	Rb-Sr whole rock	Satir and Friedrichsen, 1986
	35±5 (63–48 muscovite and 50–27 biotite)	Rb-Sr mica	
quartz vein in orthogneiss	62–43 (muscovite)		Bozkurt and Satir, 2000
quartz vein in metasediments	49.2±3.3 – 35.0±2.5 (average 45.2±2.0)	Ar-Ar white mica	Pourteau, 2011; Pourteau et al., 2013
prophyritic metagranite	553.6±8.7	<sup>207</sup> Pb- <sup>206</sup> Pb single zircon evaporation	Candan et al., 2011a
muscovite schists of core series	642–3239 (major cluster at ca. 640–670)		
granitic pebbles from a metaconglomerate	552.3±3.1 and 550.4±2.6		
prophyritic metagranite	549.0±5.4	LA-ICP-MS U-Pb zircon	
granitic pebble from a metaconglomerate	549.6±3.7		
biotite orthogneiss	554±6 – 551±5 (mean 552±2)	<sup>207</sup> Pb- <sup>206</sup> Pb single zircon evaporation	Koralay et al., 2012
leucocratic tourmaline orthogneiss	544–547 (mean 546±3)		
	552.4±6.8	ICPMS U-Pb zircon	

<sup>2</sup> ages from inclusions in garnet

<sup>3</sup> ages from matrix foliation

garnet-mica schist	2482±6 – 476±7 (610±5 to 876±5)	<sup>207</sup> Pb- <sup>206</sup> Pb single zircon evaporation	
	2455±5 – 601±7		
muscovite-quartz schist	1953±6 – 554±8		
	2569±10 – 554±26		
	1942±5 – 537±13		
	2608±5 – 480±5		
Orthogneisses	2480±72 <sup>4</sup> and 539±13 <sup>5</sup>	U–Pb zircon	Iredale et al., 2013
	1289±107 <sup>4</sup> and 495±30 Ma <sup>5</sup>		
metaconglomerate	45.9±2.0 Ma	Ar-Ar white mica	Pourteau et al., 2013

<sup>1</sup> lower intercept

## 1.2 PURPOSE AND SCOPE

The Menderes Massif is bounded by three major tectonic units, some which contains evidence for relict blueschist facies metamorphism; Lycian Nappes in the south (e.g., Collins and Robertson, 1997, 1998, 1999; Rimmelé et al., 2003a; Ring and Layer, 2003; Jolivet et al., 2004; Ring et al., 2007; Whitney et al., 2008), the İzmir-Ankara-Erzincan Neotethyan suture zone in the north (e.g., Şengör and Yılmaz, 1981 and several other reference thereafter) and Cycladic core complex in the west (with the contact of Eocene eclogite and blueschist metamorphic rocks) (e.g., Dürr et al., 1978; Okrusch and Bröcker, 1990; Okay, 2001; Ring and Layer, 2003; Ring et al., 2007; Whitney et al., 2008). In the southern submassif, blueschist facies relics include kyanite and carpholite presence in the metasedimentary rocks. Rimmelé et al. (2003b) was first to report HP relics in the massif and proposed that the HP-LT rocks are part of the metasedimentary sequence of the massif (part of the so-called marble cover) structurally below the HP–LT Lycian Nappes but above the high-grade gneissic core of the massif (see also Rimmelé et al., 2003b). This model proposes that the age of the carphiolite-bearing metaconglomerates are late Triassic and that they display conformable relationships with: (i) underlying Permian–Triassic phyllite-schist-quartzite alternation and marble intercalations and (ii) overlying Liassic–Maastrichtian marbles (partly dolomitic and partly Rudist-bearing) with metabauxite deposits. On the other hand, Ring et al. (1999) and Régnier et al. (2003, 2007) correlated the HP–LT rocks with the Cycladic blueschist unit and proposed that Cycladic unit of the southern Menderes Massif is bounded by thrust faults with the underlying Menderes cover units (along the Cycladic-Menderes thrust) and the overlying Lycian Nappes. This model was latter favoured by Whitney et al. (2008) (Figure 1.1); they have suggested, based on the differences in P–T-deformation history of the so-called cover

---

<sup>4</sup> upper intercept

schists and cover marbles of the southern Menderes Massif, that the HP–LT rocks are not part of the Menderes Massif cover sequence but are tectonically related to the Cycladic blueschist unit (see section 1.6 for more details on the metaconglomerates of the southern Menderes Massif).

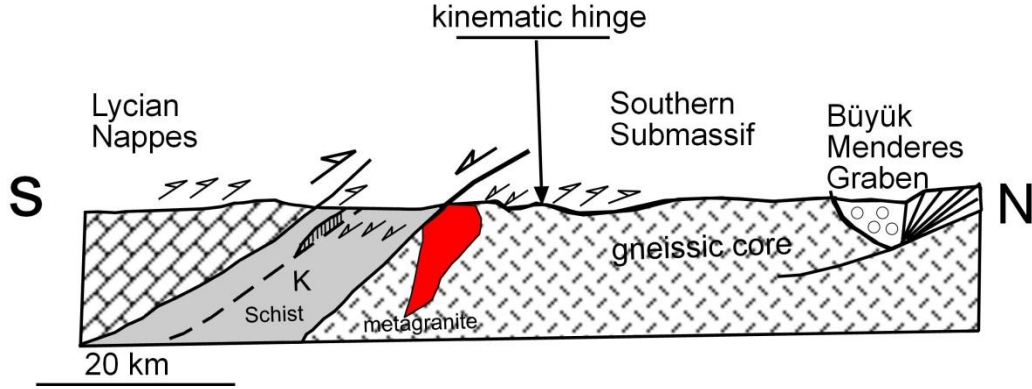


Figure 1.1 Gneissic core and overlying schist and Lycian Nappes, dash line indicates Cyclades-Menderes Thrust, K– Kurudere Village (Whitney et al., 2008; kinematic hinge is from Iredale, 2005 in Whitney et al., 2008).

As is seen from the above discussion, the origin of the HP rocks in the southern Menderes Massif is still debated and it is not clear if they belong to Cyclades or form a part of the southern submassif's metasedimentary sequence (Figure 1.2). The answers to above questions have far more implications for the better understanding of not only the Menderes Massif but whole Aegean. The present work therefore aims to employ LA-ICP-MS U-Pb method on detrital zircons separated from the kyanite-magnesiocarpholite metaconglomerates of the Southern Menderes Massif to better understand their protolith, age, provenance, metamorphic assemblages and structural features; their relationship(s) to the rest of the Southern Menderes Massif, which does not record clear evidence for a HP–LT metamorphism, will also be discussed.

This research forms a part of a TÜBİTAK project that aims to study the metasediments of the Lycian Nappes, Menderes Massif, Afyon Zone and Tavşanlı Zone. It lasted for about two-and-half-years and involves field geological mapping, structural analysis and laboratory work of the carpholite-bearing metaconglomerates in Kurudere area (Selimiye-Milas) in the southern Menderes Massif. The U-Pb-Hf detrital zircon analyses of metaconglomerates by using LA-ICP-MS method form the centre of the research. The detrital zircons of the southern Menderes Massif, except for a number of recent papers, have not previously been considered. More importantly detrital zircon ages and population seem to be the only method to test existing controversies over the age and provenance and in turn the origin of the metaconglomerates of the Southern Menderes Massif.

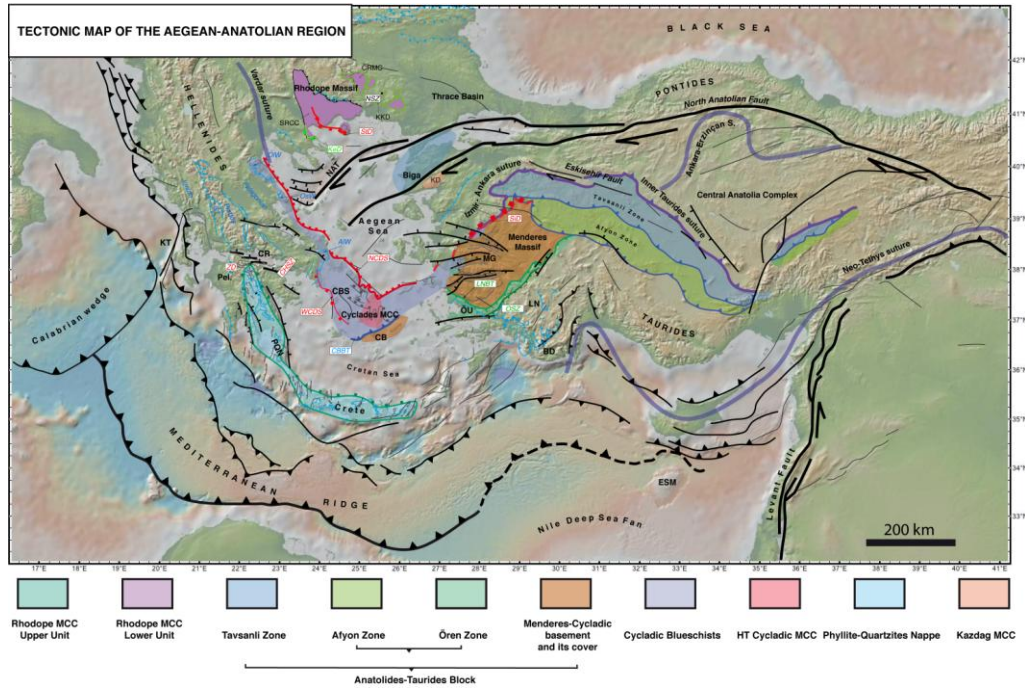


Figure 1.2. Tectonic map of the Aegean and Anatolian region showing the locations of Menderes and Cycladic massifs (from Jolivet et al., 2012). Black lines– main active structures; thick violet or blue lines– main sutures zones; thin blue lines– main thrusts in the Hellenides; NCDS– North Cycladic Detachment, SD– Simav Detachment; AIW– Almyropotamos window; BD– Bey Dagları; CB– Cycladic Basement; CBBT–Cycladic Basement basal thrust; CBS– Cycladic Blueschists; CHSZ– Central Hellenic Shear Zone; CR– Corinth Rift; CRMC– Central Rhodope Metamorphic Complex; GT– Gavrovo–Tripolitza Nappe; KD– Kazdag dome; KeD– Kerdylion Detachment; KKD– Kesebir–Kardamos dome; KT– Kephallonia Transform Fault; LN– Lycian Nappes; LNBT– Lycian Nappes Basal Thrust; MCC– Metamorphic Core Complex; MG– Menderes Grabens; NAT– North Aegean Trough; NCDS– North Cycladic Detachment System; NSZ– Nestos Shear Zone; OIW– Olympos Window; OsW– Ossa Window; OSZ– Ören Shear Zone; Pel. – Peloponnese; ÖU– Ören Unit; PQN– Phyllite–Quartzite Nappe; SiD– Simav Detachment; SRCC– South Rhodope Core Complex; StD– Strymon Detachment; WCDS– West Cycladic Detachment System; ZD– Zaroukla Detachment.

### 1.3 LOCATION OF THE STUDY AREA

The study area is located within the southern Menderes Massif in western Turkey, NE of Kurudere village, SE of Bafa Lake and SW of town of Selimiye (Milas). The metaconglomerates crop out at four hills, namely Karaburun, Çileklik and Lomburt

hills. The total amount of area 32 km<sup>2</sup>, it is included on 1/25000-scaled Turkish topographic map sheets of Muğla N19-a1 (Figures 1.3–1.5).

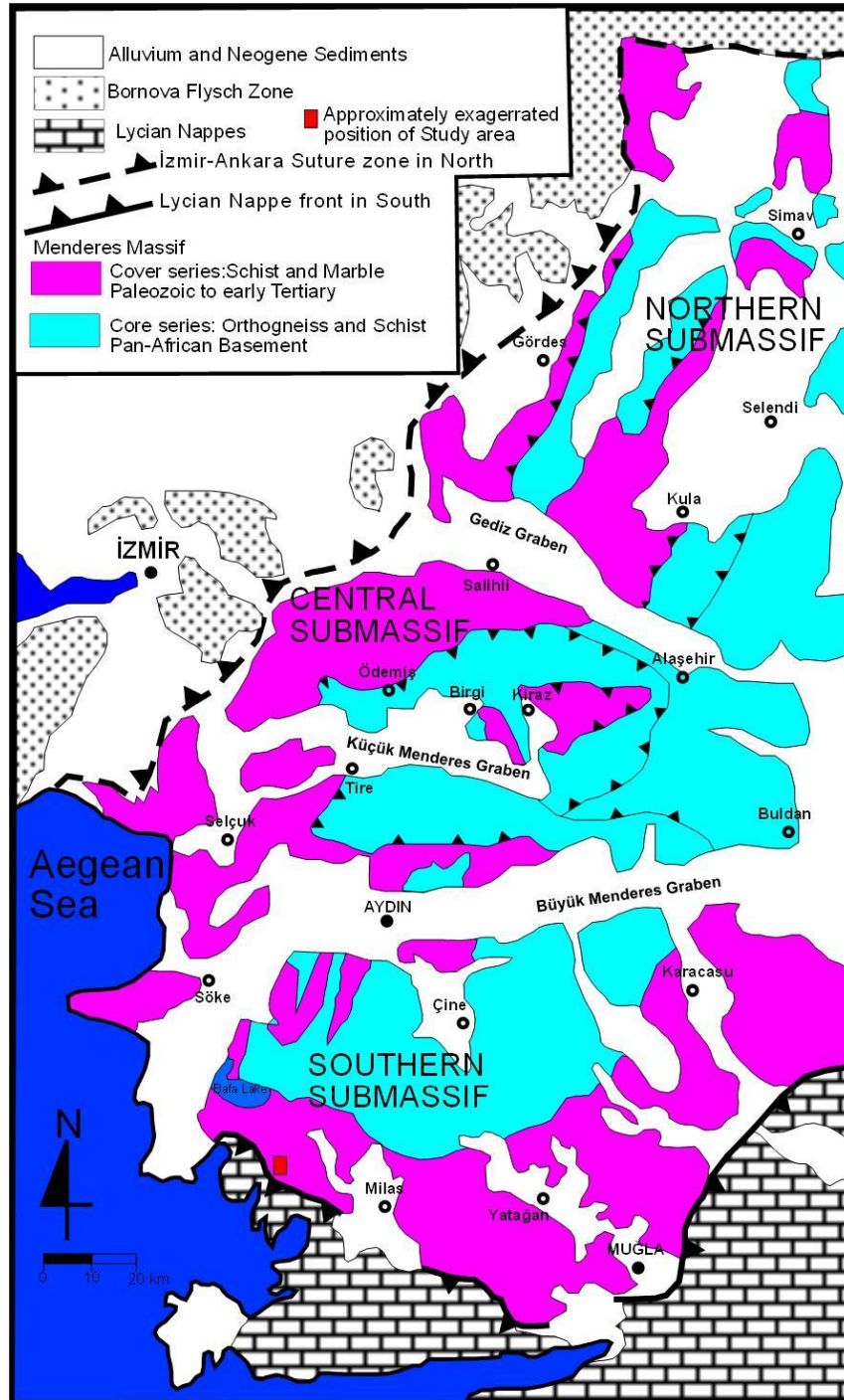


Figure 1.3 Simplified geological map of the Menderes Massif and subdivision into the submassifs (modified from Candan et al., 2000).

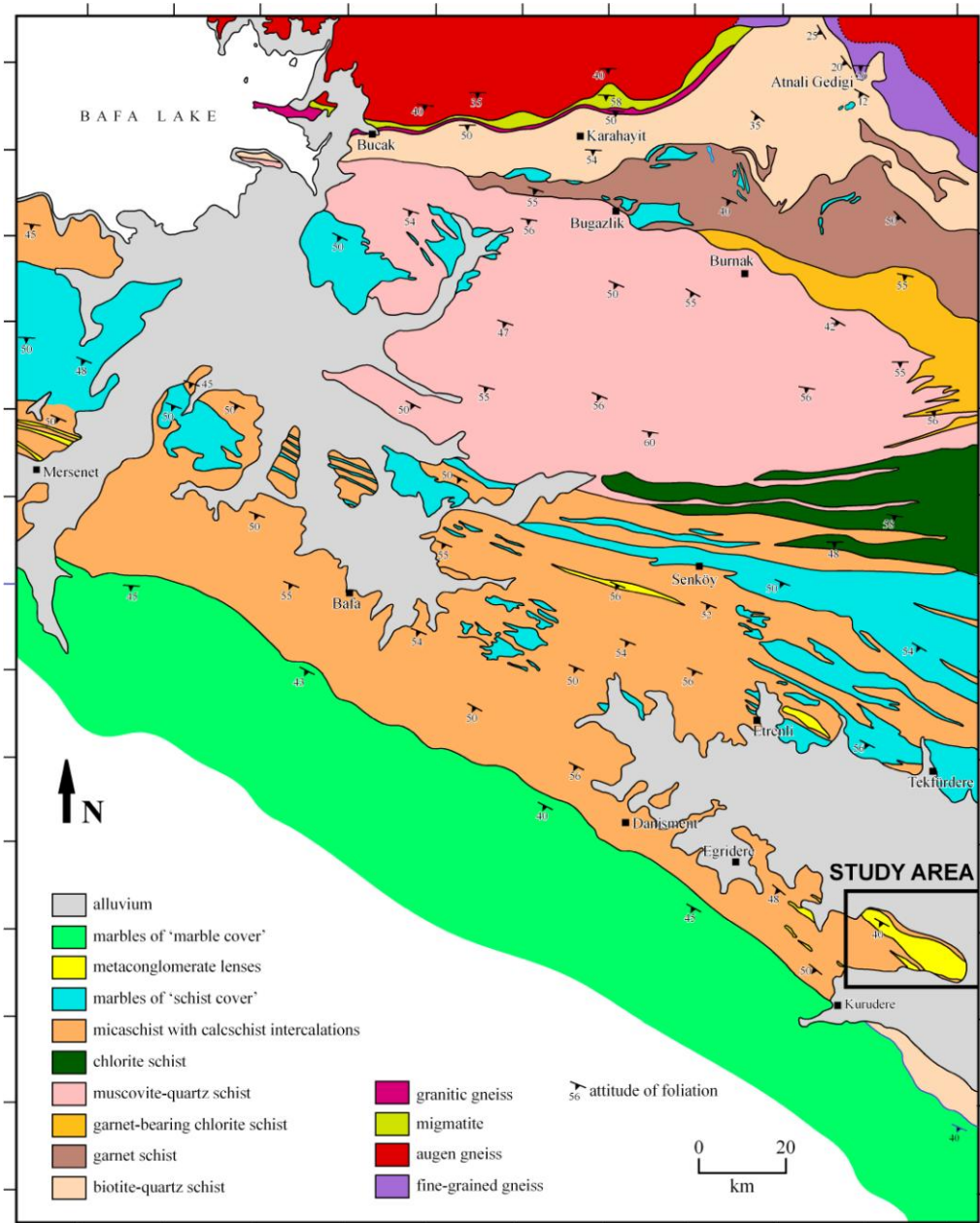


Figure 1.4 Geological map of the Bafa Lake-Selimiye area in the southern Menderes Massif (from Başarır 1970). Courtesy of Erdin Bozkurt.

## MUĞLA SHEET N19 a1

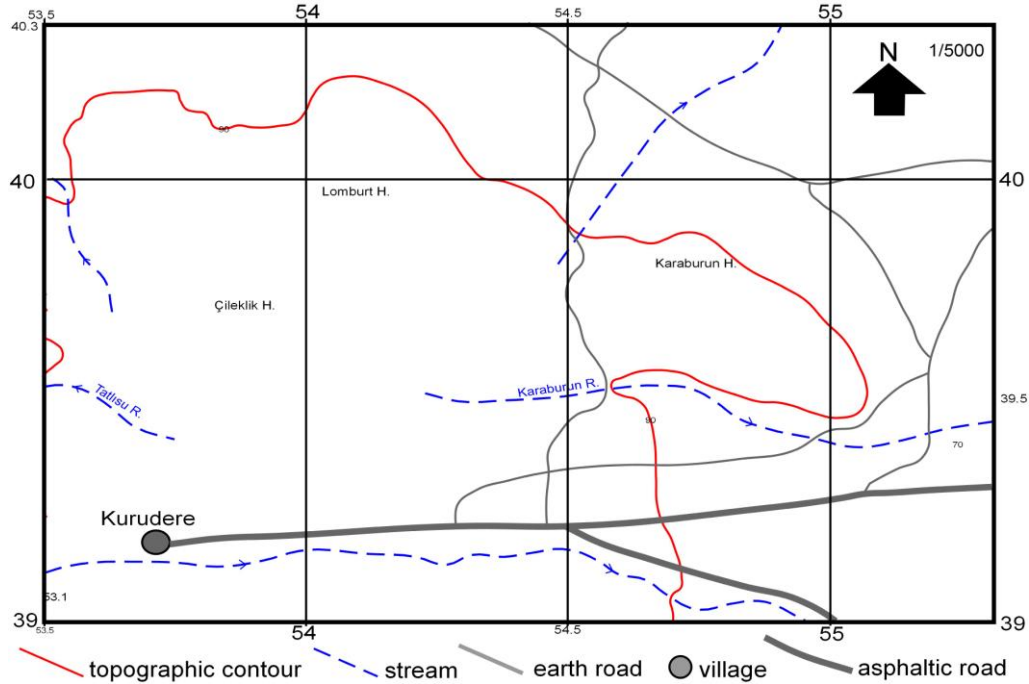


Figure 1.5 Location map showing topographic features of the study area.

### 1.4 METHODS OF STUDY

This research lasted for about two-and-half-years and involved both (i) field studies and (ii) laboratory studies.

The field studies include: (i) mapping of rock units and structural features such as folds, foliation and lineation at a scale of 1/5000, (ii) sampling for petrographic and age determination studies, (iii) measurement of attitude for foliation and lineation, (iv) detailed kinematic analysis to determine the sense of motion during deformation. Different rock units were, based on their physical appearance and mineral content, distinguished and mapped. To analyse and determine characteristic mineral assemblages and also to perform detrital zircon age determinations, each unit was sampled. All observations, detailed descriptions and coordinates were recorded in the field notebook during the excursion.

Laboratory studies were performed in Geochronology and Radiogenic Isotope Laboratory, Institute of Geoscience, Göethe Univesity of Frankfurt. Laboratory studies include (1) sample preparation: (i) crashing with jaw and roller crushers, (ii) Wilfley

table, (iii) heavy liquid, (iv) hand magnet and magnetic separation, (v) hand-picking under binocular microscopy, (vi) enclosing in epoxy resin, (vii) polishing, (viii) taking Cathodoluminescence (CL) images (a detailed explanation will be given in Appendix); (2) measurement of U-Pb isotope system contents of detrital zircons by using laser ablation induced couple mass spectrometry (LA-ICPMS). The analyses were performed with ThermoScientific Element 2 sector field ICP-MS coupled to a Resolution M-50 excimer laser system; (3) processing and interpreting the data by using an in-house MS Excel spreadsheet program (Gerdes and Zen, 2006, 2009; Millonig et al., 2012). The processed data was plotted on concordia diagram(s) by Isoplot 3.71 (Gerdes, 2012); (4) comparison of new age data and population with existing data from the Menderes Massif, Cyclades, North Africa, and from other relevant tectonic units; (5) attesting existing models over the age and origin of metaconglomerates and proposing a sound model.

## **1.5 GEOLOGICAL OVERVIEW OF SOUTHERN MENDERES MASSIF**

Menderes Massif (Parejas, 1940) forms a regional, crustal-scale, elliptical core complex, with its long axis trending in NE–SW direction, in the heart of southwestern Turkey extensional provenance; the massif covers an area of more than 40.000 km<sup>2</sup>. The Massif is a crustal-scale Tertiary metamorphic core complex (e.g., Bozkurt and Park, 1994; Lips et al., 2001; Ring and Collins, 2005) in extensional provenance of southwest Turkey. It acquired massif character during an Alpine orogeny that accompanied the latest Palaeogene collision between the Sakarya Continent and Anatolide-Tauride platform (e.g., Şengör and Yılmaz, 1981; Şengör et al., 1984) and consequent closure of the northern Neotethyan ocean. This was associated with Tertiary nappe translation, crustal thickening and consequent burial and regional high-temperature–medium pressure metamorphism, main Menderes metamorphism (MMM) (e.g., Şengör et al., 1984; Bozkurt, 1996, 2007; Bozkurt and Park, 1999; Bozkurt and Satır, 2000; Whitney and Bozkurt, 2002; Régnier et al., 2003, 2007; Rimmelé et al., 2003b; Dora, 2011 and references therein). The massif therefore contains evidence for a complex poly-tectono-metamorphic-magmatic history that involves HP–LT metamorphism prior to MMM (e.g., Candan, 1995, 1996; Candan et al., 1997, 2001, 2011b, c; Oberhänsli et al., 1997; Rimmelé et al., 2003a, b, 2006; Jolivet et al., 2004; Régnier et al., 2007; Whitney et al., 2008; Oberhänsli et al., 2010; Dora, 2011). The arrival of the massif is attributed to progressive exhumation in the footwall of several detachment faults and/or extensional shear zones during the post-orogenic Neogene N–S extensional history of the Menderes Massif (e.g., Bozkurt and Park, 1994, 1997a, b; Seyitoğlu and Scott, 1991, 1992a, b, 1994, 1996; Cohen et al., 1995; Emre and Sözbilir, 1995; Emre, 1996; Hetzel et al., 1995a, b, 1998, 2013; Hetzel and Reischmann, 1996; Rojay et al., 1998; Glodny and Hetzel, 2007; Seyitoğlu, 1997; Sarıca, 2000; Bozkurt 2001; Gessner et al., 2001a, b, c, 2004, 2013;

Gökten et al., 2001; Işık and Tekeli, 2001; Lips et al., 2001; Sözbilir, 2001, 2002; Hasözbek, 2003; Işık et al., 2003, 2004; Rimmelé et al., 2003a; Bozkurt, 2004, 2007; Bozkurt and Sözbilir, 2004, 2006; Işık, 2004; Seyitoğlu et al., 2004; Catlos and Çemen, 2005; Purvis and Robertson, 2005a, b; Purvis et al., 2005; Ring and Collins, 2005; Bacceletto and Steiner, 2005; Thomson and Ring, 2006; Çiftçi and Bozkurt, 2008, 2009a, b, 2010; Özgenç and İlbeyli, 2008; Catlos et al., 2010; Erkül, 2010; Ersoy et al., 2010a, b, 2011; Karaoğlu et al., 2010; Öner et al. 2010; van Hinsbergen, 2010; van Hinsbergen et al., 2010a, b, c; Emre et al., 2011; Hasözbek et al., 2011, 2012; Sözbilir et al., 2011; Altunkaynak et al., 2012; Catlos et al., 2012; Tatar-Erkül, 2012; Tatar-Erkül and Erkül, 2012; Çiftçi 2013; Gürboğa et al., 2013; Iredale et al., 2013; Özkaymak et al., 2013; Sümer et al., 2013).

The Massif is divided into three submassifs and E–W-trending Gediz Graben in the north and Büyük Menderes Graben in the south form the boundaries of the northern (Gördes), central (Ödemiş-Kiraz) and southern (Çine) submassifs, respectively (e.g., Dora et al. 1995; Whitney and Bozkurt, 2002; Bozkurt, 2007; Candan et al., 2011a) (Figure 1.3). It is generally accepted that the Menderes Massif is composed of a ‘gneiss core’ and a structurally overlying ‘Palaeozoic–Cenozoic cover series’ (Figures 1.3 and 1.4). The core rocks dominantly consist of augen gneisses (Şengör et al., 1984; Satır and Friedrichsen, 1986; Candan, 1995,1996; Candan et al., 1998, 2000; Oberhänsli et al., 1997, 1998). The cover rocks are made up dominantly of schists and marbles. The intensity of metamorphism increases towards the core (Bozkurt and Oberhänsli, 2001). As the study area is located within the southern Menderes Massif, the other two submassifs are not discussed in the following paragraphs.

The southern submassif is considered as the part of the massif where a complete record of its stratigraphy is well exposed. The submassif is traditionally considered to comprise two distinct lithologic associations: (1) metagranites/orthogneisses; it is known as the Precambrian (?) ‘core’ augen gneisses; (2) and structurally overlying high- to low-grade Palaeozoic–Middle Palaeocene metasedimentary sequence (e.g., Schuiling, 1962; Şengör and Yılmaz, 1981; Şengör et al., 1984; Ashworth and Evirgen, 1985; Bozkurt, 1996; Candan et al., 2001, 2011a, b, c; Gessner et al., 2001a; Whitney and Bozkurt, 2002; Erdoğan and Güngör, 2004; Whitney et al., 2008; Dora et al., 2011; Erdoğan et al., 2011; Koralay et al., 2011, 2012); the cover rocks are further divided into two units, so-called ‘*schist cover*’ and ‘*marble cover*’. Metamorphic grade increases from the metasedimentary rocks towards the gneissic core (Figure 1.6) (Whitney and Bozkurt, 2002).

The contact between core and cover rocks has been the subject of intense discussion over the last three decades and several controversial interpretations are made; all models now agree that this contact is a regional top-SSW ductile shear zone but no consensus are made over its nature and name. Thus, several different terms are used to

name this shear zone as top-S extensional shear zone Çine shear zone (Lips et al., 2001), top-S thrust fault, Selimiye shear zone (Ring et al., 1999, 2003; Gessner et al., 2001a, 2004; Régnier et al., 2003, 2007; Koralay et al., 2012), top-N extensional Kayabükü shear zone (Seyitoğlu et al., 2004) or top-S extensional southern Menderes shear zone (e.g., Bozkurt and Park, 1994; Hetzel and Reischmann, 1996; Bozkurt and Satır, 2000; Lips et al., 2001; Whitney and Bozkurt, 2002; Rimmelé et al., 2003b; Bozkurt, 2004, 2007; Seyitoğlu et al., 2004; Iredale et al., 2013). There are also claims that the shear zone is a inverted structure which operated first as a top-N contractional structure, then it was reactivated as a top-S extensional shear zone (Bozkurt 2004, 2007; Bozkurt et al., 2006).

The shear zone records a metamorphic break of about 2 kbar (equal to a missing metamorphic section of 7 km) and emplaces lower-grade metamorphic rocks over higher-grade metamorphic rocks. The orthogneisses form the footwall and the schists lie in the hanging wall. Similarly, the age of the protolith of the orthogneisses is also controversial and claims are Precambrian and/or Tertiary. One of the other characteristic feature of the southern Menderes Massif is described by presence of several stock-like and/or dyke/sill like bodies of tourmaline-rich two-mica leucogranites orthogneisses and lowermost parts of the schist cover (Bozkurt et al. 2006).

The schist envelope comprises several different lithologies, they include, from structurally lowest to highest, mica+quartz±garnet schists (widely known as paragneisses), quartz+muscovite±biotite±garnet schist (quartzite / meta-quartz arenite), pelitic schists (garnet+mica and mica+quartz±garnet±chloritoid schists) with carbonate lenses and bands, and a calcereous sequence dominated by marble with mica-schist / phyllite intercalations. The literature suggests that P–T conditions during their metamorphism reached up to ca 8 kbar and ca. 550°C at the structurally lowermost parts and ≤6 kbar and 430°C at the structurally upper parts (Whitney and Bozkurt, 2002). The age of the schists are considered to range from Precambrian to Permian (even early–middle Triassic) (Figure 1.7).

The marble cover comprises metaconglomerates with quartz and dolomite pebbles, massive marbles with local metapelite lenses and metabasites, marble with metabauxite lenses, dolomitic marble and Late Cretaceous Rudist-bearing marbles; the sequence ends with reddish-pinkish thin bedded pelagic cherty marbles with local pelitic interlayers and a metaolistostromal unit (Çağlayan et al., 1980; Konak et al., 1987; Dora et al., 2001; Özer et al., 2001; Régnier et al., 2003).

The age of the schist and marble envelope depends on regional correlations and inferences from early studies (except for the Rudist-bearing marbles). There is no single analytic data that bears on the protolith age of the schists and marbles.

The metasedimentary sequence in the southern submassif display a well-developed, regional, penetrative south-dipping foliation invariably associated with an approximately N–S-trending mineral stretching lineation; the dip of the foliation is about 30–40° but steeper dips up to 80° is also possible. The foliation, particularly towards the lower contact of the Lycian Nappes, is deformed by ~E~W-trending asymmetric and overturned folds with axes paralleling the Lycian front (e.g., Çağlayan et al., 1980; Bozkurt and Park, 1999; Whitney and Bozkurt, 2002). The regional foliation in the metasediments posses everywhere top-N kinematics and are attributed to a top–N thrust faulting during early Alpine contractional deformation and coeval main Menderes metamorphism. In and around the southern Menderes shear zone regional top-N fabrics are overprinted by exhumation-related top-to-the-S sense of shear. This presence of top-N and overprinting top-S fabrics forms the most overwhelming evidence to support the inverted nature of the southern Menderes shear zone (SMSZ) (Bozkurt et al., 2006; Whitney et al., 2002; Bozkurt 2004, 2007).

Contact between the cover schists and overlying cover marbles is also controversial. One school argues for a conformable boundary where schists and marbles form part of the same sequence (Çağlayan et al., 1980; Konak et al., 1987; Dora et al., 2001; Özer et al., 2001; Rimmelé et al., 2003b; Jolivet et al., 2004) whereas others claim for a thrust fault (Cyclades-Menderes thrust) relationship (Gessner et al., 2001a; Ring et al., 1999, 2003; Régnier et al., 2003, 2007; Whitney et al., 2008). The latter model proposes that marbles belong to Cycladic Massif in the Aegean. Gessner et al. (2001c) considered that Cyclades-Menderes thrust is coeval with Selimiye shear zone and runs subparallel to each other. Detailed studies make the structure world-widely important, because juxtaposition of different metamorphic grade rocks is not related to Tertiary extensional deformation but also with nappe stacking (Régnier et al., 2003). In contrast, there is overwhelming evidence that top-to-the-S shear sense is caused by crustal extension (e.g., Bozkurt and Park, 1994; Hetzel and Reischmann, 1996; Bozkurt et al., 1997a, b, 1999; Lips et al., 2001; Whitney and Bozkurt, 2002; Bozkurt 2004, 2007; Seyitoğlu et al., 2004; Catlos and Çemen, 2005; Iredale et al., 2013).

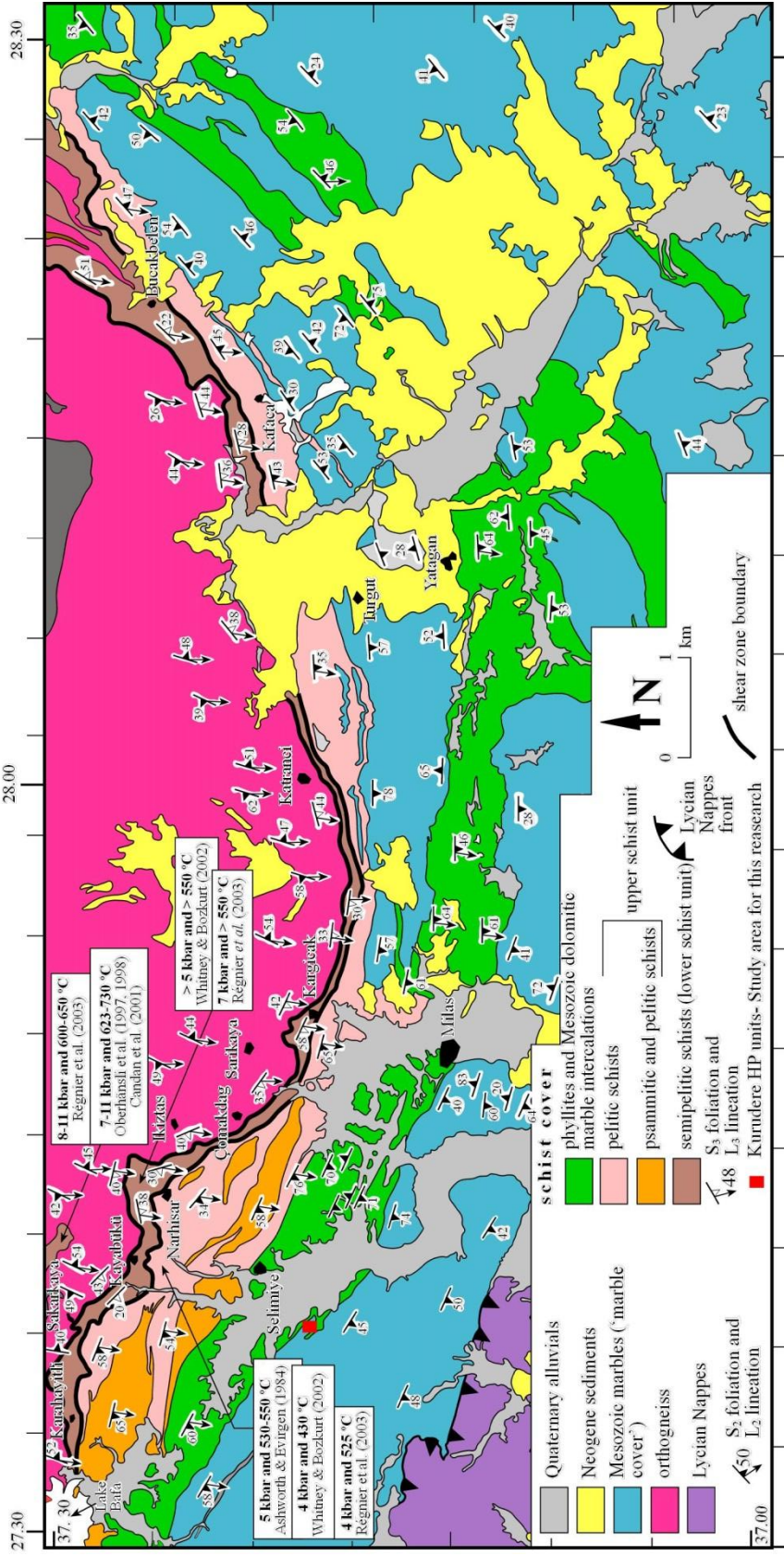


Figure 1.6 Simplified geological map of the Southern Menderes Massif (from Bozkurt, 2007).

The southern submassif is also interpreted as overturned limb of a large recumbent synform; orthogneiss in the core and younger schists in the rims (Okay, 2001). Whitney and Bozkurt (2002) disputed this model and argued that in an overturned synform the older lithologies should occur in the limbs and younger units in the core. There is also an incompatible relationship with the kinematics as well; the details are explained in Whitney and Bozkurt (2002).

The commonly accepted model in the Menderes Massif suggests that the massif character was acquired during a HT–L/MP main Menderes metamorphism (MMM), which was the result of burial beneath the southerly moving Lycian Nappes; but this model is incompatible with the dominant top-N fabrics both in the core and cover rocks of the massif. The top-to-the-S fabrics exist and they commonly occur within the southern Menderes shear zone or in other parts of the massif where top-to-the-N thrusts were reactivated as top-to-the-S normal faults. The age of top-N fabrics in this regard are also debated and claims range from Precambrian to Eocene (e.g., Bozkurt and Park, 1994; Ring et al., 1999; Gessner et al., 2001a; Oberhänsli et al., 2001; Whitney and Bozkurt, 2002; Catlos and Çemen, 2005).

The main Menderes metamorphism (MMM) is accepted as the main phase of metamorphism. There are several attempts to date the cooling ages in the southern Menderes Massif: (1) 63–48 Ma muscovite and 50–27 Ma biotite Rb-Sr mica ages (mean  $35\pm 5$  Ma; Satır and Friedrichsen 1986); (2)  $43.4\pm 1.3$ ,  $40.0\pm 1.8$  Ma,  $37.9\pm 0.4$  Ma and  $34.5\pm 1.4$  Ma  $^{40}\text{Ar}/^{39}\text{Ar}$  muscovite ages (Hetzl and Reischmann, 1996); (3)  $^{40}\text{Ar}/^{39}\text{Ar}$  muscovite age of  $32\pm 0.5$  Ma from augen gneisses (Gessner et al., 2001a); (4)  $47.1\pm 6.3$  Ma and  $42.8\pm 3.6$  Ma (average  $42\pm 5$  Ma) ages from monazite inclusions in garnets (Catlos and Çemen 2005). The evidence is therefore consistent with a Eocene age for the MMM (see Table 1.1 for details of geochronologic campaign in the southern Menderes Massif).

The other model about rock units of the Menderes Massif argues that the submassif consists of a stack of nappes (Menderes nappes) and there is no stratigraphic relationship between the so-called core and cover rocks (Ring et al., 1999; Gessner et al., 2001c, Régnier et al., 2003, 2007). The so-called core rocks are regarded as the structurally lower nappe (Çine nappe), the schist cover, the Selimiye nappe and the marble cover, the Dilek nappe. In this model, marbles of the Dilek nappe are correlated with Cycladic HP marbles and the contact between the underlying Selimiye and overlying Dilek nappes is interpreted as a thrust fault, namely the Cyclades-Menderes thrust.

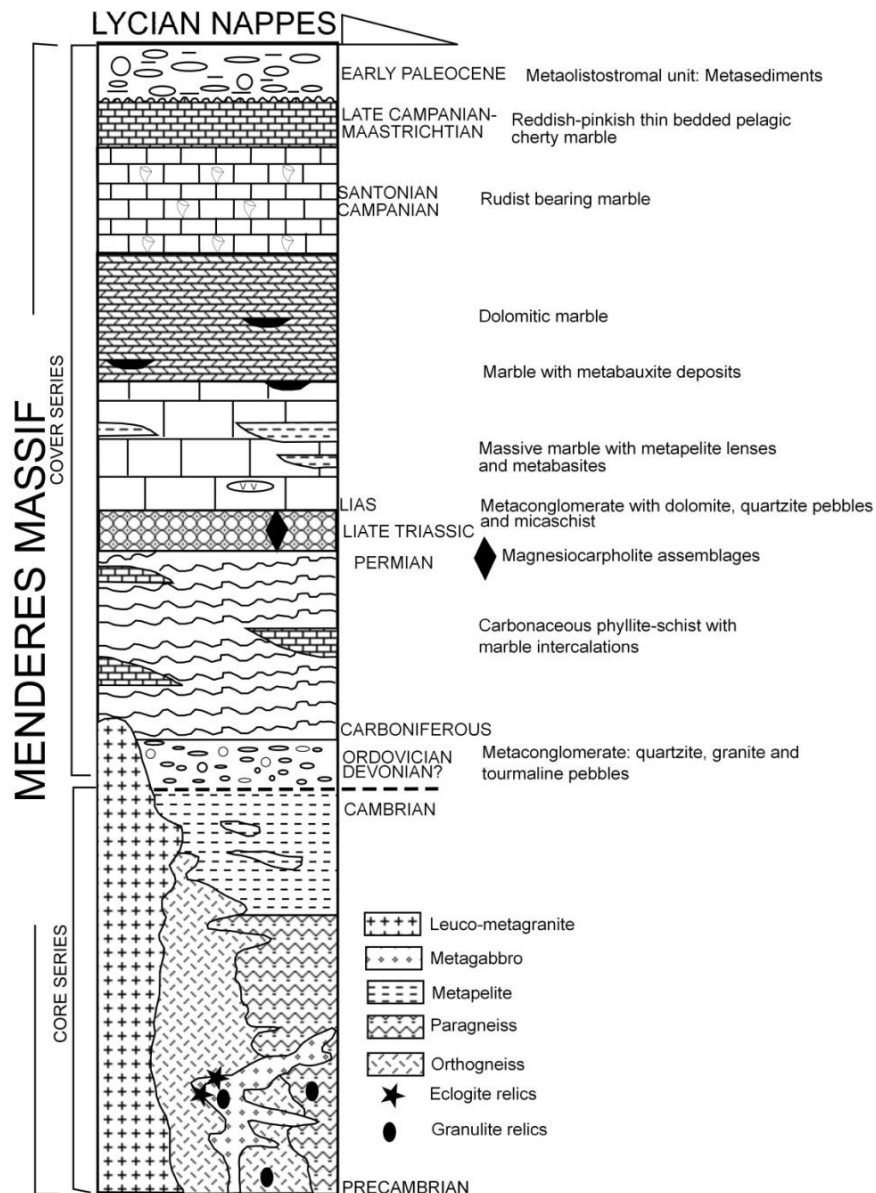


Figure 1.7 Simplified stratigraphic section of the southern Menderes Massif (from Rimmelé et al., 2003a).

## 1.6 PREVIOUS STUDIES: THE KURUDERE HP-LT ROCKS

There are several other controversial issues about the southern Menderes Massif and its complex poly-tectono-metamorphic-magmatic history but most lies outside the scope of this research. That is why previous section is mainly concentrated on some of the most crucial issues that are related to the main scope of this research.

To shed lights on some of the above-mentioned controversial issues, the metaconglomerates exposed near Kurudere (Selimiye-Milas) area are investigated. These rocks formed the subject of a number of studies and below a summary from relevant papers will briefly be presented.

Besides Lycian Nappes and eastern Mediterranean area, the blueschist facies rocks in whole southern Menderes Massif are scarce and are mostly represented by relic paraganesis (magnesiocarpholite-kyanite and chloritoid assemblages) in the metaconglomerates (Oberhänsli et al., 2001; Rimmelé et al., 2003a; Jolivet et al., 2004; Whitney et al., 2008; Pourteau et al., 2013). Three localities in the southern Menderes Massif are Nebiler village (near Kavaklıdere), near Ören (Muğla, Gökova Gulf) and Kurudere village (Selimiye-Milas). Metaconglomerates in the Kurudere village (Figures 1.4 and 1.8) forms the mostly studied key unit where HP-LT metamorphic relics were first observed and reported by Rimmelé et al. (2003a).

Metaconglomerates in the Kurudere area occur at the base of the cover marbles and is characterized by quartz pebbles within micaceous matrix; the relative abundance of micas and quartz in the matrix is variable from one location to another. There are two important studies on the Kurudere metaconglomerates by Rimmelé et al. (2003a) and Whitney et al. (2008).

Rimmelé et al. (2003a) reported magnesiocarpholite-kyanite-chlorite-quartz assemblages within quartz veins. Relic hair-like fibres of magnesiocarpholite is characteristic and locally occur with kyanite which occurs as a long and rough prisms running parallel to the magnesiocarpholite micrometer-scale fibres; the authors argued that carpholite in this particular locality is very similar to those occurrences in the eastern part of Samos (cf. Okrusch et al., 1984). Pyrophyllite is reported as secondary retrograde mineral. Phengite is rarely observed in the samples from Kurudere and their crystals show close parallelism with the kyanite crystals. A regional foliation is well-developed and is oriented in NE–SW direction and dips to the SE. Several small-scale intrafolial folds are common structural elements and many are apparent when they deform quartz veins with HP relics.

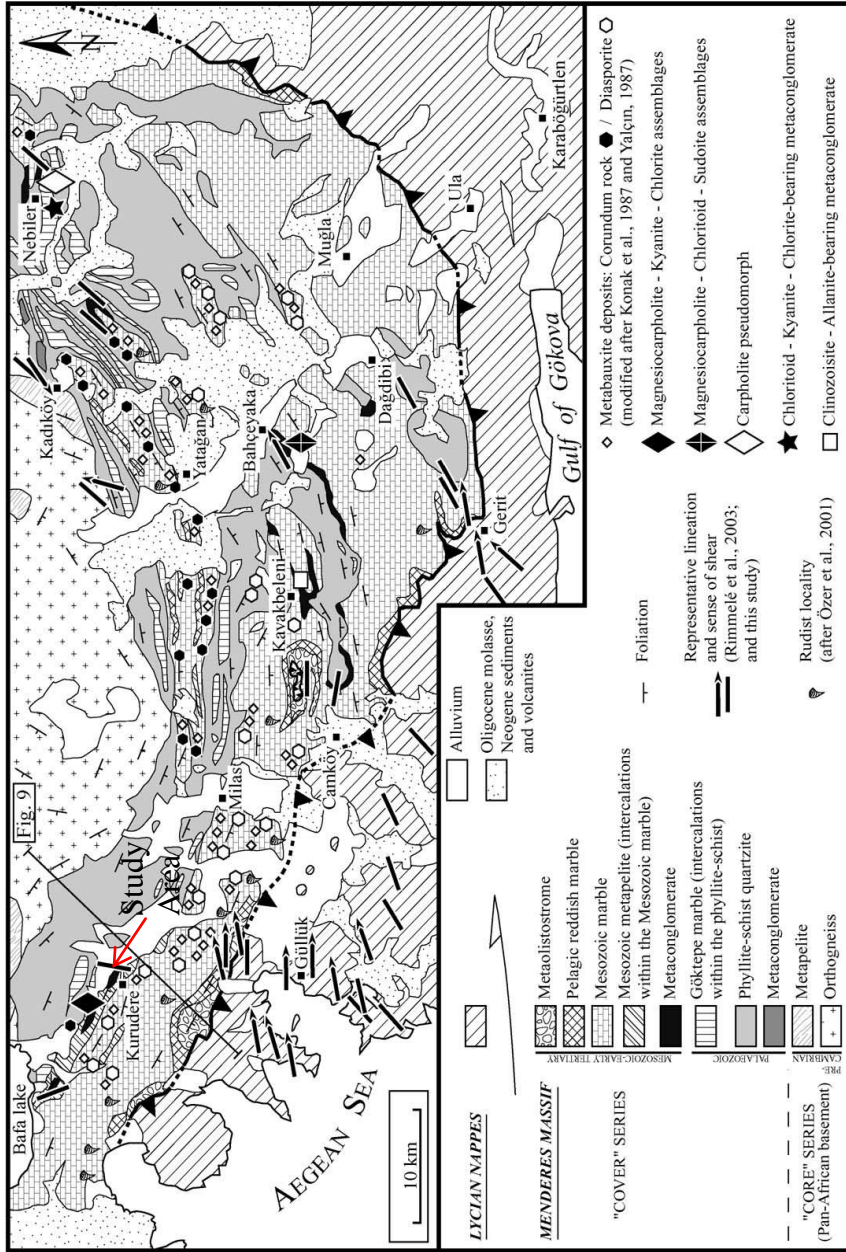


Figure 1.8 Geological map of the southern Menderes Massif showing the location and distribution of HP assemblages (from Rimmelé et al., 2003a).

The discovery of carphiolite in cover series of the southern submassif is interpreted to suggest that the MM underwent HP-metamorphism during Alpine history. P–T conditions are determined with phase equilibria as 10–12 kbar and 440 °C during Eocene which can be correlated with Eocene (40±0.4 Ma; Oberhansli et al., 1998) blueschists described in the Mesozoic marble sequence of the Dilek Peninsula (min. 10 kbar/max. 470 °C; Candan et al., 1997). Rimmelé et al. (2003a) speculated a responsible mechanism for this HP metamorphism as burial contemporaneous with Alpine subduction and nappe stacking. More recently, Pourteau et al. (2013) determined 45.9±2.0 Ma phengite (white mica) Ar-Ar age from these rocks.

Rimmelé et al. (2003a) argued for four stages for tectono-metamorphic evolution of submassif; (1) southward movement of Lycian Nappes and burial of Menderes and Cyclades massifs' sedimentary units; (2) the main Menderes Metamorphism related top-to-the-N shearing and north-verging thrusting, folding and consequent HP metamorphism. Top-to-the-N shearing triggered backthrusting of the Lycian Nappes and exhumation of the Lycian HP rocks; (3) final exhumation during Oligo–Miocene N–S extension in the footwall of km-scale low-angle detachment faults (Figure 1.9). This model was later supported by Jolivet et al. (2004). Rimmelé et al. (2003a) also argued that metasedimentary rocks in the Kurudere area form a part of Menderes 'cover' rocks but HP metamorphism was correlated with Dilek Peninsula (Cyclades) metasedimentary rocks.

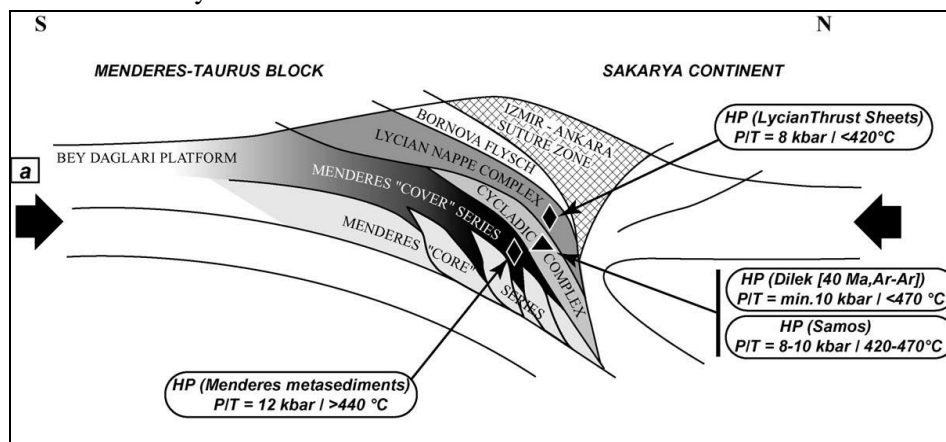


Figure 1.9 View of the accretionary complex during the Eocene showing the structural position of the main HP units in Western Anatolia (from Rimmelé et al., 2003a).

Whitney et al. (2008) studied petrology of carphiolite-bearing HP-rocks, estimated P–T conditions and discussed their tectonic significance; they have also addressed the question if these HP rocks belong to the southern Menderes Massif or they form a part of Cyclades. They have reported structural and petrological features of the Kurudere village HP-metasedimentary sequence in detail. They prepared a geological map of the

area (Figure 1.10) and defined four different lithologies: (1) quartz metaconglomerate that contains mm- to cm-scale quartz grains and aggregates. In the matrix, mm-scale phengite was observed with kyanite and chlorite. White mica is rimmed by chlorite. Kyanite is around 7 cm long in quartz veins and mm-scale in the matrix. Aligned quartz grains and kyanite define a well-developed mineral lineation; (2) strongly foliated kyanite schist interlayered with quartz-rich; the foliation is defined by fine-grained chlorite and white mica. Bigger chlorite minerals crosscut the foliation. Kyanite is up to 4 mm long; (3) concordant quartz veins within the schist; veins are commonly folded and boudinaged. Some are monomineralic but others contain kyanite crystals, up to 6 cm long, and magnesiochloritoid; (4) carbonate conglomerate in northern margin of the area; they do not contain neither HP index minerals nor quartz veins. Whitney et al. (2008) did not find chloritoid in this area and they suggest that it is conformable with 10–12 kbar and 440 °C conditions. They are more concerned with kyanite in the schists to determine metamorphism conditions. Pseudosection calculations for kyanite schists provide evidence for the stability of garnet and chloritoid but neither has been observed in the unit. On the other hand, the conditions are also stable for chloritoid which occurs in quartz veins in the schist.

The orientation of the Karaburun ridge is subparallel to strike of foliation. Foliation dips are variable. Lineation is defined by preferred parallel alignment of quartz augen. Quartz veins are general subparallel to the strike of foliation, folded and boudinaged but in places crosscutting relationships with the foliation is also evident. Quartz grains display foam-texture, curved grain boundaries and well-developed triple junctions. Kyanite and phengite grains were also deformed. Whitney et al. (2008) also documented (1) the occurrence of kyanite not only in the veins, but also in quartz-rich rocks, (2) the presence of carbonate metaconglomerate in the northern margin of the ridge, (3) absence of HP index mineral in carbonate metaconglomerates, and (4) abundance of phengite in quartz-rich rocks and schist. They have also argued that there is no textural evidence for the reaction magnesiochloritoid = kyanite + chlorite + quartz + H<sub>2</sub>O, and for the breakdown of chloritoid. Additionally, top-to-the-N sense of shear in kyanite- and phengite-bearing quartz-rich unit was interpreted as syn-kinematic with respect to the HP metamorphism whereas top-to-the-S sense of shear is observed in north of Kurudere village and are attributed to subsequent extensional deformation. The evidence is further used to suggest that the Kurudere HP rocks have a different P–T history than the so-called schist cover of the southern submassif. But it was difficult to evaluate the metamorphic history because the southern Menderes schists do not record any clues for the presence of a HP metamorphism. This piece of information highlights the importance of Kurudere HP rocks in the better understanding of the the evolution of the southern submassif.

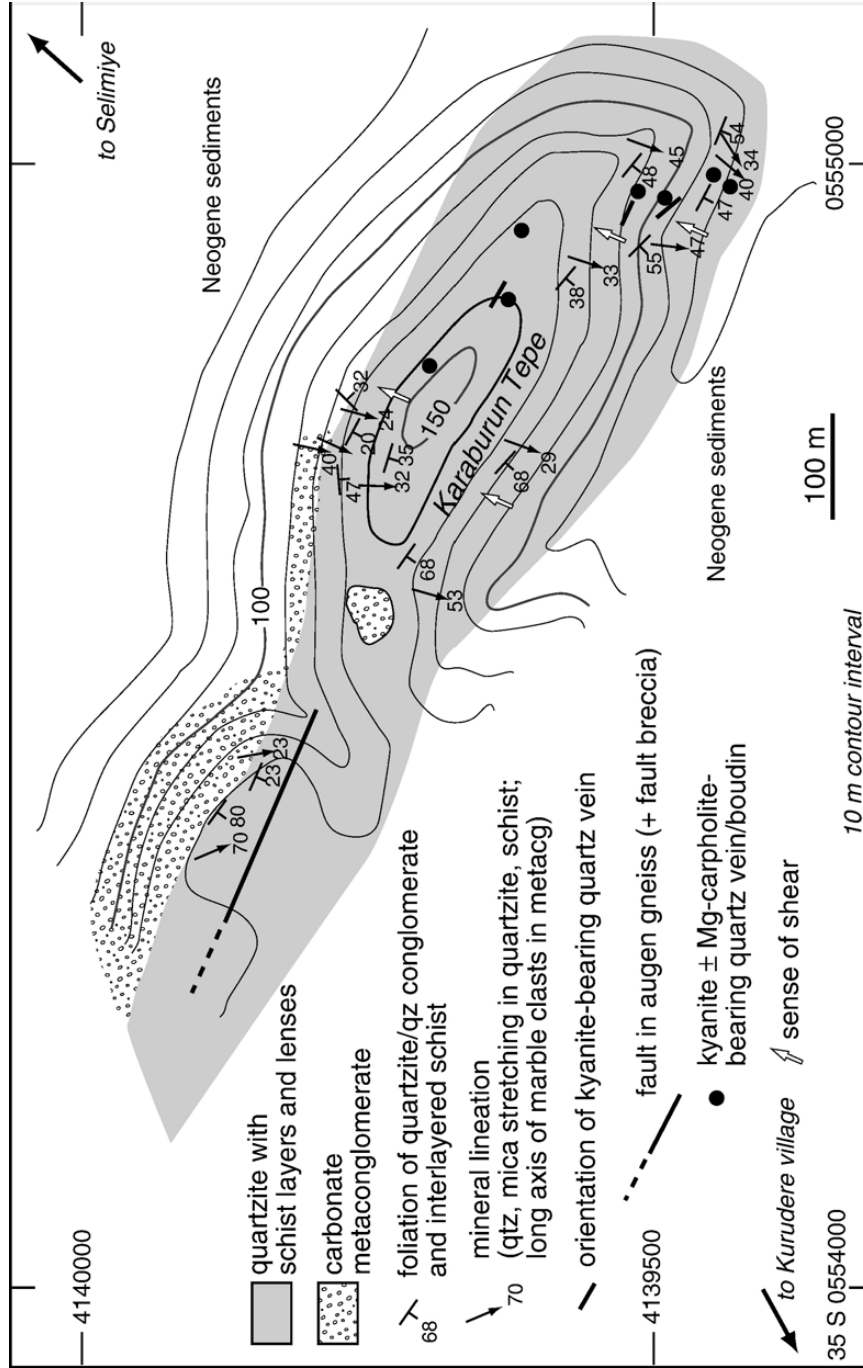


Figure I.10 Geological map of the Karaburun Ridge (from Whitney et al., 2008).

In the literature, as mentioned above, two conflicting models are proposed to discuss the origin and tectonic significance of HP metaconglomerates in the Kurudere area. One of the model argues that the HP–LT rocks are part of the metasedimentary cover to the Menderes Massif (Rimmelé et al., 2003a; Jolivet et al., 2008) while others claims that the metaconglomerates and overlying marbles are representatives of Cycladic blueschist unit (Ring et al., 1999; Gessner et al., 2001c; Whitney et al., 2008) in the southern Menderes Massif. The latter model also argues that these HP–LT rocks are lithologically very similar to those in the Cyclades; the presence of quartzite conglomerate with interlayered kyanite–chloritoid schists supports this contention (Gessner et al., 2001c). If the southern submassif HP rocks are part of the Cycladic blueschist unit, then the age of metamorphism should be middle Eocene ( $^{40}\text{Ar}/^{39}\text{Ar}$  phengite ages from Cyclades= 55–45 Ma; e.g., Wijbrans et al., 1990) and must have taken before the main Menderes metamorphism. The most recent  $45.9\pm 2.0$  Ma Ar–Ar mica age (Pourteau et al., 2013) from Kurudere metaconglomerates casts doubts on this model. This further brings an important question about the spatial and temporal relationship between HP–LT metamorphism and main Menderes metamorphism (MMM).

The kinematic evolution of the southern Menderes Massif is controversial. Relationship between deformation and metamorphism, the age of the penetrative fabrics in the augen gneisses (Neoproterozoic vs Alpine), the boundary relationships between the so-called core and cover rocks (regional Pan-African angular unconformity, thrust fault or extensional shear zone), the age of augen gneisses and other granitic rocks (Precambrian vs Tertiary), age of metasediments, origin of marbles and associated metaconglomerates form the subject of main controversies and focus of intense research over the last two decades (e.g., Bozkurt and Park, 1994; Ring et al., 1999; Bozkurt 2004, 2007; Whitney et.al., 2008; Candan et al., 2011a, b, c, 2012; Koralay et al., 2011, 2012; Gessner et al., 2013 and several other papers). Some studies argue that the main metamorphism is Alpine and associated with top-to-N fabrics that are locally crosscut by top-to-S greenschist facies extensional shear zones (e.g., Bozkurt and Park, 1997, 1999; Bozkurt, 2007; Seyitoğlu et al., 2004), whereas others attribute the primary fabric to pre-Alpine tectonic events (Neoproterozoic Pan-African orogeny) overprinted by Alpine top-to-S shear zones (Gessner et al., 2001a, 2004; Régnier et al., 2003). Both top-to-N and top-to-S fabrics occur in the southern Menderes Massif. Others argue that pervasive top-to-N fabrics are result of Alpine contractional deformation during Eocene which made it ‘massif’. Alpine contractional deformation phase is characterized by penetrative regional foliation and N–S-trending mineral lineation (Bozkurt et al., 2001). The top-to-S fabrics might occur during retrograde metamorphic evolution at greenschist facies conditions.

The carpholite-bearing metaconglomerates seem to play an important role in understanding the tectono-metamorphic history of the southern Menderes Massif.

Despite of its importance the briefly described models are not supported by overwhelming evidence. For example, the late Triassic age is based on regional correlations but no further evidence is provided. Also, the provenance of the metaconglomerates if they belong to the southern Menderes sequence or form a part of Cycladic unit is based on the presence or absence of HP relics in these rocks. There is therefore an urgent need to shed light in some of these existing controversies over the tectonic significance of the metaconglomerates.



## CHAPTER 2

### DESCRIPTION OF UNITS

#### 2.1 INTRODUCTION

Kurudere HP metamorphic rocks, mainly represented by metaconglomerates, occur at the base of the Mesozoic–Early Tertiary marble cover immediately above the Palaeozoic schists (the schist cover) in the southern Menderes Massif (Selimiye, Milas). The marble-dominated HP rocks are located structurally below the HP–LT Lycian Nappes and above the regional metamorphosed (Barrovian type) Palaeozoic schists of the southern Menderes Massif (Figures 1.3, 1.4, and 1.6–1.8). In the nappe model, they form the lowest unit of Cycladic HP unit (Dilek nappe) and lies structurally above the Selimiye nappe (Ring et al., 1999; Gessner et al., 2001c; Régnier et al., 2003, 2007).

As is summarized in Chapter 1, the metaconglomerates at the base of marbles have previously been studied by Rimmelé et al. (2003a) and Whitney et al. (2008). The previous studies have mainly concentrated on the petrology of these rocks and on estimating P–T conditions of their metamorphism. In the present study, we aimed at mapping different lithologic associations (Figure 2.1) and concentrate on the fabric elements that may bear on the regional structure of these rocks. Of course, we have also carried out detailed petrographic analyses of constituent rocks and compared our observations with already published data. Mineralogical investigations are done by using thin sections and backscattered images using scanning electron microscope.

#### 2.2 ROCK UNITS

Two different rock units are mapped in the study area: (1) metaconglomerates and (2) metapelites. In addition to all, quartz veins also form important elements of the study area.

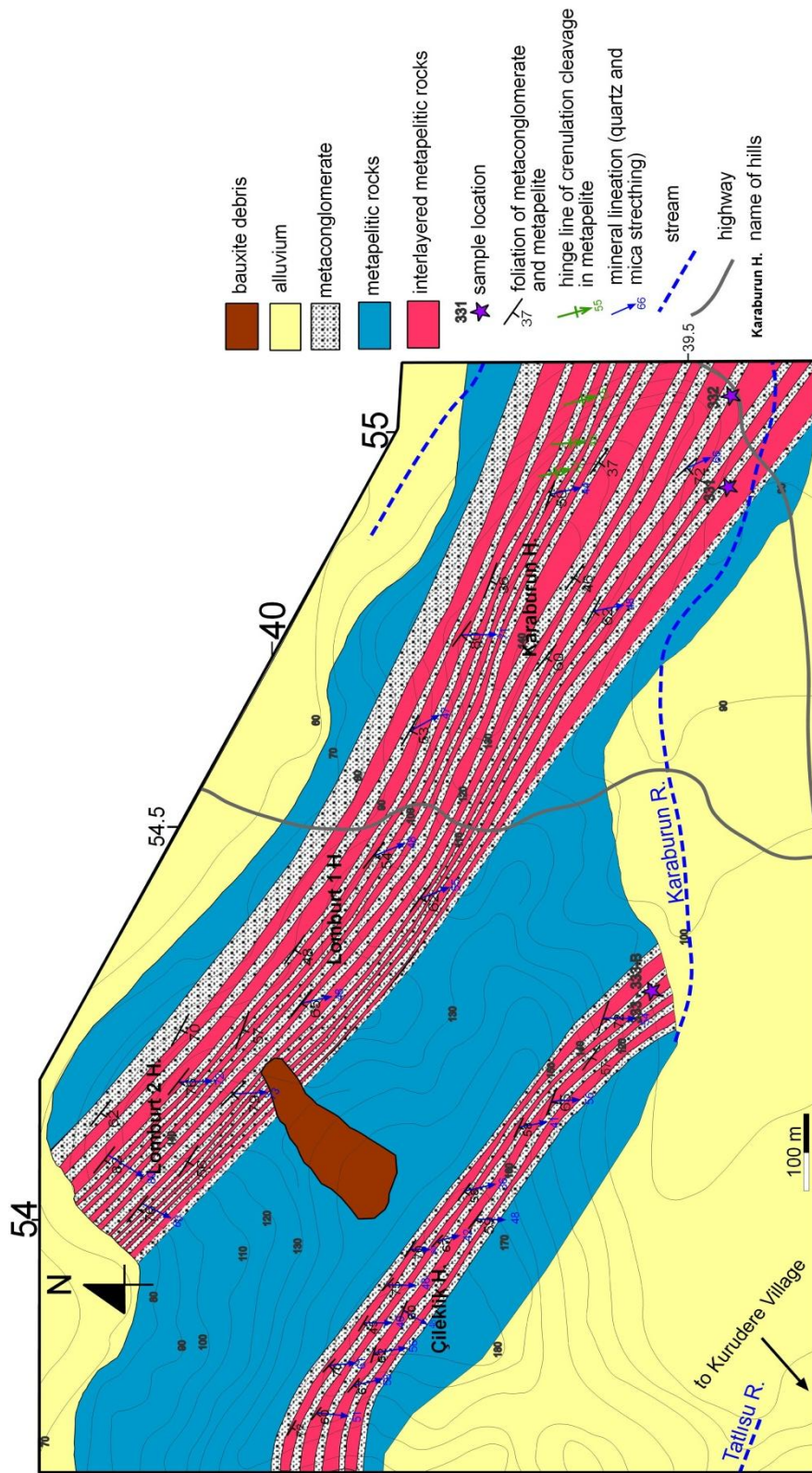


Figure 2.1 Geological map of Kurudere HP metamorphic rocks.

### 2.2.1 METACONGLOMERATES

Metaconglomerates in the southern Menderes occur at the base of the marble cover and crops out as isolated exposures at several locations in the area between Bafa Lake in the west and Nebiler (Kavaklıdere) in the east along a belt that runs for about 150 km (Rimmelé et al., 2003a). They are typical deformed and metamorphosed conglomerates, containing mainly quartz pebbles of variable sizes. Metaconglomerates are the dominant lithology in the Kurudere area; light greyish white and yellow colours are characteristic. It is a grain-supported rock, characterized mainly by white quartz pebbles within a mica-rich matrix; there are also mm- to cm-scale black quartz/quartzite pebbles (Figure 2.3). The original bedding ( $S_0$ ) is readily recognizable and is commonly separated by thin metapelites. The foliation ( $S_1$ ) is penetrative and is parallel and/or subparallel to the original bedding plane. Thickness of individual beds may reach up to ~1.5–2 metres. Because of its resistance to weathering, metaconglomerates stand out and form thin ridges in the study area (Figure 2.2); their physical appearance is therefore used as a criteria to recognize them from a distance. In some levels, the removal of the quartz pebbles from the matrix leaves behind cavities/holes, thus forming a characteristic appearance of the rock (Figure 2.3).

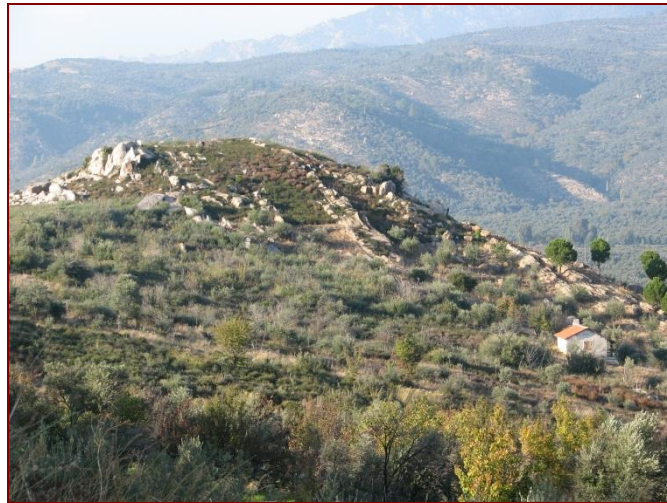


Figure 2.2 A view from thin ridges formed by metaconglomerates.

Relatively small pebbles are deformed, flattened, elongated in the plane of foliations (Figure 2.4 a–d); in many cases the long axes of elongated pebbles are aligned parallel to the mineral stretching lineation in the rock. Whereas larger pebbles resist deformation and they commonly occur as asymmetric grains with a typical  $\sigma$ -geometry, giving the rock an augen structure (Figures 2.3 and 2.4 e, f). The penetrative foliation dips to the south and is defined by the parallel alignment of micas, quartz grains and flattened quartz pebbles. The lineation is also penetrative and is mostly

defined by the parallel and preferred alignment of micas, stretched quartz grains and elongated quartz pebbles; the general trend of lineation is N-S and plunge is toward south. The deformed and elongated pebbles define a well-developed discrete object lineation and indicate the intensity of the ductile deformation that accompanied their metamorphism.

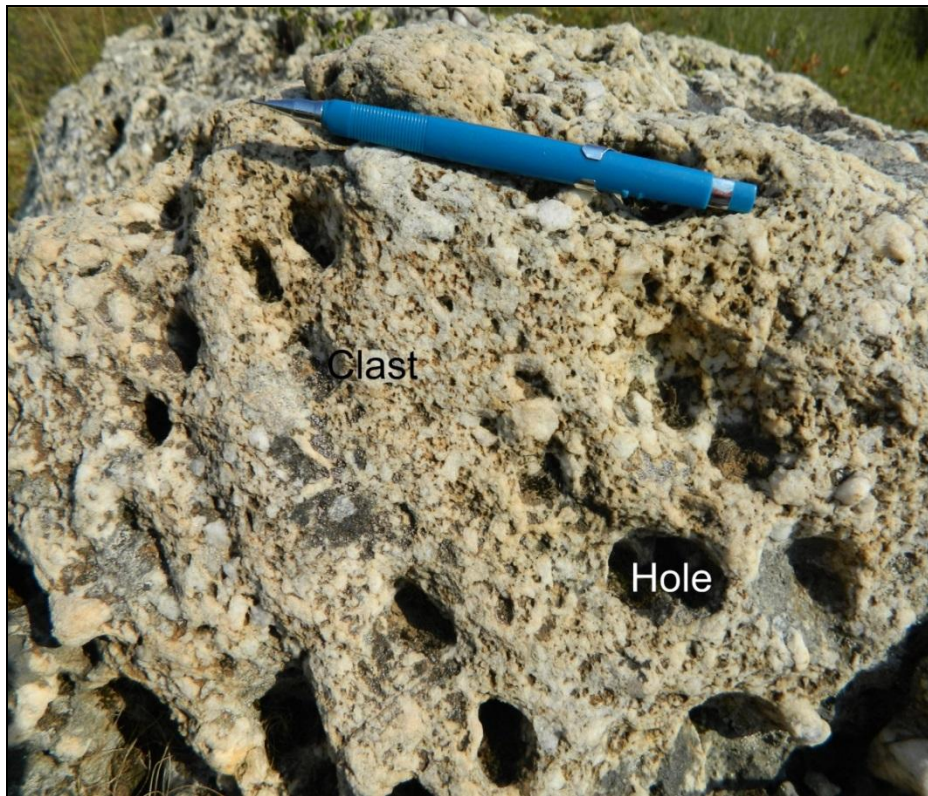


Figure 2.3 A view from the metaconglomerates. Please note abundance of holes left behind by the weatering and removal of quartz pebbles.

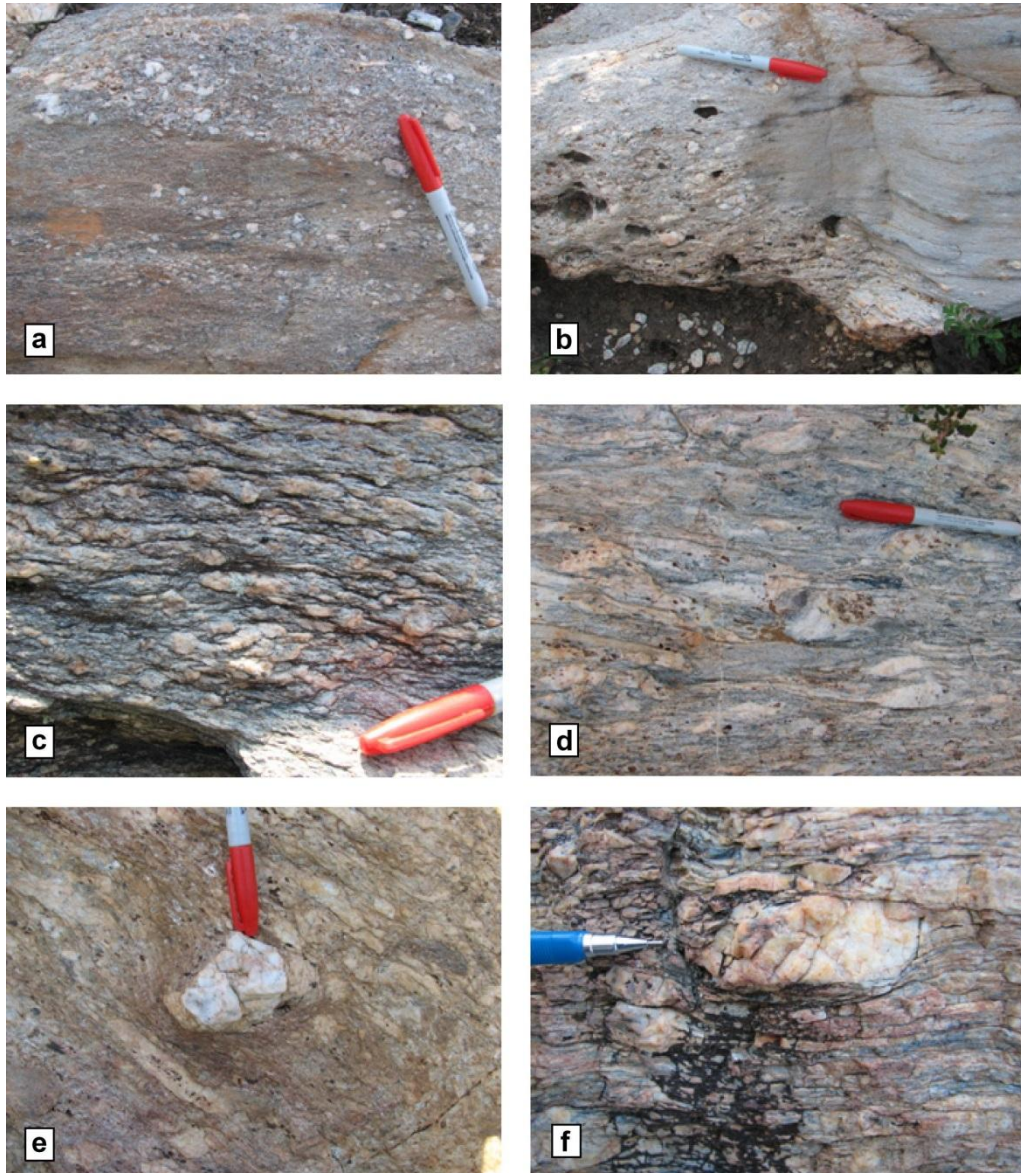


Figure 2.4 Views from the metaconglomerates. (a) There is grain size variation within the same bed where pebble-rich and pebble-poor domains seem to alternate. (b) The lateral passages between pebbly and sandy levels are also common. (c, d) In almost everywhere larger quartz pebbles are deformed, flattened and elongated in the plane of foliation. In such cases, foliation is pronounced and penetrative. (e, f) In other cases, large quartz pebbles resist deformation and appear as large porphyroclasts within a fine grained matrix foliation, thus giving the rock an augen structure. Note in (f) how relatively smaller pebbles are flattened and elongated and define the matrix foliation. Also, matrix foliation abust against the large quartz pebble.



Figure 2.5 A view from the metaconglomerate. Note the difference in the degree and intensity of deformation between relatively larger and smaller quartz pebbles. Also note that one of the larger pebbles defines  $\sigma$ -geometry, which is consistent with a top-to-the-left sense of shearing. Foliation is penetrative and well developed; elongated and flattened quartz pebbles in the foliation plane are evident.

The matrix is comprised of quartz, white mica, chlorite and kyanite. Quartz grains display undulose extinction. Mica minerals are preferably parallel aligned and define the main foliation in the rock (Figure 2.6). Quartz in the matrix tends to form equant grains whereas those larger grains occur as augen and commonly show subgrain formation with characteristic patchy and/or undulose extinction. In many cases, the larger grains are actual clasts but there are also examples of disaggregated quartz veins as well. The dominal structure, defined by the concentration of quartz and mica and as well as the grain size variation in quartz, is a very characteristic feature of matrix lithologies (Figure 2.6). Smaller quartz grains commonly are elongated and define a ribbon structure; individual quartz grains are aligned parallel to each other and define the main foliation in the rock. Larger grains show characteristic undulose extinction and perfect triple junctions (Figure 2.6). Relatively thin white mica (phengite) domains are also characteristic and occur in-between quartz-rich domains (Figure 2.6). The white-mica domains are also characteristic and observable at outcrop-scale and commonly define the main foliation in the rock.

The chlorite is also common and occurs together with phengite; it forms thin rims around the white mica grains. Twinned and deformed large kyanite also occurs as main constituent of this rock (Figures 2.7 and 2.8). This observation is consistent with that of Whitney et al. (2008) and is in conflict with that of Rimmele et al. (2003), who suggested that kyanite occurs only in the quartz veins. Accessory minerals are magnetite, zircon, rutile, epidote and apatite (Figure 2.9). Rutile, replacing magnetite, is also observed in some of the thin sections.

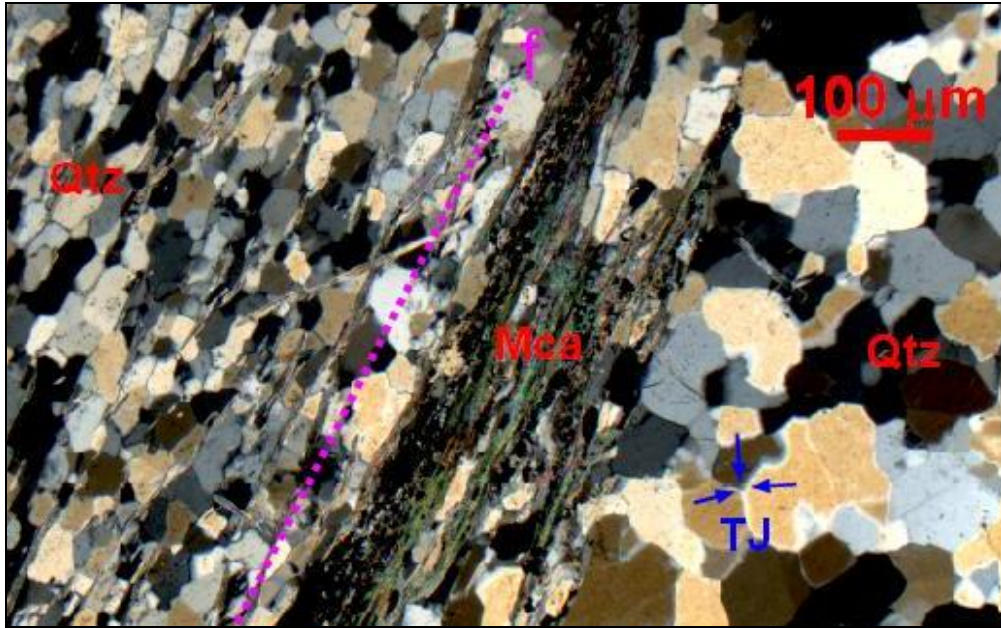


Figure 2.6 Photomicrograph from matrix of the metaconglomerate. Note domainal structure of the rock, defined by quartz- and mica-rich domains. There are also textural differences in the quartz domains. Fine-grained equant quartz grains (to the left) define a ribbon structure where long axis of elongate quartz grains define a foliation paralleling that of white mica foliation. Larger quartz grains are characteristic with their patchy and undulose extinction and define well-developed triple junctions (TJ) among the grains; this indicates the role of recovery process. Otherwise, quartz grains tend to show regular and straight boundaries with local embayments. Mica-rich domain (Mca) defines a penetrative foliation and also forms the boundary between quartz-rich domains.

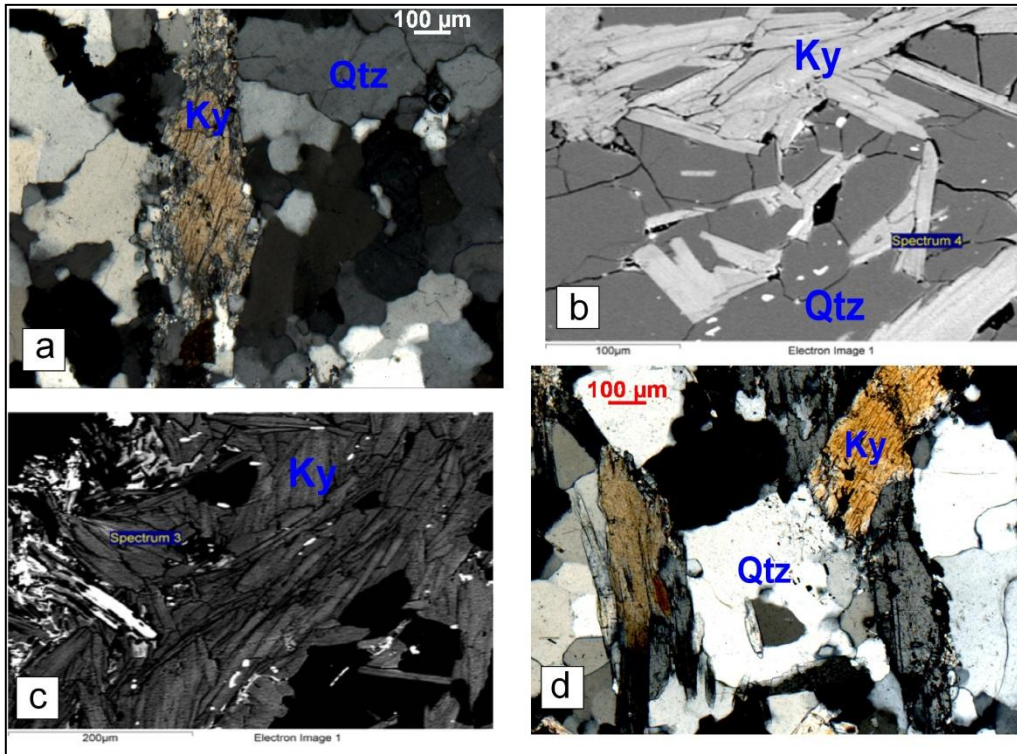


Figure 2.7 Photomicrographs from the metaconglomerate. (a–d) Microscopic (crossed polars) view of kyanite (Ky) and quartz (Qtz). Note that kyanite in (a) tends to show parallelism with the foliation in the rock. Quartz grains in both microphotograph are larger crystals and show undulatory extinction. Note also triple-grain boundary among grains in lower left corner of (d). (b, c) BSE images of kyanite and quartz.

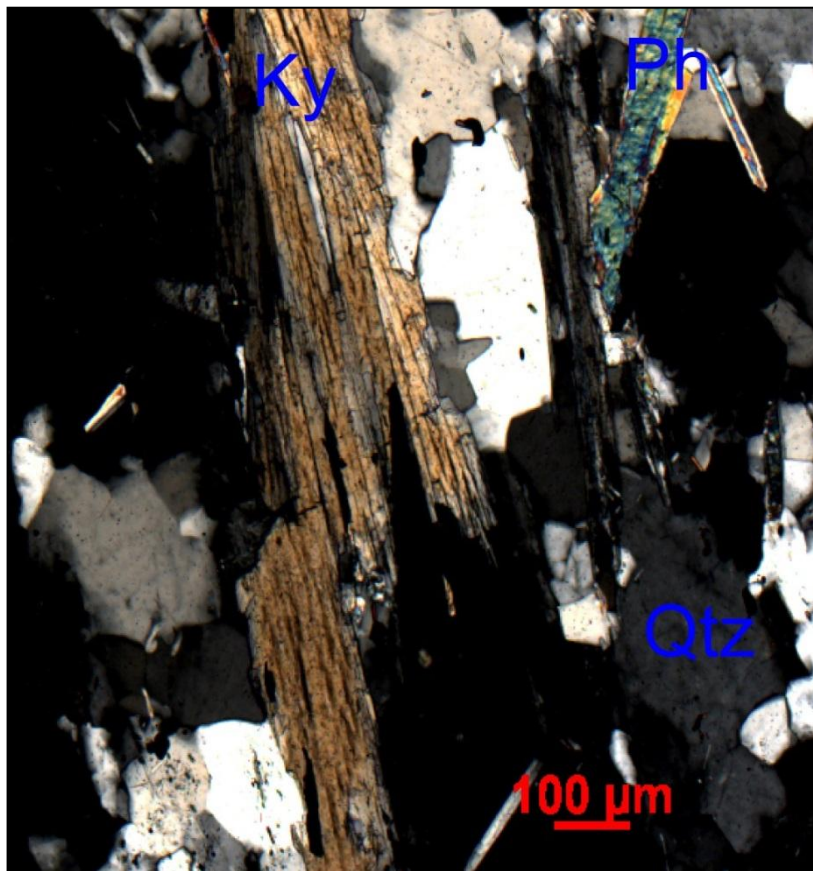


Figure 2.8 Photomicrograph (crossed polars) of a coarse kyanite (Ky) together with quartz (Qtz) and phengite (Ph) in matrix of the metaconglomerate.

Element	Weight%	Atomic%
O K	48.55	73.81
Ti K	50.85	25.75
Fe K	0.60	0.18
Totals	100.00	

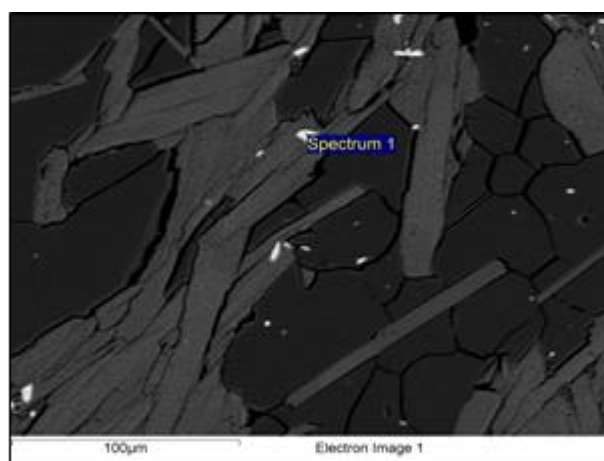


Figure 2.9 Rutile, as an accessory mineral, was determined by using SEM Jeol JSM-6490 electron microscopy and INCA software.

Because of high-grade deformation, it is hard to say if there exist graded bedding in the metaconglomerates. The pebble size may be used as an evidence but in most cases pebbles are flattened and elongated in the plane of foliation making it almost impossible to see if there was a grain size gradation within a single bed. For this reason, we have no evidence to test if the sequence or a part of sequence is upright or not. It is clear that there is both a lateral and vertical gradation between metaconglomerates and metapelites; the presence of pebbles in the metapelites can be used as a circumstantial evidence to support this contention. In some cases when one follows a metaconglomerate unit laterally, it appears that thickness of individual beds are variable along strike, suggesting channel conglomerate occurrences within sandstones and/or metapelites. In other cases, individual metaconglomerate beds pinch out laterally (Figure 2.10).



Figure 2.10 Field view illustrating lateral passages between metaconglomerate and metapelites.

The metaconglomerates occur in two distinct horizons and the metapelites lie in-between (Figure 2.1). The field observations confirm that they are very similar to one another but there is no stratigraphic evidence to test if these two levels are actually the same conglomerate horizon within the metasedimentary sequence or they represent two distinct horizons. This is very important because if the same metaconglomerate repeats in the succession, it may well be related with an overturned fold structure. Because lithological means are not strong enough to test this alternative, the structural elements – particularly their kinematics– are preferred; this will be presented and discussed in Chapter 4.

## 2.2.2 METAPELITIC ROCKS

In the study area, metapelitic rocks occur as grey to reddish coloured, mica-rich, fine-

grained unit that contains phengite lenses and boundinaged quartz veins. Penetrative foliation dips south and is invariably associated with mineral stretching lineation. Extensive folding at smaller scales and crenulation cleavage formation can be given as most characteristic features of the pelitic rocks. They are equivalent to kyanite schists of Whitney et al. (2008).

Quartz, white mica (phengite), chlorite, kyanite form main constituents whereas magnetite, rutile, tourmaline are accessory minerals. Preferred parallel alignment of micas defines the penetrative foliation in the rock; in most cases elongated quartz grains with their long axes accompany micas in defining the foliation. Large quartz grains show characteristic undulose extinction and in some samples show straight grain boundaries with triple junctions. Micas, both phengite and chlorite, form the most dominant components of the rock.

Chlorite occurs commonly as fine-grained crystals and defines the penetrative and strong foliation in the rock while coarser grains overgrow and/or cross-cut the main matrix foliation, defined by fine-grained phengite and chlorite; the coarser chlorite grains give the rock a spotted texture which can readily be recognizable in the field (Figure 2.11). In Çileklik Hill (Figure 2.1), cm-scale chlorite grains are characteristic in the metapelites but in the northern side of the study area (Lomburt Hill and Karaburun Hill), chlorite occur as fine-grained crystals, which can only be observed microscopically (Figure 2.11). Large chlorite occurs as late syn- to post-tectonic large megacrystals overprinting the main matrix foliation of the rock (Figure 2.12). The inclusions pass through large porphyroclasts and parallels the matrix foliation. The chlorite megacrysts also have random orientation, thus confirming their relative post-tectonic nature. In all examples, chlorite appears to be the product of retrogression and may well be related to the exhumation of HP rocks but this lies outside scope of present research and requires detailed fabric analyses together with detailed analytical work. Kyanite is also characteristic and occurs as larger crystals. Fibrous and/or prismatic crystals of magnesocarphiolite are also observed (Figure 2.13).

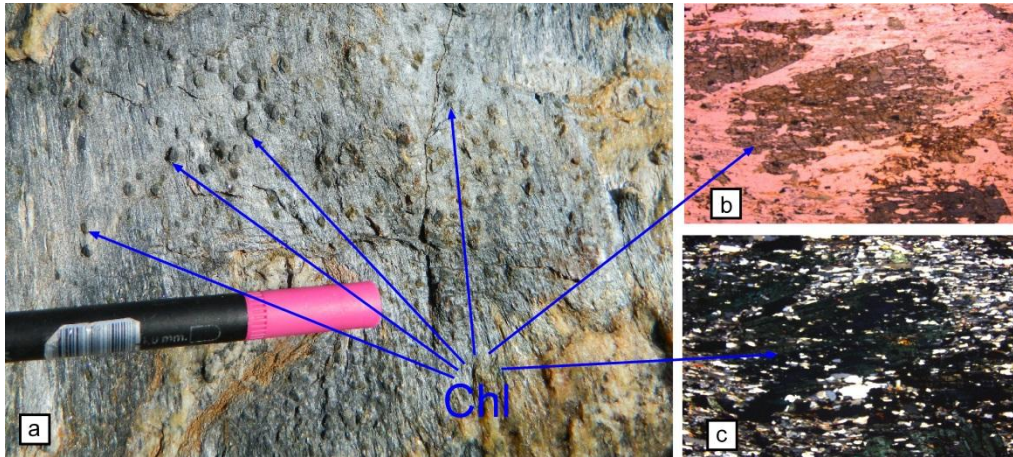


Figure 2.11 (a) Field view from coarse (cm-scale) chlorite grains in metapelites. Note how they overgrow the main foliation in the rock and gives the rock a characteristic appearance, spotted texture. (b) The coarse chlorite occurs as high relief, strongly pleochroic (from pale light blue to dark blue) mineral under microscope (plane light view). (c) Parallel and lamellar extinction of chlorite in crossed polars microscopic view is characteristic.

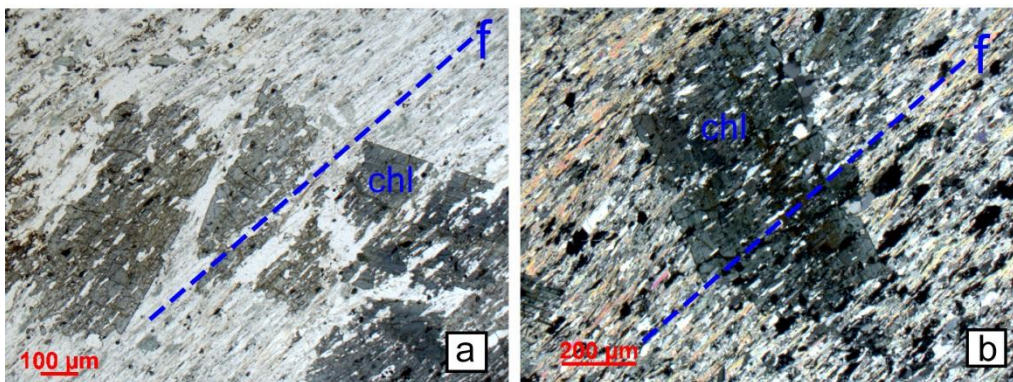


Figure 2.12 Photomicrographs (plane light) of post-tectonic chlorite (Chl) porphyroblasts overprinting older matrix foliation (f). Note random orientation of large porphyroblasts in (a) with respect to the main foliation. Note also how inclusions in the porphyroblasts are parallel to, and pass into, the matrix foliation.



Figure 2.13 Microscopic view of carpholite (Car) crystals in infolded metapelite.

Metapelitic rocks are not homogeneous; in some locations (e.g., in the area between Çileklik Hill and Lomburt Hill; Figure 2.1) they are finer-grained, contains small quartz pebbles (Figures 2.14a and 2.15) and are interlayered with quartzite (Figure 2.14b). Where they are interlayered with quartzite, small-scale folds are common. The quartz veins are also abundant (Figure 2.14c) and they are commonly boundinaged; in some cases the quartz veins are disrupted into smaller pieces, which appear as pebbles in the metapelites. Crenulation cleavage is best determined in this level of the metapelites. In all cases, their structural attitudes (strike and dip of foliation, trend of lineation) of the metapelites remain constant throughout the mapped. The most and common structure of the metapelitic rocks is the presence of crenulation cleavage. A detailed information will be given in Chapter 4.

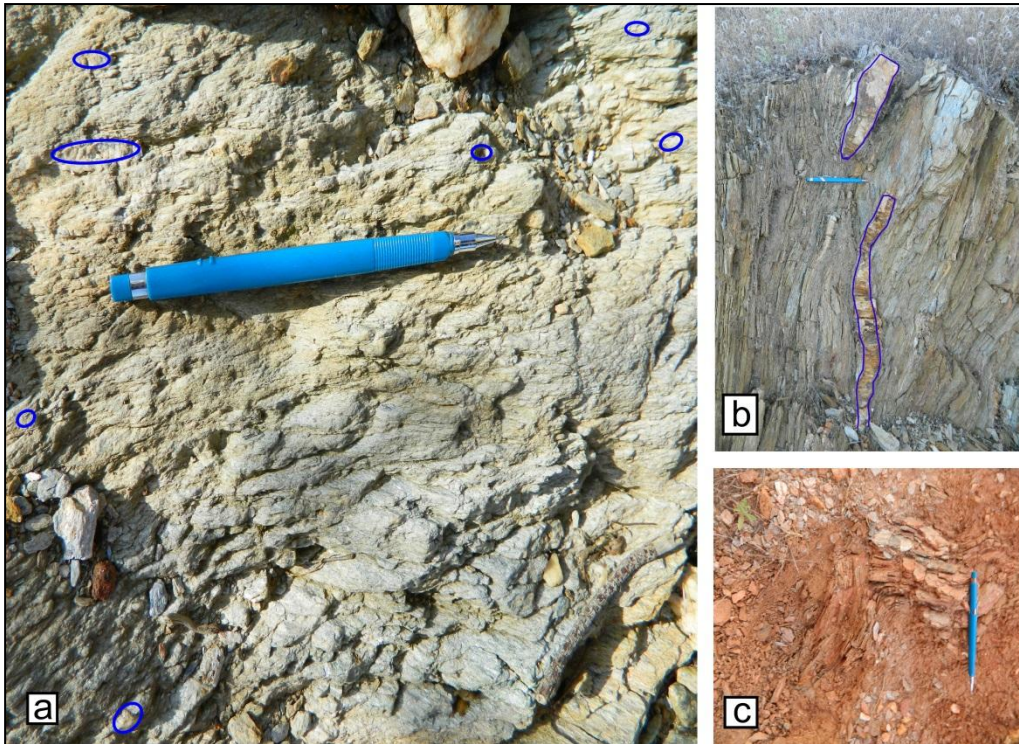


Figure 2.14 Views of metapelites exposed in the area between Çileklik Hill and Lomburt Hill (see Figure 2.1 for location): (a) quartz pebbles in the metapelite; (b) boudinaged quartz veins within fine-grained metapelitic unit; (c) folded in reddish metapelitic unit.

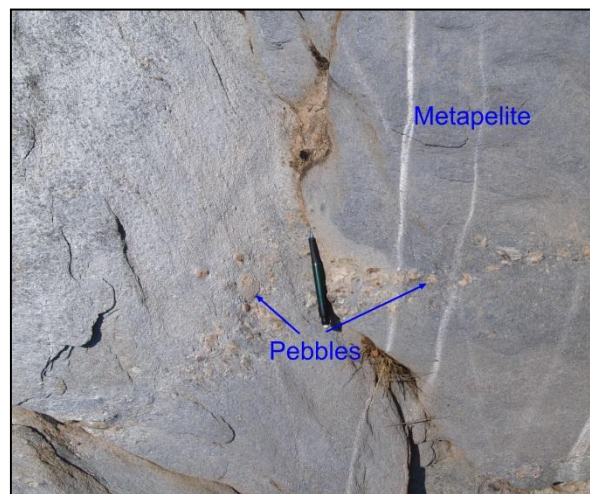


Figure 2.15 A view from a large flattened quartz pebble in the metapelites. Note that the pebble is large enough to appear as a thin layer within pelites.

### 2.2.3 QUARTZ VEINS

Folded, boudinaged, cm- to m-scale quartz veins (magnesiocarpholite-kyanite-chlorite-quartz) are common features of the metapelites; they display sharp but concordant relationships with the main foliation of the metapelites (Figures 2.16 and 2.17). They are important because these veins are interpreted as synmetamorphic (Candan et al., 2011a) elements in the Kurudere area.



Figure 2.16 A close-up view of a quartz vein is within the metapelite rocks. Pen is about 13-cm long.

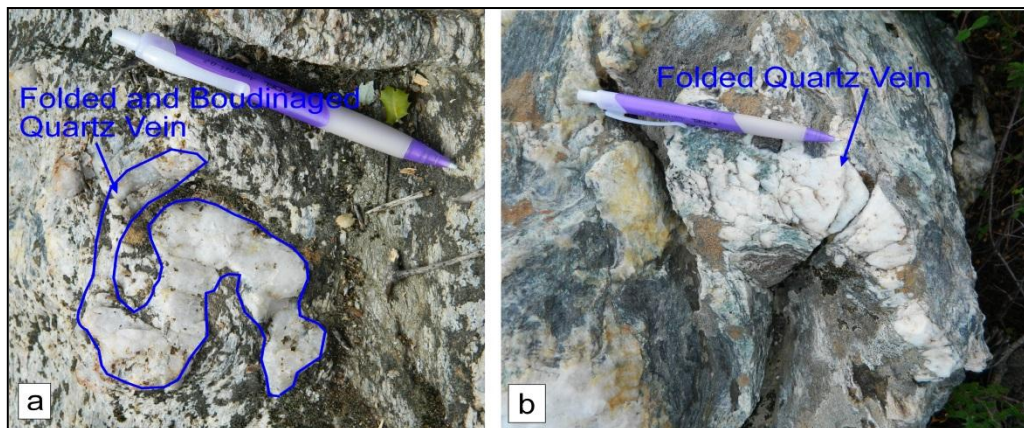


Figure 2.17 Views from deformed and folded quartz veins. Note S-shape geometry of the vein (a) and thickening in the hinge zone (b) of folds.

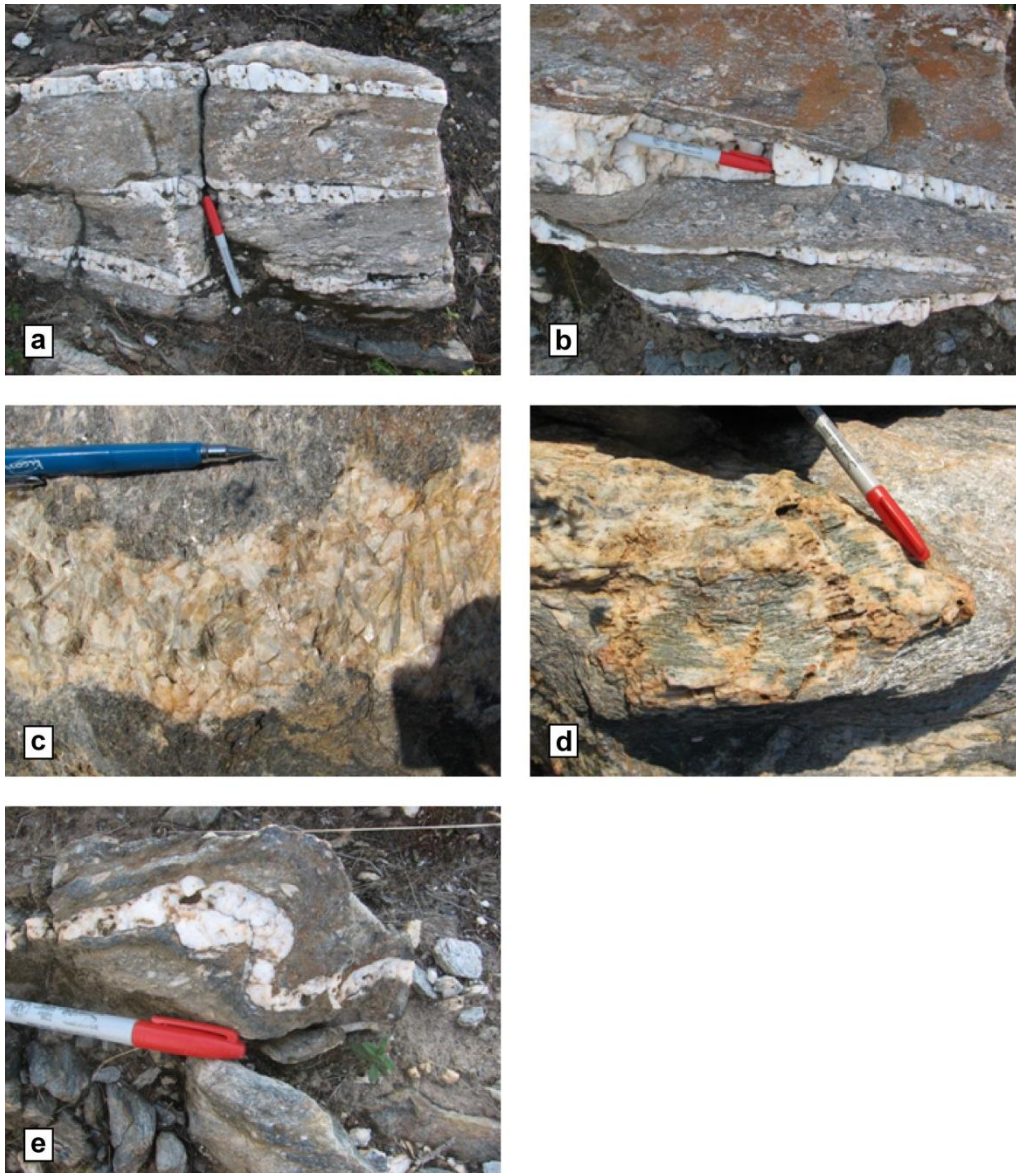


Figure 2.18. Views from the quartz veins in the Kurudere area: (a, b) monomineralic milky quartz veins within the metaconglomerate unit; (c) kyanite-quartz vein; note blue kyanite blades with random orientation; (d) a quartz vein characterized by dense magnesiochloritoid fibers; (e) a deformed/folded milky quartz vein.

Some of the quartz veins are monomineralic and contains coarse quartz grains (Figure 2.18a, b), but some others contain large blue kyanite blades and magnesiocarpholite fibers (Figure 2.18 c, d). One of the quartz veins at Karaburun Ridge contains cm-scale kyanite within folded and occur within black metapelitic unit (Figure 2.20). The orientation of kyanite blades with respect to the general trend of the quartz veins is variable; there is no preferred orientation. The large kyanite crystals provide evidence for crystal-scale deformation where they are bent or even folded. White mica, phengite, is common around large kyanite crystals.

Magnesiocarpholite  $[(\text{Fe}, \text{Mn}, \text{Mg})\text{Al}_2(\text{Si}_2\text{O}_6)(\text{OH})]$  occurs as thin fibrolites within the quartz veins and has been used as the evidence of HP metamorphism in this section of the southern Menderes Massif (cf. Rimmelé et al., 2003b; Whitney et al., 2008). They occur as green coloured elongate, fibrous or thin prismatic crystals (Figures 2.18d and 2.19); carpholite is also observed as inclusions within quartz crystals. The chlorite is also commonly found within these rocks. Magnesiocarpholite is also used in estimating P–T conditions of HP metamorphism in Kurudere area (see Chapter 1 for details). Magnite and rutile form accessory minerals in the quartz veins.

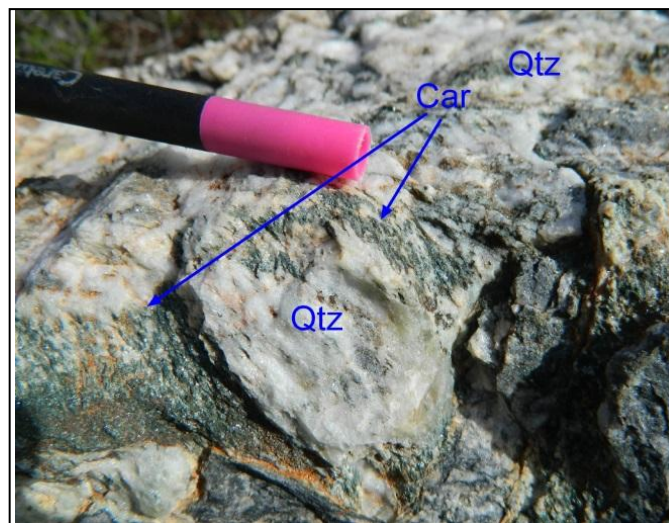


Figure 2.19 A field view from fibrous magnesiocarpholite (Car) in a quartz vein (Qtz).

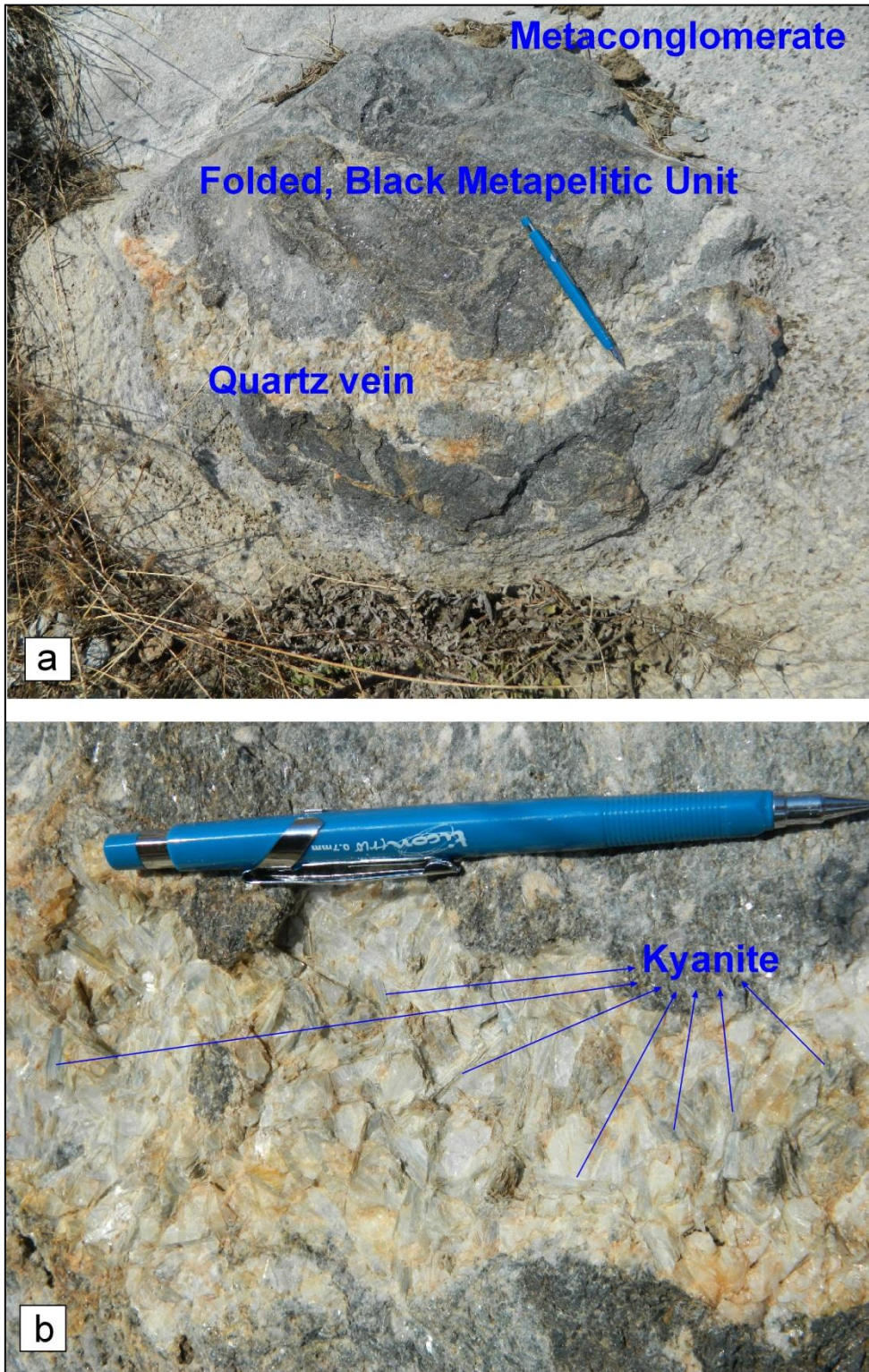


Figure 2.20 A view from kyanite-bearing quartz vein in folded black metapelite unit. Coordinates: 35555015E/ 4139481N. Pencil is about 13-cm long.

## CHAPTER 3

### U-Pb GEOCHRONOLOGY AND Hf ISOTOPE DATA

#### 3.1 INTRODUCTION

Dating the rocks and their metamorphism/deformation forms the most important and may be the most difficult stage during a geological research. This has been achieved by using several different methods; some of these techniques have to be used collectively to acquire a full and a more sound geological history. U-Pb and Pb-Pb ages (on zircon, monazite, titanite, allanite and xenotime) by conventional, evaporation, SHRIMP or ICP-MS laser ablation methods are commonly used in dating the crystallization age of magmatic rocks. In some cases, similar ages are used to date metamorphism and associated deformation. Cooling and exhumation history of lower-middle crustal rocks, both magmatic and metamorphic rocks, are dated by radiometric (Ar-Ar, Rb-Sr and K-Ar mica and amphibole ages) and/or by thermochronologic (apatite and zircon fission track ages; and apatite U-Th/He thermochronometry) methods. In this way, the tectonic versus erosional denudation mechanisms are tested and alternative exhumation models are proposed. In high pressure rocks, mica ages are commonly used to date the age of metamorphism and associated deformation as well; this basically depends on the temperature conditions of metamorphism. Stratigraphic and/or palaeontological (if fossils are present) means are used in dating the (meta)sedimentary rocks. Dating of detrital zircons are recently used as one of the most prestigious method in dating the (meta)sedimentary rocks; the zircon population is also used to test alternative provenance(s) for sedimentary influx. This, in turn, is used in palaeogeographic reconstructions.

As is described in the Introduction Chapter, the age of the HP rocks in Kurudere area is based on regional correlations and there is no analytical data to support this contention. Also, the origin of the HP rocks is highly debated: i.e., (i) if they belong to the Menderes sequence or (ii) they form a part of Cycladic HP sequence and are tectonically transported into their present configuration. To shed light to the existing questions and controversies, a U-Pb geochronology and Hf isotope analyses are carried out on samples from the HP rocks of the Kurudere area. The HP metaconglomerates were possibly sourced from different sedimentary provenance(s) and that they may contain detrital zircon peculiar to a specific provenance/source. U-Pb isotope system is measured to determine the age of detrital zircons and in turn the sedimentation age of metaconglomerates; the age of youngest zircon puts a lower limit

to sedimentation age. Whereas Hf isotope is measured to have idea about provenance of the metaconglomerates. Laser ablation induced couple mass spectrometry method (LA-ICPMS) is used for measuring because of its sensitive ion counter system. It is relatively a cheap and quick method and one can measure several zircon grains in a day.

In this chapter, procedure(s) for sampling, process of mineral separation and analytical methods, based on laboratory experience and available literature, are described. The reasons of why detrital zircons and laser ablation induced couple mass spectrometry method (LA-ICPMS) are also explained.

### 3.2 MATERIAL

Sampling is the first and important step in radiometric dating. After determining which mineral to date and method for deciphering the geological problem, samples are taken from freshest part of relevant lithology; the location, stratigraphic position and field characteristics of each sample are noted. The sample location is chosen according to stratigraphic/structural position/importance and lithological characteristics.

Four samples were taken from the metaconglomerates in Karaburun and Çileklik hills (Figure 2.1, Table 3.1). Fine-grained metapelites were not sampled because they hardly contain enough number of detrital zircons.

Table 3.1. List of samples from Kurudere metaconglomerates.

sample number	lithology	Location	coordinates	measured isotope system
331	metaconglomerate	Karaburun Hill	35554906°E 4139463°N	U-Pb and Hf isotope systems
332		Karaburun Hill	355550376°E 4139445°N	
333 333B		Çileklik Hill	35554290°E 4139561°N	

### 3.3 MINERAL SEPARATION

In geochronological studies, specific minerals should be separated. There are different methods. During this study, zircon grains are separated. Mineral separation and subsequent analyses were done in Geochronology and Radiogenic Isotope Laboratory,

Institute of Geoscience, Goethe University of Frankfurt. The order and variety of separation process is variable according to capacity of laboratories. In Frankfurt, there are six different steps for zircon separation from field up to mass spectrometer stage; they are:

1. crushing,
2. wilfley table,
3. heavy liquid,
4. magnetic separator,
5. hand picking,
6. epoxy, polishing and cathodoluminescence

These steps are briefly explained in Appendix A.

### 3.4 METHOD

The basic principles of absolute dating are radioactivity and halflife. Mass spectrometry (MS) is widely used to: (i) generate ions from compounds by any suitable method, (ii) separate these ions by their mass-to-charge ratio ( $m/z$ ) and (iii) detect them qualitatively and quantitatively by their respective  $m/z$  and abundance. The analyses may be ionized thermally, by electric fields or by impacting energetic electrons, ions or photons. The ions can be single ionized atoms, clusters, molecules or their fragments or associates. Ion separation is effected by static or dynamic electric or magnetic fields (Gross, H.J., 2010). The above-given definition has been useful with additions since 1963.

There are many different combinations of machines and they vary according to aim of study. The mechanism of a mass spectrometer is outlined in Figure 3.1. It is possible to measure different element's ratio by using different configurations of mass spectrometers. To determine the relevant method, lithology of the samples, minerals to date, isotope system and amount of elements in the minerals must be considered.

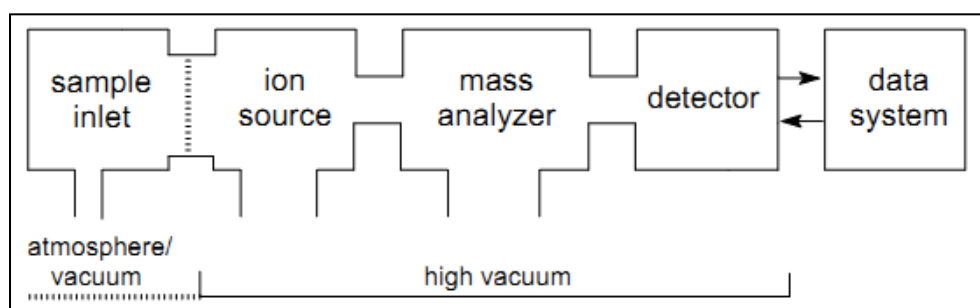


Figure 3.1 Simplified scheme of a mass spectrometer (from Gross, H.J., 2010).

In this study, detrital zircons are analysed. Laser ablation induced couple mass spectrometry method (LA-ICPMS) is chosen as the most relevant method because the machine can measure low amount of U-Pb concentration (for younger events) with sensitive ion detector. Drilling the mineral with laser beam just takes 53 seconds per spot and the error range is less than other methods. But corrections and software are complex and data process needs long-lasting experience.

### **3.4.1 FEATURES OF ZIRCON AND ISOTOPIC SYSTEMS**

Zircon ( $ZrSiO_4$ ) is zirconium orthosilicate and common accessory mineral of sedimentary, igneous and metamorphic rocks. Zircon keeps substantial chemical and isotopic information in its structure which is caused to use it in a wide range of geochemical investigations, including studies on the evolution of Earth's crust and mantle and age determination (Finch and Hanchar, 2003 and references therein). The mean abundance of  $HfO_2$  in zircon is 2.0 wt%, and it consists of trace amounts of P, U and Th and rare-earth elements (REE) (e.g., Hoskin and Schaltegger, 2003; Zlatkin, 2011). In zircon, uranium (U) is more compatible than lead (Pb). So amount of non-radiogenic Pb is less in zircon that makes data process easier.

Not only chemical composition, but also closure temperatures are effective factors to choose mineral for measuring. Closure temperature is the temperature value when a mineral starts to be a crystal; mineral becomes a close system while mass is still an open system. Each mineral has different closure temperatures. The closure temperature of U-Pb isotopic system in zircon is more than  $850^\circ C$  (Davis et al., 2003); this means it forms at the beginning of magma process or recrystallized under high-grade metamorphism. Also thermal events may affect the zircons by overgrowing rims around inherited cores or may disturb their structure which can be seen on their zoned texture. Disturbed zonation might be a clue for resetting isotopic clock or lead loss. So, CL images are taken to examine internal structures and to determine the proper spots for measuring.

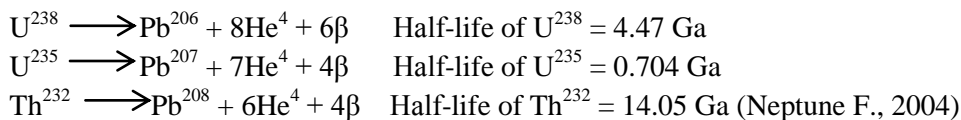
Another advantage of zircon is its durability. Zircon may be reprocessed through the rock cycle and still keeps durability. Zircon is a major mineral in the Earth's oldest known dated rocks. If the system has zircon once, it stays in there. This feature of the mineral makes detrital zircons more important and valuable for provenance analysis. A mixed sedimentary population of zircons will resist to metamorphism even the metamorphic grade is so high. During metamorphism, if suitable temperature is reached and fluids are present, zircons may have overgrowths as rims around older cores. On the other hand, durability of zircon is challenged and may be misleading because multiple sedimentary events and/or low-grade metamorphic events might be ignored and/or missed out because no overgrowths may develop.

Detrital zircons are reliable sources for U-Pb and Hf isotopes measurements. Because of the high compatibility of Hf in zircon, the Lu-Hf system is considered as more resistant than U-Pb system and the mineral's initial  $^{176}\text{Hf}/^{177}\text{Hf}$  ratio is usually preserved even when the U-Pb system was reset (cf. Kinny and Maas, 2003 and references therein).

### 3.4.1.1 U-Pb SYSTEMS

This method establishes the time of origin of a rock by means radioactive half-life of uranium (U)/thorium (Th) to lead (Pb). Uranium (U) is radioactive (parent) element and has two radioactive isotopes:  $\text{U}^{238}$  and  $\text{U}^{235}$ . Lead (Pb) is radiogenic (daughter) element and end product of Uranium. It has 4 isotopes:  $\text{Pb}^{204}$ ,  $\text{Pb}^{206}$ ,  $\text{Pb}^{207}$  and  $\text{Pb}^{208}$  (Dickin, 2005).

Common lead ( $\text{Pb}^{204}$ ) is any lead from a rock or mineral that is contained in the mineral when it forms; it is not a product of radioactivity of uranium or thorium. Common lead is used for correction in data processing and it forms an important parameter to obtain more reliable results. U-Pb system has long half-life, and this gives a chance to date the oldest rocks.

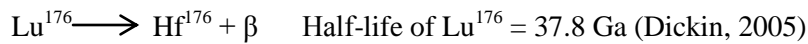


$\text{Pb}^{204}$  is non-radiogenic isotope.  
 $\text{Pb}^{206}$  is daughter isotope of  $\text{U}^{238}$ .  
 $\text{Pb}^{207}$  is daughter isotope of  $\text{U}^{235}$ .  
 $\text{Pb}^{208}$  is daughter isotope of  $\text{Th}^{232}$  (Dickin, 2005).

Uranium (U) and thorium (Th) elements are incompatible in the mantle, but they are compatible in the crust. During crystallisation of magma, U and Th are concentrated in the liquid phase and attend to the silica-rich magma. Therefore felsic compositions are more enriched in U and Th than mafic compositions and crustal rocks have more U and Th concentration than mantle rocks (Geyh and Schleicher, 1990; Dickin, 2005). It signs that granitic rocks have perfect materials for U-Pb dating.

### 3.4.1.2 Hf ISOTOPE

Lutetium is the heaviest rare earth element (REE) and has two isotopes;  $\text{Lu}^{175}$  and radioactive  $\text{Lu}^{176}$ . The latter decays to  $\text{Hf}^{176}$  with  $\beta$ -emission or  $\text{Y}^{176}$  with electron capture which is so rare (Dickin, 2005).



Lutetium-hafnium (Lu-Hf) isotopic system is used as a clue for the crustal events (e.g., Patchett et al., 1981; Kinny and Maas, 2003; Zlatkin, 2011). Mother isotope  $\text{Lu}^{176}$  radioactively decays to daughter isotope  $\text{Hf}^{176}$  with  $\beta$ -decay. The half-life of the reaction is 37.8 Ga.

Lu/Hf model age is used for determining formation age of mineral (Geyh and Schleicher, 1990). The Lu/Hf ratios may provide to date metamorphic events. Not only garnet but also zircon, monazite, apatite contain Hf isotope in their lattice which is very resistant to Hf mobility and contamination (Dickin, 2005).

$\text{Hf}^{176}/\text{Hf}^{177}$  ratio, standardized to CHUR and multiplied by 10000 and called as  $\epsilon\text{Hf}$  value and is measured to determine the source of grain. Hf enters the residual magma faster than Lu during magma process. Differentiation during formation of the Earth's crust led to lower Lu/Hf ratio in crust while higher ratio in the mantle. During the time, as a result of radioactivity of Lu, amount of Hf increases in the mantle whereas low initial Hf isotope ratio in crustal rocks (Dickin, 2005). So positive  $\epsilon\text{Hf}$  value remarks juvenile crustal source, negative  $\epsilon\text{Hf}$  value indicates reworked crustal source (e.g., Patchett et al., 1981; Dickin, 2005; Zlatkin, 2011).

If zircon crystallizes from juvenile crustal source, U-Pb and Lu-Hf ages will be close to each other. But if there is a reworking process, isotopic clock will reset for U-Pb but Hf isotope system will be resistant. Both ages will be discordant to each other. That's why U-Pb age is needed for interpretation of  $\epsilon\text{Hf}$  value for provenance analysis (e.g., Dickin, 2005; Zlatkin, 2011 and reference therein).

### **3.4.1.3 U-Pb-Hf COMBINATION FOR ZIRCON**

The combination of U-Pb-Hf isotopic systems provides more reliable provenance data for detrital zircons. For each zircon U-Pb age is calculated and different aged grains are analysed for Hf isotope at the almost same spot place with U-Pb data. Isotopic study of single-grain of detrital zircon is commonly used in determining different detrital populations derived from various sources. U-Pb system allows calculation of crystallization ages;  $\epsilon\text{Hf}$  value is an indicator of crustal provenance. Plotting the two datum in the same graph means recognition of crustal forming events and reworking events as well as the provenance of the grains. It is also possible to comment if a magma mixed or not (cf. Zlatkin, 2011).

### 3.4.2 INTERPRETATION OF CL IMAGES

Zircons from the same sample may have various types of zonations and crystal shapes. Idiomorphic and xenomorphic grains with oscillatory, sectored and convolute zoning are possible (Figure 3.2).

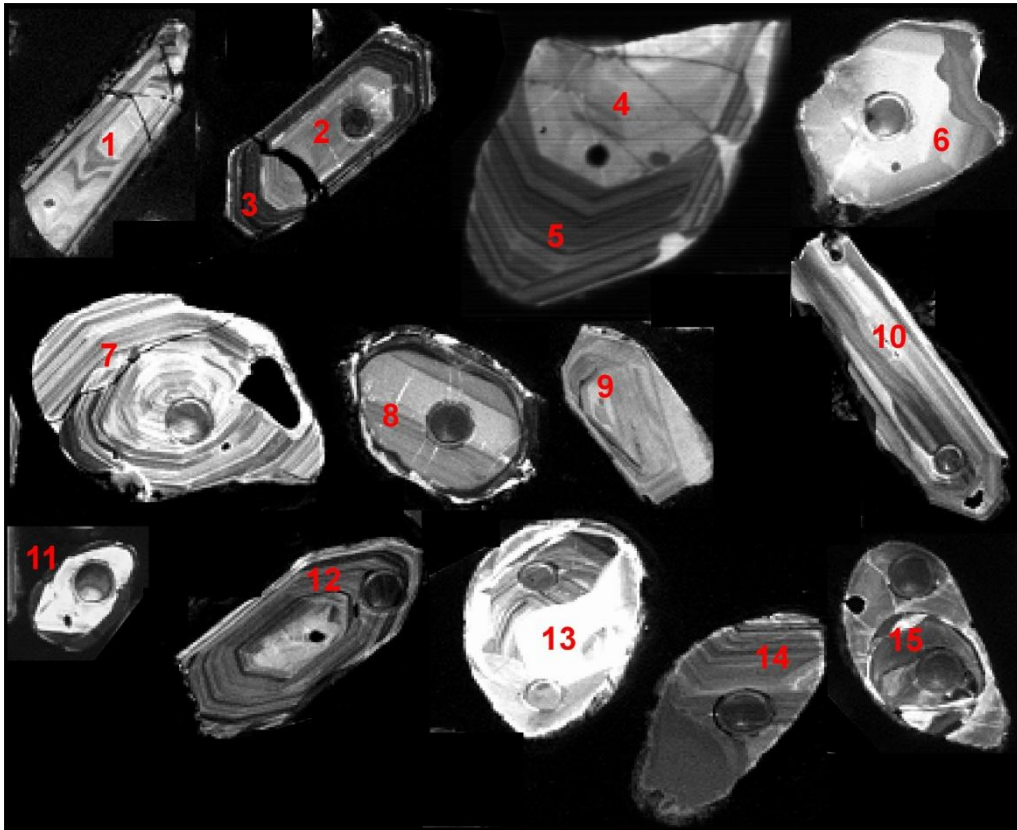


Figure 3.2 CL images showing different zone structure of zircons which may occur in the same sample (Sample 331): (1) disrupted zoned texture, convolute zonation in an idiomorphic crystal; (2, 3) relatively U-less core and U-rich rim with oscillatory zoning; (4, 5) sector zoned inherited core with U-rich oscillatory zoned rim; (6) sector zonation of a grain; (7) perfect, bright oscillatory zoning; (8) xenomorphic grain with metamorphic rim; (9) disturbed oscillatory zoning in idiomorphic crystal; (10) idiomorphic crystal with oscillatory zonation; (11) U-poor core and U-rich rim in xenomorphic crystal; (12) composite zircon –inherited core and magmatic growth; (13, 14) partly preserved zonation and recrystallization; (15) xenomorphic grain with inherited core and rim without zonation (featureless) (from samples 331, 332, 333, 333B).

### 3.4.3 ANALYTICAL PROCESS

U-Pb isotope ratio to determine the age of the rock units for detrital zircons was measured with laser ablation induced couple mass spectrometer (LA-ICPMS) in Geochronology and Radiogenic Isotope Laboratory, Institute of Geoscience, Göethe University of Frankfurt. The analyses were performed with ThermoScientific Element 2 ICP-MS coupled to a Resolution M-50 excimer laser system. The laser is transported onto the grains from the laser beam with a flow of the noble gas (argon or/and helium) and mass spectrometer is calibrated to measuring of appropriate isotope masses. Laser spot-sizes were between 33–50 micrometer, depending on the U content and size of the zircon grains (Gerdes and Zen, 2006; Zen et al., 2007). After per 30 spots, standarts GJ-1 (606 Ma), Felix (500 Ma), Plesovice (350 Ma) and 91500 (1050 Ma) were measured to check the calibration of the machine and determine constant values for data processing (Slama et al., 2007). The spots should be decided before starting analyses. If there exist, cores and rims of the zircons should be analysed separately; perfectly zoned and crack-free parts of the zoned structure to be selected for analysis (Figure 3.3).

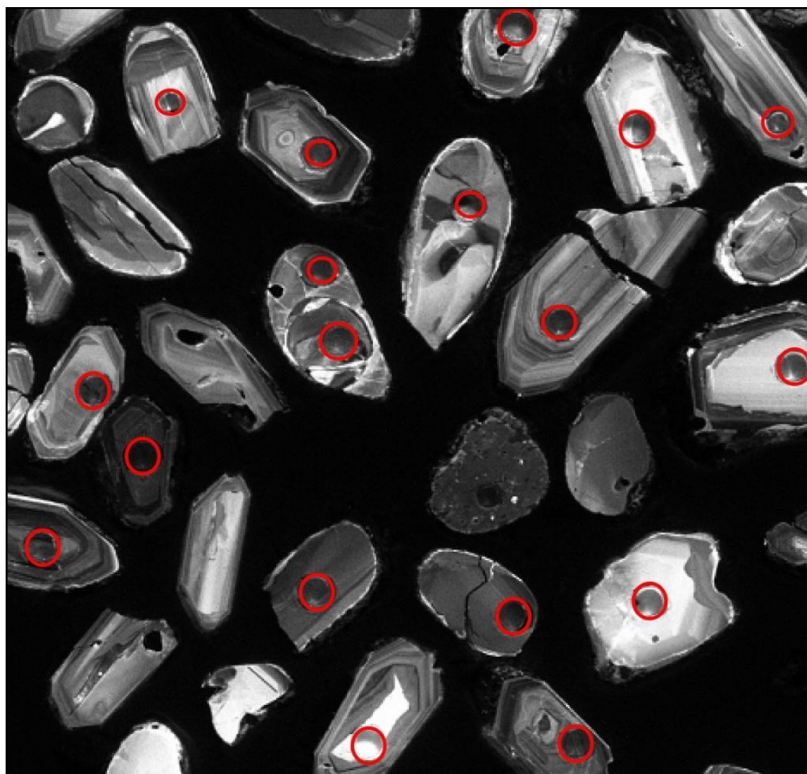


Figure 3.3 CL images and ablated spots for measuring U-Pb and Hf isotope ratio. Red circles shows location of spots.

$\text{Hf}^{176}/\text{Hf}^{177}$  and  $\text{Lu}^{176}/\text{Hf}^{177}$  ratios were measured in ThermoScientific Neptune multi-collector ICP-MS, coupled to RESOLUTION laser system with 50 micrometer spot-size, following the method described by Gerdes and Zeh (2006) and Zeh et al. (2007). Hf isotope should be measured almost at the same spot location with U-Pb measurement. GJ-1 was measured as standard for Hf isotope.

The raw data is processed by using an in-house MS Excel spreadsheet program (Gerdes and Zen, 2006, 2009; Millonig et al., 2012). The processed data is plotted on concordia diagrams by Isoplot 3.71 (Ludwig, 1990).

### 3.5 RESULTS

CL images of detrital zircons from picked samples and U-Pb detrital zircon ages from HP metaconglomerates are given in Figures 3.6, 3.9, 3.12, 3.15 and Table B.1 in Appendix A. The results are plotted on concordia diagrams (Figures 3.4, 3.7, 3.10 and 3.13) and probability/density diagrams (Figures 3.5, 3.8, 3.11, 3.14 and 3.16) using Isoplot (Ludwig, 2003). All data are processed with 2 sigma uncertainties. Only 90–110% concordant data points are plotted. The percentage of Neoproterozoic, Paleoproterozoic and Mezoproterozoic ages are shown with piecharts on probability/density diagrams based on the geologic time scale 2012.

The youngest concordant grain's age is  $298 \pm 5$  Ma, (conc. 104%), Asselian, lowest Permian age (Figures 3.13; Table B.1 in Appendix A). Zircon grain is idiomorphic, oscillatory zoned. U-rich (dark colored) and U-less (light colored) light beams are clearly seen (Figure 3.13, Table B.1).

The oldest grain is Mezoarchean in age ( $3020 \pm 16$  Ma; conc. 101%) (Figure 3.13; Table B.1). The grain is composite zircon and inherited core was measured. Relatively core has more U concentration than rim but both of them are in light color (Figure 3.13).

The large number of grains belongs to Cambrian ( $541.0 \pm 1.0$  to  $485.4 \pm 1.9$  million years), Ordovician ( $485.4 \pm 1.9$  to  $443.4 \pm 1.5$  million years) and Cryogenian (850–635 million years; Neoproterozoic) ages. There is no or a few zircon grains in 1.1–1.7 Ga time interval and it is remarkable in almost all dated samples (Figure 3.16; Table B.1). Less number or absence of 1.1–1.7 Ga (Mezoproterozoic) old grains marks northern Gondwana provenance (cf. Gebauer, 1993) and is common signature of detrital zircons from the Menderes and the Cycladic massifs.

In probability/density plots peaks occur in Late Cambrian and Early Ordovician time interval (Figures 3.5, 3.8, 3.11, 3.14 and 3.16). There are sharp decrease in number of detrital zircons in Early Cambrian ( $541 \pm 0.3$  to  $509 \pm 1.7$  mya), Tonian (1000 to 850

mya; early Neoproterozoic) and beginning of Mezoproterozoic (1,600 to 1,000 mya); this is also used as typical profile for Northern Gondwana Terranes (cf. Gebauer, 1993). The density of grains in Paleoproterozoic (2,500 to 1,600 mya) and Archean (before 2,500 mya) is not as much as pre-Mezoproterozoic ages but amount of Statherian (1,800 to 1,600 mya) and Orosirian (2,050 to 1,800 mya) age grains are observed. Late Paleoproterozoic ages are rare but the population of NeoArchean (2,800 to 2,500 mya) ages increases. All samples belong to the same lithology, so all data is combined and plotted in single probability/density diagram (Figure 3.16).

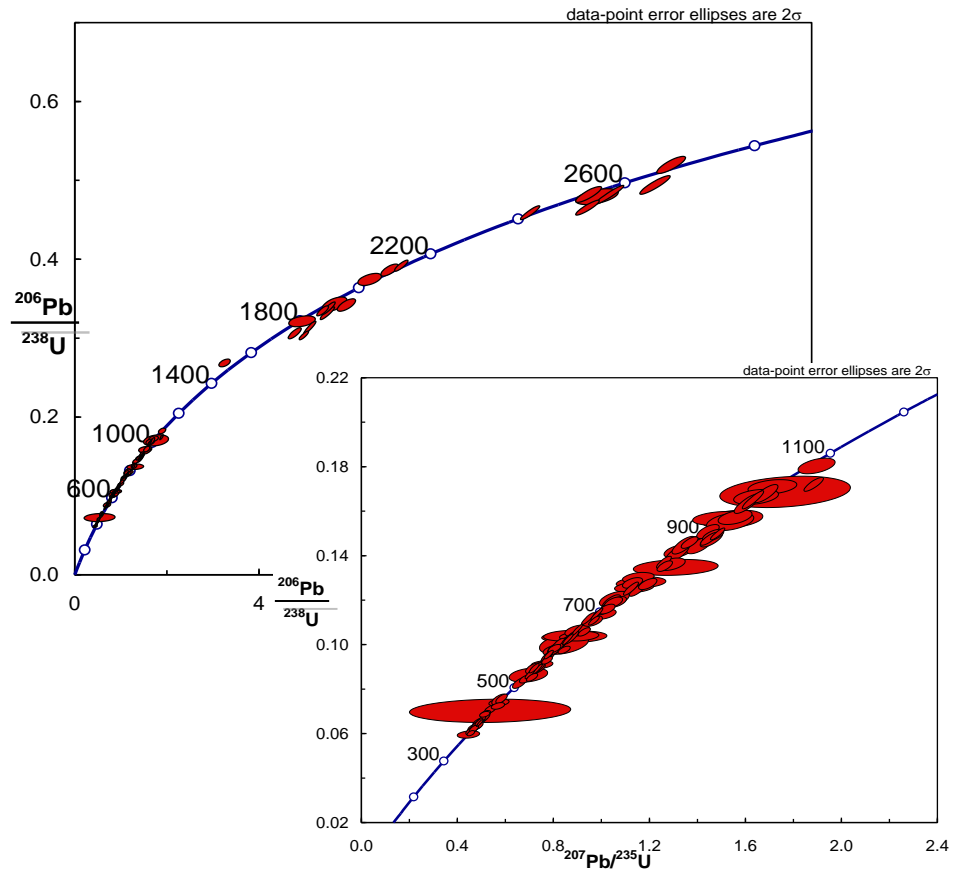


Figure 3.4 U-Pb concordia diagram of detrital zircon ages from sample 331.

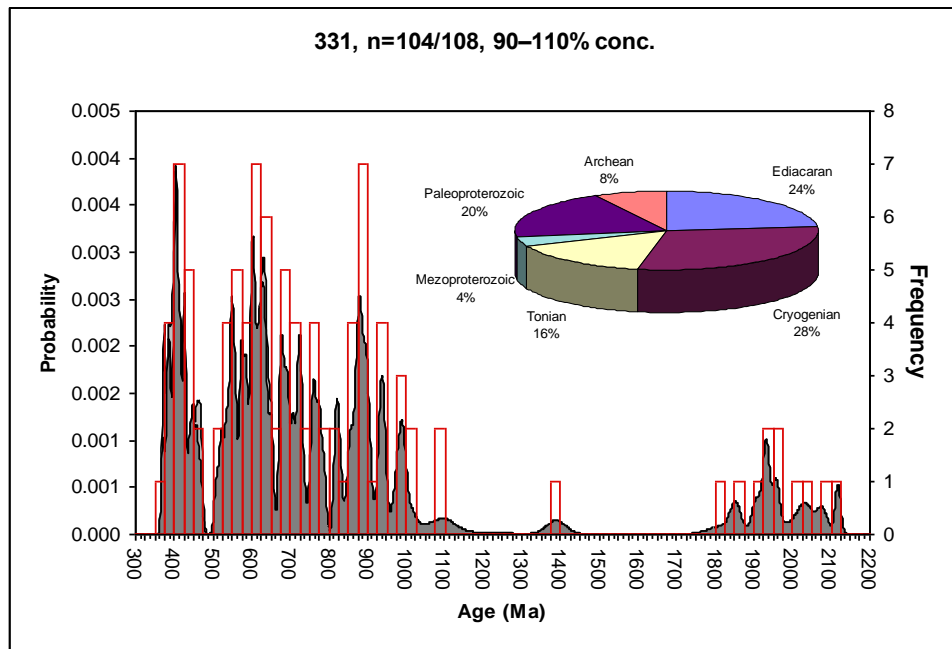


Figure 3.5 Probability/density plot of detrital zircons from sample 331.

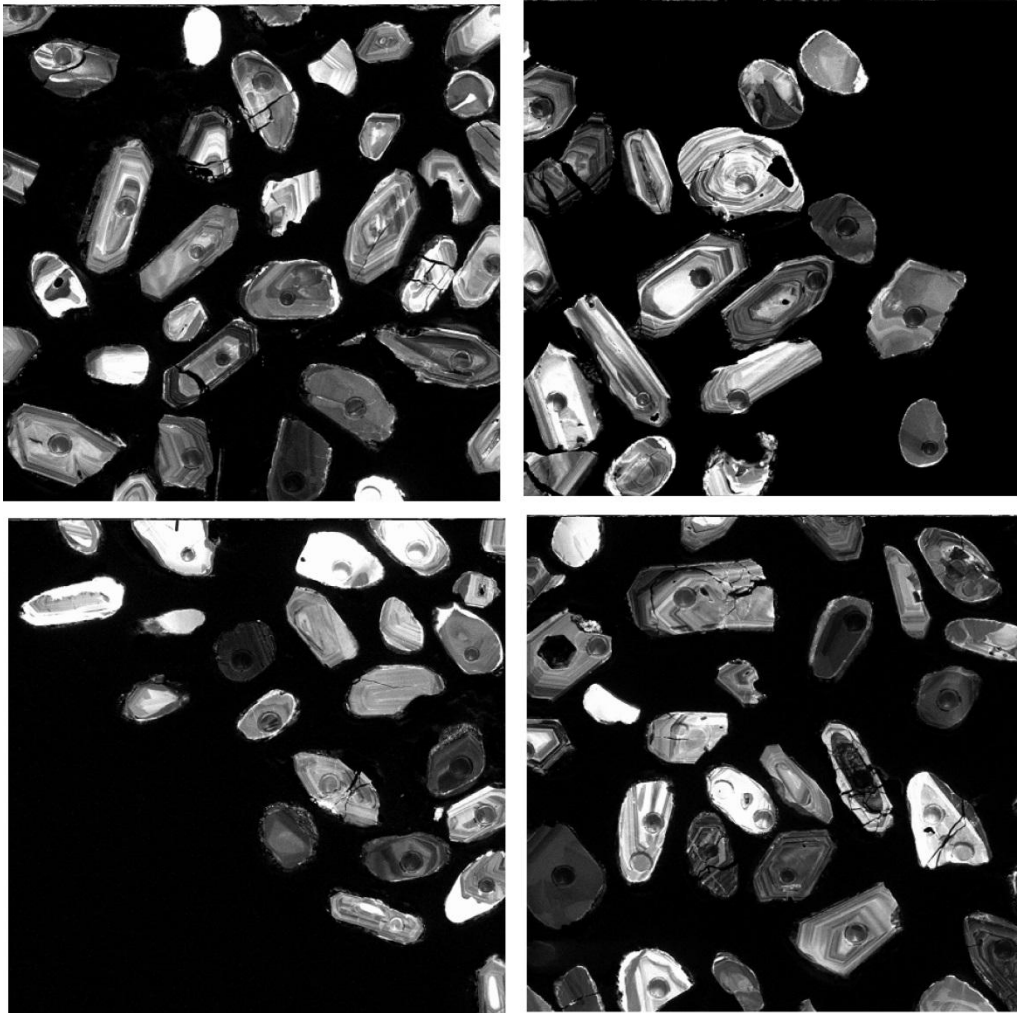


Figure 3.6 CL images of analyzed detrital zircons in sample 331.

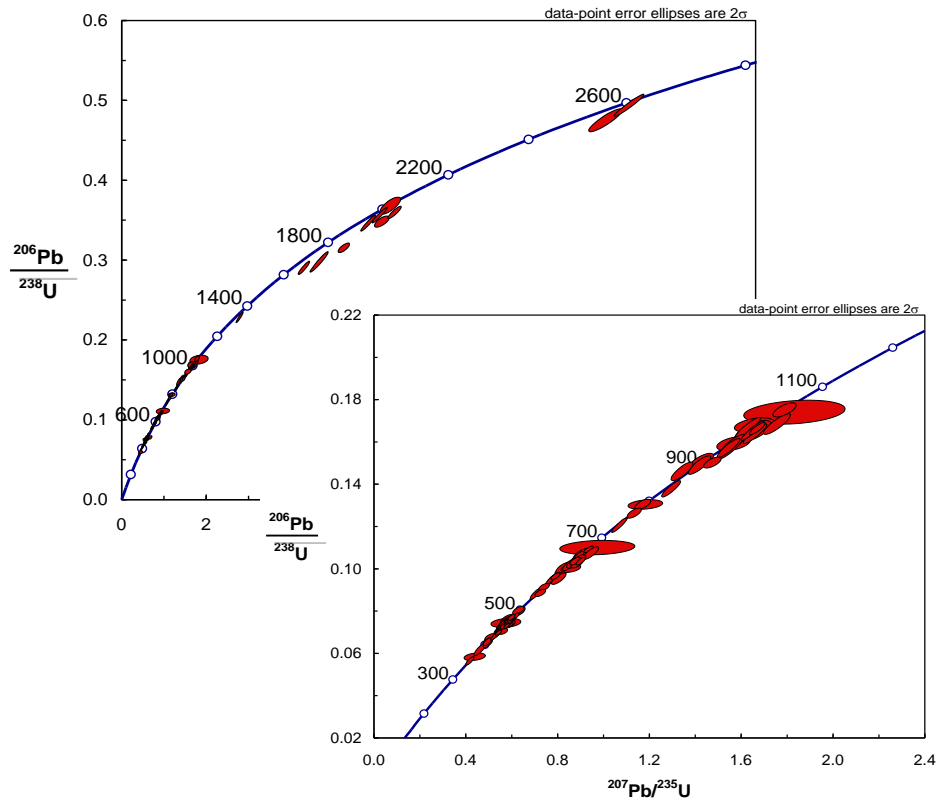


Figure 3.7 U-Pb concordia diagram of detrital zircon ages from sample 332.

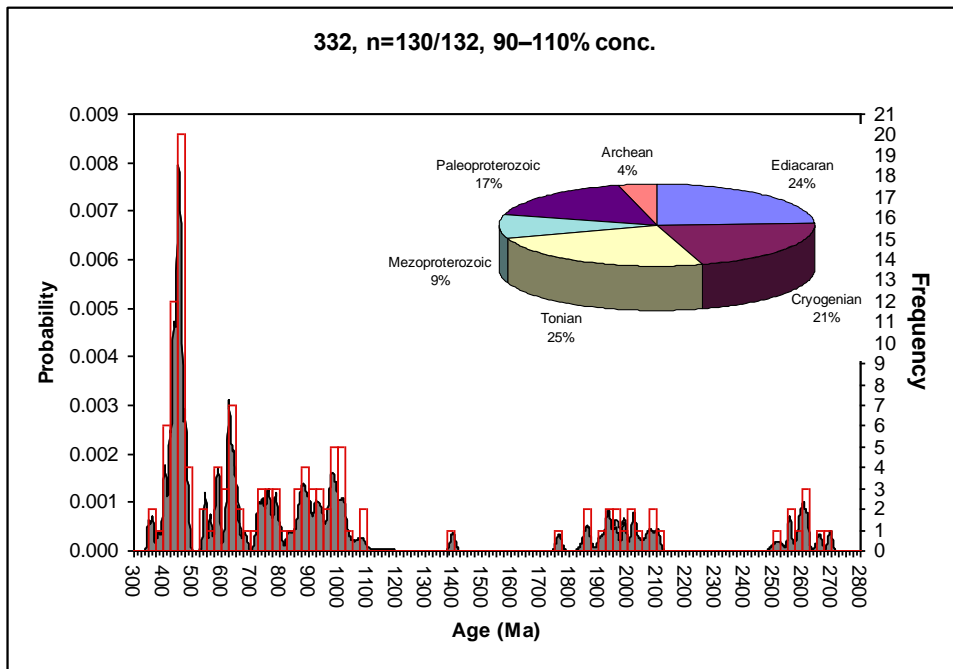


Figure 3.8 Probability/density plot of detrital zircons from sample 332.

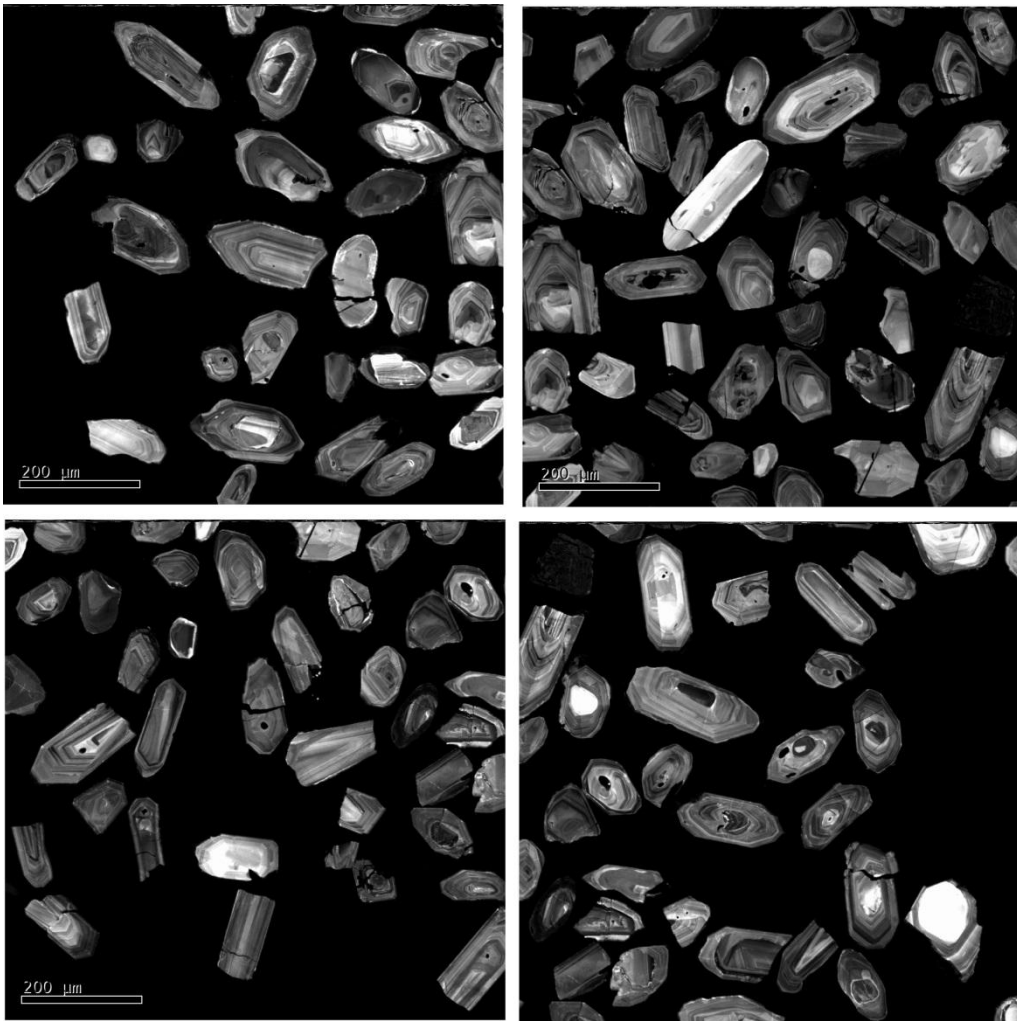


Figure 3.9 CL images of detrital zircons picked from sample 332.

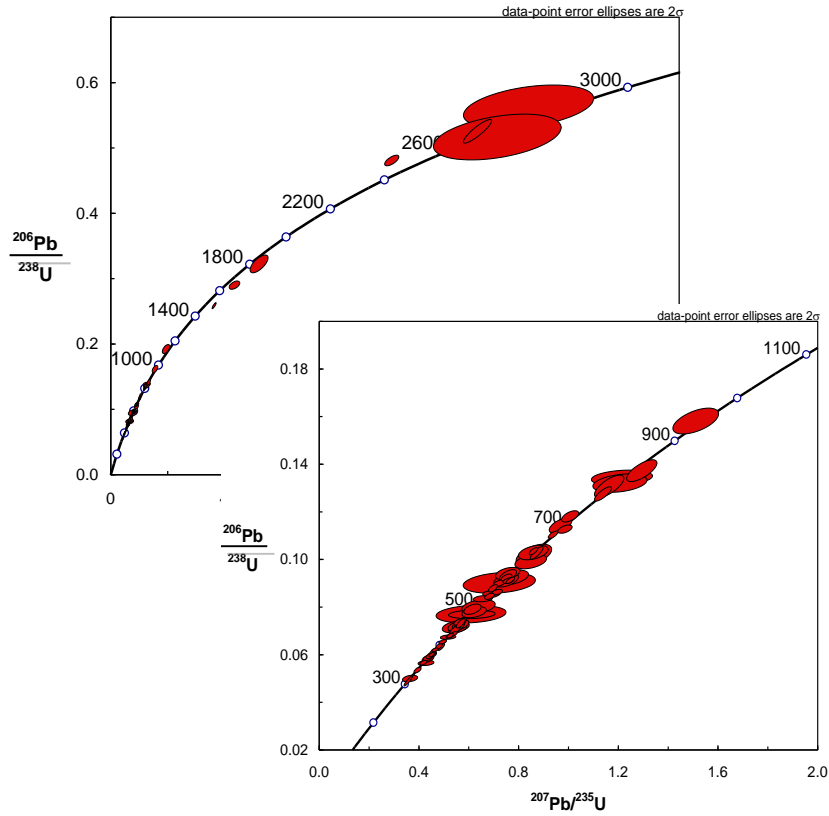


Figure 3.10 U-Pb concordia diagram of detrital zircon ages from sample 333.

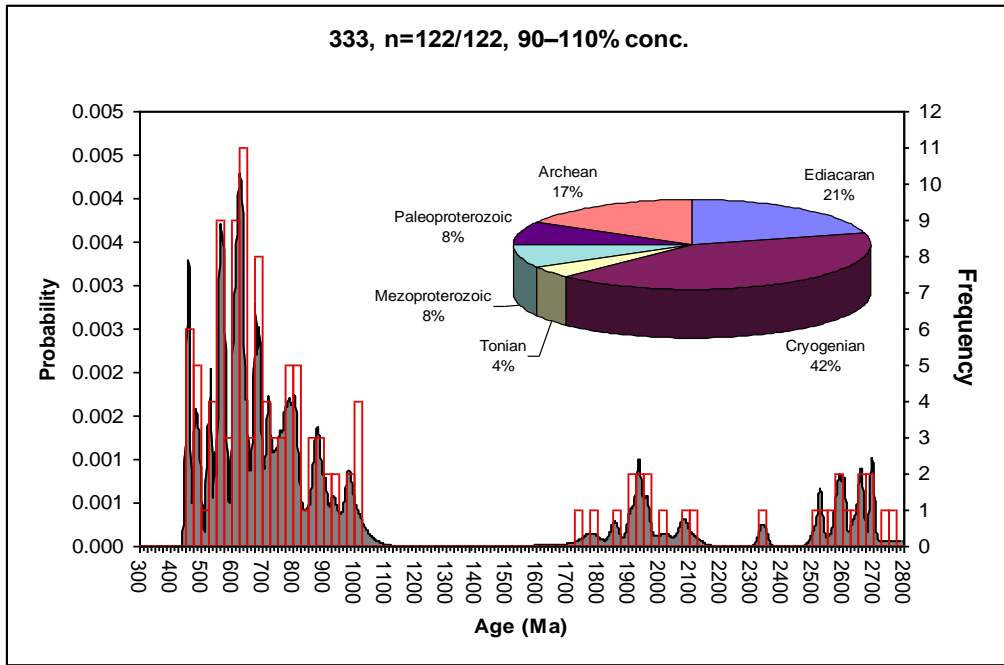


Figure 3.11 Probability/density plots of detrital zircons from sample 333.

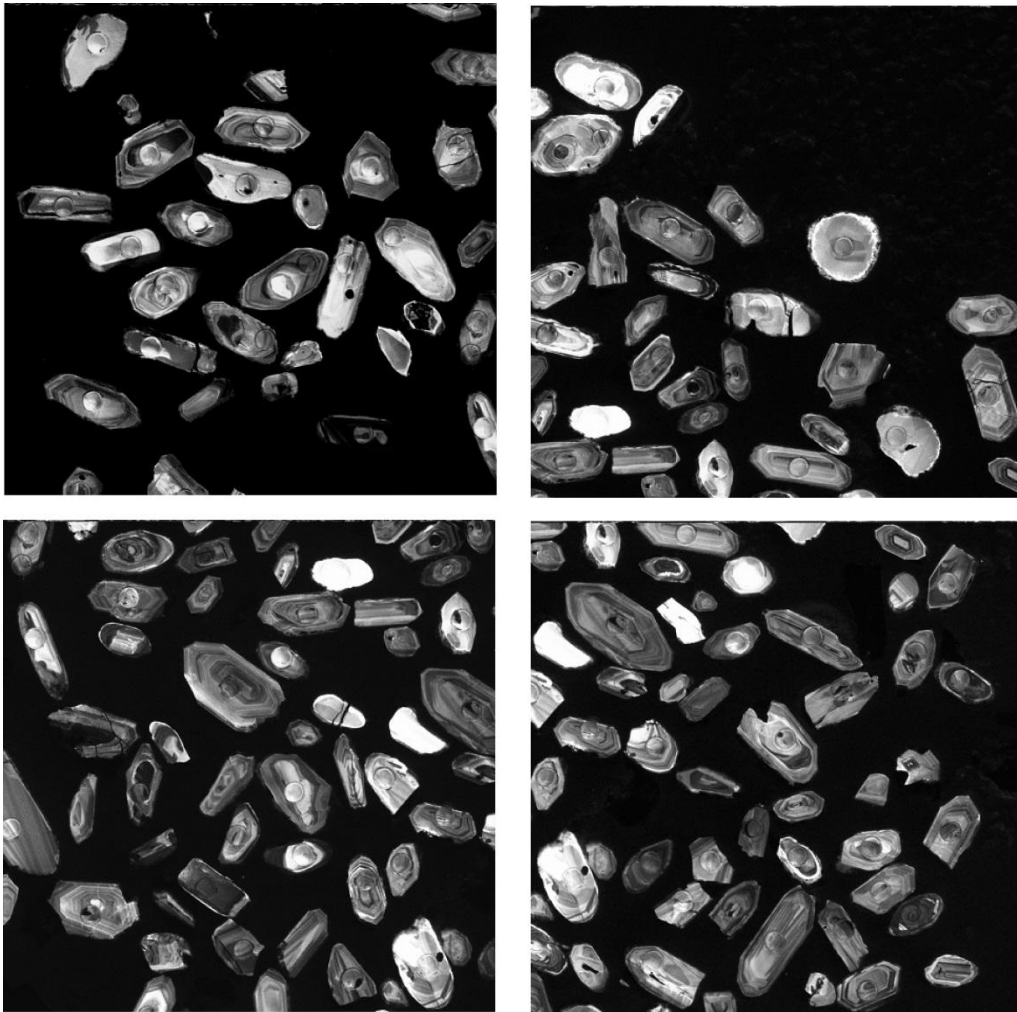


Figure 3.12 CL images of analysed detrital zircons belong to sample 333.

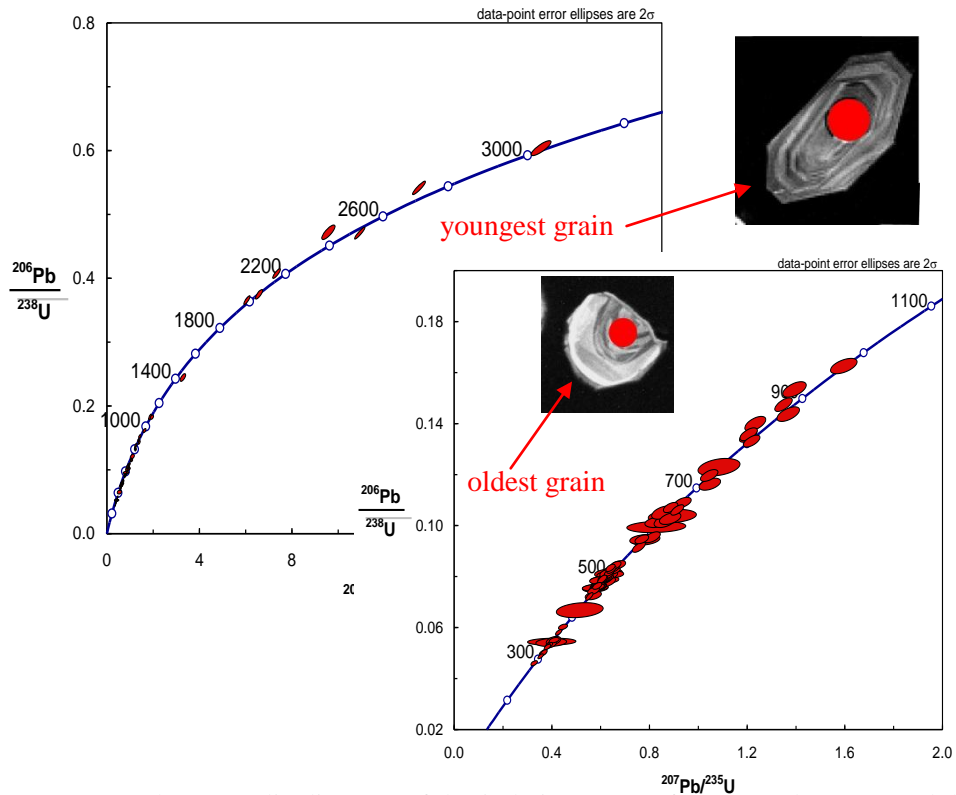


Figure 3.13 U-Pb concordia diagram of detrital zircon ages from sample 333B and the youngest zircon grain with U-rich core and U-poor rim.

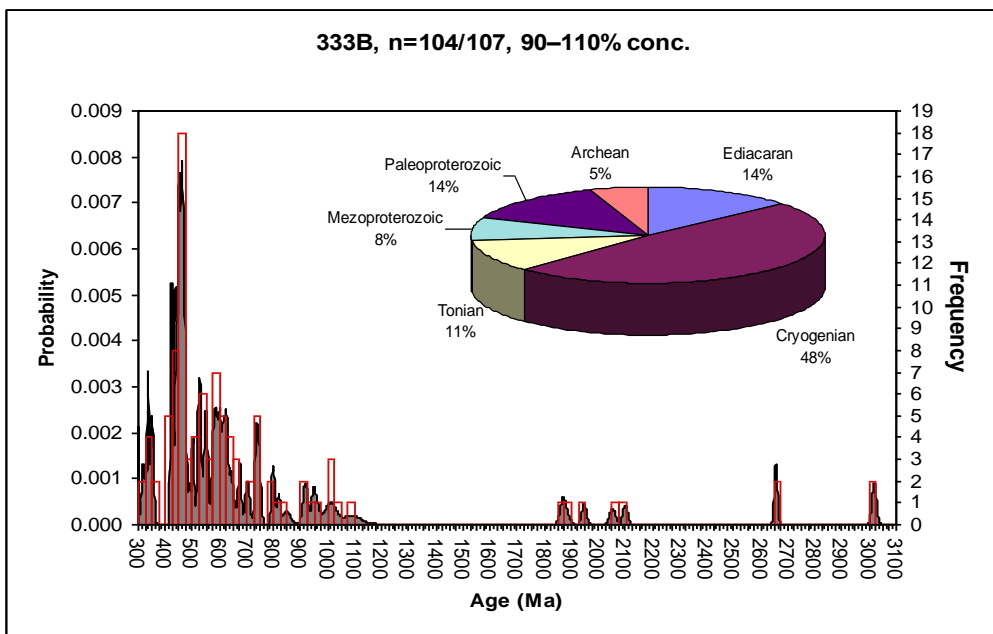


Figure 3.14 Probability/density plot of detrital zircons from sample 333B.

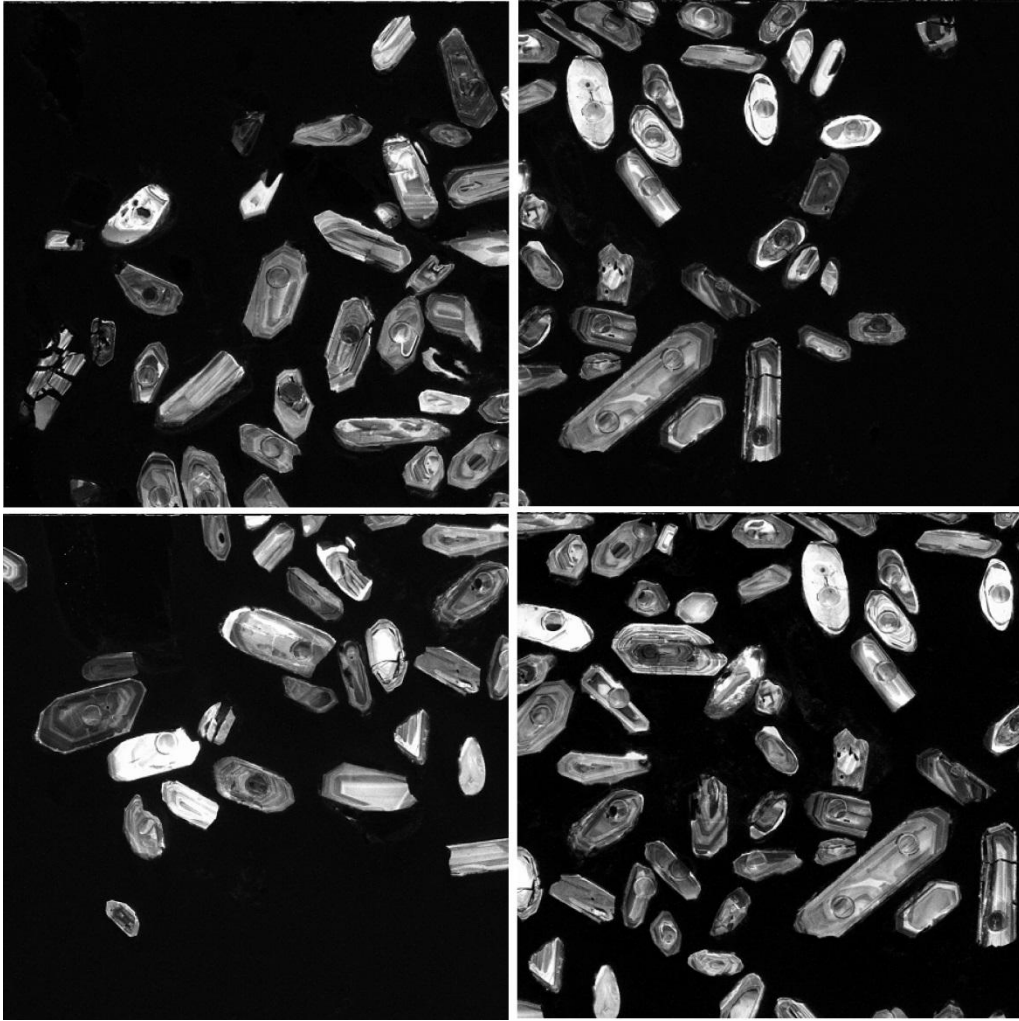


Figure 3.15 CL images of analysed detrital zircons picked from sample 333B.

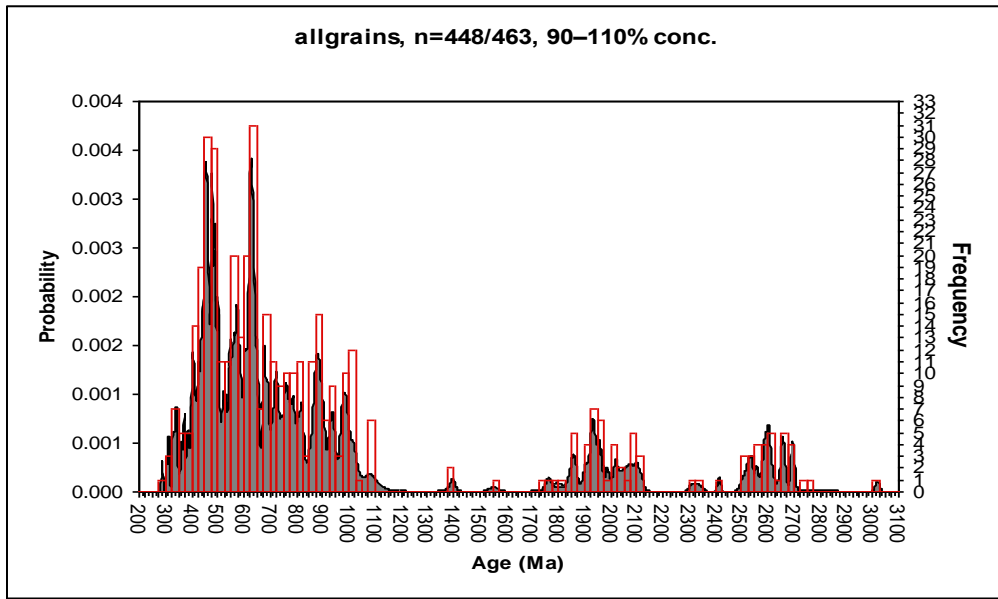


Figure 3.16 Probability/density plot of all processed detrital zircon grains.

For measuring  $\epsilon_{\text{Hf}}$  value, zircon grains with concordant ages were chosen. Younger (<1000 Ma) and older (>1000 Ma) grains and all grains were plotted in the diagram together with their U-Pb ages (Figures 3.17, 3.18 and 3.19; Table B.2) (DM= Depleted Mantle,  $T_{\text{DM}}$ = model age).

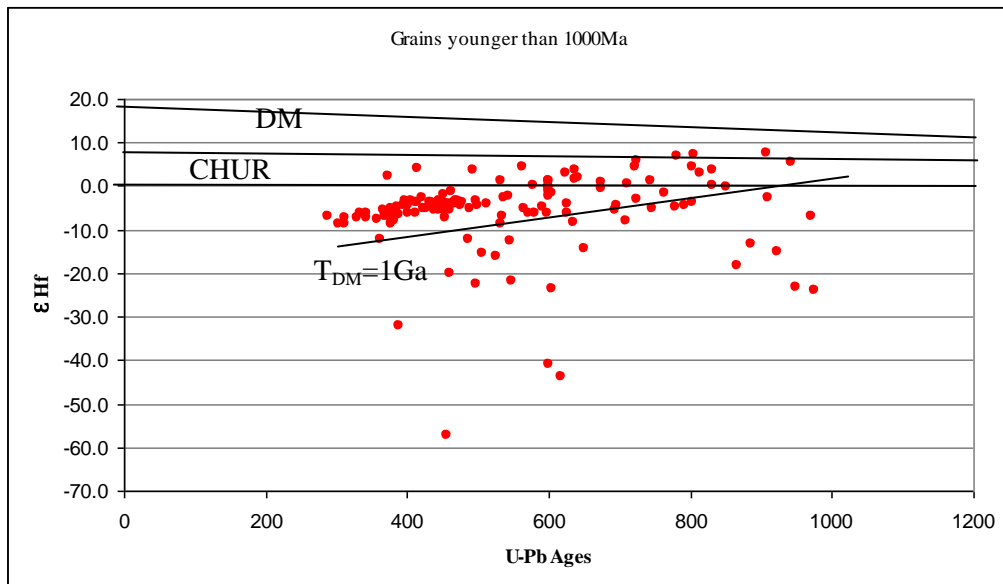


Figure 3.17 U-Pb-Hf plot of detrital zircons younger than 1000 Ma.

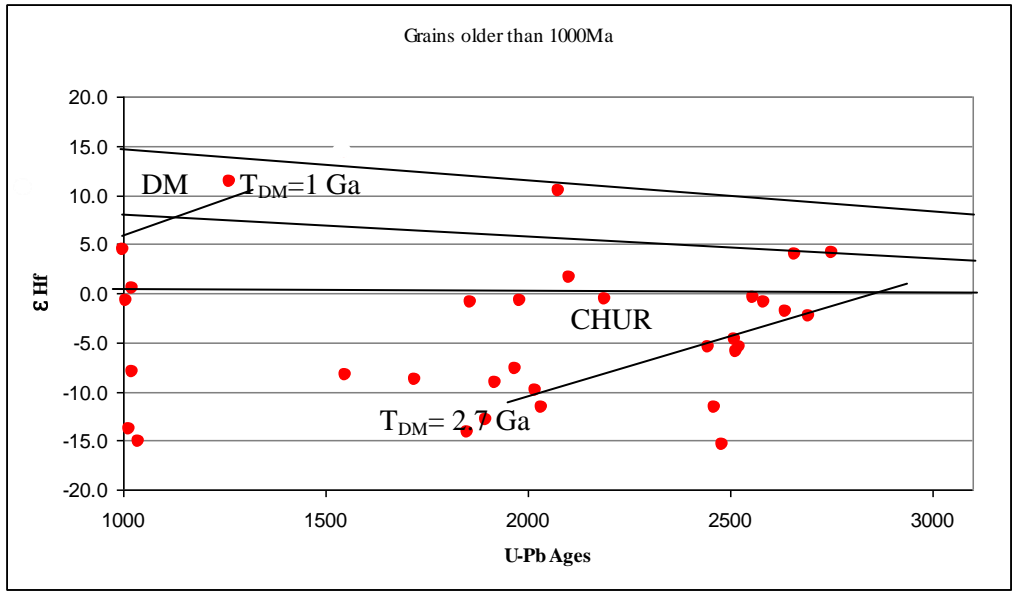


Figure 3.18 U-Pb-Hf plot of concordant detrital zircon grains older than 1000 Ma.

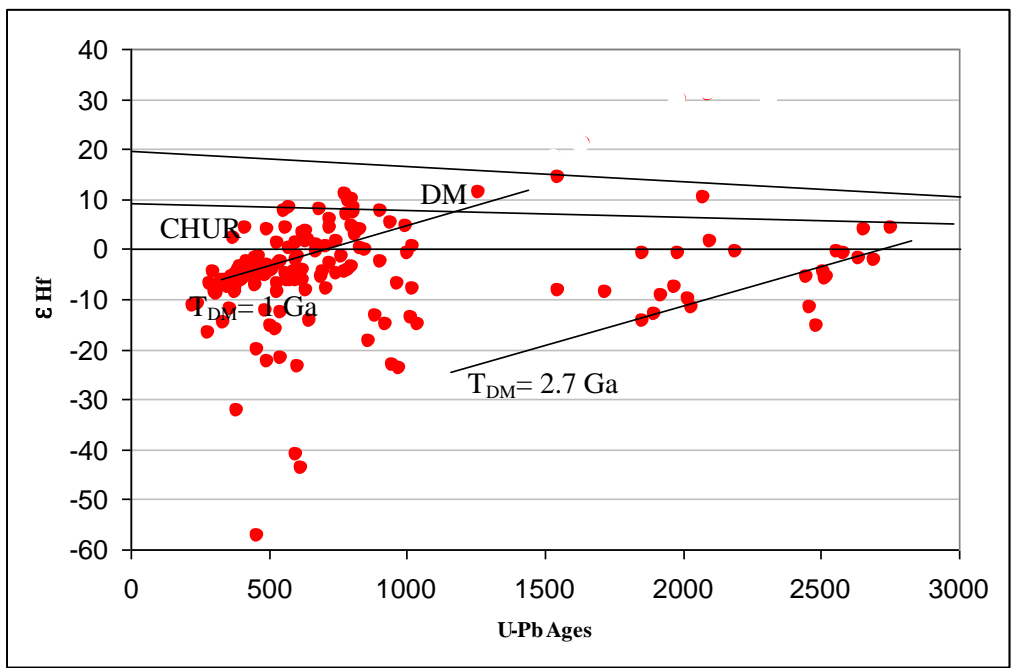


Figure 3.19 U-Pb-Hf plot of all concordant zircon grains.

Hundred and fortyfour grains, which are younger than Mezoproterozoic, were measured for  $\epsilon\text{Hf}$  values. 77% of relatively younger grains (< 1000 Ma) have negative (-)  $\epsilon\text{Hf}$  values; this indicates a reworked crustal source. 23% of younger grains belong to juvenile crustal sources. Most of the reworked sourced-grains'  $T_{\text{DM}}$  age is around 1.0 Ga. There is almost no depleted mantle sourced grains in younger sequence (Figure 3.19). There are three Cambrian grains with  $T_{\text{DM}}$  ages older than 2.7 Ga and have the highest  $\epsilon\text{Hf}$  negative values.

$\epsilon\text{Hf}$  values of forty older grains (>1000 Ma) were measured. 62.5% of these grains have negative  $\epsilon\text{Hf}$  values and less number of the grains belong to juvenile crustal source.  $T_{\text{DM}}$  ages are between 1.0 and 2.7 Ga and there are two Siderian grains with  $T_{\text{DM}}$  ages older than 2.7 Ga; they belong to a reworked crustal source.

The importance of  $\epsilon\text{Hf}$  values and U-Pb ages will be discussed briefly in Chapter 5.



## **CHAPTER 4**

### **STRUCTURAL GEOLOGY**

#### **4.1 INTRODUCTION**

In this chapter, detailed information about macro- and micro-scale geological structures observed and investigated during both field and laboratory studies will be given. The kinematics of fabric elements will also be presented and their tectonic significance discussed.

#### **4.2 STRUCTURAL FEATURES**

The most common structures in Kurudere area are foliation, lineation, crenulation cleavage and mesofolds. In the following sections these structures will be described briefly.

##### **4.2.1 FOLIATION AND LINEATION**

‘Foliation’ is used here as a general term to define penetrative planar structures which formed as a result of homogeneous deformation in a body of rock. In the study area, the metasedimentary units are characterized by a well-developed, penetrative, south-dipping foliation; it is the most obvious structure both at macroscopic scale in the field and at microscopic scale (Figures 4.1, 4.2 and 4.3a).

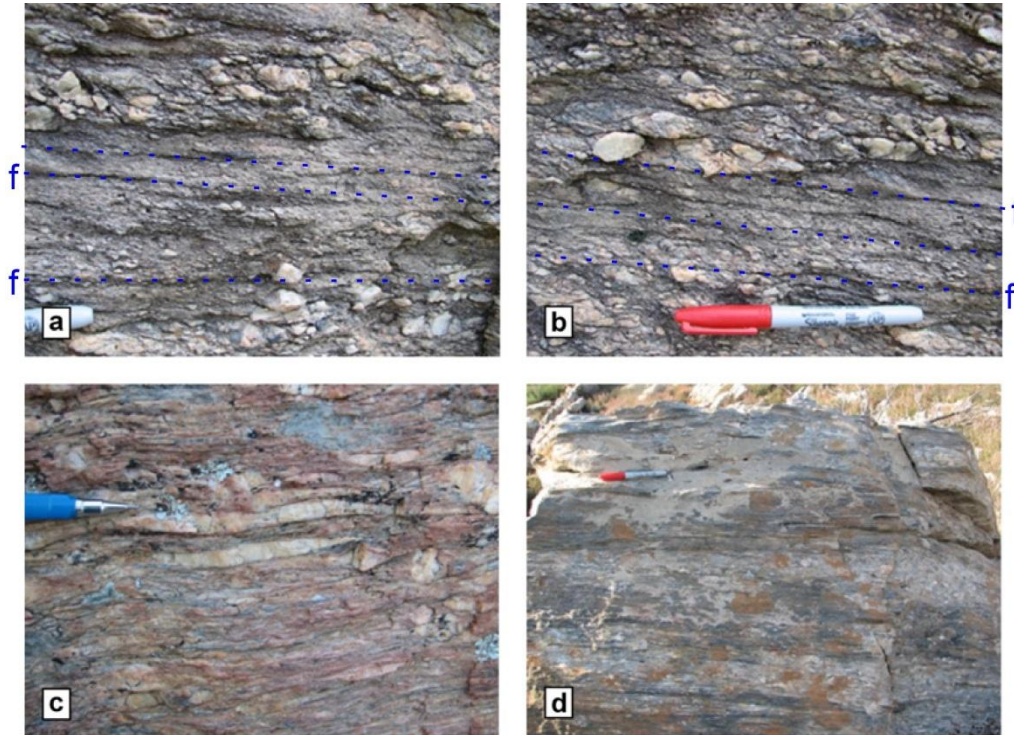


Figure 4.1. (a, b) Field appearances of foliation in the metaconglomerates. Note that it is pronounced and penetrative in the fine-grained parts and is defined by the preferred parallel alignment of micas and quartz grains. Larger quartz pebbles are either flattened in the plane of foliation or stand out as resistant porphyroclasts, giving the rock an augen structure (f–foliation). (c) Where deformation is intense, many quartz pebbles are flattened and elongated; together with micas and fine quartz grains; flattened grains define the main foliation in the rock. (d) Field view of the foliation in the metapelitic rocks. Pencil is about 13-cm long.

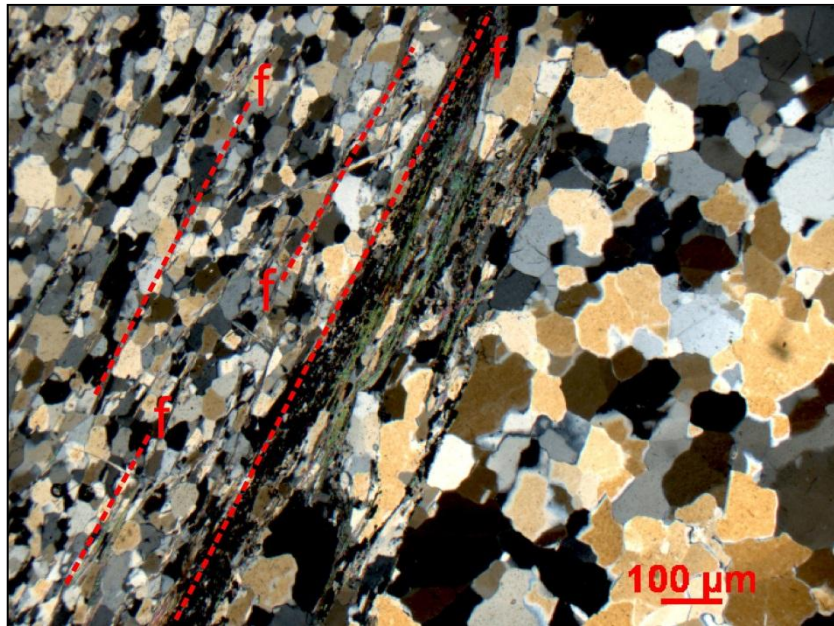


Figure 4.2 S-dipping foliation at microscopic scale where it is defined by the preferred parallel alignment of mica minerals and long axis of quartz ribbons. Note the dominal structure defined by alternating quartz- and mica-rich domains. Note also texture and size of quartz grains in quartz-domains as well.

Foliation is defined by parallel alignment of micas, long axis of quartz ribbons and long axis of flattened and elongated quartz pebbles. Microscopically, 001 surfaces of mica flakes show preferred parallel alignment that defines the main foliation in the rock. The dominal structure defined by mica- and quartz-rich domains give the rock a gneiso-structure and indicates both the intensity of deformation and high-degree of metamorphism. Foliation in the metapelites is relatively more pronounced and defined mostly by parallel alignment of micas together with quartz; if quartz pebbles are present, they also show parallelism with its axes (Figure 4.3a). Deformation of the foliation by small-scale wrinkles are common (Figure 4.3b). Foliation parallel quartz veins are mostly deformed and boundinaged within the plane of foliation (Figure 4.3)

The general strike of the foliation is constant throughout the study area; northwest–southeast (Figures 2.1 and 4.4a) striking foliation dips to the south. The amounts vary between 32° and 78°.

The other penetrative structure is the mineral stretching lineation; it is well-defined by the preferably aligned mica and quartz grains and the long axes of flattened and

elongated quartz pebbles in the metaconglomerate. The general trend of moderately ( $40^\circ$ ) south-plunging lineation is approximately N–S (Figure 4.4b).

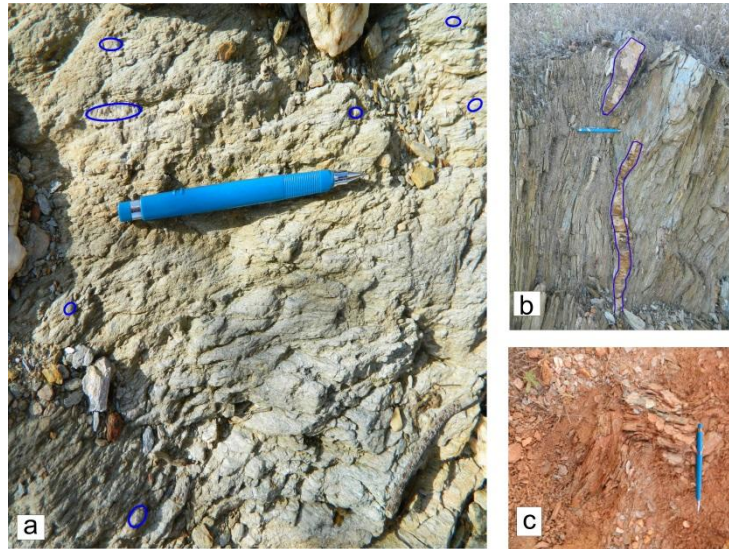


Figure 4.3 Views from metapelites in the area between Çileklik Hill and Lomburt Hill (see Figure 2.1 for location): (a) quartz pebbles (indicated by blue circles) in metapelites, (b) small-scale fold in a reddish metapelitic unit, (c) boudinaged quartz veins in fine-grained metapelitic unit. Note how quartz veins are disrupted and isolated within the metapelites in (c). Pencil is about 13-cm long.

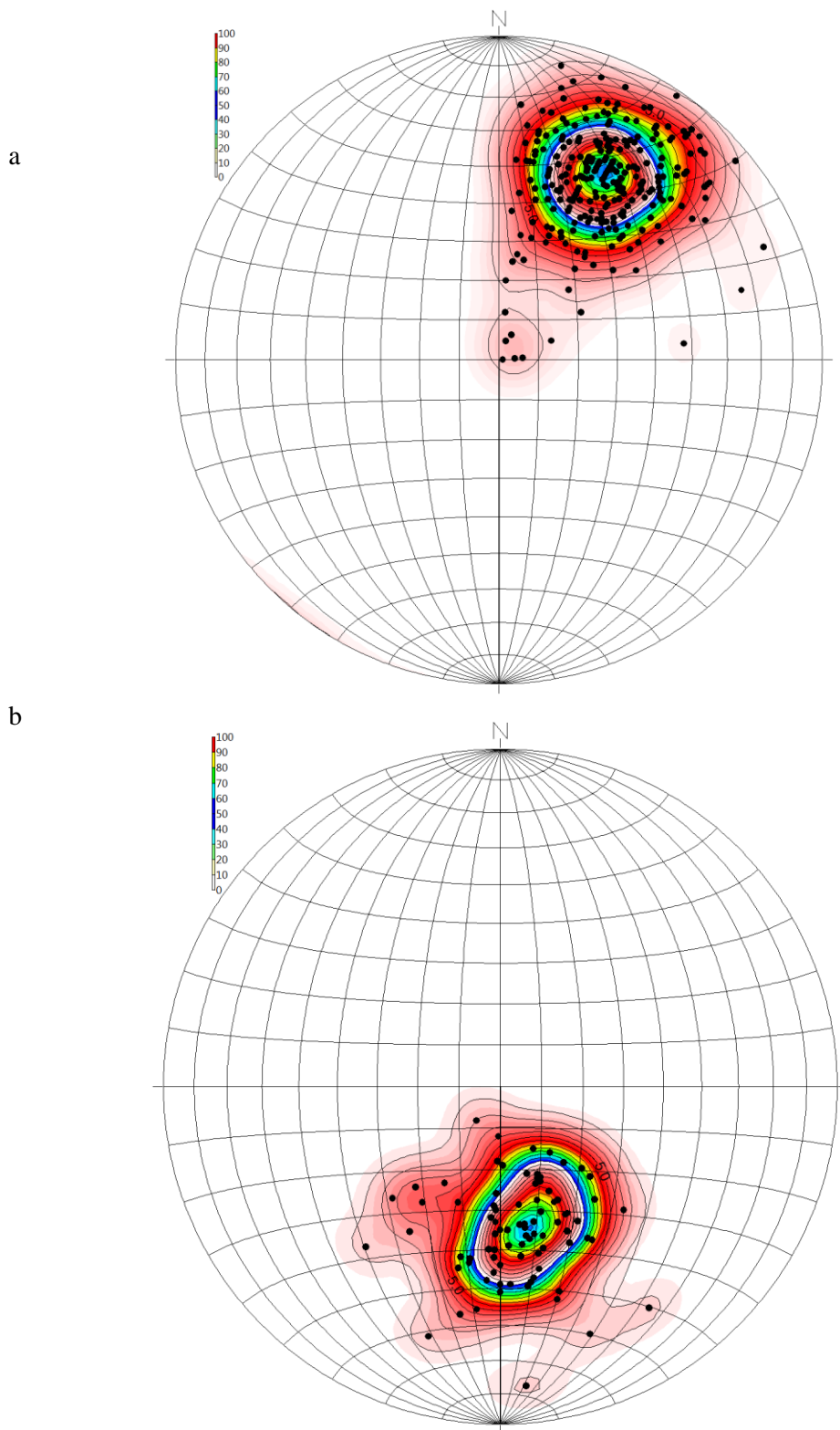


Figure 4.4 Stereonet pole plots of (a) south-dipping foliation and (b) almost N-S-trending mineral stretching lineation in the Kurudere area (Rockworks16).

#### 4.2.2 CRENULATION CLEAVAGE

Crenulation cleavage (tectonic secondary cleavage) is the another common structure in the study area (Figure 4.4a). It is more pronounced and penetrative in the metapelitic rocks than metaconglomerates. It commonly occurs a discrete asymmetric crenulation cleavage.

Crenulation cleavage appears as harmonic wrinkles deforming a pre-existing foliation. The new foliation cuts across the old foliation and is defined either by both limbs of symmetric crenulations or by long limb of asymmetric crenulations. Old foliation is preserved in microlithons as the hinge of symmetric crenulations and/or as the short limbs of asymmetric crenulations. Width of microlithons depends on wavelength of the crenulations. Crenulation cleavage is observed both in macroscopic and microscopic scales (Figure 4.5) as asymmetric discrete crenulation cleavage with rounded hinges. These structures indicate localization of shearing whereas the development of shear bands that cut across a pre-existing foliation and define new cleavage domains. Because there are observable displacements along crenulation cleavages, some are termed as shear cleavage as well (Figure 4.6). The general trend of the hinge lines of crenulation cleavages is 140–190 and average plunge is 35° southeastward (Figure 4.7a).

The crenulation cleavages suggest either a change in the direction of principle stress or an axial surface fabric formation related to the development of a larger scale fold(s) (cf. Dupee, 2005; Twiss and Moores, 2007). Symmetric zonal crenulation may form as a response to shortening parallel to a pre-existing foliation. The old foliation is rotated toward low angles to the axial surfaces of the new crenulations, which form the new foliation. Solution of new material from the limbs may create the new foliation. Such symmetric crenulations, which may have rounded or sharp hinges commonly occur in the core of a lower-order fold, where the crenulation foliation is subparallel to the axial surface of the fold. In this model, the direction of maximum shortening is normal to the crenulation foliation (Figure 4.8).

Asymmetric crenulation can form by shortening at a low angle to the initial foliation. The axial surface of kink develop at a high angle to the original foliation and are parallel to a new crenulation foliation defined by the short limbs of the crenulations in which the old foliation rotates into subparallel with the new foliation. There is no net shearing of the body parallel to the new foliation, and the axis of maximum shortening is normal to the new foliation. An asymmetric crenulation can develop from a symmetric one by preferential solution of components from one set of limbs (Figure 4.9).

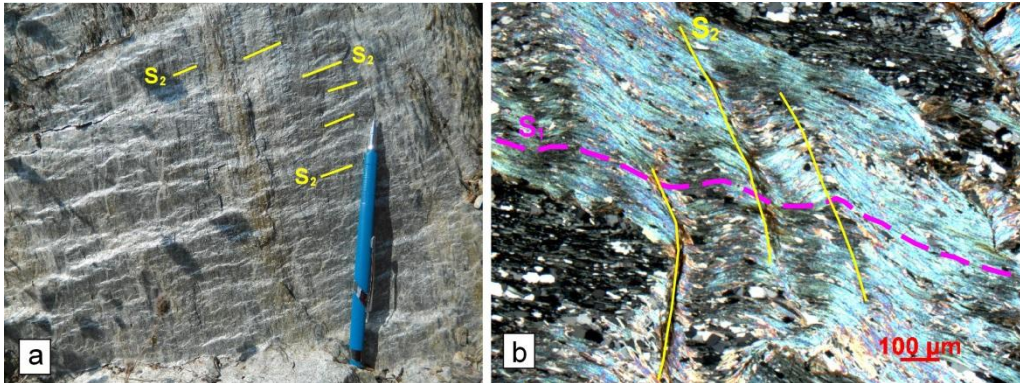


Figure 4.5 (a) Field view and (b) photomicrograph of crenulation cleavage in metapelites. S<sub>1</sub>– older foliation, S<sub>2</sub>– crenulation cleavage.



Figure 4.6 A view from shear cleavage developed in the metapelites. Note millimetric-scale displacement along discrete cleavages.

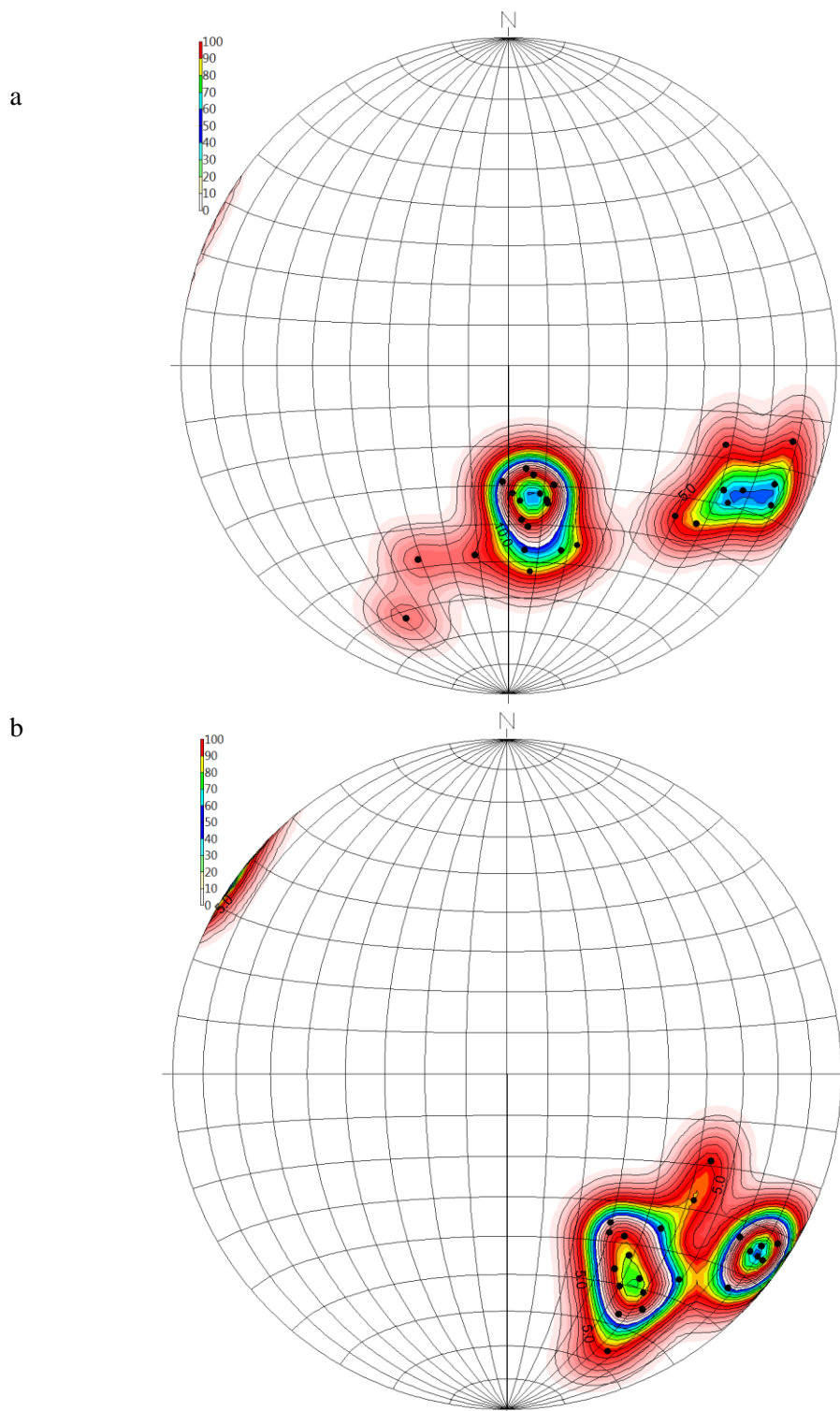


Figure 4.7 Stereonet pole plots of (a) hinge line of crenulation in metapelites, and (b) hinge line of folds (fold axis) in the metaconglomerates (Rockworks16).

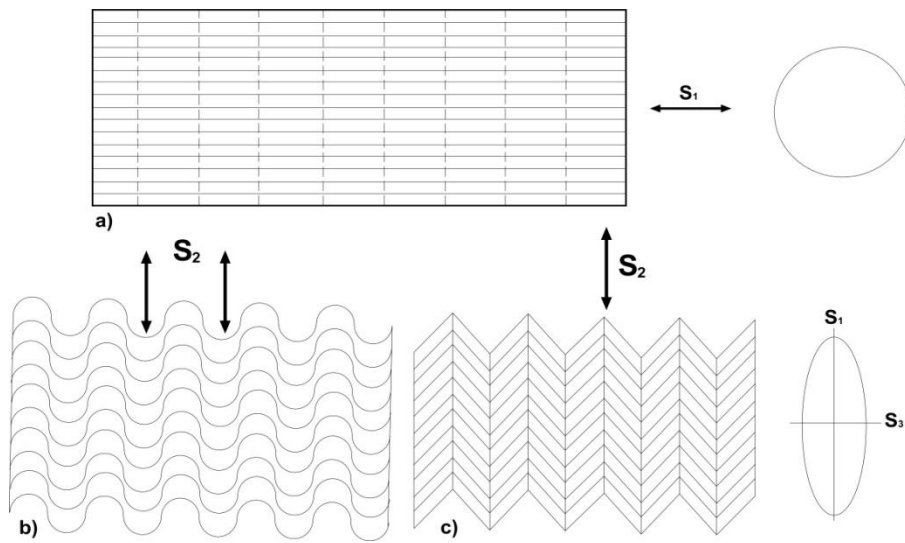


Figure 4.8 Mechanism of a symmetrical crenulation foliation  $S_2$  by buckling  $S_1$ . (a) Initial foliation  $S_1$  parallel to the direction of maximum shortening. (b) Shortening generates symmetrical crenulation by buckling or (c) chevron style of crenulation (from Twiss and Moores, 2007).

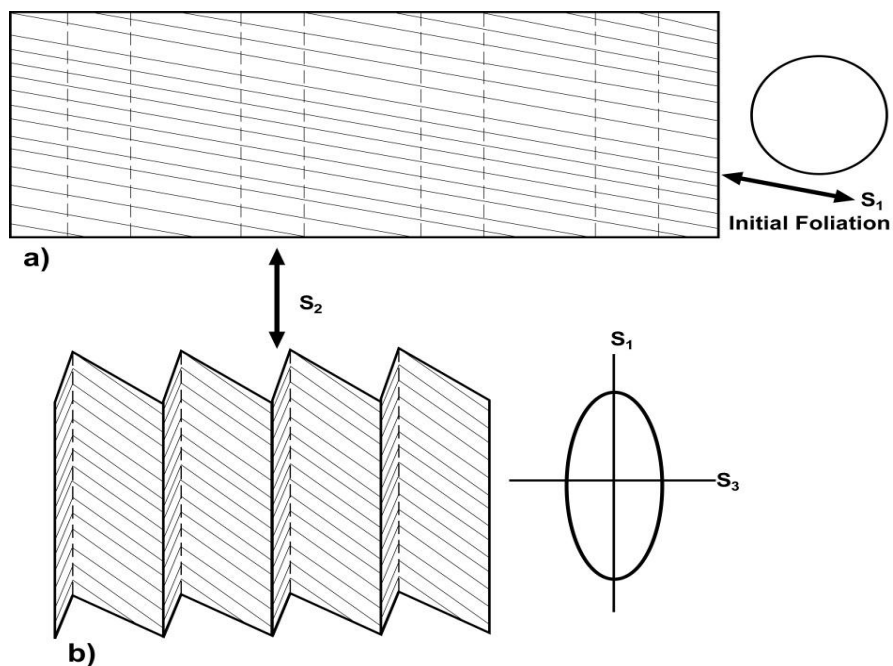


Figure 4.9 Production of asymmetrical crenulation foliation  $S_2$  by buckling of  $S_1$ . (a) Initial foliation  $S_1$  is at a low angle to the direction of maximum shortening. (b) Asymmetric crenulation is occurred by buckling of  $S_1$ .  $S_1$  has rotated to a low angle

with the crenulation axial surface and defines the short limb of the crenulation. Hinges may be sharp or rounded (Twiss and Moores, 2007).

### 4.2.3 FOLDS

Folds form the most prominent structural elements of the HP rocks in the Kurudere area. They deform the main foliation and occur as asymmetric and/or overturned mesoscale structures. Their geometry and kinematics vary between northern and southern parts of the study area; typical S- and Z-geometries are possible. The structure is more pronounced where there is a contrasting rheology: quartz veins and flattened/elongated quartz pebbles or thin sandstone horizons in the coarse metaconglomerates make the folds to appear more clearly. For this reason these structures are commonly observed in metaconglomerates (Figures 4.10 and 4.11).

Folds are also obvious where dark, black-greyish fine-grained (sandstone or sandy mudstone) intercalations are present within the metaconglomerates. The thinly bedded mica-rich layers are commonly strongly folded. Unfortunately many of the observed examples of such folds are not in their position; most are obvious on loose blocks of the metaconglomerates and this makes it almost impossible to measure the attitudes of these structures. Where developed, the folds occur as small-scale undulations with well developed hinge lines (Figure 4.11a, b). The asymmetry and shape of mesofolds are used to determine sense of shearing during their formation (see next section). The general trend of the hinge lines is in NW–SE direction where average plunge is about 26° southeastward (Figure 4.7b).



Figure 4.10 Folded thin, fine-grained dark metapelitic unit within the metaconglomerates, Karaburun Ridge.

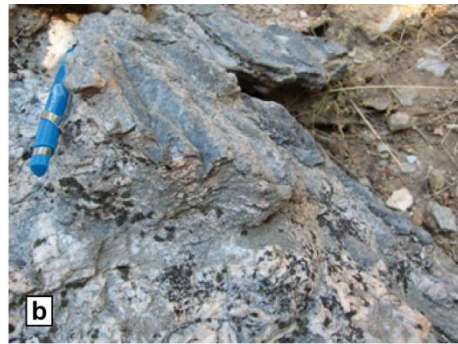


Figure 4.11 General views from mesoscales folds in the metaconglomerates. (a, b) Folds are obvious where metaconglomerates contain thick dark layers of more sandy levels; in such cases the geometry of the wrinkles and the hinge lines of the folds are obvious for inspection; (c) an overturned intrafolial fold with its axes almost parallel to the foliation; (d) where quartz veins are present, folds become more pronounced; (e, f) Z- and S-geometries are common; in these photographs they indicate top-to-the-north and top-to-the-south sense of shear respectively; (g, h) flattened quartz pebbles in folded structures.

### 4.3 KINEMATIC INDICATORS

The kinematics of deformation of the metaconglomerates formed one of the most important stages of this research. It was not considered as one of the aims of the thesis study at the beginning of the research. Field observations, particularly occurrence of metaconglomerates at two distinct horizons and the possibility that they may represent the same stratigraphic level in the metasedimentary sequence, made it crucial to explore further if the two horizons display the same sense of shear or not. If the two metaconglomerate horizons represent the same stratigraphic level, and if each horizon shows opposite kinematics; this may indicate an overturned fold. Otherwise they either represent different metaconglomerate levels or there is a fault somewhere in-between. These differences made it crucial to explore further about the sense of shear in each metaconglomerate horizon. Below, a brief summary is given.

The main foliation in the metasedimentary rocks shows kinematic indicators that bear on the sense of motion during their metamorphism and associated deformation. Characteristic kinematic indicators include stair-stepping geometry of quartz pebbles and coarse mineral grains/porphyroclasts, orientation of hinge line of folds and fractures in megacrystals, the asymmetry and shape of mesofolds and C-S fabrics. The resistant quartz grains and pebbles isolated within the matrix foliation forms the most overwhelming evidence about the movement direction in the field. Oriented thin sections are investigated to confirm field observations and to realize the movement of direction at microscopic scale.

Kinematic indicators in Karaburun and Lomburt hills (see Figure 2.1 for location) are consistent with a top-to-the-south direction of movement at both macroscopic and microscopic scale (Figure 4.12) while those in the south, top-to-the-north shearing (Figure 4.13). The opposite sense of shearing in two distinct horizons of the metaconglomerate is an important observation. In the following lines and figures, evidence that supports sense of shearing will briefly be presented.

The geometry and shape of folds are also used as a kinematic indicator, and in all cases they are in-line with other kinematic indicators. Z- and S-geometries are common

(Figure 4.11e, f). The folds in the northern metaconglomerate horizon are consistent with top-to-the-south sense of movement, whereas those in the north, top-to-the-south shearing, thus confirming other kinematic indicators.

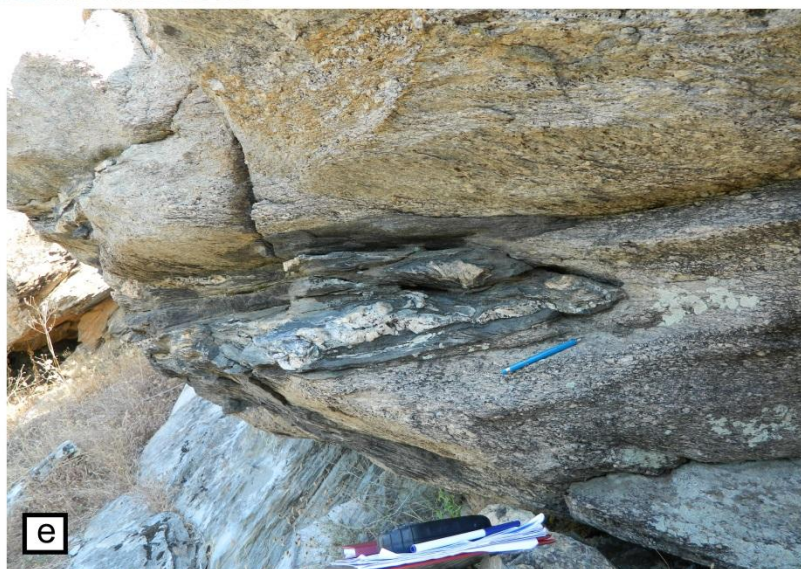
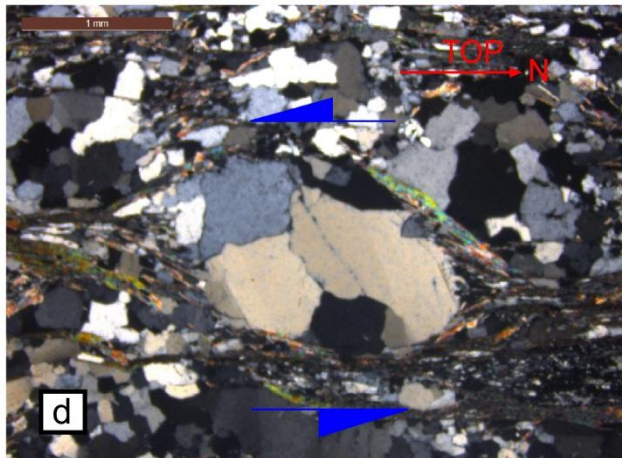
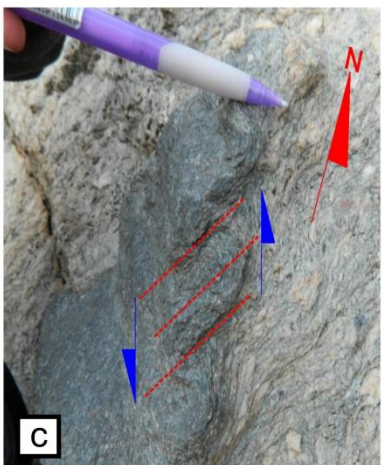


Figure 4.12 Views of kinematic indicators from northern side of study area: (a, e) Mesofolds in the metaconglomerates; the folds are obvious where metapelites intercalations occur. (b) Microscopic view of quartz grain oriented oblique to the main foliation in the rock. The long axis of quartz grain defines the S-foliation whereas the matrix foliation, C surfaces; (c) Mesoscale en-échelon folds in the metaconglomerate; (d) Poorly-developed  $\sigma$ -geometry defined by a large quartz porphyroclasts and dynamically recrystallized mantle around it. Note that the quartz is dynamically recrystallized into smaller subgrains. The undulose extinction of new grains is evident. Note also thin blade of white mica defining the S-foliation in the rock. The stair-stepping geometry defined by larger grain and deformed mantle is evident. The C-S fabric development in (b) and (d) forms overwhelming evidence for movement sense. The asymmetry and shape of the folds are considered to suggest sense of shear. All of these meso- and micro-structures are consistent in indicating a top-to-the-south sense of shear. Thin sections are cut parallel to the mineral stretching lineation and perpendicular to the main foliation in the sample.

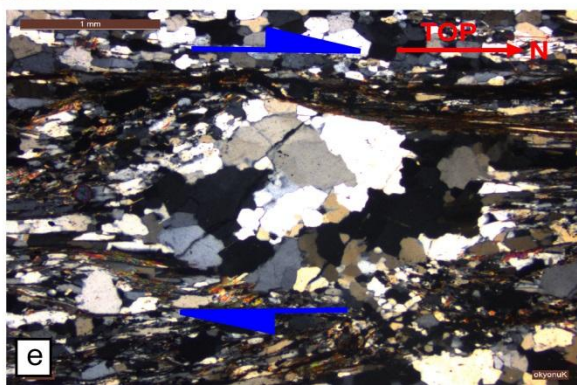
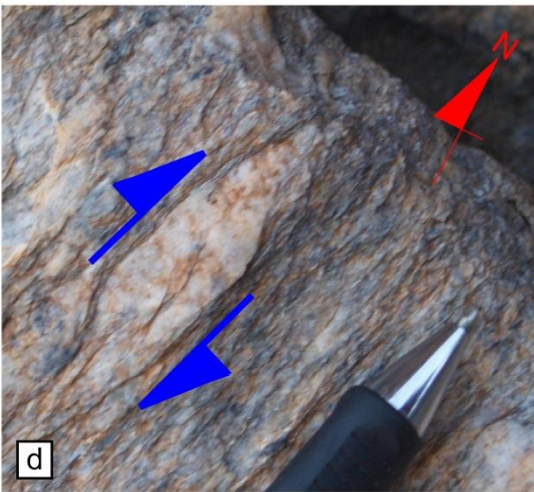
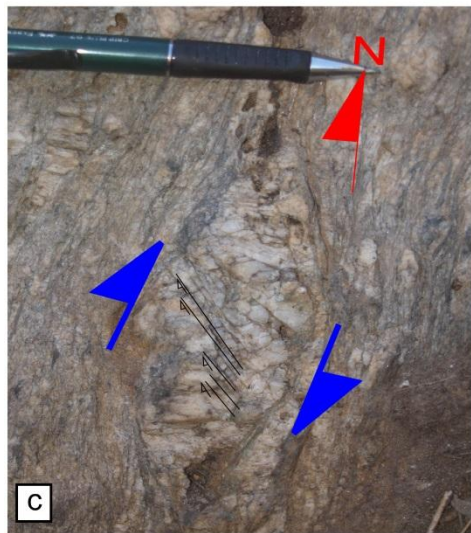
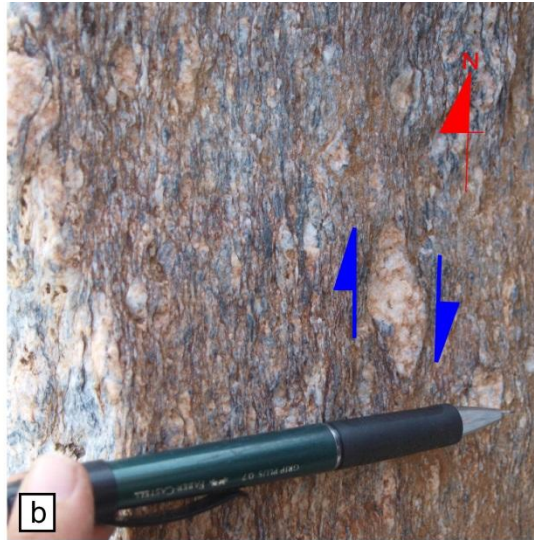
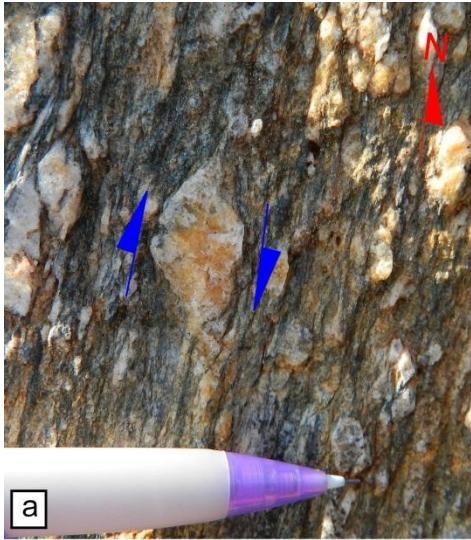


Figure 4.13 Top-to-the-north kinematic indicators in Çileklik hill in the south of the study area. (a–d)  $\sigma$ -type quartz porphyroclasts and pebbles embedded within a fine-grained matrix of quartz, white mica and chlorite. Note how matrix foliation wraps around porphyroclasts and deformed pebbles. In all, the stair-stepping geometry of recrystallized and/or elongated tails is pronounced. (e) Microscopic view of a quartz pebble. The quartz grain is dynamically recrystallized into subgrains, each of which show characteristic undulose extinction. The boundaries of subgrains are irregular/serrated and indicates that grain-boundary migration is an important deformation mechanism subsequent to subgrain formation. Deformation band formation and kinking are also characteristic. The long axis of the porphyroclast defines the S-foliation whereas matrix foliation of white mica and fine-grained quartz represent the C-foliation.



## **CHAPTER 5**

### **DISCUSSION**

Measurements of U-Pb and Hf systems in detrital zircons of the metaconglomerates in Kurudere HP quartz-metaconglomerate are first reliable geochronological data from the southern Menderes Massif. The existing questions relates to (i) the age of the unit and (ii) the origin of the metaconglomerates; that is if they belong to the Cyclades or form part of the marble cover succession in the Menderes Massif, will all be addressed below.

#### **5.1 AGE OF THE METACONGLOMERATES**

The youngest concordant detrital zircon age(s) will form a lower limit to the sedimentation age of the rock samples; that is the protolith age must be younger than the youngest zircon. The ca. 298 Ma (Asselian, earliest Permian) is the youngest zircon in the metaconglomerates. This indicates that the age of sedimentation could be any age younger than earliest Permian, thus supporting the proposed late Triassic age. At this stage because there is no further evidence, a late Triassic age by Rimmerle et al. (2003b) is accepted.

#### **5.2 ORIGIN OF THE METACONGLOMERATE**

The origin of metaconglomerates is more difficult to interpret. Because there are two schools suggesting differing terranes for the origin of the metaconglomerates, the Cycladic and Menderes massifs must be considered equally. Here the source/provenance of sediments to the metaconglomerates needs to be tested. To do that the available literature will briefly be summarized to see if detrital zircon populations in the Cycladic and Menderes metasediments have clear and pronounced differences.

##### **5.2.1 CYCLADIC MASSIF**

Crustal deformation in Aegean backarc has occurred progressively during slab retreat. Extension started with exhumation of Rhodope Massif in the Eocene and migrated

southwards through Cyclades and Menderes Massif in the Oligocene and early Miocene.

Cyclades was described as an extensional core complex (Lister et al., 1984) because it shows very similar structures, both in time and space, as cordilleran-type core complexes: (i) a ductile shear zone with mylonitic rocks, (ii) elongated domes with long axes parallel to the stretching lineation, (iii) syn-tectonic granitic magmatism, (iv) progressive deformation during decreasing temperature conditions through first by mylonitization then progressively by more brittle deformation to cataclasis in the immediate footwall of low-angle faults and (v) structurally overlying unmetamorphosed rocks.

The Cyclades is located in the back-arc of the southward retreating Aegean subduction zone in the central Aegean Sea (cf. Bolhar et al., 2010 and references therein). Stratigraphically, Cycladic blueschist unit contains (i) Variscan orthogneissic basement with Hercynian ages (e.g., Keay, 1998; Engel and Reischmann, 1998; Ring et al., 1999; Tomaschek and Ballhaus, 1999; Tomaschek et al., 2001, 2008; Philippon et al., 2012 and references therein), (ii) the sedimentary cover with depositional age between Early Carboniferous to Eocene (e.g., Dürr et al., 1978; Dubois and Bignot, 1979; Pohl, 1999; Philippon et al., 2012), (iii) an ophiolitic *mélange* (e.g., Ring et al., 1999). The Variscan basement and sedimentary cover series were intruded by Triassic granitoids (e.g., Reischmann, 1997; Ring et al., 1998, 1999; Philippon et al., 2012).

In Eocene time, this sequence experienced a high pressure-low temperature (HP-LT) metamorphism during the closure of Neotethys; later overprinting high temperature-low pressure (HT-LP) Barrovian-type metamorphism during Oligo-Miocene time was related to exhumation (e.g., Ring et al., 1999; Keay and Lister, 2002; Jolivet et al., 2012). Dilek/Selçuk nappes in Dilek Peninsula have the same metamorphic evolution with Cyclades and are considered as the continuation of the Cycladic HP rocks in the Menderes Massif (Ring et al., 1999 other references).

Keay et al. (2001, 2002) reported results of an extensive geochronological work in the pre-Carboniferous metasediments of the Cyclades. Several peaks were identified during Precambrian time: 2900–2850, 2500–2450, 2050–2000, 1900–1800 and 1700–1650 Ma. Less amount of Mesoproterozoic age is noteworthy. Peaks are also distinguishable for 1000–950 Ma (Tonian) and 900–800 Ma (Cryogenian-snowball Earth) intervals. For Paleozoic time, bimodal distribution in 650–550 Ma and 400–450 Ma intervals are significant for the Cyclades (Figure 5.1).

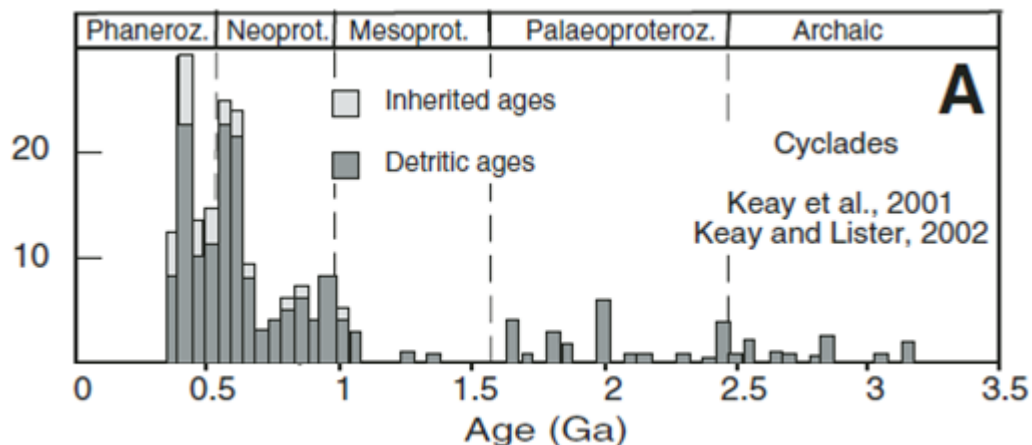


Figure 5.1 Published detrital zircon ages from the Cyclades Massif (Keay et al., 2001; Keay and Lister, 2002).

### 5.2.2 SOUTHERN MENDERES MASSIF

The geology of the Menderes Massif is described in Chapter 1. Here a brief summary will be presented. The southern Menderes has a typical tri-partite lithologic associations: (i) a metagranitic rocks that forms the so-called ‘*core*’ of the massif; it is mainly represented by orthogneisses (traditionally known as augen gneisses) of largely Precambrian age and subordinate metasediments and gabbroic rocks; (ii) so-called ‘*cover schists*’: they are composed of variable mica-quartz schists with or without garnet, psammitic rocks and intercalated marbles. The age of the sequence is largely considered as early Paleozoic–Ediacaran; and (iii) so-called marble cover of dominantly marbles with metabauxite occurrence at several different levels. Dolomites and rudist-bearing exposures are also described (see section 1.5 for further details).

The boundaries between core and cover schists and cover schist-marble formed the subject of controversies over the last three decades and several different interpretations are made (see also section 1.1-1.5).

The massif possesses a regional foliation with mostly top-to-the-north motion; it is attributed to so-called main Menderes metamorphism. It is a prograde metamorphism that reached amphibolite facies conditions at the structurally lowest levels and gradually decreases upward to low greenschist facies conditions. It occurred in the Eocene time (Bozkurt 1996; Hetzel et al., 1998; Bozkurt and Park, 1999; Whitney and Bozkurt 2002; Régnier et al., 2003, 2007 and the references therein). The age of the main Menderes Massif is considered as Eocene (~35 Ma;  $^{40}\text{Ar}/^{39}\text{Ar}$  mica cooling ages; see Table 1.1 for details and references).

There is also evidence for a top-to-the-south low-greenschist facies overprint associated with the deformation along, and exhumation in footwall of, the southern Menderes shear zone. Similar top-to-the-south fabrics are observed at different structural levels within the southern Menderes and they are attributed to reactivation of top-north thrust faults (e.g., Bozkurt and Park, 1997, 1999; Rimmelé et al., 2003; Bozkurt, 2004, 2007; Bozkurt et al., 2006; Whitney et al., 2008). The age of shear zone deformation and top-to-the-south fabrics are not dated geochronologically; an inference of Oligocene–early Miocene is based on regional correlations. The southern Menderes Massif was therefore interpreted as an incipient core complex of extensional type (Bozkurt and Park 1994 and several papers thereafter).

To summarize, there is no reported evidence of HP metamorphism from the schists of the southern Menderes Massif but the marble cover does. The metaconglomerates in the Kurudere area form the lowest part of the marble cover; the age of metamorphism is recently reported as  $45.2 \pm 2.0$  Ma ( $^{40}\text{Ar}/^{39}\text{Ar}$  phengite age; Pourteau et al., 2013). This age correlates well with the age data from Cycladic blueschists. The absence of evidence for HP metamorphism in cover schists and core augen gneisses further suggests that marble cover of the southern Menderes Massif have different tectono-metamorphic history compared to the rest of massif and that the core and schist cover of the massif have occupied tectonic setting different than that of marble cover or the two assemblages occurred and experienced different histories at different structural levels.

The most recent data about the detrital zircon geochronology from the Menderes Massif has already been given in section 1.1 and it will not be repeated here. These ages are from the lowestmost lithologies of the schist cover and are represented by four samples and about 150 zircon grains; it is therefore not clear to us if the available detrital zircon ages are statistically useful for comparison or not. There is also no data from the so-called marble cover rocks.

### **5.2.3 COMPARISON OF CYCLADES AND SOUTHERN MENDERES MASSIF**

Similarities and differences between Cyclades and Menderes Massif are important parameters to understand the geological evolution of Western Anatolia. Both massifs are considered to be linked each other and form a part of Median Crystalline Belt (Dürr et al., 1978) which is one of the world's typical blueschist belts (Candan et al., 1997). On the other hand, Ring et al. (1999) argued that both massifs do not correlate: Cyclades and Menderes Massif have entirely different age of basement, architecture, pre-Alpine and Alpine deformation history. Cyclades has Variscan basement that close to the Eurasian margin in the Triassic whereas Menderes Massif has Pan-African basement and was not affected by the Variscan orogeny. Two massifs were

amalgamated before the deposition of Mesozoic cover (Jolivet et al., 2012). Puzzling the other data and the occurrence of Triassic intrusions in both massifs indicates that they have mostly same Precambrian evolution, different Paleozoic history and similar Mesozoic cover processes (cf. Keay and Lister, 2002; Jolivet et al., 2012). Because the Menderes Massif have thicker crust it provides to preserve pre-extensional structures better than Cyclades; the total amount of extension in the Menderes is therefore less than in Cyclades (Jolivet and Brunn, 2008; Jolivet et al., 2012).

When examined closely, there are several differences and similarities to be accounted. The first one relates to the basement/core of the both massifs. While Cyclades are characterized by Variscan orthogneissic basement with Hercynian ages, the core of the southern Menderes is widely made up of Precambrian orthogneisses with subordinate schists and gabbros (they show relict HP metamorphism). The absence of Variscan granites and Hercynian ages in the southern Menderes is characteristic and this is used as a key point to distinguish between the two.

It is obvious that the core and cover schists of the southern Menderes Massif and marble cover have different metamorphic histories. If the two rock associations have formed a part of the Menderes succession, Palaeozoic schists and Precambrian orthogneisses must have experienced Eocene HP metamorphism or there should not be evidence of HP metamorphism in the marbles and metaconglomerates. This piece of evidence has been the main criteria of those suggesting a Cycladic origin for the marbles of the southern Menderes Massif (Ring et al., 1999; Gessner et al. 2004; Whitney et al. 2008). The new ca. 45 Ma phengite age (Pourteau et al., 2013) confirms this ascertain.

### **5.3 PROVENANCE OF KURUDERE METACONGLOMERATES**

Discovery of Fe-Mg-carpholite in the marble cover sequence of the Menderes Massif indicates a HP metamorphism (Rimmelé et al., 2003b; Whitney et al., 2008). Absence of HP relicts in the core and cover schists of the Menderes Massif made the researchers to explore more about the origin and provenance of the HP rocks in the southern Menderes Massif. The HP assemblages suggest that these rocks were buried to, at least, 35 km in a cold gradient (up to 12 kbar, 450–500°C) (cf. Whitney et al., 2008; Jolivet et al., 2012). On the other hand, core and cover schists were subjected to temperatures in excess of about 500°C at relatively low pressures (6–8 kbar; Whitney and Bozkurt, 2002) during the Eocene. This further means that the two rock associations behaved as two distinct terranes during the Eocene and do not belong to each other. The Ar-Ar phengite age of 45.2±2.0 Ma (Pourteau et al., 2013) from the Kurudere metaconglomerates further suggests that Kurudere HP rocks share synchronous metamorphism and evolution with the Cycladic blueschist unit. It is off course necessary to question the fact that single age data may not be enough to make a

firm conclusion but the meaning of the available data needs to be stated and discussed in any case.

The number and type of metamorphic events in both massifs are also different. As mentioned above Cyclades has two metamorphic events: HP in the Eocene and overprinting Barrovian-type greenschist facies metamorphism during the Oligo–Miocene time (e.g., Oberhänsli et al., 1998; Jolivet et al., 2012; Keay and Lister, 2002; Pourteau et al., 2013 and several other references therein). Except the Kurudere HP metamorphic unit, there are no HP relics in southern Menderes Massif schists. The main Menderes metamorphism is a regional Barrovian-type event and occurred during the Eocene. The available age data therefore suggest that HP metamorphism in the Cyclades and regional Barrovian metamorphism in the Menderes Massif must have occurred almost at the same time and that both massifs occupied different tectonic settings and/or occurred at differing structural levels during the Eocene. This further indicates that the presence and/or absence of Eocene HP metamorphism can be used as an evidence to distinguish between the Cyclades and Menderes Massif.

The similarities between the Kurudere HP metaconglomerates and the Cycladic blueschist unit are not arise from the age of metamorphism but also from the newly documented U–Pb ages and probability-density plots of detrital zircons.

The comparison between basements of two massifs has been complex before Palaeozoic time. Both massifs and Kurudere HP units have almost the same profile in Mesoproterozoic ages (e.g., Keay et al., 2001; Keay and Lister, 2002; Zlatkin et al., 2013); lack and/or less amount of ages between 1200–1700 Ma interval indicates northern margin of Gondwana as a provenance (cf. Gebauer, 1993; Keay and Lister, 2002).

In Cryogenian (850 to 635 Ma; Neoproterozoic) is cited as the beginning of sedimentation of protolith of the ‘gneiss core’ in the southern Menderes Massif (Şengör and Satır, 1984); the sediments therefore lack of 900–700 Ma zircons (Kröner and Şengör, 1990). Recently published data from the Southern Menderes Massif clearly displayed decreasing trend between 900–700 Ma (Zlatkin et al., 2013) and support this idea. While Menderes Massif was derived from north Africa, primitive magmatic rocks produced in Cyclades during the development of an active continental margin (Reischmann et al., 1991; Keay and Lister, 2002), this range of detrital zircon ages (900–700 Ma) are common in the Kurudere metaconglomerates (Figures 3.16 and 5.2).

There is also bimodal distribution of zircon ages in 650–550 Ma interval from both the Cyclades and the Menderes Massif. Thus statistically wave-like (bimodal) distribution

of 550–650 Ma detrital zircons from the Kurudere HP rocks are very similar to that of Cyclades and the Menderes and symbolize Pan-African orogeny (Figures 5.1–5.3).

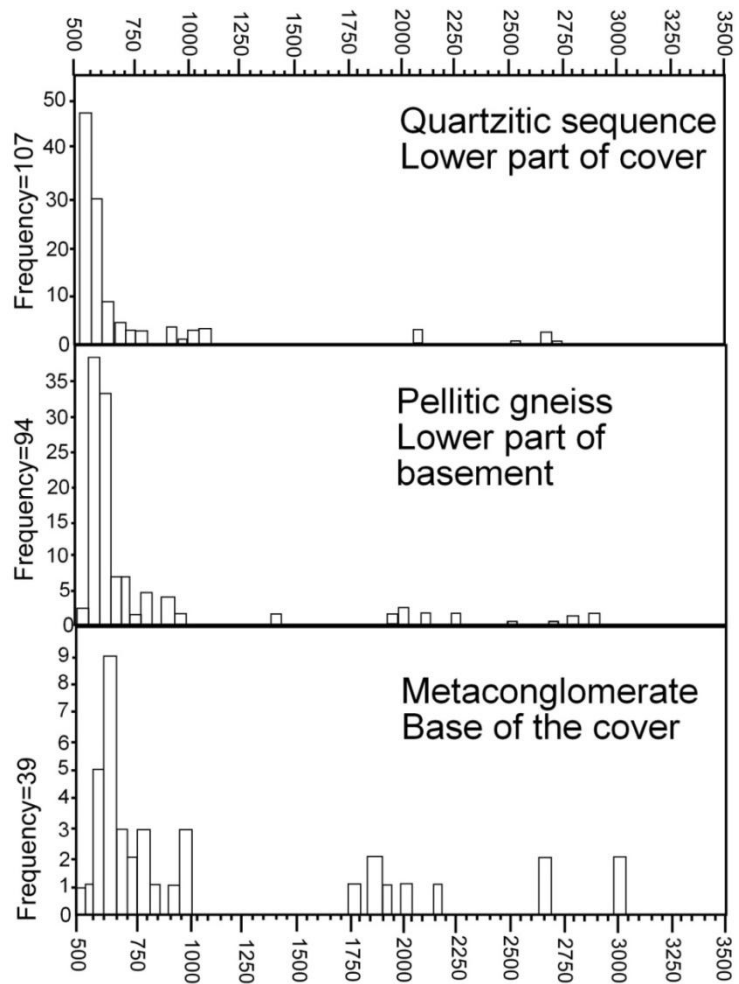


Figure 5.2 Published probability-density plots of detrital zircon from Southern Menderes Massif schists (from Zlatkin et al., 2013).

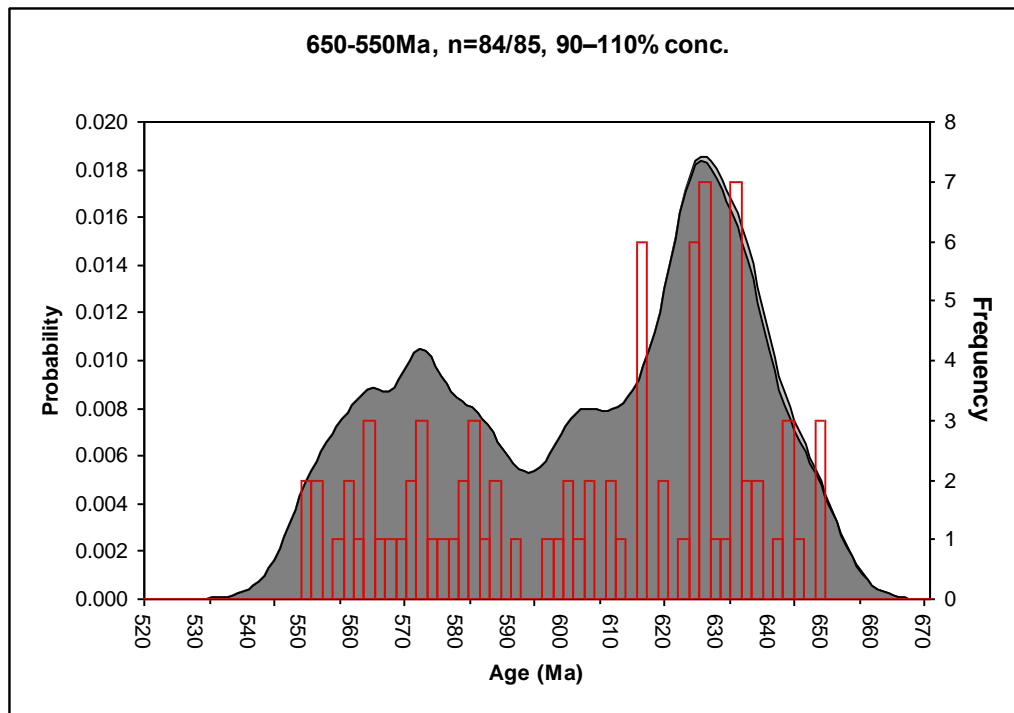


Figure 5.3 Bimodal distribution of detrital zircon ages between 550 and 650 Ma that symbolize two distinct stages of during Pan-African Orogeny.

Şengör et al. (1984) argued that late Ordovician–early Devonian ( $453.0 \pm 0.7$  to  $393.3 \pm 2.5$  Ma, Gradstein and Ogg, 2004) in the Menderes Massif corresponds to a tectonically quiet period with limited number of magmatic activity. Thus, there is a very low probability for the sediments derived from the Menderes to contain 450–400 Ma zircons in contrast to Cyclades (Keay and Lister, 2002). The presence of many Ordovician and Silurian detrital zircon ages (Figure 3.16) from the Kurudere HP metaconglomerates supports a more Cycladic origin.

The youngest zircon grain ( $298 \pm 5$  Ma) in Kurudere HP units, as mentioned above, is Asselian ( $299.0 \pm 0.8$  to  $294.6 \pm 0.8$  mya) and has oscillatory zoning typical for magmatic activity. It is proposed that this grain may belong to a 280–330 Ma, magmatic activity as recorded by Meinhold et al. (2008).

$\epsilon_{\text{Hf}}$  values are noteworthy to determine differences between the Menderes Massif and the Kurudere HP metaconglomerates. In the southern Menderes Massif, generally, grains younger than 1000 Ma have (+)  $\epsilon_{\text{Hf}}$  values, sourced from a juvenile crust, and  $T_{\text{DM}}$  ages are around 1.0 Ga. For older grains ( $> 1000$  Ma)  $\epsilon_{\text{Hf}}$  values are scattered (Zlatkin et al., 2013; Figure 5.4). But younger grains ( $< 1000$  Ma) for the Kurudere rocks have (-)  $\epsilon_{\text{Hf}}$  values, suggesting reworked crustal source;  $T_{\text{DM}}$  range extends

from 0.71 up to 3.57 Ga. For older grains (>1000 Ma) the values are scattered as expected (Figures 3.19–3.21). The  $\epsilon_{\text{Hf}}$  values of the Kurudere metaconglomerates are therefore not consistent with southern Menderes data. The discrepancy between  $\epsilon_{\text{Hf}}$  values from the southern Menderes schists and Kurudere metaconglomerates is pronounced and is therefore used to favour a Cycladic origin for the metaconglomerates. During Neotethyan magmatic activity, Early–Middle Ordovician age zircons were reworked in the Cyclades. In Kurudere HP units, high population of (-)  $\epsilon_{\text{Hf}}$  values may indicate this process (cf. Meinhold et al., 2008).

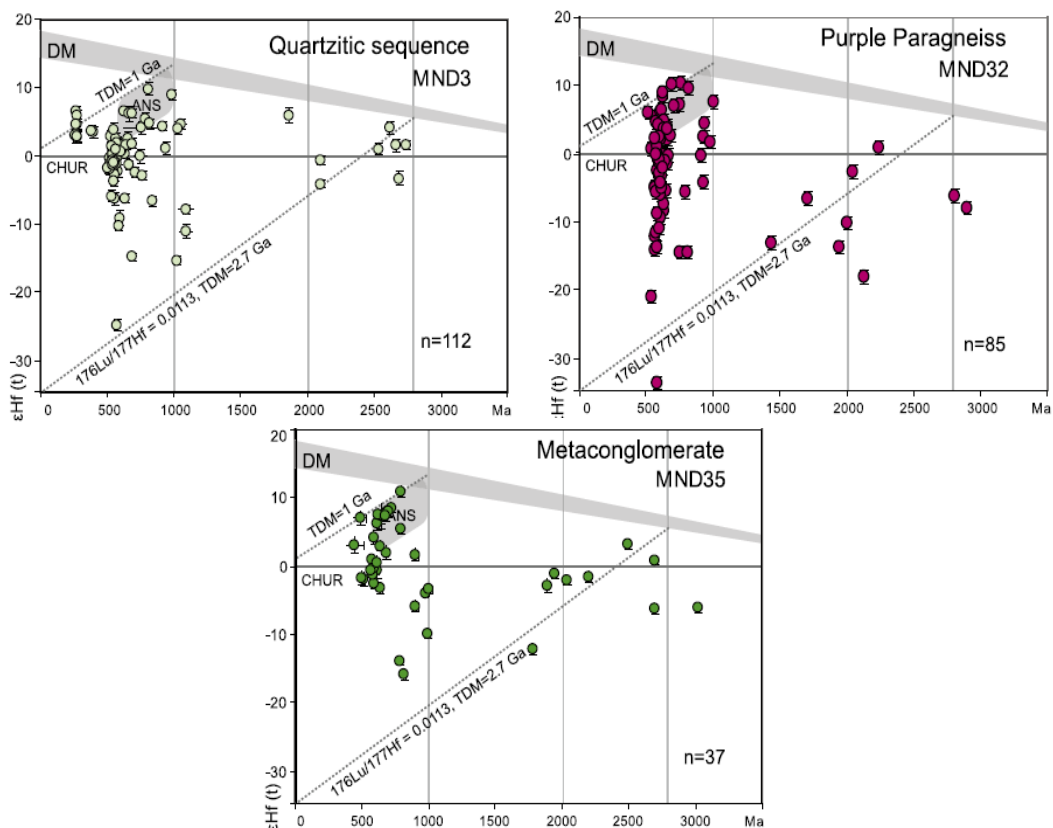


Figure 5.4.  $\epsilon_{\text{Hf}}$  values southern Menderes Massif (Zlatkin et al., 2013).

## 5.4 INTERPRETATION OF STRUCTURAL DATA

The metaconglomerates form the most important lithologic association in the Kurudere area and occur at two distinct horizons. Their lithologic characteristics suggest that they may represent the same conglomerate horizon but repeat owing to large-scale structure(s) in the region. The senses of kinematics in two horizons are opposite to each other. The meso- and micro-scale structures, as illustrated in the previous section, are consistent with top-to-the-south shearing in the north and top-to-

the-north shearing in the south. When plotted in a schematic cross-section (Figure 4.14), the distribution of metaconglomerates and kinematic indicators suggest a north-vergent recumbent anticline just below the marbles. Similar structures are mapped, using distribution and repetition of metabauxites in the marbles, within the structurally overlying marble sequence (Çağlayan et al., 1980; Bozkurt and Park, 1999).

It must be remembered that any viable structural model should demonstrate the facing direction of metaconglomerate beds in the Kurudere area. Because of intense deformation there is no primary structures preserved in the metaconglomerates. It is therefore not possible to determine and comment on which way the beds are facing. The overturned anticline model is based on the assumption that flexure-slip was the mechanism of folding.

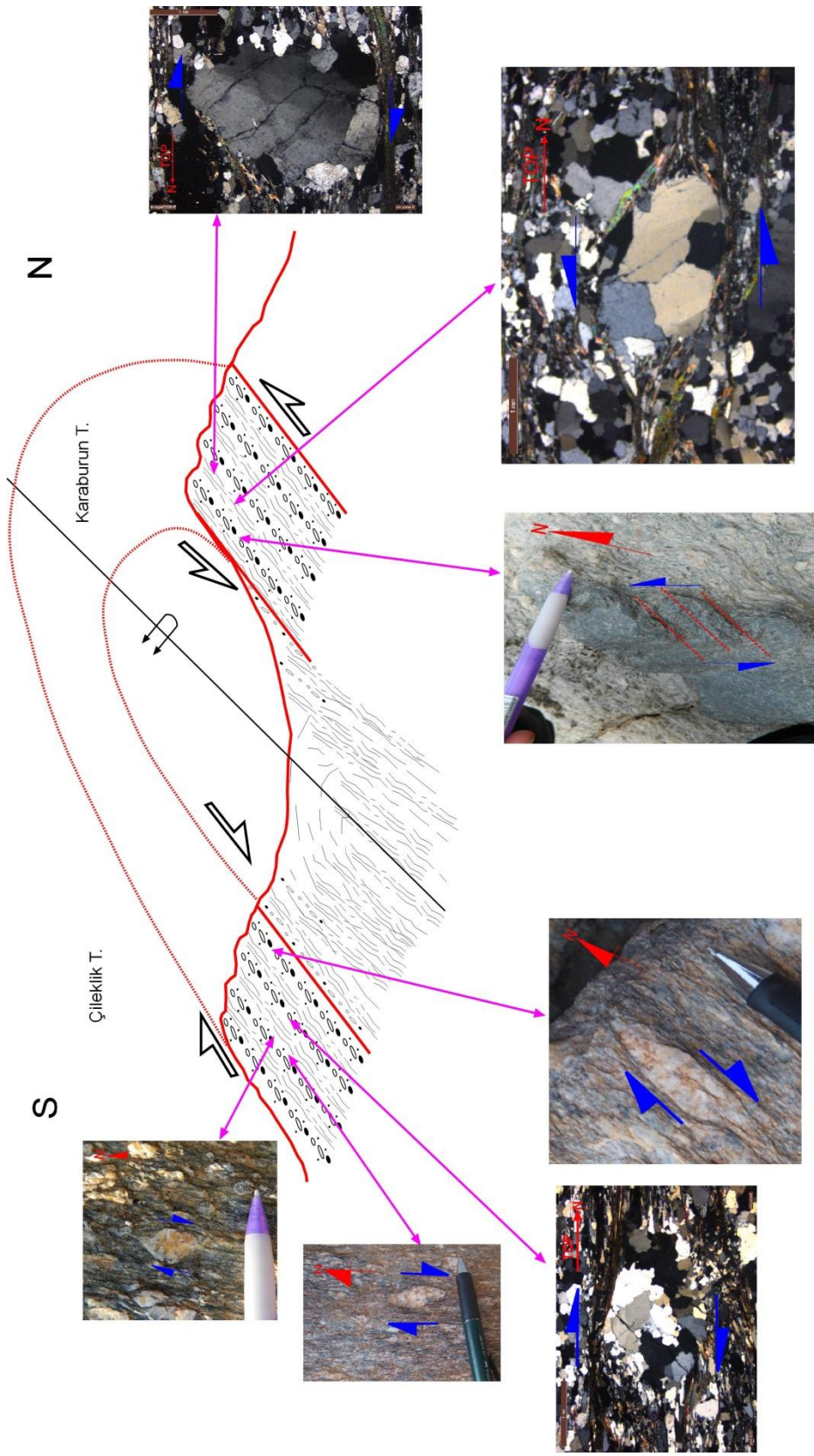


Figure 5.5 Schematic cross-section across the study area and interpretation of kinematic data.



## CHAPTER 6

### CONCLUSIONS

The main results and conclusions reached during this research can be summarized as follows:

1. Of the ~450 concordant detrital zircon ages from four samples of the Kurudere HP quartz metaconglomerates, the youngest grain is Asselian (earliest Permian) in age ( $298\pm 5$  Ma, conc. 104%) and the oldest grain is Mezoarchean in age ( $3020\pm 16$  Ma; conc. 101%). The youngest grain supports previous contentions that the metaconglomerate is late Triassic in age. But care must be taken, because it may be slightly older or may well be early Jurassic as well.
2. The metaconglomerates occur as two distinct horizons in the Kurudere area and they show opposing sense of shearing. Considering that the flexural slip was the mechanism of folding, the kinematics indicates the presence of an overturned anticline. But care must also be taken here because any viable model should be supported by the facing direction, which was not possible to determine.
3. The pattern in probability/density plots of detrital zircon ages, particularly (i) the dominance of Ordovician to Cryogenian (Neoproterozoic) zircons and (ii) lack of zircons in Mesoproterozoic ages (1.1–1.7 Ga), are consistent with a northern Gondwana provenance for the source of protolith to the metaconglomerates.
4. Majority of detrital zircon grains (out of 144 grains) have negative (-)  $\epsilon_{\text{Hf}}$  values and indicates a reworked crustal source; the rest are possibly from a juvenile crustal sources.
5. Presence of many Ordovician and Silurian detrital zircon grains, as well as  $\epsilon_{\text{Hf}}$  values –very distinct from those reported in the southern Menderes metasediments– are similar to those reported from the Cycladic rocks.
6. The Kurudere HP rocks and possibly the overlying marble series in the southern Menderes Massif may therefore belong to the Cycladic blueschist units, thus supporting previous contentions (Ring et al., 1999; Gessner et al., 2001c, 2004; Régnier et al., 2003, 2007; Whitney et al., 2008). The occurrence of north-vergent overturned fold and associated kinematics are consistent with a top-north emplacement of the Cycladic unit above the Menderes sequence and this might have taken place sometime after Eocene but before late Oligocene.



## REFERENCES

- Altunkaynak, Ş., Dilek, Y., Genç, C.Ş., Sunal, G., Gertisser, R., Furnes, H., Foland, K.A., Yang, J., 2012. Spatial, temporal and geochemical evolution of Oligo–Miocene granitoid magmatism in western Anatolia, Turkey. *Gondwana Research* 21, 961–986.
- Ashworth, J.R., and Evirgen, M.M. (1985) Plagioclase relations in pelites, central Menderes Massif, Turkey: I. The peristerite gap with coexisting kyanite. *Journal of Metamorphic Geology*, 3.207-218.
- Başarı, E., 1970, Bafa gölü doğusunda kalan Menderes masifi güney kanadının jeolojisi ve petrografisi: Ege Univ. Fen Fak. Jeoloji Kürsüsü İlmi Rap. Ser., 102, 44 s.
- Beccalotto, L., Steiner, C. , 2005. Evidence of two-stage extensional tectonics from the northern edge of the Edremit Graben, NW Turkey. *Geodinamica Acta* 18, 283–297.
- Bolhar, R., Ring, U. and Allen, C.M., 2010. An integrated zircon geochronological and geochemical investigation into the Miocene plutonic evolution of the Cyclades, Aegean Sea, Greece: Part 1: Geochronology. *Contrib Mineral Petrol*, 160: 719–742, DOI 10.1007/s00410-010-0504-4.
- Bozkurt, E., 1996. Metamorphism of Palaeozoic schists in the southern Menderes Massif: field, petrographic, textural and microstructural evidence. *Turkish Journal of Earth Sciences* 5, 105–121.
- Bozkurt, E., 2001a. Neotectonics of Turkey – a synthesis. *Geodinamica Acta (Paris)* 14, 3–30.
- Bozkurt, E., 2004. Granitoid rocks of the southern Menderes Massif (southwest Turkey): field evidence for Tertiary magmatism in an extensional shear zone. *International Journal of Earth Sciences* 93, 52–71.
- Bozkurt, E., 2007. Extensional v. contractional origin for the southern Menderes shear zone, SW Turkey: tectonic and metamorphic implications. *Geological Magazine* 144, 191–210.
- Bozkurt, E. and Oberhänsli, R., 2001. Menderes Massif (western Turkey): structural, metamorphic and magmatic evolution – a synthesis. *International Journal of Earth Sciences* 89, 679–708.

- Bozkurt, E., Park, R.G. 1994. Southern Menderes Massif: an incipient metamorphic core complex in western Anatolia, Turkey. *Journal of the Geological Society, London* 151, 213–216.
- Bozkurt, E., Park, R.G., 1997a. Evolution of a mid-Tertiary extensional shear zone in the Southern Menderes Massif, western Turkey. *Bulletin of Geological Society of France* 168, 3–14.
- Bozkurt, E., Park, 1997b. Microstructures of deformed grains in the augen gneisses of Southern Menderes Massif and their tectonic significance, western Turkey. *Geologische Rundschau*, 86, 101–119.
- Bozkurt, E., Park, R.G., 1999. The structure of the Palaeozoic schists in the southern Menderes Massif, western Turkey: a new approach to the origin of the main Menderes metamorphism and its relation to the Lycian Nappes. *Geodinamica Acta* 12, 25–42.
- Bozkurt, E., Park, R.G., 2001. Discussion on the evolution of the Southern Menderes Massif in SW Turkey as revealed by zircon dating. *Journal of the Geological Society, London* 158, 393–395.
- Bozkurt, E., Satır, M., 2000. The southern Menderes Massif (Western Turkey): geochronology and exhumation history. *Geological Journal* 35, 285–296.
- Bozkurt, E. and Sözbilir, H., 2004. Tectonic evolution of the Gediz Graben: field evidence for an episodic, two-stage extension in western Turkey *Geol. Mag.*, 141: 63–79.
- Bozkurt, E., Winchester, J.A., Mittwede, S.K., Ottley, C.J. 2006. Geochemistry and tectonic implications of leucogranites and tourmalines of the Southern Menderes Massif, Southwest Turkey. *Geodinamica Acta* 19, 363–390.
- Bozkurt, E. and Sözbilir, H., 2006. Evolution of the Large-scale Active Manisa Fault, Southwest Turkey: Implications on Fault Development and Regional Tectonics. *Geodinamica Acta*, 19, p.427-453.
- Candan, O., 1995. Menderes Masifinde kalıntı granolit fasiyesi metamorfizması. *Turkish Journal of Earth Sciences* 4, 35–55 [in Turkish with English abstract].
- Candan, O., 1996. Çine Asmasifindeki (Menderes Masifi) gabroların metamorfizması ve diğer asmasiflerle karşılaştırılması. *Turkish Journal of Earth Sciences* 5, 123–139 [in Turkish with English abstract].

Candan, O., Dora, O.Ö., Oberhänsli, R., Koralay, O.E., Çetinkaplan, M., Akal, C., Satır, M., Chen, F., Kaya, O., 2011b. Stratigraphy of Pan-African basement of the Menderes Massif and the relationship with late Neoproterozoic/Cambrian evolution of the Gondwana. *MTA Bulletin* 142, 25–68.

Candan, O., Dora, O.Ö., Oberhänsli, R., Oelsner, F.C., Dürr, S., 1997. Blueschist relics in the Mesozoic series of the Menderes Massif and correlation with Samos Island. *Schweizerische Mineralogische und Petrographische Mitteilungen* 77, 95–99.

Candan, O., Dora, O.Ö., Oberhänsli, R., Çetinkaplan, M., Partzsch, J.H., Warkus, F.C., Dürr, S., 2001. Pan-African high-pressure metamorphism in the Precambrian basement of the Menderes Massif, western Anatolia, Turkey, *International Journal of Earth Sciences* 89, 793–811.

Candan, O., Koralay, O.E., Akal, C., Kaya, O., Oberhänsli, R., Dora, O.Ö., Konak, N., Chen, F., 2011a. Supra-Pan-African unconformity between core and cover series of the Menderes Massif/Turkey and its geological implications. *Precambrian Research* 184, 1–23.

Candan, O., Dora, Ö., Oberhänsli, R., Çetinkaplan, M., Partzsch, J. H. ve Dürr, S., 2000. Pan-African high-pressure metamorphism in the Precambrian basement of the Menderes Massif, Western Anatolia-Turkey. *Third International Turkish Geology Symposium., Middle East Technical University - Ankara*, 275.

Catlos, E.J., Çemen, I., 2005. Monazite ages and rapid exhumation of the Menderes Massif, western Turkey. *International Journal of Earth Sciences* 94, 204–217.

Catlos, J.E., Baker, C., Sorensen, S.S., Çemen, İ., Hançer, M. 2010. Geochemistry, geochronology, and cathodoluminescence imagery of the Salihli and Turgutlu granites (central Menderes Massif, western Turkey): implications for Aegean tectonics. *Tectonophysics* 488, 110–130.

Catlos, E., Jacob, L., Oyman, T., Sorensen, S., 2012. Long-term exhumation of an Aegean metamorphic core complex granitoids in the northern Menderes Massif, western Turkey. *American Journal of Science* 312, 534–571.

Cohen, H.A., Dart, C.J., Akyüz, H.S., Barka, A.A., 1995. Syn-rift sedimentation and structural development of Gediz and Büyük Menderes graben, western Turkey. *Journal of the Geological Society, London* 152, 629–638.

- Collins, A.S., Robertson A. H. F., 1997. The Lycian Melange, southwest Turkey: an emplaced accretionary complex. *Geology* 25: 255±258.
- Collins, A.S., Robertson, A. H. F., 1998. Processes of Late Cretaceous to Late Miocene episodic thrust-sheet translation in the Lycian Taurides, SW Turkey. *Journal of the Geological Society, London* 155: 759±772.
- Collins, A. S., Robertson, A. H. F., 1999. Evolution of the Lycian Allochthon, western Turkey, as a north-facing Late Palaeozoic to Mesozoic rift and passive continental margin. *Geology Journal*, 34, 107-138.
- Çağlayan, A.M., Öztürk, E.M., Öztürk, Z., Sav, H. and Akat, U., 1980. Structural observations on the southern Menderes Massif. *Publication Chamber Geological Engineering Turkey (in Turkish with English summary)*, 10, 9-17.
- Çiftçi, N.B., 2013. In-situ stress field and mechanics of fault reactivation in the Gediz Graben, Western Turkey. *Journal of Geodynamics* 65, 136–147.
- Çiftçi, N.B., Bozkurt, E., 2008. Folding of the Gediz Graben Fill, SW Turkey: Extensional and/or Contractual Origin? *Geodinamica Acta* 21, 145–167.
- Çiftçi, N.B., Bozkurt, E., 2009a. Facies and evolution of the Mioocene to Recent sedimentary fill of the Gediz Graben, SW Turkey. *Sedimentary Geology* 216, 49–79.
- Çiftçi, N.B., Bozkurt, E., 2009b. Pattern of normal faulting in the Gediz Graben, SW Turkey. *Tectonophysics*, 473, 234–260.
- Çiftçi, N.B., Bozkurt, E. 2010. Structural evolution of the Gediz Graben, SW Turkey: temporal and spatial variation of the graben fill. *Basin Research* 22, 846–873.
- Davis D.W., Williams I.S., Krogh T.E., 2003. Historical development of zircon geochronology. In: *Reviews in mineralogy and geochemistry* (editors: Hancher J.M., Hoskin P.W.O.). Mineralogical Society of America, 53: 145-181
- Dickin, A., 2005. *Radiogenic Isotope Geology. Second Edition.* Cambridge University Press.
- Dora, O.Ö., 2011. Historical evolution of the geological research in the Menderes Massif. *MTA Bulletin* 142, 1–23.
- Dora , O. Ö., Candan, O., Kaya, O., Koralay, E. and Akal, C., 2005. Menderes Masifi Çine Asmasıfındaki Koçarlı - Bafa -Yatağan - Karacasu arasında uzanan gnays /şist dokanağının niteliği: Jeolojik, tektonik, petrografik ve jeokronolojik bir yaklaşım.

YDABÇAG - 101 Y 132 nolu Türkiye Bilimsel ve Teknolojik Araştırma Kurumu projesi, 197s (yayımlanmamış).

Dora, O. Ö., Candan, O., Dürr, S., Oberhansli, R., 1995. New evidence on the geotectonic evolution of the Menderes Massif. In: Pişkin, Ö. , Ergin M., Savaşçın, M. Y., Tarcan, G., Proceedings of the International Earth Sciences Colloquium on the Aegean Region, 9±14 October 1995, Izmir- GuÈlluÈk, Turkey, 53±72.

Dürr S, Altherr R, Keller J, Okrusch M, Seidel E. 1978. The median Aegean Crystalline belt: stratigraphy, structure, metamorphism and magmatism. In: Closs H, Roeder DR, Schmidt, K., Alps, Apennines, Hellenides. Schweizerbart, Stuttgart, 455±477.

Dupee, M.E., 2005. Porphyroblast Kinematics and Crenulation Cleavage Development in the Aureole of the Mooselookmeguntic Pluton , Western Maine (PHD thesis).

Emre, T., 1996. Geology and tectonics of Gediz Graben. Turkish Journal of Earth Sciences 5, 171–185 [in Turkish with English abstract].

Emre, T., Sözbilir, H., 1995. Field evidence for metamorphic core complex, detachment faulting and accommodation faults in the Gediz and Büyük Menderes grabens, western Anatolia. In: Pişkin, Ö., Ergün, M., Savaşçın, M.Y., Tarcan, G. (Eds.), International Earth Sciences Colloquium on Aegean Regions (IESCA) Proceedings 1, pp. 73–93.

Emre, T., Tavlan, M., Akkiraz, M.S., Işın tek, İ., 2011. Stratigraphy, sedimentology and palynology of the Neogene–Pleistocene(?) rocks around Akçaşehir-Tire-İzmir (Küçük Menderes Graben, Western Anatolia). Turkish Journal of Earth Sciences 20, 27–56.

Engel, M., Reischmann, T., 1998. Single zircon geochronology of orthogneisses from Paros, Greece. Bull. Geol. Soc. Greece, 22/3, 91-99.

Erdoğan, B., Akay, E., HasözbeK, A., 2011. Emplacement characteristics of the gneissic granites in the Menderes Massif (western Anatolia) and their implications of the tectonic evolution of the massif: new field observations and radiogenic age determinations. MTA Bulletin 142, 165–190.

Erdoğan, E., Güngör, T., 2004. The problem of the core-cover boundary of the Menderes Massif and an emplacement mechanism for regionally extensive gneissic granites, Western Anatolia (Turkey). Turkish Journal of Earth Sciences 13, 15–36.

Erkül, F., 2010. Tectonic significance of synextensional ductile shear zones within the Early Miocene Alaçamdağ granites, northwestern Turkey. *Geological Magazine* 147, 611–637.

Ersoy, E.Y., Helvacı, C., Sözbilir, H., 2010a. Tectono-stratigraphic evolution of the NE–SW-trending superimposed Selendi basin: implications for late Cenozoic crustal extension in Western Anatolia, Turkey. *Tectonophysics* 488, 210–232.

Ersoy, E.Y., Helvacı, C., Palmer, M.R., 2010b. Mantle source characteristics and melting models for the early-middle Miocene mafic volcanism in Western Anatolia: Implications for enrichment processes of mantle lithosphere and origin of K-rich volcanism in post-collisional settings. *Journal of Volcanology and Geothermal Research* 198, 112–128.

Ersoy, E.Y., Helvacı, C., Palmer, M.R. 2011. Stratigraphic, structural and geochemical features of the NE-SW-trending Neogene volcano-sedimentary basins in western Anatolia: implications for association of supradetachment and transtensional strike-slip basin formation in extensional tectonic setting. *Journal of Asian Earth Sciences* 41, 159–183.

Fedo, Ch., Sircombe, K. M., Rainbird, R. H., 2003, Detrital zircon analysis of the sedimentary record. In: Hanchar, J., M., Hoskin, P., W., O., (ed): *Zircon. Reviews in Mineralogy and Geochemistry*, 53, 277-303.

Finch, R., Hanchar, J., 2003. Structure and Chemistry of Zircon and Zircon-Group Minerals. In: *Reviews in mineralogy and geochemistry* (editors: Hanchar J.M., Hoskin P.W.O.), Mineralogical Society of America, 53: 1-26.

Fossen, H., 2010. *Structural Geology. Cambridge University Press. ISBN-13 978-0-511-77282-5.*

Gebauer, D., 1993, The Pre-Alpine evolution of the continental crust of the Central Alps—An overview, in Raumer, J.F.v., and Neubauer, F., eds., *Pre-Mesozoic geology in the Alps: Berlin, Springer-Verlag*, p. 93–117.

Gerdes A., Zeh A. 2006. Combined U–Pb and Hf isotope LA-ICP-MS analyses of detrital zircons: comparison with SHRIMP and new constraints for the provenance and age of an Armorican metasediment in Central Germany. *Earth and Planetary Science Letters*, 249: 47–61.

Gerdes, A., Zen, A., 2009. Zircon formation versus zircon alteration — New insights from combined U–Pb and Lu–Hf in-situ LA-ICP-MS analyses, and consequences for

the interpretation of Archean zircon from the Central Zone of the Limpopo Belt. *Chemical Geology*, 261: 230-243.

Gessner, K., Collins, A.S., Ring, U., Güngör, T., 2004. Structural and thermal history of poly-orogenic basement: U–Pb geochronology of granitoid rocks in the southern Menderes Massif, western Turkey. *Journal of the Geological Society, London* 161, 93–101.

Gessner, K., Ring, U., Johnson, C., Hetzel, R., Passchier, C.W., Güngör, T., 2001a. An active bivergent rolling-hinge detachment system: Central Menderes metamorphic core complex in western Turkey. *Geology* 29, 611–614.

Gessner, K., Piazzolo, S., Güngör, T., Ring, U., Kroner, A., Passchier, C.W., 2001b. Tectonic significance of deformation patterns in granitoid rocks of the Menderes nappes, Anatolide belt, southwest Turkey. *International Journal of Earth Sciences* 89, 766–780.

Gessner, K., Ring, U., Passchier, C.W., Güngör, T., 2001c. How to resist subduction: evidence for large-scale out-of-sequence thrusting during Eocene collision in western Turkey. *Journal of the Geological Society, London* 158, 769–784.

Gessner, K., Gallardo, A. L., Markwitz, V., Ring, U., Thomson, N., S., 2013 (in press). What caused the denudation of the Menderes Massif: Review of crustal evolution, lithosphere structure, and dynamic topography in southwest Turkey. *Gondwana Research* (2013), doi: [10.1016/j.gr.2013.01.005](https://doi.org/10.1016/j.gr.2013.01.005)

Geyn, A.M., Schleicher, H., 1990. Absolute Age Determination, Physical and Chemical Dating Methods and Their Application. Springer-Verlag.

Glodny, J., Hetzel, R., 2007. Precise U–Pb ages of syn-extensional Miocene intrusions in the central Menderes Massif, western Turkey. *Geological Magazine* 144, 235–246.

Gökten, E., Havzaoğlu, Ş., Şan, Ö., 2001. Tertiary evolution of the central Menderes Massif based on structural investigations of metamorphics and sedimentary cover rocks between Salihli and Kiraz (western Turkey). *International Journal of Earth Sciences* 89, 745–756.

Gray, D. R., 1977. Morphologic classification of crenulation cleavages. *Journal of Geology*, v. 85, p. 229-235.

Gross, H. J., 2010. Mass Spectrometry, 2nd Edition. Springer.

Gürboğa, Ş., Koçyiğit, A., Ruffet, G., 2013. Episodic two-stage extensional evolutionary model for southwestern Anatolian graben–horst system: New field data from the Erdoğmuş-Yenigediz graben (Kütahya). *Journal of Geodynamics* 65, 176–198.

Hasözbeğ, A. (2003). The Geology, Petrology and the Evolution of the Eđrigöz Magmatic Complex. *MSc.* (in English).

Hasözbeğ, A., Erdoğın, B., Satır, M., Siebel, W., Akay, E., Dođın, G.D., Taubald, H., 2012. Al-in-hornblende thermobarometry and Sr-Nd-O-Pb isotopic compositions of the Early Miocene Alaçam Granite in NW Anatolia (Turkey). *Turkish Journal of Earth Science* 21, 37–52.

Hasözbeğ, A., Satır, M., Erdoğın, B., Akay, E., Siebel, W., 2011. Early Miocene post-collisional magmatism in NW Turkey: geochemical and geochronological constraints. *International Geology Review* 53, 1098–1119.

Hetzel, R., Reischmann, T., 1996. Intrusion age of Pan-African augen gneisses in the southern Menderes Massif and the age of cooling after Alpine ductile extensional deformation. *Geological Magazine* 133, 565–72.

Hetzel, R., Passchier, C.W., Ring, U., Dora, Ö.O., 1995a. Bivergent extension in orogenic belts: The Menderes massif (southwestern Turkey). *Geology* 23, 455–458.

Hetzel, R., Romer, R.L., Candan, O., Passchier, C.W., 1998. Geology of the Bozdağ area, central Menderes Massif, SW Turkey: Pan-African basement and Alpine deformation. *Geologische Rundschau* 87, 394–406.

Hetzel, R., Ring, U., Akal, C., Troesch, M., 1995b. Miocene NNE-directed extensional unroofing in the Menderes massif, southwestern Turkey. *Journal of the Geological Society, London* 152, 639–654.

Hetzel, R., Zwingmann, H., Mulch, A., Gessner, K., Akal, C., Hampel, A., Güngör, T., Petschick, R., Mikes, T., Wedin, F., 2013. Spatio-temporal evolution of brittle normal faulting and fluid infiltration in detachment fault systems - a case study from the Menderes Massif, western Turkey. *Tectonics*, DOI: 10.1002/tect.20031 (in press).

Hoskin P.W.O., Schaltegger U., 2003. The composition of zircon and igneous and metamorphic petrogenesis. *Reviews in mineralogy and geochemistry* (editors: Hancher J.M., Hoskin P.W.O.), Mineralogical Society of America, 53: 27-62.

Işık, V., 2004. Kuzey Menderes Masifi'nde Simav makaslama zonunun mikrotektonik özellikleri, Batı Anadolu, Türkiye. Türkiye Jeoloji Bülteni 47, 49–91 [in Turkish with English abstract].

Işık, V., Tekeli, O., 2001. Late orogenic crustal extension in the northern Menderes massif (western Turkey): evidence for metamorphic core complex. *International Journal of Earth Sciences* 89, 757–765.

Işık, V., Seyitoğlu, G., Çemen, İ., 2003. Ductile-brittle transition along the Alaşehir detachment fault and its structural relationship with the Simav detachment fault, Menderes Massif, western Turkey. *Tectonophysics* 374, 1–18.

Işık, V., Tekeli, O., Seyitoğlu, G., 2004. The  $^{40}\text{Ar}/^{39}\text{Ar}$  age of extensional ductile deformation and granitoid intrusion in the northern Menderes core complex: implications for the initiation of extensional tectonics in western Turkey. *Journal of Asian Earth Sciences* 23, 555–566.

Jolivet, L., Brun, J.-P., 2010. Cenozoic geodynamic evolution of the Aegean. *International Journal of Earth Sciences* 99, 109–138.

Jolivet, L., Augier, R., Faccenna, C., Negro, F., Rimmelé, G., Agard, P., Robin, C., Rossetti, F., Crespo-Blanc, A., 2008. Subduction, convergence and the mode of backarc extension in the Mediterranean region. *Bulletin. Société Géologique de France* 179 (6), 525–550.

Jolivet, J., Rimmelé, G., Oberhänsli, R., Goffé, B., Candan, O., 2004. Correlation of syn-orogenic tectonic and metamorphic events in the Cyclades, the Lycian Nappes and the Menderes Massif. Geodynamic implications. *Bulletin de la Société Géologique de France* 175, 217–238.

Jolivet, L., Lecomte, E., Huet, B., Denèle, Y., Lacombe, O., Labrousse, L., Le Pourhiet, L., Mehl, C., 2010. The North Cycladic Detachment System. *Earth and Planetary Science Letters* 289, 87–104.

Jolivet, L., Faccenna, C., Huet, B., Labrousse, L., Le Pourhiet, L., Lacombe, O., Lecomte, E., Burov, E., Denèle, Y., Brun, J.-P., Philippon, M., Paul, A., Salaün, G., Karabulut, H., Piromallo, C., Monié, P., Gueydan, F., Okay, A.I., Oberhänsli, R., Pourteau, R., Augier, R., Leslie, G. and Driussi, O. 2012. Aegean tectonics: strain localisation, slab tearing and trench retreat. *Tectonophysics*, <http://dx.doi.org/10.1016/j.tecto.2012.06.011>.

Karaoğlu, Ö., Helvacı, C., Ersoy, E.Y., 2010. Petrogenesis and  $^{40}\text{Ar}/^{39}\text{Ar}$  geochronology of the volcanic rocks of the Uşak-Güre basin, western Türkiye. *Lithos* 119, 193–210.

Keay, S., 1998. The Geological Evolution of the Cyclades, Greece: Constraints from SHRIMP U-Pb Geochronology. PHD thesis.

Keay, S., Lister, G., Buick, I., 2001. The timing of partial melting, Barrovian metamorphism and granite intrusion in the Naxos metamorphic core complex, Cyclades, Aegean Sea, Greece. *Tectonophysics* 342, 275–312.

Keay, S., Lister, G., 2002. African provenance for the metasediments and metaigneous rocks of the Cyclades, Aegean Sea, Greece. *Geology* 30 (3), 235–238.

Kinny P.D., Maas R., 2003. Lu-Hf and Sm-Nd isotope systems in zircon. In: *Reviews in mineralogy and geochemistry* (editors: Hancher J.M., Hoskin P.W.O.). Mineralogical Society of America, 53:327-341.

Koralay, O.E., Candan, O., Akal, C., Özcan, O.Ö., Chen, F., Satır, M., Oberhänsli, R., 2011. The geology and geochronology of the Pan-African and Triassic granitoids in the Menderes Massif, western Anatolia, Turkey. *MTA Bulletin* 142, 69–119.

Koralay, O.E., Candan, O., Chen, F., Akal, C., Oberhänsli, R., Satır, M., Dora, O.Ö., 2012. Pan-African magmatism in the Menderes Massif: geochronological data from leucocratic tourmaline orthogneisses in western Turkey. *International Journal of Earth Sciences* 101, 2055–2081.

Kröner, A., and Şengör, A.M.C., 1990. Archean and Proterozoic ancestry in late Precambrian to early Paleozoic crustal elements of southern Turkey as revealed by single-zircon dating: *Geology*, v. 18, p. 1186–1190.

Lips, A.L.W., Cassard, D., Sözbilir, H., Yılmaz, H., 2001. Multistage exhumation of the Menderes Massif, western Anatolia (Turkey). *International Journal of Earth Sciences* 89, 781–792.

Loos, S., Reischmann, T., 1999. The evolution of the southern Menderes Massif in SW Turkey as revealed by zircon datings. *Journal of the Geological Society, London* 156, 1021–1030.

Ludwig, K.R., 2003. *Isoplot 3.00: A Geochronological Toolkit for Microsoft Excel*. Berkeley Geochronology Center Special Publication 4, 70 p.

- Meinhold, G., Reischmann, T., Kostopoulos, D., Lehnert, O., Matukov, D., Sergeev, S., (2008). Provenance of sediments during subduction of Palaeotethys: detrital zircon ages and olistolith analysis in Palaeozoic sediments from Chios Island, Greece. *Palaeogeogr Palaeoclimatol Palaeoecol* 263:71–91. doi:[10.1016/j.palaeo.2008.02.013](https://doi.org/10.1016/j.palaeo.2008.02.013).
- Millonig, L. J., Gerdes, A., and Groat, L. A. (2012). The effect of amphibolite facies metamorphism on the U – Th – Pb geochronology of accessory minerals from meta-carbonatites and associated meta-alkaline rocks. *Chemical Geology*, 1–11. doi:10.1016/j.chemgeo.2012.10.039.
- Neptune, F.,(2004). In Situ U-Pb Zircon Dating Using Laser Ablation-Multi Ion Counting-ICP-MS (LA-MIC-ICP-MS).
- Oberhänsli, R., Partzsch, J. H., Çetinkaplan, M. ve Candan, O., 1998. HP record in the Lycian nappes (Western Turkey). Third International Turkish Geology Symposium, Middle East Technical University, Ankara, 274.
- Oberhänsli, R., Candan, O., Wilke, F., 2010. Geochronological Evidence of Pan-African Eclogites from the Central Menderes Massif, Turkey. *Turkish Journal of Earth Sciences* 19, 431–447.
- Oberhänsli, R., Candan, O., Dora, O.Ö., Dürr, S., 1997. Eclogites within the Menderes Massif, western Turkey. *Lithos* 41, 135–150.
- Okay, A.I., 2001. Stratigraphic and metamorphic inversions in the central Menderes Massif: a new structural model. *International Journal of Earth Sciences* 89, 709–727.
- Okrusch, M., Richter, P. and Katsikatsos, G. (1984). High-pressure rocks of Samos, Greece. In: Dixon, J. E. and Robertson, A. H. F. *The Geological Evolution of the Eastern Mediterranean*. Geological Society, London, Special Publications 17, 529–536.
- Okrusch, M., Bröcker, M., 1990. Eclogites associated with highgrade blueschists in the Cyclades archipelago, Greece: A review. *Eur. J. Mineral.* 2, 451-478.
- Öner, Z., Dilek, Y., Kadioğlu, Y.K., 2010. Geology and geochemistry of the synextensional Salihli granitoid in the Menderes core complex, western Anatolia, Turkey. *International Geology Review* 52, 336–368.
- Özer, S., Sözbilir, H., Özkar-Tansel, I., Toker, V. and Sari, B., 2001. Stratigraphy of Upper Cretaceous - Paleocene sequences in the southern Menderes massif (W. Turkey). *Int Jour. Earth Sci.*, 89: 852-866.

- Özgenç, İ., İlbeyli, N., 2008. Petrogenesis of the Late Cenozoic Eğrigöz pluton in Western Anatolia, Turkey: implications for magma genesis and crustal processes. *International Journal of Earth Sciences* 50, 375–391.
- Özkaymak, Ç., Sözbilir, H., Uzel, B., 2013. Neogene–Quaternary evolution of the Manisa Basin: Evidence for variation in the stress pattern of the İzmir-Balıkesir Transfer Zone, western Anatolia. *Journal of Geodynamics* 65, 117–135.
- Parejas, E., 1940. Le flysch Cretace des environs de smyrne: inst. Geol. Univ. 1st., 6.
- Patchett P.J., Kuovo O., Hedge C.E., Tatsumoto M., 1981. Evolution of continental crust and mantle heterogeneity: evidence from Hf isotopes. *Contributions to Mineralogy and Petrology*, 78: 279–297.
- Philippon, M., Brun, J.-P., and Gueydan, F. (2012). Deciphering subduction from exhumation in the segmented Cycladic Blueschist Unit (Central Aegean, Greece). *Tectonophysics*, 524-525, 116–134. doi:10.1016/j.tecto.2011.12.025.
- Pohl, W., Belocky, R., 1999. Metamorphism and Metallogeny in the Eastern Alps. *Mineralium Deposita* 34, 614-629.
- Pourteau, A., 2011. Closure of the Neotethys Ocean in Anatolia: structural, petrologic and geochronologic insights from low-grade high-pressure metasediments, Afyon Zone. PhD Thesis, Universität Potsdam, urn:nbn:de:kobv:517-opus-57803 pp.
- Pourteau, a., Sudo, M., Candan, O., Lanari, P., Vidal, O., and Oberhänsli, R. (2013). Neotethys closure history of Anatolia: insights from  $^{40}\text{Ar}$ - $^{39}\text{Ar}$  geochronology and P-T estimation in high-pressure metasedimentary rocks. *Journal of Metamorphic Geology*, n/a–n/a. doi:10.1111/jmg.12034
- Purvis, M., Robertson, A., Pringle, M., 2005a.  $\text{Ar}^{40}$ - $\text{Ar}^{39}$  dating of biotite and sanidine in tuffaceous sediments and related intrusive rocks: implications for the Early Miocene evolution of the Gördes and Selendi basins, W Turkey. *Geodinamica Acta* 18, 239–253.
- Purvis, M., Robertson, A.H.F., 2005b. Miocene sedimentary evolution of the NE–SW-trending Selendi and Gördes basins, W Turkey: implications for extensional processes. *Sedimentary Geology* 174, 31–62.
- Reischmann, T., Kröner, A., Todt, W., Dürr, S., and Şengör, A.M.C., 1991, Episodes of crustal growth in the Menderes Massif, W. Turkey, inferred from zircon dating: *Terra Abstracts*, v. 3, p. 34.

- Régnier, J.L., Mezger, J.E., Passchier, C.W., 2007. Metamorphism of Precambrian–Palaeozoic schists of the Menderes core series and contact relationships with Proterozoic orthogneisses of the western Cine Massif, Anatolide belt, western Turkey. *Geological Magazine* 144, 67–104.
- Régnier, J.L., Ring, U., Passchier, C.W., Gessner, K., Güngör, T., 2003. Contrasting metamorphic evolution of metasedimentary rocks from the Çine and Selimiye nappes in the Anatolide belt, western Turkey. *Journal of Metamorphic Geology* 21, 699–721.
- Rimmelé, G., Oberhänsli, R., Goffé, B., Jolivet, L., Candan, O., Çetinkaplan, M., 2003a. First evidence of high-pressure metamorphism in the ‘Cover Series’ of the southern Menderes Massif. Tectonic and metamorphic implications for the evolution of the SW Turkey. *Lithos* 71, 19–46.
- Rimmelé, G., Jolivet, L., Oberhänsli, R., Goffé, B., 2003b. Deformation history of the high-pressure Lycian Nappes and implications for tectonic evolution of SW Turkey. *Tectonics* 22, 1007–1029.
- Rimmelé, G., Oberhänsli, R., Candan, O., Goffé, B., Jolivet, L., 2006. The wide distribution of HP-LT rocks in the Lycian Belt (Western Turkey): implications for accretionary wedge geometry. In: Robertson, A.H.F., Mountrakis, D. (Eds.), *Tectonic Development of the Eastern Mediterranean Region*: Geological Society, London, Special Publications 260, pp. 447–466.
- Ring, U., Collins, A.S., 2005. U-Pb SIMS dating of syn-kinematic granites: timing of core-complex formation in the northern Anatolide belt of western Turkey. *Journal of the Geological Society, London* 162, 289–298.
- Ring, U., Johnson, C., Hetzel, R., Gessner, K., 2003. Tectonic denudation of a Late Cretaceous-Tertiary collisional belt: regionally symmetric cooling patterns and their relation to extensional faults in the Anatolide belt of western Turkey. *Geological Magazine* 140, 421–441.
- Ring, U., Gessner, K., Güngör, T., Passchier, C.W., 1999. The Menderes Massif of western Turkey and the Cycladic Massif in the Aegean – do they really correlate? *Journal of Geological Society, London* 156, 3–6.
- Ring, U., Will, T., Glodny, J., Kumerics, C., Gessner, K., Thomson, S., Güngör, T., Monié, P., Okrusch, M., Drüppel, K., 2007. Early exhumation of high-pressure rocks in extrusion wedges: Cycladic blueschist unit in the eastern Aegean, Greece, and Turkey. *Tectonics* 26, doi:10.1029/2005TC001872.

Ring, U., Layer, P. W., 2003. High-pressure metamorphism in the Aegean, eastern Mediterranean: underplating and exhumation from the Late Cretaceous until the Miocene to recent above the retreating Hellenic subduction zone. *Tectonics* 22(3), p23, 1022. doi:10.1029/2001TC001350.

Rojay, B., Göncüoğlu, M. C., Tectonic setting of some Paleozoic metamorphics in Northern Anatolia, Turkey. 'Paleozoic geodynamics domains and their alpidic evolution in the Tethys IGCP Project No 276', 276, (1998), p.97-102.

Sarıca, N., 2000. The Plio-Pleistocene age of Büyük Menderes and Gediz grabens and their tectonic significance on N-S extensional tectonics in west Anatolia: mammalian evidence from the continental deposits. *Geological Journal* 35, 1-24.

Satır, M., Friedrichsen, H., 1986. The origin and evolution of the Menderes Massif, W-Turkey: a rubidium/strontium and oxygen isotope study. *Geologie Rundschau* 75, 703-714.

Schuiling, R. D. 1962. On petrology, age and structure of the Menderes migmatite complex (SW Turkey). General Directorate of Mineral Research and Exploration Institute of Turkey (MTA) Bulletin, 58, 71-84.

Seyitoğlu, G., 1997. Late Cenozoic tectono-sedimentary development of the Selendi and Uşak-Güre basins: a contribution to the discussion on the development of east-west and north trending basins in western Turkey. *Geological Magazine* 134, 163-175.

Seyitoğlu, G., Scott, B.C., 1991. Late Cenozoic crustal extension and basin formation in west Turkey. *Geology Magazine* 28, 155-166.

Seyitoğlu, G., Scott, B.C., 1992a. The age of the Büyük Menderes Graben (west Turkey) and its tectonic implications. *Geological Magazine* 129, 239-242.

Seyitoğlu, G., Scott, B.C., 1992b. Late Cenozoic volcanic evolution of the northeastern Aegean region. *Journal of Volcanology and Geothermal Research* 54, 157-176.

Seyitoğlu, G., Scott, B.C., 1994. Late Cenozoic basin development in west Turkey – Gördes Basin tectonics and sedimentation. *Geological Magazine* 131, 631-637.

Seyitoğlu, G., Scott, B.C., 1996. The cause of N-S extensional tectonics in western Turkey: tectonic escape vs back-arc spreading vs orogenic collapse. *Journal of Geodynamics* 22, 145-153.

Seyitođlu, G., Iřık, V., emen, İ., 2004. Complete Tertiary exhumation history of the Menderes Massif, western Turkey: an alternative working hypothesis. *Terra Nova* 16, 358–63.

Slama, J., Kosler, J., Crowley, J. L., Gerdes, A., Hanchar, J., Horstwood, M., Morris, G., Nasdala, L., Norberg, N., Schaltegger, U., Tubrett, M., Whitehouse, M., 2007. Pleřovice zircon – a new natural standard for U-Pb and Hf isotopic microanalysis. 17th Annual Goldschmidt conference, Cologne.

Sözbilir, H., 2001. Geometry of macroscopic structures with their relations to the extensional tectonics: field evidence from the Gediz detachment, western Turkey. *Turkish Journal of Earth Sciences* 10, 51–67.

Sözbilir, H., 2002. Geometry and origin of folding in the Neogene sediments of the Gediz Graben, western Anatolia, Turkey. *Geodinamica Acta* 15, 277–288.

Sözbilir, H., Sarı, B., Uzel, B., Sümer, Ö., Akkiraz, S., 2011. Tectonic implications of transtensional supradetachment basin development in an extension-parallel transfer zone: the Kocaçay Basin, western Anatolia, Turkey. *Basin Research* 23, 423–448.

Sümer, Ö., İnci, U., Sözbilir, H., 2013. Tectonic evolution of the Söke Basin: Extension-dominated transtensional basin formation in western part of the Büyük Menderes Graben, Western Anatolia, Turkey. *Journal of Geodynamics* 65, 148–175.

Şengör, A.M.C., Yılmaz, Y., 1981. Tethyan evolution of Turkey: a plate tectonic approach. *Tectonophysics* 75,181–241.

Şengör, A.M.C., Satır, M., Akkök, R., 1984. Timing of tectonic events in the Menderes Massif, western Turkey: implications for tectonic evolution and evidence for Pan-African basement in Turkey. *Tectonics* 3, 693–707.

Tatar-Erkül, S. 2012. Petrogenetic evolution of the Early Miocene Alaçamdağ volcano-plutonic complex, northwestern Turkey: implications for the geodynamic framework of the Aegean region. *International Journal of Earth Sciences* 101, 197–219.

Tatar-Erkül, S., Erkül, F., 2012. Magma interaction processes in syn-extensional granitoids: The Tertiary Menderes Metamorphic Core Complex, western Turkey. *Lithos* 142-143, 16–33.

Thomson, S.N., Ring, U., 2006. Thermochronologic evaluation of postcollision extension in the Anatolide orogen, western Turkey, *Tectonics*, 25, TC3005, doi:10.1029/2005TC001833.

Tomaschek, F., Ballhaus, C., 1999. The Vari Unit on Syros (Aegean Sea) and its relation to the Attic-Cycladic Crystalline Complex. *Journal of Conference Abstracts* 4, 72.

Tomaschek, F., Kennedy, A., Keay, S., Ballhaus, C., 2001. Geochronological constraints on Carboniferous and Triassic magmatism in the Cyclades: SHRIMP U–Pb ages of zircons from Syros, Greece. *Journal of Conference Abstracts* 6 (1), 315.

Tomaschek, F., Keiter, M., Kennedy, A.K., Ballhaus, C., 2008. Pre-Alpine basement within the Northern Cycladic Blueschist Unit on Syros Island, Greece. *Z. Dtsch. Ges. Geowiss.* 159, 521–532. doi:10.1127/1860-1804/2008/0159-0521.

Twiss, R. J. and Moores, E. M., 2007, *Structural Geology*, 2nd edition. *New York: H.W. Freeman and Company*.

van Hinsbergen, D.J.J., 2010. A key extensional metamorphic complex reviewed and restored: the Menderes Massif of western Turkey. *Earth Science Reviews* 102, 60–76.

van Hinsbergen, D.J.J., Dekkers, M.J., Bozkurt, E., Koopman, M., 2010a. Exhumation with a twist: Paleomagnetic constraints on the evolution of the Menderes metamorphic core complex, western Turkey, *Tectonics*, 29, doi:10.1029/2009TC002596.

van Hinsbergen, D.J.J., Dekkers, M.J., Koç, A., 2010c. Testing Miocene Remagnetization of Bey Dağları: Timing and Amount of Neogene Rotations in SW Turkey. *Turkish Journal of Earth Sciences* 19, 123–156.

van Hinsbergen, D.J.J., Kaymakcı, N., Spakman, W., Torsvik, T.H., 2010b. Reconciling the geological history of western Turkey with plate circuits and mantle tomography. *Earth and Planetary Science Letters* 297, 674–686.

Whitney, D.L., Bozkurt, E., 2002. Metamorphic history of the southern Menderes Massif, western Turkey. *Geological Society of America Bulletin* 114, 829–838.

Whitney, D.L., Teyssier, C., Vanderhaeghe, O., 2004. Gneiss domes and crustal flow, in *Gneiss Domes*. In: Whitney, D.L., Teyssier, C., Siddoway, C.S. (Eds.), *Orogeny*, Geological Society of America Special Paper 380, pp. 15–33.

Whitney, D.L., Teyssier, C., Kruckenberg, S.C., Morgan, V.L., Iredale, L.J., 2008. High-pressure–low-temperature metamorphism of metasedimentary rocks, southern Menderes Massif, western Turkey. *Lithos* 101, 218–232.

Zlatkin, O., 2011. Neoproterozoic basement and Lower Paleozoic siliciclastic cover of the Menderes Massif (Western Taurides): a U-Pb-Hf zircon perspective. Master Thesis.

Zeh A., Gerdes A., Klemd R., Barton J. M. 2007. Archean to Proterozoic crustal evolution of the Limpopo Belt (South Africa/Botswana): constraints from combined U–Pb and Hf isotope analyses of zircon. *Journal of Petrology*, 48: 1605–1639.

Zeh A., Gerdes A., Millonig, I., 2011. Hafnium isotope record of the Ancient Gneiss Complex, Swaziland, southern Africa: evidence for Archaean crust–mantle formation and crust reworking between 3.66 and 2.73 Ga. *Journal of the Geological Society*, 168: 953–963.



## **APPENDICES**

### **APPENDIX A**

#### **PROCESS OF MINERAL SEPARATION**

Separating zircon grains in whole massive rock is based on physical separation techniques. Steps of techniques may get differ in different laboratories. In Frankfurt, six steps were applied for zircon separation from field up to mass spectrometer stage; they are:

- 1 crushing,
- 2 wilfley table,
- 3 heavy liquid,
- 4 magnetic separator,
- 5 hand picking,
- 6 epoxy, polishing and cathodoluminescence imaging.

#### **CRUSHING**

Crushing was done in Sample Preparation Laboratory, Department of Geological Engineering, Dokuz Eylül University (Figure A.1). Firstly, weathered parts are removed by help of a hammer and the rest massive parts are broken into smaller pieces in a jaw crusher. Gap between jaws should be adjusted for each sample according to its hardness. The ideal size of the grains is around 2-3 cm in diameter. The jaw crushed must be cleaned carefully after each sample because contamination is not tolerated. Then, the processed samples are put into a roller crusher gets to get finer grains. To measure U-Pb system in zircons with LA-ICP-MS, sample must be crushed down to 0.25  $\mu\text{m}$ .

Some of the laboratories use sieve during roller crushing. Different range sieves are used to separate finer grains. Coarser grains are processed in roller crusher to get finer pieces. But in Dokuz Eylül University and Goethe University sieving is not used because it is considered as a time consuming process.



Figure A.1 A view of a roller crushed in the crushing laboratory of the Department of Geological Engineering in Dokuz Eylül University.

### **WILFLEY TABLE**

Wilfley table stage was also performed in Sample Preparation Laboratory, Department of Geological Engineering, Dokuz Eylül University. The table is also known as shaking table, concentrating table and gravity shaker.

About 0.25  $\mu\text{m}$ -size fragments are put into a wilfley table to separate light minerals (like mica and quartz) from heavy minerals. Powder of a sample is put on the sample container, the grains are separated as the table shakes according to their density. For a better separation, velocity of sample flow, intensity of water flow, frequency of shaking and slope of table must be well adjusted manually according to the of the sample (Figure A.2). Heavy and light minerals accumulate in different decks (decks 1 and 2 and decks 3 and 4, respectively; see Figure A.2).

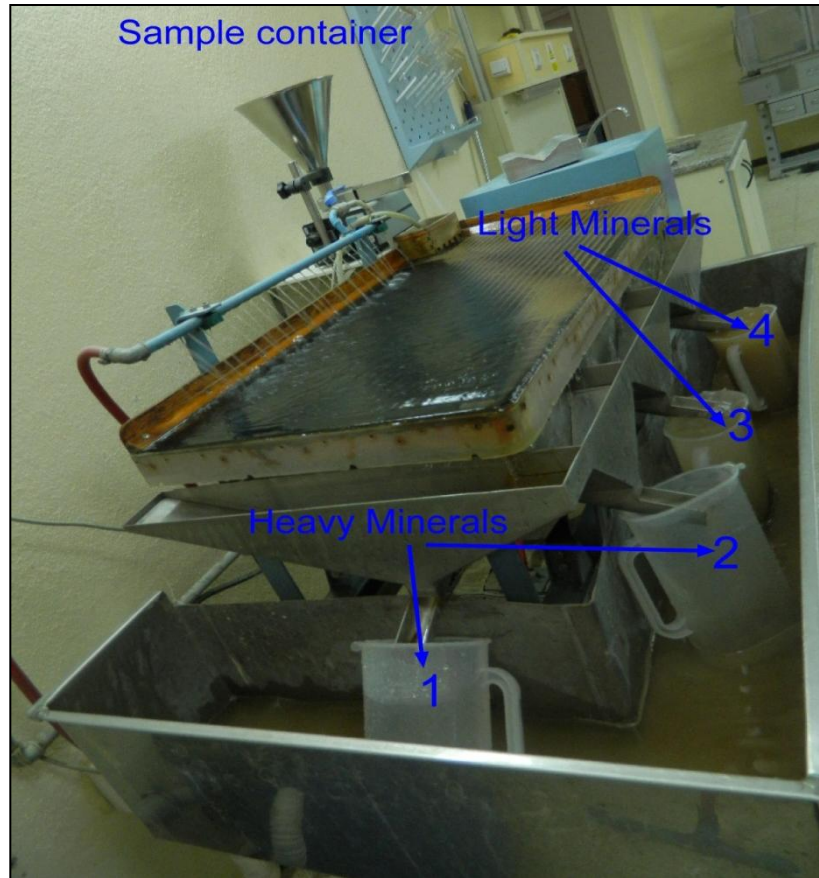


Figure A. 1 Wilfley table with water and manually adjusted. Light and heavy minerals separation is seen.

When separation of grains is complete for a sample, heavy concentrates in two of the decks (decks 1 and 2) are transferred to different containers and put into an oven to get dry. Light parts are generally thrown but we kept them in case we may need them for other purposes. After complete drying of samples, two containers are taken out. One of them is packed and saved for future use; the second is used in the next step, heavy liquid. Generally, after wilfley table, magnetic separator is performed. But in Göethe University/Frankfurt, heavy liquid is performed to save time because the duration of magnetic separator depends on the amount of sample.

### **HEAVY LIQUID**

In the third stage, a heavy liquid –bromoform ( $\text{CHBr}_3$ ,  $d= 2.88 \text{ g/cm}^3$ ) – is used (Figure A.3). During this step, perfect separation between relatively heavier and heaviest minerals is performed.



Figure A.2 The heavy liquid bromoform and sample are mixed in a glass; then wait for sometime until the heavier and heaviest minerals are separated according to their relative density with respect to the density of the liquid. Then the mixture is run through separating funnel.

The heavier part is packed and heaviest part is put in a fume hood and waited for sometime until it loses bromoform. Then, the heaviest portion is dried and prepared for magnetic separation.

### **MAGNETIC SEPARATION**

Magnetic separator is used to separate minerals based on their magnetic properties; trademark Frantz Isodynamic Magnetic Separator is used in this process (Figure A.4). The magnetic separator contains two large electromagnets and the mineral separates pass on a metal way in-between electromagnets. The intensity of the magnetic field and/or slope of the metal way are specifically adjusted for target mineral. Zircon is non-magnetic under 1.6 A. For zircon separation 0.4 A, 0.8A, 1.2 A, 1.6 A intensities are used and after magnetic separation, the powder above 1.6 A is taken for hand picking.



Figure A.3 View of a magnetic separator in Geochronology and Radiogenic Isotope Laboratory, Institute of Geoscience, Göethe University of Frankfurt.

### **HAND PICKING**

The non-magnetic part ( $> 1.6 \text{ A}$ ) of the mineral separate from magnetic separator is studied under binocular microscope (Figure A.5) and zircons are hand picked. Zircon is high relief, prismatic, bright and generally transparent mineral. It is not so difficult to distinguish it from other minerals, except apatite and experience is needed for a easy pick up of zircons.

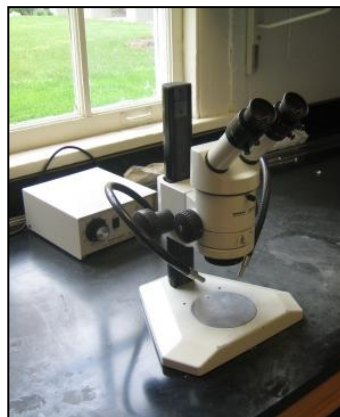


Figure A. 4 View of a binocular microscope.

### **EPOXY, POLISHING AND CATHODOLUMINESCENCE IMAGES**

After picking enough number of zircon grains (this about 100–110 grains for sediments and 55 grains for magmatic rocks), they are mounted in a epoxy tablet and then polished to expose their inner zonation with Ar gas (Figure A.6).



Figure A.5 View of mounted and polished zircon grains ready for cathodoluminescence imaging.

Cathodoluminescence (CL) images of zircons are taken to see zoned structure clearly (Figure A.7); spot locations are selected on CL images. The CL images are obtained in a JEOL-JSM-6490 scanning electron microscope in Geochronology and Radiogenic Isotope Laboratory, Institute of Geoscience, Göethe University of Frankfurt.

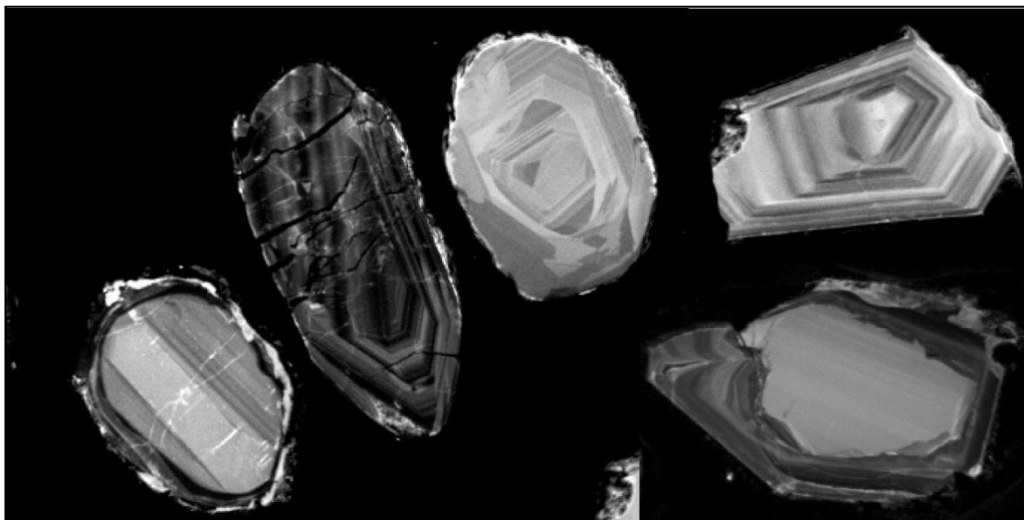


Figure A.6 Cathodoluminescence images of detrital zircons from Kurudere metaconglomerates (sample 331).

After taking CL images and determining spot locations, zircons are ready U-Pb for analyses. In this study, laser ablation induced couple mass spectrometry method (LA-ICPMS) is performed.

## APPENDIX B

### LIST OF U-Pb AND Hf DATA

In the tables below, processed, concordant and discordant U-Pb and  $\epsilon$ Hf data are presented with sample numbers, spot numbers, ratio of measured isotopes and concordant and discordant data. For U-Pb systems, basically Pb isotopes, U isotopes and Th<sup>232</sup> were measured. Additionally, Hg<sup>204</sup> were measured because of having the same atomic number with common lead (Pb<sup>204</sup>) and to determine the precise age of the minerals.

To calculate  $\epsilon$ Hf value,  $T_{DM}$  ages, Lu/Hf ration and Hf/Hf ratio were measured.

Table B.1 The list of U-Pb isotope measurements.

grain	$^{207}\text{Pb}^a$ (cps)	$\text{U}^b$ (ppm)	$\text{Pb}^b$ (ppm)	$\frac{\text{Th}^b}{\text{U}}$	$^{206}\text{Pb}^c$ (%)	$\frac{^{206}\text{Pb}^d}{^{238}\text{U}}$ (%)	$\pm 2\sigma$	$\frac{^{207}\text{Pb}^d}{^{235}\text{U}}$ (%)	$\pm 2\sigma$	$\frac{^{207}\text{Pb}^d}{^{206}\text{Pb}^d}$ (%)	$\pm 2\sigma$	$\text{rho}^e$	$\frac{^{206}\text{Pb}}{^{238}\text{U}}$ (Ma)	$\pm 2\sigma$	$\frac{^{207}\text{Pb}}{^{235}\text{U}}$ (Ma)	$\pm 2\sigma$	$\frac{^{207}\text{Pb}}{^{206}\text{Pb}}$ (Ma)	$\pm 2\sigma$	conc. (%)
<b>Sample 331</b>																			
A66	7048	222	16	0	0	0	2	1	3	0	3	1	427	7	422	11	391	63	109
A72	22388	65	46	3	3	0	2	5	7	0	6	0	1849	38	1827	57	1801	110	103
A73	12874	37	16	1	1	0	4	5	7	0	6	1	1840	59	1863	61	1890	107	97
A74	7570	93	23	1	1	0	2	1	6	0	6	0	934	15	880	37	745	124	125
A75	1288	28	3	0	0	0	2	1	4	0	4	0	598	11	595	18	582	77	103
A76	1957	55	4	0	0	0	2	1	4	0	4	0	491	7	491	17	494	87	99
A77	2976	52	6	0	0	0	2	1	4	0	4	0	685	13	677	21	653	78	105
A78	13846	137	24	0	0	0	2	2	2	0	2	1	916	15	940	15	996	33	92
A79	2555	63	4	0	1	0	2	1	5	0	4	0	441	9	428	16	356	91	124
A80	22723	71	25	0	0	0	2	5	2	0	1	1	1860	25	1887	17	1918	21	97
A81	2807	26	6	1	1	0	2	2	4	0	3	0	1006	17	1030	24	1083	65	93
A82	9302	13	7	0	3	0	2	11	3	0	3	1	2560	38	2513	32	2475	49	103
A83	2573	38	6	0	1	0	2	2	3	0	3	1	906	17	931	21	988	57	92
A85	71360	109	54	0	0	0	2	11	2	0	1	1	2439	40	2519	20	2584	14	94
A86	5312	131	9	1	1	0	3	0	6	0	5	0	348	9	346	18	331	123	105
A87	1747	51	4	0	0	0	2	1	4	0	4	0	462	8	463	15	469	80	98
A88	6964	80	14	0	0	0	2	2	3	0	2	1	909	14	936	16	1000	40	91
A89	1876	33	5	1	0	0	2	1	9	0	9	0	643	12	670	48	764	196	84
A90	13852	263	29	0	0	0	1	1	2	0	1	1	676	10	688	9	726	24	93
A091	20776	73	27	1	0	0	2	5	2	0	2	1	1798	26	1822	20	1848	29	97
A93	7013	62	9	0	4	0	2	1	8	0	7	0	755	14	753	41	746	155	101

Table B.1 (continued)

grain	$^{207}\text{Pb}^a$ (cps)	$\text{U}^b$ (ppm)	$\text{Pb}^b$ (ppm)	$\frac{\text{Th}^b}{\text{U}}$	$^{206}\text{Pb}^c$ (%)	$\frac{^{206}\text{Pb}^d}{^{238}\text{U}}$ (%)	$\pm 2\sigma$	$\frac{^{207}\text{Pb}^d}{^{235}\text{U}}$ (%)	$\pm 2\sigma$	$\frac{^{207}\text{Pb}^d}{^{206}\text{Pb}^d}$ (%)	$\pm 2\sigma$	rho <sup>e</sup>	$\frac{^{206}\text{Pb}}{^{238}\text{U}}$ (Ma)	$\pm 2\sigma$	$\frac{^{207}\text{Pb}}{^{235}\text{U}}$ (Ma)	$\pm 2\sigma$	$\frac{^{207}\text{Pb}}{^{206}\text{Pb}}$ (Ma)	$\pm 2\sigma$	conc. (%)
<b>Sample 331</b>																			
A94	4335	180	9	0	0	0	5	0	6	0	4	1	299	13	315	16	437	81	69
A95	4232	161	10	0	0	0	2	0	3	0	3	1	374	6	373	9	365	58	103
A96	7463	80	18	1	0	0	2	2	4	0	4	0	1019	15	1037	27	1073	75	95
A97	6711	210	16	0	0	0	2	1	3	0	3	0	428	6	432	12	452	65	95
A98	7271	87	13	1	1	0	2	1	3	0	3	0	786	11	777	17	751	57	105
A99	75150	125	80	1	0	0	2	10	3	0	2	1	2372	41	2452	29	2519	40	94
A100	2618	48	6	1	0	0	2	1	5	0	5	0	640	10	659	27	726	111	88
A101	931	13	2	1	4	0	5	0	26	0	26	0	599	30	360	83	-987	757	-61
A107	16816	259	37	1	1	0	3	1	4	0	3	1	736	20	745	21	772	58	95
A108	16800	265	61	0	1	0	5	4	5	0	1	1	965	40	1608	38	2595	21	37
A109	16244	608	52	0	0	0	2	1	3	0	2	1	550	13	557	14	585	45	94
A110	1206	41	3	0	0	0	2	1	4	0	4	1	460	11	463	17	476	83	97
A111	29038	39	22	0	2	1	2	12	3	0	2	1	2631	37	2633	24	2634	31	100
A112	1989	34	4	0	2	0	2	1	5	0	5	0	604	13	612	24	644	101	94
A113	2127	31	4	0	1	0	3	1	5	0	5	1	701	19	703	28	708	98	99
A114	2236	41	7	2	0	0	2	1	5	0	4	0	649	12	651	22	658	87	99
A115	59807	225	120	1	1	0	2	10	2	0	2	1	2187	34	2392	23	2571	27	85
A116	3573	107	9	0	0	0	2	1	3	0	2	1	477	7	497	10	593	46	80
A117	29706	98	18	0	5	0	3	3	6	0	5	0	930	24	1330	42	2050	86	45
A118	7345	21	8	0	2	0	2	6	3	0	3	1	2045	30	2033	29	2020	48	101
A119	1793	36	5	1	0	0	2	1	4	0	4	0	729	13	690	22	564	86	129
A120	3817	111	8	0	0	0	2	1	5	0	4	0	446	8	447	17	455	96	98

Table B.1 (continued)

grain	$^{207}\text{Pb}^a$ (cps)	$\text{U}^b$ (ppm)	$\text{Pb}^b$ (ppm)	$\frac{\text{Th}^b}{\text{U}}$	$^{206}\text{Pb}^c$ (%)	$\frac{^{206}\text{Pb}^d}{^{238}\text{U}}$ (%)	$\pm 2\sigma$	$\frac{^{207}\text{Pb}^d}{^{235}\text{U}}$ (%)	$\pm 2\sigma$	$\frac{^{207}\text{Pb}^d}{^{206}\text{Pb}^d}$ (%)	$\pm 2\sigma$	$\rho^e$	$\frac{^{206}\text{Pb}}{^{238}\text{U}}$ (Ma)	$\pm 2\sigma$	$\frac{^{207}\text{Pb}}{^{235}\text{U}}$ (Ma)	$\pm 2\sigma$	$\frac{^{207}\text{Pb}}{^{206}\text{Pb}}$ (Ma)	$\pm 2\sigma$	conc. (%)
<b>Sample 331</b>																			
A121	17680	45	22	1	0	0	2	7	2	0	2	1	2103	30	2090	20	2077	28	101
A122	19577	661	55	0	0	0	2	1	2	0	1	1	547	12	556	10	593	20	92
A123	54280	143	70	1	2	0	2	10	3	0	2	1	2296	46	2413	28	2513	31	91
A124	13177	461	29	0	2	0	2	0	6	0	6	0	384	8	395	20	461	125	83
A125	8815	1770	31	0	2	0	3	0	6	0	5	0	108	3	110	6	156	119	69
A126	11220	504	35	1	0	0	2	0	2	0	1	1	402	8	405	8	424	24	95
A128	11873	410	40	1	0	0	2	1	3	0	1	1	535	11	539	11	553	31	97
A129	5313	125	14	1	0	0	2	1	3	0	2	1	638	14	670	15	779	44	82
A130	1360	47	4	0	0	0	3	1	5	0	4	1	537	14	566	20	684	80	79
A134	9549	150	16	1	13	0	6	1	51	0	51	0	436	26	434	200	424	1139	103
A135	9886	233	17	0	5	0	3	1	14	0	14	0	399	12	460	53	775	289	51
A136	10038	131	23	1	2	0	2	2	5	0	5	0	931	18	943	33	974	98	96
A137	34567	505	98	1	0	0	2	2	3	0	2	1	1001	18	1002	16	1003	32	100
A138	13284	289	36	0	0	0	2	1	2	0	1	1	759	14	764	12	777	24	98
A139	27201	801	85	0	0	0	2	1	2	0	1	1	682	13	674	11	646	23	105
A140	5410	249	16	0	0	0	2	0	3	0	3	1	386	8	389	11	408	58	94
A141	4802	220	15	1	1	0	2	0	3	0	2	1	396	9	394	11	383	56	103
A142	7155	288	20	0	0	0	2	1	3	0	2	1	415	8	425	11	485	53	85
A143	6412	222	17	1	0	0	2	1	4	0	3	1	440	10	435	13	411	66	107
A144	21537	573	60	0	0	0	2	1	2	0	1	1	693	13	693	11	694	18	100
A145	20860	622	62	0	0	0	2	1	2	0	1	1	627	12	629	11	638	19	98

Table B.1 (continued)

grain	$^{207}\text{Pb}^a$ (cps)	$\text{U}^b$ (ppm)	$\text{Pb}^b$ (ppm)	$\frac{\text{Th}^b}{\text{U}}$	$^{206}\text{Pb}^c$ (%)	$\frac{^{206}\text{Pb}^d}{^{238}\text{U}}$ (%)	$\pm 2\sigma$	$\frac{^{207}\text{Pb}^d}{^{235}\text{U}}$ (%)	$\pm 2\sigma$	$\frac{^{207}\text{Pb}^d}{^{206}\text{Pb}^d}$ (%)	$\pm 2\sigma$	rho <sup>e</sup>	$\frac{^{206}\text{Pb}}{^{238}\text{U}}$ (Ma)	$\pm 2\sigma$	$\frac{^{207}\text{Pb}}{^{235}\text{U}}$ (Ma)	$\pm 2\sigma$	$\frac{^{207}\text{Pb}}{^{206}\text{Pb}}$ (Ma)	$\pm 2\sigma$	conc. (%)
<b>Sample 331</b>																			
A146	13630	395	41	0	0	0	2	1	3	0	2	1	616	12	608	12	578	38	106
A147	29787	865	86	0	0	0	2	1	2	0	1	1	651	12	651	10	648	17	101
A148	5437	245	15	0	0	0	2	0	3	0	3	1	394	9	401	12	439	59	90
A149	7991	111	13	2	0	0	3	1	3	0	2	1	580	14	582	14	590	42	98
A150	25025	160	31	1	0	0	2	2	2	0	1	1	986	18	982	14	972	19	101
A151	66172	125	45	0	0	0	2	6	2	0	1	1	1873	32	1902	19	1934	18	97
A152	6924	135	9	0	0	0	2	1	3	0	1	1	442	10	477	10	646	29	68
A153	5282	63	6	0	0	0	2	1	3	0	2	1	604	12	600	14	584	53	104
A154	30173	417	39	0	0	0	2	1	2	0	1	1	627	12	628	11	632	21	99
A155	12233	158	15	0	0	0	2	1	3	0	1	1	600	12	618	12	682	30	88
A156	7961	160	11	1	0	0	2	0	3	0	2	1	412	9	411	10	408	45	101
A157	8159	150	9	0	3	0	2	0	9	0	8	0	370	8	373	27	387	188	96
A158	3847	77	6	0	0	0	2	1	3	0	3	1	467	10	466	13	459	57	102
A159	9211	123	13	0	0	0	2	1	3	0	2	1	632	14	637	14	653	35	97
A160	12105	219	16	0	1	0	3	1	4	0	3	1	466	12	459	16	422	72	110
A161	4563	108	8	1	0	0	2	1	3	0	1	1	427	10	439	10	501	28	85
A162	2660	36	4	1	0	0	2	1	3	0	2	1	602	12	637	14	763	44	79
A163	56056	201	25	0	0	0	2	2	3	0	1	1	763	18	1115	18	1885	15	40
A164	9808	102	15	1	0	0	2	1	2	0	1	1	757	14	777	13	836	30	91
A165	11490	75	14	2	0	0	2	1	3	0	2	1	850	19	852	18	856	41	99
A166	6467	143	9	0	0	0	2	1	3	0	2	1	418	9	421	11	441	47	95

Table B.1 (continued)

grain	$^{207}\text{Pb}^a$ (cps)	$\text{U}^b$ (ppm)	$\text{Pb}^b$ (ppm)	$\frac{\text{Th}^b}{\text{U}}$	$^{206}\text{Pb}^c$ U (%)	$\frac{^{206}\text{Pb}^d}{^{238}\text{U}}$ (%)	$\pm 2\sigma$ (%)	$\frac{^{207}\text{Pb}^d}{^{235}\text{U}}$ (%)	$\pm 2\sigma$ (%)	$\frac{^{207}\text{Pb}^d}{^{206}\text{Pb}^d}$ (%)	$\pm 2\sigma$ (%)	$\rho^e$	$\frac{^{206}\text{Pb}}{^{238}\text{U}}$ (Ma)	$\pm 2\sigma$ (Ma)	$\frac{^{207}\text{Pb}}{^{235}\text{U}}$ (Ma)	$\pm 2\sigma$ (Ma)	$\frac{^{207}\text{Pb}}{^{206}\text{Pb}}$ (Ma)	$\pm 2\sigma$ (Ma)	conc. (%)
<b>Sample 331</b>																			
A168	9702	141	13	0	0	0	2	1	3	0	2	1	583	13	582	13	579	35	101
A169	5784	74	8	1	0	0	2	1	3	0	2	1	565	10	592	12	693	42	82
A170	21298	196	28	1	1	0	2	1	3	0	2	1	725	15	723	16	718	46	101
A171	73100	90	41	1	0	0	2	9	2	0	1	1	2123	40	2293	22	2448	14	87
A172	12697	93	16	1	1	0	2	1	3	0	2	1	871	17	891	18	943	45	92
A173	59406	106	35	0	0	0	2	5	2	0	1	1	1714	31	1887	20	2083	18	82
A174	22685	304	29	0	0	0	2	1	2	0	1	1	575	11	579	10	597	26	96
A178	43404	97	31	0	0	0	2	5	2	0	1	1	1753	32	1836	19	1931	16	91
A179	32077	73	41	0	1	1	2	10	5	0	4	0	2816	46	2475	45	2207	74	128
A180	11801	147	12	0	1	0	2	1	4	0	3	1	510	12	512	15	518	59	98
A181	14699	246	13	0	3	0	3	0	8	0	7	0	303	9	307	21	339	161	89
A182	6848	145	10	0	0	0	2	1	3	0	2	1	414	10	417	11	437	46	95
A183	5360	105	7	1	1	0	2	0	4	0	3	1	404	8	402	12	389	66	104
A184	5794	102	7	1	0	0	2	0	4	0	3	1	404	9	403	12	398	61	102
A185	9508	70	10	1	4	0	4	1	10	0	9	0	615	23	620	47	639	198	96
A186	3301	35	4	1	0	0	2	1	3	0	2	1	711	16	714	15	725	40	98
A188	9895	157	14	0	0	0	2	1	2	0	1	1	550	10	548	10	540	29	102
A189	10798	91	14	1	0	0	2	1	3	0	2	1	871	18	863	17	842	40	103
A190	12466	163	17	1	0	0	2	1	3	0	1	1	608	13	612	12	626	29	97
A191	82763	553	104	1	1	0	2	2	3	0	2	1	976	20	972	17	964	32	101
A192	4468	47	7	1	0	0	2	1	5	0	4	0	732	17	730	25	723	88	101

Table B.1 (continued)

grain	$^{207}\text{Pb}^a$ (cps)	$\text{U}^b$ (ppm)	$\text{Pb}^b$ (ppm)	$\frac{\text{Th}^b}{\text{U}}$	$^{206}\text{Pbc}^c$ (%)	$\frac{^{206}\text{Pbd}^d}{^{238}\text{U}}$ (%)	$\pm 2\sigma$	$\frac{^{207}\text{Pbd}^d}{^{235}\text{U}}$ (%)	$\pm 2\sigma$	$\frac{^{207}\text{Pbd}^d}{^{206}\text{Pbd}^d}$ (%)	$\pm 2\sigma$	rho <sup>e</sup>	$\frac{^{206}\text{Pb}}{^{238}\text{U}}$ (Ma)	$\pm 2\sigma$	$\frac{^{207}\text{Pb}}{^{235}\text{U}}$ (Ma)	$\pm 2\sigma$	$\frac{^{207}\text{Pb}}{^{206}\text{Pb}}$ (Ma)	$\pm 2\sigma$	conc. (%)
<b>Sample 331</b>																			
A193	88022	75	45	1	0	0	2	13	2	0	1	1	2591	42	2651	20	2696	14	96
A194	39379	76	30	1	0	0	2	5	2	0	1	1	1842	33	1897	20	1958	16	94
A195	78509	191	126	2	0	0	2	12	2	0	1	1	2534	43	2574	20	2605	11	97
A196	12906	166	19	1	0	0	2	1	3	0	2	1	573	12	588	14	642	45	89
A197	32255	230	43	1	0	0	2	1	3	0	2	1	886	20	901	18	938	35	94
A198	2825	36	4	1	0	0	3	1	9	0	9	0	532	15	535	40	549	194	97
A199	8044	142	9	0	1	0	3	0	4	0	4	1	388	10	389	14	395	80	98
A200	7153	141	9	1	1	0	2	0	4	0	3	1	381	9	381	13	384	70	99
A201	5302	70	7	1	1	0	2	1	5	0	4	1	549	12	552	20	565	86	97
A202	12494	165	18	1	0	0	2	1	2	0	1	1	602	12	606	11	621	27	97
A203	7428	160	10	0	0	0	2	0	3	0	2	1	405	8	404	9	400	37	101
A204	5778	113	7	0	0	0	2	0	4	0	3	1	389	9	383	14	342	77	114
A205	8819	123	13	0	0	0	2	1	2	0	1	1	619	12	618	11	612	30	101
<b>Sample 332</b>																			
A06	62754	85	42	0	1	0	1	10	2	0	1	1	2429	30	2474	17	2511	17	102
A07	84637	135	49	0	9	0	2	7	7	0	7	0	1893	33	2148	63	2402	112	81
A08	4628	104	8	0	1	0	2	1	4	0	4	0	461	8	466	16	493	88	94
A9	51561	76	35	0	1	0	2	10	2	0	1	1	2347	30	2413	17	2469	17	108
A10	21124	34	12	0	1	0	2	7	2	0	2	1	1853	27	2111	22	2372	30	106
A11	3303	63	5	0	1	0	2	1	4	0	4	0	543	8	554	17	598	79	103
A12	61286	86	39	0	0	0	1	10	2	0	1	1	2318	28	2413	16	2495	15	97



Table B.1 (continued)

grain	$^{207}\text{Pb}^a$ (cps)	$\text{U}^b$ (ppm)	$\text{Pb}^b$ (ppm)	$\frac{\text{Th}^b}{\text{U}}$	$^{206}\text{Pb}^c$ (%)	$\frac{^{206}\text{Pb}^d}{^{238}\text{U}}$ (%)	$\pm 2\sigma$	$\frac{^{207}\text{Pb}^d}{^{235}\text{U}}$ (%)	$\pm 2\sigma$	$\frac{^{207}\text{Pb}^d}{^{206}\text{Pb}^d}$ (%)	$\pm 2\sigma$	$\rho^e$	$\frac{^{206}\text{Pb}}{^{238}\text{U}}$ (Ma)	$\pm 2\sigma$	$\frac{^{207}\text{Pb}}{^{235}\text{U}}$ (Ma)	$\pm 2\sigma$	$\frac{^{207}\text{Pb}}{^{206}\text{Pb}}$ (Ma)	$\pm 2\sigma$	conc. (%)	
<b>Sample 332</b>																				
A41	12906	198	20	0	1	0	2	1	2	0	2	1	1	642	9	650	12	678	41	95
A42	3709	75	6	1	1	0	2	1	3	0	3	1	1	463	7	516	13	758	58	61
A43	4548	110	8	1	0	0	2	1	3	0	2	1	1	459	8	477	10	564	45	81
A44	4448	79	8	1	0	0	2	1	3	0	2	1	1	545	8	552	11	581	44	94
A45	14601	114	24	1	2	0	2	2	4	0	4	0	0	1021	15	1005	28	970	82	105
A46	5205	123	10	0	0	0	2	1	2	0	2	1	1	477	7	484	8	515	33	93
A47	8703	207	14	0	0	0	1	1	2	0	2	1	1	439	6	448	8	494	33	89
A48	9254	145	19	2	0	0	1	1	2	0	2	1	1	626	9	631	11	651	41	96
A49	3956	93	7	0	0	0	1	1	3	0	2	1	1	478	6	489	11	537	51	89
A50	6048	137	10	0	1	0	2	1	3	0	3	1	1	463	8	461	12	449	57	103
A51	3599	87	7	0	0	0	2	1	3	0	3	1	1	454	7	470	12	547	57	83
A52	5842	68	10	1	0	0	2	1	2	0	2	1	1	802	11	795	13	774	39	104
A53	18459	463	36	1	0	0	2	1	2	0	1	1	1	452	7	460	7	501	22	90
A54	10799	192	18	0	0	0	1	1	2	0	1	1	1	592	8	590	9	583	31	101
A55	244173	339	186	1	0	0	1	10	1	0	1	1	1	2326	26	2451	14	2557	10	91
A56	3380	23	4	1	11	0	3	1	14	0	14	0	0	681	17	697	72	747	285	91
A57	10946	169	22	2	0	0	1	1	2	0	2	1	1	627	9	642	11	695	40	90
A58	30190	263	51	1	0	0	1	2	2	0	1	1	1	1009	13	1008	11	1006	18	100
A59	77550	389	97	0	0	0	1	3	2	0	1	1	1	1388	17	1525	14	1720	20	81
A60	9909	131	11	1	6	0	2	0	9	0	9	0	0	420	7	406	32	324	207	130
A61	81675	164	64	1	0	0	1	7	2	0	1	1	1	1851	22	2168	14	2483	13	75
A62	27848	331	41	0	0	0	1	1	2	0	1	1	1	744	10	765	9	826	21	90

Table B.1 (continued)

grain	$^{207}\text{Pb}^a$ (cps)	$\text{U}^b$ (ppm)	$\text{Pb}^b$ (ppm)	$\frac{\text{Th}^b}{\text{U}}$	$^{206}\text{Pbc}^c$ (%)	$\frac{^{206}\text{Pbd}}{^{238}\text{U}}$ (%)	$\pm 2\sigma$	$\frac{^{207}\text{Pbd}}{^{235}\text{U}}$ (%)	$\pm 2\sigma$	$\frac{^{207}\text{Pbd}}{^{206}\text{Pbd}}$ (%)	$\pm 2\sigma$	$\text{rho}^e$	$\frac{^{206}\text{Pbd}}{^{238}\text{U}}$ (Ma)	$\pm 2\sigma$	$\frac{^{207}\text{Pbd}}{^{235}\text{U}}$ (Ma)	$\pm 2\sigma$	$\frac{^{207}\text{Pb}}{^{206}\text{Pb}}$	$\pm 2\sigma$	conc. (%)	
<b>Sample 332</b>																				
A63	6210	151	11	0	0	0	2	1	2	0	1	1	451	8	449	8	440	27	103	
A64	14769	226	23	0	0	0	1	1	2	0	1	1	635	9	650	9	704	27	90	
A65	12977	232	21	1	2	0	2	1	5	0	4	0	457	10	463	19	492	96	93	
A66	5532	132	9	0	0	0	2	1	3	0	2	1	448	7	460	10	519	50	86	
A72	8792	214	16	0	0	0	1	1	2	0	2	1	476	6	476	8	472	35	101	
A73	9801	135	16	1	0	0	2	1	3	0	2	1	623	10	654	13	761	42	82	
A74	6006	143	11	1	0	0	1	1	2	0	2	1	451	6	455	8	474	37	95	
A75	6719	135	14	1	0	0	2	1	2	0	2	1	606	9	593	10	541	35	112	
A76	7239	166	12	0	0	0	1	1	2	0	2	1	457	7	465	8	507	33	90	
A87	7864	312	21	0	0	0	2	1	3	0	1	1	436	10	444	10	484	27	90	
A88	11709	39	19	2	0	0	2	6	3	0	2	1	2020	41	2026	28	2031	36	99	
A93	65674	194	74	1	3	0	2	5	4	0	3	1	1690	37	1800	32	1929	51	88	
A94	3179	76	9	1	0	0	2	1	3	0	2	1	651	15	651	15	649	46	100	
A95	8760	200	22	0	0	0	2	1	3	0	2	1	656	14	674	14	731	36	90	
A96	5449	213	13	0	0	0	2	0	4	0	3	1	376	9	384	11	432	57	87	
A97	46296	411	26	0	2	0	15	1	19	0	11	1	283	43	497	76	1657	195	17	
A98	10554	273	24	0	0	0	3	1	3	0	1	1	543	13	541	12	531	33	102	
A99	9755	118	28	2	0	0	2	2	3	0	1	1	1004	22	1029	18	1081	28	93	
A100	5587	206	14	0	0	0	2	1	3	0	2	1	441	10	449	12	486	48	91	
A101	8418	328	22	1	0	0	4	0	5	0	2	1	385	16	384	16	377	54	102	
A102	7879	307	20	0	0	0	2	1	3	0	1	1	422	10	426	9	448	25	94	
A103	6504	162	18	1	0	0	2	1	3	0	2	1	521	12	564	13	743	35	70	

Table B.1 (continued)

grain	$^{207}\text{Pb}^a$ (cps)	$\text{U}^b$ (ppm)	$\text{Pb}^b$ (ppm)	$\frac{\text{Th}^b}{\text{U}}$	$^{206}\text{Pbc}^c$ (%)	$\frac{^{206}\text{Pbd}^d}{^{238}\text{U}}$ (%)	$\pm 2\sigma$	$\frac{^{207}\text{Pbd}^d}{^{235}\text{U}}$ (%)	$\pm 2\sigma$	$\frac{^{207}\text{Pbd}^d}{^{206}\text{Pbd}^d}$ (%)	$\pm 2\sigma$	$\text{rho}^e$	$\frac{^{206}\text{Pbd}^d}{^{238}\text{U}}$ (Ma)	$\pm 2\sigma$	$\frac{^{207}\text{Pb}}{^{206}\text{Pb}}$	$\pm 2\sigma$	conc. (%)		
<b>Sample 332</b>																			
A104	11586	459	36	1	0	0	2	1	3	0	1	1	460	10	453	9	416	22	111
A105	2824	77	8	1	0	0	2	1	3	0	2	1	585	13	598	14	647	42	90
A106	9721	386	22	0	0	0	3	0	3	0	2	1	351	10	353	10	366	44	96
A107	16916	360	39	0	0	0	2	1	3	0	1	1	658	15	663	14	681	29	97
A108	29281	349	58	0	0	0	2	2	2	0	1	1	987	21	988	16	992	17	99
A109	9443	130	25	1	0	0	2	2	3	0	1	1	952	21	956	17	964	30	99
A110	20133	99	38	2	0	0	2	4	3	0	1	1	1640	35	1695	22	1763	18	93
A111	5597	212	15	1	0	0	3	0	3	0	2	1	402	10	408	12	440	53	91
A112	11885	105	15	1	13	0	3	1	13	0	12	0	605	16	625	61	699	263	87
A113	93852	173	108	1	0	0	2	12	2	0	1	1	2589	49	2605	23	2617	10	99
A114	12873	297	24	1	0	0	2	1	4	0	3	1	440	10	443	13	459	60	96
A115	10279	392	26	0	0	0	2	1	3	0	1	1	434	10	438	9	460	27	94
A116	9519	332	27	1	0	0	2	1	3	0	2	1	455	10	461	11	488	40	93
A117	5288	186	12	0	0	0	2	0	3	0	2	1	407	9	408	11	414	52	98
A118	31532	414	83	2	0	0	2	2	3	0	1	1	938	21	951	16	981	20	96
A119	3122	102	8	1	0	0	2	1	4	0	3	1	467	11	464	14	450	64	104
A120	3222	102	7	1	0	0	2	1	4	0	3	1	418	10	415	14	398	73	105
A121	2800	105	8	1	0	0	2	1	3	0	2	1	439	10	441	12	456	55	96
A122	21653	163	26	1	2	0	5	1	10	0	9	0	579	29	644	51	875	187	66
A123	44671	185	62	2	0	0	4	5	4	0	1	1	1678	52	1761	31	1861	19	90
A124	6248	85	14	1	0	0	2	1	3	0	1	1	895	20	895	17	896	31	100
A125	19687	241	45	1	0	0	2	2	3	0	1	1	993	23	980	17	950	24	104

Table B.1 (continued)

grain	$^{207}\text{Pb}^a$ (cps)	$\text{U}^b$ (ppm)	$\text{Pb}^b$ (ppm)	$\frac{\text{Th}^b}{\text{U}}$	$^{206}\text{Pbc}$ (%)	$\frac{^{206}\text{Pbd}}{^{238}\text{U}}$ (%)	$\pm 2\sigma$	$\frac{^{207}\text{Pbd}}{^{235}\text{U}}$ (%)	$\pm 2\sigma$	$\frac{^{206}\text{Pbd}}{^{206}\text{Pb}}$ (%)	$\pm 2\sigma$	$\rho^e$	$\frac{^{206}\text{Pb}}{^{238}\text{U}}$ (Ma)	$\pm 2\sigma$	$\frac{^{207}\text{Pb}}{^{235}\text{U}}$ (Ma)	$\pm 2\sigma$	$\frac{^{207}\text{Pb}}{^{206}\text{Pb}}$ (Ma)	$\pm 2\sigma$	conc. (%)
<b>Sample 332</b>																			
A126	11053	380	26	0	0	0	2	1	3	0	1	1	427	10	433	10	468	32	91
A127	22187	363	32	0	2	0	2	1	4	0	4	1	520	12	570	19	774	75	67
A128	20776	174	2	0	0	0	889	0	889	0	10	1	5	45	13	121	1929	175	0
A129	8321	199	23	1	0	0	2	1	3	0	2	1	624	14	624	13	622	35	100
A130	5574	124	14	1	0	0	2	1	3	0	2	1	641	15	647	15	671	40	95
A131	21924	427	53	1	0	0	2	1	3	0	1	1	734	16	737	13	746	20	98
A132	6977	141	11	1	0	0	2	1	3	0	2	1	427	10	493	12	812	40	53
A133	4688	176	12	0	0	0	2	1	3	0	2	1	436	10	441	11	465	44	94
A136	32519	460	74	1	0	0	2	1	3	0	2	1	879	20	863	17	823	34	107
A137	10987	386	28	0	0	0	3	1	3	0	2	1	463	11	467	11	489	36	95
A138	67584	246	96	1	0	0	2	6	2	0	1	1	1915	39	1950	21	1988	12	96
A139	5382	210	15	1	0	0	2	1	3	0	2	1	439	10	438	11	433	39	102
A140	49037	86	50	1	1	0	2	11	3	0	1	1	2508	52	2561	26	2603	21	96
A141	15880	388	44	1	0	0	2	1	3	0	1	1	631	14	634	13	647	31	97
A142	4022	162	12	0	0	0	2	1	3	0	2	1	454	10	453	11	450	39	101
A143	29797	238	56	0	0	0	2	3	2	0	1	1	1320	28	1350	19	1398	16	94
A144	11712	156	30	2	0	0	2	1	3	0	2	1	903	19	898	19	885	45	102
A145	5686	184	13	0	0	0	2	1	3	0	2	1	447	10	450	12	467	48	96
A146	67754	218	81	0	0	0	2	6	2	0	1	1	1964	39	1991	21	2020	12	97
A147	4291	53	12	2	0	0	3	2	4	0	3	1	985	23	989	25	999	60	99
A148	10076	162	13	1	7	0	3	0	9	0	8	0	363	9	368	27	401	187	90
A149	1324	36	4	1	0	0	2	1	5	0	4	1	586	14	621	22	749	86	78

Table B.1 (continued)

grain	$^{207}\text{Pb}^a$ (cps)	$\text{U}^b$ (ppm)	$\text{Pb}^b$ (ppm)	$\frac{\text{Th}^b}{\text{U}}$	$^{206}\text{Pbc}^c$ (%)	$\frac{^{206}\text{Pbd}}{^{238}\text{U}}$ (%)	$\pm 2\sigma$	$\frac{^{207}\text{Pbd}}{^{235}\text{U}}$ (%)	$\pm 2\sigma$	$\frac{^{207}\text{Pbd}}{^{206}\text{Pbd}}$ (%)	$\pm 2\sigma$	$\text{rho}^e$	$\frac{^{206}\text{Pb}}{^{238}\text{U}}$ (Ma)	$\pm 2\sigma$	$\frac{^{207}\text{Pb}}{^{235}\text{U}}$ (Ma)	$\pm 2\sigma$	$\frac{^{207}\text{Pb}}{^{206}\text{Pb}}$ (Ma)	$\pm 2\sigma$	conc. (%)
<b>Sample 332</b>																			
A150	7711	125	9	0	3	0	2	1	9	0	9	0	460	11	460	35	458	198	100
A151	18114	125	19	1	0	0	2	1	3	0	1	1	831	18	842	15	868	24	96
A152	13001	77	13	1	0	0	2	2	3	0	1	1	941	21	948	16	964	24	98
A153	14054	30	7	1	10	0	3	2	10	0	10	0	1035	26	1056	67	1099	191	94
A154	3700	42	5	1	0	0	2	1	3	0	2	1	586	13	589	14	600	46	98
A155	19090	102	17	0	0	0	2	2	3	0	1	1	979	21	992	16	1022	21	96
A156	11591	45	5	1	12	0	3	1	10	0	10	0	444	12	502	42	773	212	57
A157	659	6	1	1	0	0	2	1	6	0	6	0	636	15	656	30	723	117	88
A158	2376	43	3	0	0	0	2	0	3	0	2	1	408	9	407	11	401	54	102
A159	32752	26	14	1	0	0	3	10	3	0	1	1	2174	57	2443	31	2675	20	81
A160	5010	80	6	0	0	0	2	1	3	0	2	1	453	11	447	11	418	43	108
A161	9660	145	11	1	0	0	2	1	3	0	2	1	457	10	453	11	433	42	106
A162	10783	138	13	1	0	0	2	1	3	0	1	1	582	13	578	11	563	25	103
A163	6246	101	7	0	0	0	2	1	3	0	2	1	442	10	445	10	457	34	97
A164	15831	166	18	1	0	0	2	1	3	0	1	1	643	14	642	13	638	30	101
A165	40515	275	33	1	2	0	3	1	4	0	3	1	615	15	614	19	612	71	101
A166	9841	108	10	1	0	0	3	1	5	0	4	1	470	12	464	17	434	79	108
A167	4172	71	5	0	0	0	2	1	3	0	2	1	452	11	447	11	421	41	107

Table B.1 (continued)

grain	$^{207}\text{Pb}^a$ (cps)	$\text{U}^b$ (ppm)	$\text{Pb}^b$ (ppm)	$\text{Th}^b$ U	$^{206}\text{Pb}^c$ (%)	$^{206}\text{Pb}^d$ $^{238}\text{U}$ (%)	$\pm 2\sigma$	$^{207}\text{Pb}^d$ $^{235}\text{U}$ (%)	$\pm 2\sigma$	$^{207}\text{Pb}^d$ $^{206}\text{Pb}^d$ (%)	$\pm 2\sigma$	$^{206}\text{Pb}$ $^{238}\text{U}$ (Ma)	$\pm 2\sigma$	$^{207}\text{Pb}$ $^{235}\text{U}$ (Ma)	$\pm 2\sigma$	$^{207}\text{Pb}$ $^{206}\text{Pb}$ (Ma)	$\pm 2\sigma$	conc. (%)	
A86	10064	235	24	1	0	0	1	1	2	0	2	1	572	7	593	11	674	42	85
A87	10570	398	30	1	1	0	1	1	5	0	5	0	423	5	423	17	427	108	99
A91	7957	314	20	0	0	0	2	0	2	0	2	1	398	6	398	8	396	40	101
A92	36258	759	41	0	0	0	5	1	9	0	7	1	332	17	475	34	1244	139	27
A93	9995	538	22	0	0	0	3	0	3	0	1	1	266	7	285	8	443	33	60
A94	15066	59	25	2	2	0	2	4	4	0	3	1	1632	26	1696	29	1777	55	92
A95	10450	351	19	0	0	0	1	0	2	0	1	1	330	4	338	5	397	32	83
A96	6921	297	19	0	0	0	1	0	3	0	3	0	386	5	379	9	338	58	114
A97	15463	189	18	0	0	0	12	1	13	0	6	1	568	65	730	71	1264	116	45
A98	7076	170	18	1	0	0	1	1	2	0	2	1	572	7	570	11	562	44	102
A99	19262	536	54	1	0	0	2	1	4	0	3	1	576	12	573	16	562	66	102
A100	7825	215	19	1	0	0	1	1	2	0	2	1	518	7	534	9	601	35	86
A101	8106	313	21	1	0	0	2	0	2	0	1	1	397	7	404	8	442	30	90
A102	12082	216	27	0	0	0	2	1	3	0	2	1	721	11	709	14	668	48	108
A103	7236	197	18	0	0	0	1	1	2	0	2	0	535	6	548	11	601	48	89
A104	9084	197	19	1	0	0	1	1	3	0	2	0	557	6	553	11	534	51	104
A105	2896	56	8	0	0	0	2	1	8	0	8	0	814	15	809	47	795	168	102
A106	7870	203	19	1	0	0	1	1	4	0	4	0	532	6	531	15	526	77	101
A107	9238	347	21	0	0	0	2	0	2	0	1	1	380	6	382	6	397	30	96
A108	6130	150	14	1	1	0	2	1	4	0	4	0	532	8	537	17	561	78	95
A110	20558	390	52	1	0	0	1	1	2	0	2	0	675	7	713	11	832	38	81
A111	7114	197	20	1	0	0	1	1	2	0	2	1	545	7	538	9	510	35	107

**Sample 333**

Table B.1 (continued)

grain	$^{207}\text{Pb}^a$ (cps)	$\text{U}^b$ (ppm)	$\text{Pb}^b$ (ppm)	$\text{Th}^b$ U	$^{206}\text{Pbc}^c$ (%)	$\frac{^{206}\text{Pbd}}{^{238}\text{U}}$ (%)	$\pm 2\sigma$	$\frac{^{207}\text{Pbd}}{^{235}\text{U}}$ (%)	$\pm 2\sigma$	$\frac{^{207}\text{Pbd}}{^{206}\text{Pbd}}$ (%)	$\pm 2\sigma$	$\text{rho}^e$	$\frac{^{206}\text{Pbd}}{^{238}\text{U}}$ (Ma)	$\pm 2\sigma$	$\frac{^{207}\text{Pbd}}{^{235}\text{U}}$ (Ma)	$\pm 2\sigma$	$\frac{^{207}\text{Pb}}{^{206}\text{Pb}}$ (Ma)	$\pm 2\sigma$	conc. (%)	
<b>Sample 333</b>																				
A112	31853	1017	76	1	0	0	2	1	2	0	1	1	442	7	457	8	534	30	83	
A113	14643	352	32	0	0	0	1	1	2	0	1	1	565	7	579	8	634	27	89	
A114	5407	160	9	0	0	0	2	0	7	0	6	0	317	7	316	19	305	146	104	
A115	8324	314	20	0	0	0	2	0	2	0	2	1	386	6	382	7	357	38	108	
A116	7530	297	18	0	0	0	1	0	2	0	2	0	390	4	388	7	376	45	104	
A117	9004	333	22	1	0	0	1	0	3	0	3	0	383	5	392	11	445	70	86	
A118	10192	254	30	2	0	0	1	1	2	0	2	1	525	6	529	10	548	45	96	
A119	20379	340	31	1	5	0	2	1	13	0	12	0	480	9	485	50	513	274	94	
A120	11634	199	26	1	0	0	1	1	2	0	2	1	690	8	698	12	723	44	95	
A121	11361	402	31	1	0	0	1	1	2	0	2	0	431	4	438	8	475	43	91	
A122	23880	535	49	0	0	0	1	1	2	0	2	0	564	6	574	10	615	45	92	
A123	10033	352	23	0	0	0	2	1	2	0	2	1	422	7	416	8	381	35	111	
A124	6271	260	17	1	0	0	2	0	4	0	4	0	367	8	367	14	369	88	99	
A125	12517	252	14	0	4	0	2	0	9	0	9	0	281	6	277	23	246	208	114	
A126	5962	192	14	1	0	0	1	1	2	0	2	1	426	5	429	7	443	35	96	
A127	12087	408	26	1	0	0	2	0	3	0	3	0	378	6	379	11	385	65	98	
A127c	8214	209	21	1	0	0	1	1	5	0	5	0	519	6	513	20	484	104	107	
A128	5764	184	12	0	0	0	2	0	3	0	2	1	402	7	397	9	365	50	110	
A129	14943	731	37	0	0	0	4	0	4	0	1	1	310	11	310	11	310	34	100	
A130	8191	273	16	1	0	0	2	0	3	0	2	1	339	6	337	9	323	56	105	
A131	6355	208	13	0	1	0	1	0	6	0	6	0	357	5	362	19	396	135	90	
A134	16826	592	173	1	0	0	1	6	1	0	1	1	1483	17	1962	13	2513	13	59	

Table B.1 (continued)

grain	$^{207}\text{Pb}^a$ (cps)	$\text{U}^b$ (ppm)	$\text{Pb}^b$	$\text{Th}^b$	$^{206}\text{Pbc}^c$ (%)	$\frac{^{206}\text{Pb}^d}{^{238}\text{U}}$ (%)	$\pm 2\sigma$ (%)	$\frac{^{207}\text{Pb}^d}{^{235}\text{U}}$ (%)	$\pm 2\sigma$ (%)	$\frac{^{207}\text{Pb}^d}{^{206}\text{Pb}^d}$ (%)	$\pm 2\sigma$ (%)	$\rho^e$	$\frac{^{206}\text{Pb}}{^{238}\text{U}}$ (Ma)	$\pm 2\sigma$ (Ma)	$\frac{^{207}\text{Pb}}{^{206}\text{Pb}}$ (Ma)	$\pm 2\sigma$ (Ma)	conc. (%)		
A135	5743	200	14	0	0	0	0	1	1	2	0	0	425	4	428	8	443	44	96
A136	8648	296	20	1	0	0	0	2	0	3	0	0	369	6	367	10	353	66	105
A137	27022	355	39	1	0	0	0	1	1	2	0	1	636	7	631	7	611	24	104
A138	12553	505	29	0	0	0	0	1	0	2	0	1	378	5	378	6	376	36	101
A139	4498	157	9	0	1	0	0	1	0	3	0	1	357	5	355	8	338	53	106
A140	7114	172	14	1	1	0	0	2	1	3	0	0	460	7	454	13	421	69	109
A141	6146	242	15	0	0	0	0	1	0	2	0	0	393	5	388	8	355	49	111
A142	12263	524	28	1	3	0	0	4	0	10	0	0	313	12	327	27	423	196	74
A143	3824	101	11	1	0	0	0	2	1	5	0	0	561	8	647	22	961	89	58
A144	15966	252	24	0	0	0	0	2	1	3	0	1	527	10	612	12	942	32	56
A145	96421	465	135	1	0	0	0	1	4	2	0	1	1470	18	1549	13	1660	15	89
A146	11271	277	20	1	5	0	0	1	1	10	0	0	421	5	435	37	508	222	83
A147	6307	158	15	1	0	0	0	2	1	3	0	0	494	8	485	13	441	66	112
A148	55435	305	132	0	0	0	0	2	13	2	0	1	2141	28	2664	16	3089	11	69
A149	32278	997	16	0	5	0	0	3	0	7	0	0	86	2	166	11	1535	125	6
A150	16813	205	13	0	0	0	0	2	1	3	0	1	396	9	444	9	698	26	57
A151	9132	71	10	1	0	0	0	2	1	2	0	1	775	14	773	13	768	30	101
A152	5835	95	6	0	0	0	0	2	0	3	0	1	375	6	373	10	361	60	104
A153	5656	83	6	0	0	0	0	1	0	2	0	0	410	5	408	8	398	48	103
A154	15570	177	20	0	0	0	0	1	1	2	0	1	677	7	673	8	658	25	103
A155	15649	215	115	1	0	0	0	1	10	2	0	1	2528	28	2424	19	2339	25	108
A156	97782	119	33	0	1	0	0	2	5	3	0	1	1501	34	1855	25	2279	26	66

Sample 333

Table B.1 (continued)

grain	$^{207}\text{Pb}^a$ (cps)	$\text{U}^b$ (ppm)	$\text{Pb}^b$ (ppm)	$\text{Th}^b$ U	$^{206}\text{Pbc}^c$ (%)	$\frac{^{206}\text{Pbd}^d}{^{238}\text{U}}$ $\pm 2\sigma$ (%)	$\frac{^{207}\text{Pbd}^d}{^{235}\text{U}}$ $\pm 2\sigma$ (%)	$\frac{^{207}\text{Pbd}^d}{^{206}\text{Pbd}^d}$ $\pm 2\sigma$ (%)	rho <sup>e</sup>	$\frac{^{206}\text{Pb}}{^{238}\text{U}}$ $\pm 2\sigma$ (Ma)	$\frac{^{207}\text{Pb}}{^{235}\text{U}}$ $\pm 2\sigma$ (Ma)	$\frac{^{207}\text{Pb}}{^{206}\text{Pb}}$ $\pm 2\sigma$ (Ma)	conc. (%)				
<b>Sample 333</b>																	
A169	2348	124	14	1	1	0	2	1	5	0	579	12	571	24	539	106	108
A170	10894	323	24	1	2	0	4	1	11	0	365	15	472	43	1032	211	35
A171	52528	85	48	1	44	0	12	1	48	0	625	72	902	339	1658	865	38
A172	10945	219	34	1	6	0	2	1	7	0	800	18	805	42	816	145	98
A173	44589	538	80	1	20	0	4	1	16	0	557	22	552	72	529	347	105
A174	5356	221	22	0	2	0	4	1	10	0	575	21	544	44	415	214	138
A175	2359	130	14	1	1	0	3	1	5	0	564	14	568	24	581	104	97
A176	13399	556	75	1	1	0	2	1	4	0	697	14	687	19	654	68	107
A177	8571	610	50	1	1	0	2	1	5	0	444	9	447	20	466	112	95
A178	5532	160	15	1	5	0	4	1	17	0	447	16	474	67	609	363	73
A179	7305	261	28	0	2	0	3	1	6	0	609	15	624	29	678	120	90
A180	2461	143	12	1	2	0	2	1	6	0	484	12	489	25	517	130	94
A181	81946	105	75	1	57	0	7	1	22	0	724	49	761	125	873	431	83
A182	11503	1298	254	0	0	0	2	3	3	1	1168	23	1489	25	1981	41	59
A182 c	56177	160	93	0	0	1	3	13	3	1	2721	64	2674	31	2638	24	103
A183	7161	466	33	0	0	0	2	1	3	1	439	9	441	12	450	54	97
A184	13509	254	124	1	69	0	8	1	32	0	433	34	489	134	762	660	57
A185	6613	109	18	1	11	0	3	1	12	0	721	19	669	62	500	262	144
A187	6103	424	30	0	0	0	2	1	3	0	457	10	455	12	443	53	103
A188	3105	101	11	0	1	0	4	1	7	0	624	22	630	33	651	125	96
A189	2680	87	12	0	0	0	2	1	4	0	807	17	844	24	941	71	86

Table B.1 (continued)

grain	$^{207}\text{Pb}^a$ (cps)	$\text{U}^b$ (ppm)	$\text{Pb}^b$ (ppm)	$\frac{\text{Th}^b}{\text{U}}$	$^{206}\text{Pbc}$ (%)	$\frac{^{206}\text{Pbd}}{^{238}\text{U}}$ (%)	$\pm 2\sigma$	$\frac{^{207}\text{Pbd}}{^{235}\text{U}}$	$\pm 2\sigma$ (%)	$\frac{^{207}\text{Pbd}}{^{206}\text{Pbd}}$	$\pm 2\sigma$ (%)	$\text{rho}^e$	$\frac{^{206}\text{Pbd}}{^{238}\text{U}}$ (Ma)	$\pm 2\sigma$ (Ma)	$\frac{^{207}\text{Pb}}{^{206}\text{Pb}}$	$\pm 2\sigma$ (Ma)	conc. (%)		
<b>Sample 333</b>																			
A190	27510	21	38	2	39	1	6	14	14	0	12	0	2681	124	2722	137	2753	203	97
A191	11407	610	55	1	3	0	3	1	8	0	8	0	447	12	442	30	419	173	107
A192	7726	526	42	0	1	0	2	1	5	0	5	0	454	10	441	20	369	112	123
A193	6075	426	30	0	0	0	2	1	3	0	3	1	460	10	456	12	439	57	105
A199	6547	159	34	1	1	0	3	2	5	0	4	1	948	25	937	31	911	85	104
A200	6252	393	31	0	1	0	2	1	5	0	5	0	449	10	445	18	424	101	106
A201	27510	21	39	2	37	1	5	15	13	0	12	0	2878	114	2796	129	2738	194	105
A202	5993	421	32	0	1	0	2	1	5	0	4	0	452	10	454	18	467	92	97
A203	7511	523	40	0	0	0	2	1	3	0	2	1	455	9	455	10	456	39	100
A204	17273	839	81	0	0	0	2	1	3	0	1	1	629	13	636	12	659	30	95
A205	29927	112	46	1	22	0	12	3	23	0	20	1	1120	124	1276	185	1549	376	72
A206	7863	133	38	1	2	0	3	2	5	0	4	1	1115	32	1084	37	1023	91	109
A207	29397	208	85	1	1	0	3	5	5	0	4	1	1783	55	1848	44	1922	66	93
A208	18008	512	58	1	8	0	4	1	19	0	18	0	479	18	482	75	497	406	96
A209	32688	736	80	1	13	0	3	1	9	0	8	0	498	14	501	35	515	179	97
A210	12022	216	31	2	12	0	7	1	48	0	48	0	508	32	596	243	947	973	54
A211	6967	227	33	1	1	0	3	1	4	0	3	1	791	22	783	23	761	60	104
A212	13126	1013	315	1	1	0	2	5	2	0	1	1	1529	31	1829	21	2190	16	70
A213	26122	986	108	1	4	0	3	1	7	0	6	0	569	15	581	30	628	131	91

Table B.1 (continued)

grain	$^{207}\text{Pb}^a$ (cps)	$\text{U}^b$ (ppm)	$\text{Pb}^b$ (ppm)	$\text{Th}^b$ U	$^{206}\text{Pb}^c$ U (%)	$\frac{^{206}\text{Pb}^d}{^{238}\text{U}}$ (%)	$\pm 2\sigma$ (%)	$\frac{^{207}\text{Pb}^d}{^{235}\text{U}}$ (%)	$\pm 2\sigma$ (%)	$\frac{^{207}\text{Pb}^d}{^{206}\text{Pb}^d}$ (%)	$\pm 2\sigma$ (%)	$\rho_e$	$\frac{^{206}\text{Pb}}{^{238}\text{U}}$ (Ma)	$\pm 2\sigma$ (Ma)	$\frac{^{207}\text{Pb}}{^{235}\text{U}}$ (Ma)	$\pm 2\sigma$ (Ma)	$\frac{^{207}\text{Pb}}{^{206}\text{Pb}}$ (Ma)	$\pm 2\sigma$ (Ma)	conc. (%)
<b>Sample 333B</b>																			
A147	20335	217	15	0	13	0	4	0	12	0	12	0	256	10	268	30	372	267	69
A148	78302	546	35	0	5	0	4	1	7	0	6	1	303	10	611	31	2019	99	15
A149	66986	490	51	0	17	0	4	1	13	0	13	0	361	13	746	73	2187	223	16
A150	6266	240	14	0	0	0	3	1	5	0	4	1	368	9	459	18	946	86	39
A151	5699	244	13	0	0	0	3	0	6	0	5	0	342	8	345	18	366	124	93
A152	10215	534	24	1	4	0	2	0	10	0	10	0	235	4	242	23	302	232	78
A153	35423	642	72	1	0	0	2	1	3	0	3	1	586	10	602	15	661	59	89
A154	76425	558	57	0	0	0	5	2	5	0	1	1	604	29	1066	35	2192	25	28
A155	10375	402	22	0	0	0	2	0	5	0	4	0	333	7	337	13	368	94	91
A156	27194	142	42	2	0	0	2	3	2	0	1	1	1306	19	1527	17	1848	25	71
A157	9019	126	18	1	0	0	2	1	6	0	6	0	747	16	745	35	739	129	101
A158	18004	599	55	2	0	0	2	1	3	0	2	1	428	7	451	10	571	47	75
A159	9968	298	19	1	1	0	2	0	4	0	4	0	343	6	347	12	375	83	92
A160	11178	195	25	1	1	0	2	1	3	0	3	0	708	11	726	18	782	64	91
A161	66089	429	38	0	24	0	5	0	22	0	22	0	290	14	356	69	808	453	36
A162	8313	189	10	1	4	0	3	0	14	0	14	0	272	9	268	34	235	319	116
A163	8537	129	17	1	0	0	2	1	5	0	5	0	754	12	783	30	866	109	87
A164	52197	747	48	1	13	0	3	0	13	0	13	0	288	7	326	36	605	271	48
A165	7540	264	16	1	0	0	3	0	5	0	4	1	331	9	353	15	499	96	66
A166	24517	387	28	1	12	0	2	0	13	0	13	0	338	8	339	38	342	290	99
A167	21661	400	96	0	57	0	15	1	25	0	20	1	382	57	653	128	1754	364	22
A168	14237	341	42	2	0	0	2	1	3	0	2	1	570	9	619	12	803	43	71

Table B.1 (continued)

grain	$^{207}\text{Pb}^a$ (cps)	$\text{U}^b$ (ppm)	$\text{Pb}^b$ (ppm)	$\frac{\text{Th}^b}{\text{U}}$	$^{206}\text{Pb}^c$ (%)	$\frac{^{206}\text{Pb}^d}{^{238}\text{U}}$ (%)	$\pm 2\sigma$ (%)	$\frac{^{207}\text{Pb}^d}{^{235}\text{U}}$ (%)	$\pm 2\sigma$ (%)	$\frac{^{206}\text{Pb}^d}{^{206}\text{Pb}}$ (%)	$\pm 2\sigma$ (%)	$\text{rho}^e$	$\frac{^{206}\text{Pb}}{^{238}\text{U}}$ (Ma)	$\pm 2\sigma$ (Ma)	$\frac{^{207}\text{Pb}}{^{235}\text{U}}$ (Ma)	$\pm 2\sigma$ (Ma)	$\frac{^{207}\text{Pb}}{^{206}\text{Pb}}$ (Ma)	$\pm 2\sigma$ (Ma)	conc. (%)
<b>Sample 333B</b>																			
A170	10033	236	24	1	0	0	2	1	3	0	2	1	558	10	556	13	548	49	102
A171	5110	131	11	0	0	0	2	1	3	0	2	1	484	8	495	11	544	49	89
A172	10804	412	25	1	0	0	2	0	3	0	2	1	358	7	366	8	418	38	86
A173	11974	330	23	0	0	0	2	1	2	0	1	1	448	7	446	8	439	33	102
A174	15073	1055	46	0	0	0	3	0	3	0	2	1	289	8	309	9	466	34	62
A178	5535	243	12	0	0	0	2	0	3	0	2	1	325	5	327	8	342	50	95
A179	13242	211	13	0	0	0	3	1	5	0	4	1	378	12	550	21	1346	71	28
A180	12193	536	119	3	7	0	3	1	10	0	10	0	651	17	853	62	1422	190	46
A181	13928	579	45	0	0	0	5	1	5	0	2	1	478	23	504	21	625	39	76
A182	16787	506	38	1	0	0	2	0	2	0	2	1	364	6	382	8	492	40	74
A183	6560	282	14	0	0	0	2	0	3	0	2	1	330	6	339	8	400	46	83
A184	15025	457	25	1	0	0	2	0	3	0	3	1	295	6	298	8	327	57	90
A185	18679	930	53	1	0	0	2	0	3	0	2	1	342	7	342	9	343	53	100
A186	16401	153	25	2	6	0	2	1	9	0	8	0	618	12	711	45	1015	171	61
A187	15668	547	28	0	0	0	2	0	5	0	4	0	293	6	301	12	362	94	81
A188	97529	1505	70	1	22	0	4	0	18	0	18	0	182	7	276	44	1169	348	16
A189	17214	769	45	0	0	0	2	0	4	0	3	0	356	6	355	11	345	71	103
A190	6476	286	15	0	0	0	2	0	3	0	3	1	312	6	315	9	342	59	91
A191	11072	346	79	1	5	0	2	2	6	0	6	0	950	18	978	38	1040	114	91
A192	14909	685	37	1	0	0	2	0	4	0	3	1	318	8	346	11	539	60	59
A193	44268	415	28	0	17	0	5	0	19	0	19	0	242	12	251	44	335	425	72
A194	57246	308	35	1	19	0	4	1	20	0	19	0	405	16	502	82	969	398	42

Table B.1 (continued)

grain	$^{207}\text{Pb}^a$	$\text{U}^b$	$\text{Pb}^b$	$\text{Th}^b$	$^{206}\text{Pb}^c$	$\frac{^{206}\text{Pb}^d}{^{238}\text{U}}$	$\pm 2\sigma$	$\frac{^{207}\text{Pb}^d}{^{235}\text{U}}$	$\pm 2\sigma$	$\frac{^{207}\text{Pb}^d}{^{206}\text{Pb}}$	$\pm 2\sigma$	$\text{rho}^e$	$\frac{^{206}\text{Pb}}{^{238}\text{U}}$	$\pm 2\sigma$	$\frac{^{207}\text{Pb}}{^{235}\text{U}}$	$\pm 2\sigma$	$\frac{^{207}\text{Pb}}{^{206}\text{Pb}}$	$\pm 2\sigma$	conc.	
	(cps)	(ppm)	(ppm)	U	(%)		(%)		(%)		(Ma)	(%)		(Ma)		(Ma)	(%)	(%)	(%)	
<b>Sample 333B</b>																				
A195	8096	174	11	1	2	0	2	0	17	0	17	0	348	8	383	55	595	363	59	
A196	25402	988	53	0	0	0	2	0	3	0	3	1	328	5	331	7	349	43	94	
A197	7187	268	13	0	0	0	2	0	3	0	3	1	289	5	292	8	318	58	91	
A198	26676	726	40	1	1	0	2	0	7	0	6	0	290	6	292	17	312	144	93	
A199	11320	310	26	1	0	0	2	1	3	0	3	1	469	9	463	12	435	59	108	
A200	45683	508	42	0	10	0	3	1	12	0	12	0	400	11	453	46	729	254	55	
A201	66813	444	38	0	28	0	5	0	31	0	31	0	307	14	381	104	861	636	36	
A202	14448	388	8	0	0	0	14	0	14	0	3	1	133	18	164	22	642	64	21	
A203	11096	977	105	0	0	0	2	1	2	0	1	1	664	12	925	12	1612	14	41	
A204	9329	64	7	0	19	0	3	1	15	0	15	0	411	14	426	54	509	322	81	
A205	6516	223	10	0	0	0	2	0	3	0	2	1	253	4	253	6	252	52	100	
A206	11846	262	18	0	2	0	2	0	11	0	11	0	399	9	392	38	348	252	115	
A207	11012	525	313	0	81	0	475	0	476	0	42	1	43	206	186	1622	2971	671	1	
A208	39712	328	26	1	19	0	4	0	16	0	15	0	305	12	344	48	618	334	49	
A209	23417	278	73	1	39	0	38	1	53	0	36	1	210	80	510	237	2260	627	9	
A210	12189	211	19	1	2	0	2	1	8	0	7	0	454	10	429	27	293	169	155	
A211	9662	81	11	1	7	0	3	1	15	0	14	0	646	17	603	69	441	322	147	
A212	61933	641	42	0	15	0	3	0	14	0	14	0	287	8	283	35	251	312	114	
A213	11743	239	22	1	0	0	3	1	5	0	4	1	528	14	451	19	73	103	720	
A214	16595	227	28	1	0	0	2	1	3	0	2	1	626	13	636	15	672	49	93	

Table B.1 (continued)

grain	$^{207}\text{Pb}^a$ (cps)	$\text{U}^b$ (ppm)	$\text{Pb}^b$ (ppm)	$\frac{\text{Th}^b}{\text{U}}$	$^{206}\text{Pb}^c$ (%)	$\frac{^{206}\text{Pb}^d}{^{238}\text{U}}$ (%)	$\pm 2\sigma$ (%)	$\frac{^{207}\text{Pb}^d}{^{235}\text{U}}$	$\pm 2\sigma$ (%)	$\frac{^{207}\text{Pb}^d}{^{206}\text{Pb}^d}$ (%)	$\pm 2\sigma$ (%)	$\text{rho}^e$	$\frac{^{206}\text{Pb}}{^{238}\text{U}}$ (Ma)	$\pm 2\sigma$ (Ma)	$\frac{^{207}\text{Pb}}{^{235}\text{U}}$ (Ma)	$\pm 2\sigma$ (Ma)	$\frac{^{207}\text{Pb}}{^{206}\text{Pb}}$	$\pm 2\sigma$ (Ma)	conc. (%)
<b>Sample 333B</b>																			
A215	11574	355	18	0	1	0	2	0	3	0	3	1	304	5	305	8	314	59	97
A217	8743	167	14	1	0	0	2	1	5	0	4	0	482	9	482	18	481	92	100
A218	15822	473	23	0	0	0	2	0	7	0	7	0	281	6	345	21	803	138	35
A219	37087	402	27	0	14	0	3	0	16	0	15	0	300	9	310	43	385	346	78
A220	6424	134	7	0	1	0	3	0	14	0	14	0	285	9	340	43	735	297	39
A392	3989	194	14	0	0	0	2	1	3	0	3	1	444	6	453	11	501	55	89
A393	3189	129	14	0	1	0	2	1	3	0	3	0	631	9	642	15	681	57	93
A394	8199	300	39	1	0	0	2	1	3	0	2	1	644	11	700	14	882	40	73
A395	8574	319	34	0	0	0	2	1	2	0	2	1	669	10	673	12	687	38	97
A396	3088	130	11	0	3	0	2	1	7	0	7	0	470	7	477	28	510	153	92
A397	2901	165	15	0	2	0	2	1	5	0	5	0	544	8	547	22	561	109	97
A399	4198	280	20	0	0	0	2	1	3	0	2	1	459	7	445	10	372	50	123
A400	3341	212	16	0	0	0	1	1	3	0	2	1	475	7	474	10	471	48	101
A401	5137	332	26	1	0	0	1	1	3	0	2	1	456	7	473	10	556	47	82
A402	6073	268	36	2	2	0	2	1	6	0	6	0	632	9	615	28	551	128	115
A403	3654	113	17	1	0	0	2	1	3	0	2	1	810	12	834	16	897	47	90
A404	4185	288	21	0	0	0	2	1	3	0	2	1	469	7	471	10	483	49	97
A405	4762	238	19	1	2	0	2	1	6	0	6	0	453	7	448	22	422	129	107
A406	2734	174	13	0	0	0	2	1	4	0	3	0	465	7	461	13	444	72	105
A407	3849	225	17	0	0	0	2	1	3	0	3	1	457	8	448	12	401	62	114
A408	2476	147	11	0	1	0	2	1	4	0	4	0	478	8	479	17	484	92	99
A409	4247	279	20	0	0	0	2	1	3	0	2	1	455	7	454	10	450	48	101

Table B.1 (continued)

grain	$^{207}\text{Pb}^a$ (cps)	$\text{U}^b$ (ppm)	$\text{Pb}^b$ (ppm)	$\text{Th}^b$ U	$^{206}\text{Pb}^c$ (%)	$\frac{^{206}\text{Pb}^d}{^{238}\text{U}}$ (%)	$\pm 2\sigma$ (%)	$\frac{^{207}\text{Pb}^d}{^{235}\text{U}}$ (%)	$\pm 2\sigma$ (%)	$\frac{^{207}\text{Pb}^d}{^{206}\text{Pb}}$ (%)	$\pm 2\sigma$ (%)	$\text{rho}^e$	$\frac{^{206}\text{Pb}}{^{238}\text{U}}$ (Ma)	$\pm 2\sigma$ (Ma)	$\frac{^{207}\text{Pb}}{^{206}\text{Pb}}$ (Ma)	$\pm 2\sigma$ (Ma)	conc. (%)	
<b>Sample 333B</b>																		
A412	3752	134	11	1	9	0	2	1	14	0	14	0	455	9	467	54	527	86
A413	3977	256	18	0	0	0	2	1	3	0	2	1	449	7	445	10	425	106
A414	4366	205	20	1	0	0	2	1	3	0	2	1	499	9	545	12	742	67
A415	2899	164	13	1	3	0	2	1	7	0	7	0	441	7	440	27	435	101
A416	3285	197	15	1	0	0	2	1	3	0	3	0	459	7	463	12	487	94
A417	7386	309	32	0	0	0	1	1	2	0	2	1	632	9	627	11	610	103
A418	4573	109	18	1	0	0	2	1	3	0	2	1	907	13	922	17	958	95
A419	2286	112	9	1	2	0	2	1	7	0	7	0	470	9	469	29	468	100
A420	3908	246	16	0	2	0	2	0	6	0	6	0	391	6	405	21	488	80
A421	2772	105	14	2	0	0	2	1	6	0	6	0	594	10	597	28	607	98
A422	2830	161	14	0	0	0	2	1	4	0	3	0	525	8	524	15	515	102
A423	30204	280	97	1	0	0	2	5	2	0	1	1	1629	23	1734	16	1863	87
A424	86325	214	147	1	0	1	2	17	2	0	1	1	2873	36	2960	18	3020	95
A425	9193	225	41	1	0	0	2	2	3	0	2	1	1016	19	1011	19	1002	101
A426	8796	395	53	2	1	0	2	1	4	0	4	0	564	9	606	20	768	73
A427	3688	145	19	1	0	0	3	1	4	0	3	1	742	19	783	24	899	83
A428	3193	207	15	0	0	0	1	1	3	0	3	0	469	7	462	12	426	110
A429	2933	161	13	1	0	0	2	1	4	0	4	0	495	7	530	17	684	72
A430	4747	225	22	1	0	0	2	1	3	0	3	0	517	8	546	14	668	77
A431	2438	126	10	0	2	0	2	1	6	0	6	0	509	7	506	24	495	103
A432	4804	324	23	0	0	0	1	1	3	0	2	1	445	6	444	10	441	101
A433	3068	159	13	1	0	0	2	1	6	0	6	0	484	11	485	25	490	99

Table B.1 (continued)

grain	$^{207}\text{Pb}^a$ (cps)	$\text{U}^b$ (ppm)	$\text{Pb}^b$ (ppm)	$\frac{\text{Th}^b}{\text{U}}$	$^{206}\text{Pbc}^c$ (%)	$\frac{^{206}\text{Pbd}}{^{238}\text{U}}$ (%)	$\pm 2\sigma$ (%)	$\frac{^{207}\text{Pbd}}{^{235}\text{U}}$	$\pm 2\sigma$ (%)	$\frac{^{207}\text{Pbd}}{^{206}\text{Pbd}}$	$\pm 2\sigma$ (%)	$\text{rho}^e$	$\frac{^{206}\text{Pbd}}{^{238}\text{U}}$	$\pm 2\sigma$ (Ma)	$\frac{^{207}\text{Pbd}}{^{235}\text{U}}$	$\pm 2\sigma$ (Ma)	$\frac{^{207}\text{Pb}}{^{206}\text{Pb}}$	$\pm 2\sigma$ (Ma)	conc. (%)
<b>Sample 333B</b>																			
A434	4889	226	23	0	0	0	2	1	3	0	2	1	613	9	611	13	604	50	101
A435	3916	255	19	0	0	1	1	1	3	0	2	1	452	6	467	10	541	46	84
A436	3046	189	14	0	0	2	1	1	4	0	3	0	470	7	484	15	549	76	86
A437	4308	251	22	0	0	2	1	1	3	0	2	1	537	8	530	11	500	51	107
A438	4790	274	19	0	1	1	1	1	4	0	3	0	442	6	448	14	482	75	92
A444	4333	232	19	0	0	2	1	1	3	0	3	1	514	8	509	12	485	56	106
A445	6953	297	26	0	0	2	1	1	3	0	2	1	504	8	557	12	780	46	65
A446	6555	217	31	1	0	2	1	1	2	0	2	1	755	11	756	13	756	41	100
A447	3575	213	16	0	0	2	1	1	3	0	3	0	461	7	496	13	661	64	70
A448	21074	127	51	1	0	2	2	6	2	0	1	1	1926	27	1988	18	2052	21	94
A449	3027	176	12	0	0	2	1	1	3	0	2	1	447	7	457	11	506	55	88
A450	6110	208	26	1	0	1	1	1	2	0	2	1	742	10	761	12	817	38	91
A451	4302	278	22	1	1	2	1	1	3	0	2	1	486	8	484	11	479	54	101
A452	3352	115	14	1	2	0	2	1	6	0	6	0	620	11	616	30	603	131	103
A453	10453	362	49	1	0	2	1	1	2	0	2	1	760	12	750	12	722	34	105
A454	4777	297	23	1	1	2	1	1	4	0	3	0	433	6	430	13	418	75	104
A455	3285	176	14	1	0	2	1	1	5	0	4	0	460	8	466	17	492	94	94
A456	15996	771	77	1	0	1	1	1	2	0	1	1	575	8	591	8	655	25	88
A457	3099	196	14	0	0	2	1	1	3	0	3	0	453	7	470	12	552	61	82
A458	2838	89	9	1	0	2	1	1	4	0	3	1	515	12	562	17	756	63	68
A459	3059	163	13	1	1	2	1	1	5	0	4	0	464	8	494	18	631	91	74
A460	5845	377	26	0	0	2	1	1	3	0	3	0	428	7	430	12	439	68	97

Table B.1 (continued)

grain	$^{207}\text{Pb}^a$ (cps)	$\text{U}^b$ (ppm)	$\text{Pb}^b$ (ppm)	$\text{Th}^b$ U	$^{206}\text{Pb}^c$ (%)	$\frac{^{206}\text{Pb}^d}{^{238}\text{U}}$ (%)	$\pm 2\sigma$ (%)	$\frac{^{207}\text{Pb}^d}{^{235}\text{U}}$ (%)	$\pm 2\sigma$ (%)	$\frac{^{207}\text{Pb}^d}{^{206}\text{Pb}}$ (%)	$\pm 2\sigma$ (%)	rho <sup>e</sup>	$\frac{^{206}\text{Pb}}{^{238}\text{U}}$ (Ma)	$\pm 2\sigma$ (Ma)	$\frac{^{207}\text{Pb}}{^{206}\text{Pb}}$ (Ma)	$\pm 2\sigma$ (Ma)	conc. (%)		
<b>Sample 333B</b>																			
A461	3749	225	18	0	0	0	2	1	3	0	2	1	510	8	528	11	609	47	84
A462	6565	363	31	0	1	0	1	1	3	0	3	0	534	7	540	13	562	57	95
A463	3466	176	14	1	2	0	2	1	8	0	8	0	446	7	453	29	486	171	92
A464	3682	225	15	0	0	0	1	1	4	0	3	0	438	6	442	13	463	74	95
A465	4042	213	19	1	0	0	2	1	3	0	3	0	508	7	520	14	573	65	89
A466	9127	275	37	0	0	0	1	1	2	0	2	1	816	11	815	12	812	34	100
A467	14968	685	68	1	0	0	1	1	2	0	1	1	581	8	596	9	653	31	89
A468	3549	147	14	0	1	0	2	1	4	0	4	0	597	12	590	20	561	84	106
A469	4625	158	22	1	0	0	2	1	2	0	2	1	753	11	753	13	751	40	100
A470	54851	299	153	2	0	0	2	7	2	0	1	1	2056	28	2077	17	2099	17	98
A471	7339	494	32	0	1	0	2	1	4	0	4	0	431	6	430	15	421	88	102
A472	3137	196	15	0	1	0	2	1	4	0	4	0	451	7	456	16	481	85	94
A473	2417	137	11	1	3	0	2	1	8	0	7	0	485	9	509	31	616	157	79
A474	4492	218	24	0	0	0	2	1	3	0	2	1	674	10	727	14	894	46	75
A475	6610	654	33	1	0	0	2	0	3	0	2	1	308	5	307	7	298	53	103
A476	4622	259	20	0	0	0	2	1	3	0	2	1	466	7	481	10	554	48	84
A477	3545	229	17	0	0	0	2	1	2	0	2	1	471	7	471	9	472	41	100
A478	5309	365	27	0	0	0	1	1	3	0	2	1	475	7	469	9	439	45	108
A480	3999	260	18	0	3	0	1	1	8	0	7	0	434	6	434	27	433	166	100
A481	16455	678	58	0	1	0	2	1	3	0	2	1	529	8	517	11	466	45	114
A482	4503	210	24	1	1	0	2	1	5	0	5	0	571	9	574	23	586	107	97
A483	11995	428	201	0	0	0	2	10	2	0	1	1	2316	31	2436	16	2539	11	91

Table B.1 (continued)

grain	$^{207}\text{Pb}^a$ (cps)	$\text{U}^b$ (ppm)	$\text{Pb}^b$ (ppm)	$\frac{\text{Th}^b}{\text{U}}$	$^{206}\text{Pb}^c$ (%)	$\frac{^{206}\text{Pb}^d}{^{238}\text{U}}$ (%)	$\pm 2\sigma$	$\frac{^{207}\text{Pb}^d}{^{235}\text{U}}$ (%)	$\pm 2\sigma$	$\frac{^{207}\text{Pb}^d}{^{206}\text{Pb}^d}$ (%)	$\pm 2\sigma$	$\rho^e$	$\frac{^{206}\text{Pb}}{^{238}\text{U}}$ (%)	$\pm 2\sigma$	$\frac{^{207}\text{Pb}}{^{235}\text{U}}$ (Ma)	$\pm 2\sigma$	$\frac{^{207}\text{Pb}}{^{206}\text{Pb}}$ (Ma)	$\pm 2\sigma$	conc. (%)
<b>Sample 333B</b>																			
A485	2705	159	11	0	1	0	2	1	5	0	4	0	436	7	441	17	468	98	93
A486	5157	265	24	1	0	0	2	1	6	0	5	0	476	9	528	24	760	113	63
A487	8719	276	27	1	0	0	3	1	4	0	2	1	497	14	586	16	947	41	53
A488	7452	369	33	1	0	0	2	1	2	0	2	1	540	8	556	9	620	33	87
A489	5175	148	22	1	0	0	2	1	3	0	2	1	842	13	830	16	800	49	105
A490	4958	149	23	1	1	0	2	1	3	0	2	1	771	12	762	16	734	50	105
A491	5080	192	21	0	0	0	2	1	3	0	2	1	662	10	674	14	714	49	93
A492	7803	150	23	2	8	0	2	1	12	0	12	0	553	10	565	53	615	254	90
A493	1760	55	8	2	2	0	2	1	9	0	9	0	636	13	648	45	691	189	92
A499	2546	104	12	1	0	0	2	1	4	0	4	0	630	11	642	20	687	77	92
A500	53369	165	88	0	0	0	2	12	2	0	1	1	2582	33	2624	16	2656	11	97
A501	5504	121	23	1	0	0	1	2	3	0	3	0	931	12	976	22	1081	63	86
A502	4469	289	22	1	0	0	2	1	4	0	3	0	436	7	440	13	462	70	94
A503	5452	358	24	0	0	0	2	1	3	0	2	1	447	7	451	10	471	51	95
A504	45282	305	111	1	0	0	1	5	2	0	1	1	1856	24	1900	15	1948	17	95
A505	4876	191	22	1	0	0	1	1	3	0	3	0	639	9	665	17	755	64	85
A507	5056	322	19	0	4	0	2	0	10	0	9	0	378	7	395	32	497	207	76
A508	7281	394	33	1	1	0	2	1	3	0	3	1	489	8	503	13	565	62	87
A509	5917	191	23	0	0	0	2	1	2	0	2	1	735	11	730	13	718	40	102
A510	3536	158	16	1	0	0	2	1	3	0	2	1	598	10	598	13	599	49	100

Table B.2 List of  $\epsilon_{\text{Hf}}$  values of different zircon grains.

Sample/spot number	$^{176}\text{Yb}/^{177}\text{Hf}$ <sub>a</sub>	$\pm 2\sigma$	$^{176}\text{Lu}/^{177}\text{Hf}$ <sub>a</sub>	$\pm 2\sigma$	$^{178}\text{Hf}/^{177}\text{Hf}$	$^{180}\text{Hf}/^{177}\text{Hf}$	$\text{Sig}_{\text{b}}^{\text{Hf}}$ (V)	$^{176}\text{Hf}/^{177}\text{Hf}$	$\pm 2\sigma$	$^{176}\text{Hf}/^{177}\text{Hf}_{(0)}$	$\epsilon_{\text{Hf}}(t)$ <sub>d</sub>	$\pm 2\sigma$	$T_{\text{DM}}$ <sub>e</sub> (Ga)	age <sup>f</sup> (Ma)	$\pm 2\sigma$
331_72	0.0	0	0.00044	0	0.00154	0.00324	15	0.281174	0	0.281157	-11.6	0.7	3.01	2035	9
331_73	0.0	0	0.00033	0	0.00139	0.00341	12	0.281223	0	0.281211	-12.9	0.7	2.96	1897	9
331_75	0.0	0	0.00093	0	0.00136	0.00364	12	0.282243	0	0.282233	-6.2	0.7	1.53	598	9
331_76	0.0	0	0.00136	0	0.00112	0.00337	15	0.282339	0	0.282326	-5.3	0.9	1.39	489	9
331_77	0.1	0	0.00182	0	0.00185	0.00409	9	0.282600	0	0.282576	7.9	0.9	0.82	685	9
331_78	0.0	0	0.00121	0	0.00125	0.00255	14	0.281871	0	0.281851	-13.2	0.7	2.15	886	9
331_80	0.0	0	0.00033	0	0.00153	0.00397	10	0.281582	0	0.281571	-1.0	1.0	2.28	1858	9
331_81	0.0	0	0.00089	0	0.00123	0.00275	11	0.281927	0	0.281910	-8.1	0.8	1.98	1021	9
331_82	0.0	0	0.00054	0	0.00128	0.00405	11	0.281035	0	0.281009	-5.5	0.9	3.07	2524	9
331_83	0.0	0	0.00117	0	0.00137	0.00317	12	0.282442	0	0.282422	7.5	0.8	1.03	908	9
331_85	0.0	0	0.00015	0	0.00116	0.00279	15	0.280884	0	0.280877	-11.6	0.8	3.36	2463	9
331_85	0.0	0	0.00015	0	0.00116	0.00279	15	0.280884	0	0.280883	-57.1	0.8	4.14	457	9
331_88	0.0	0	0.00098	0	0.00144	0.00362	13	0.282152	0	0.282135	-2.7	0.7	1.59	909	9
331_90	0.0	0	0.00041	0	0.00146	0.00337	14	0.282496	0	0.282490	5.8	0.9	0.98	724	9
331_91	0.0	0	0.00048	0	0.00139	0.00340	12	0.281218	0	0.281201	-14.2	0.8	3.00	1853	9
331_93	0.0	0	0.00083	0	0.00117	0.00390	12	0.282612	0	0.282600	10.8	0.8	0.74	776	9
331_94	0.0	0	0.00092	0	0.00131	0.00348	13	0.282393	0	0.282388	-7.3	0.7	1.35	302	9
331_95	0.0	0	0.00120	0	0.00145	0.00335	13	0.282622	0	0.282614	2.3	1.0	0.88	374	9
331_96	0.0	0	0.00061	0	0.00157	0.00366	12	0.282287	0	0.282275	4.4	1.0	1.28	1001	9
331_97	0.0	0	0.00148	0	0.00148	0.00393	11	0.282369	0	0.282357	-5.4	0.7	1.35	439	9
331_98	0.1	0	0.00201	0	0.00168	0.00320	11	0.282592	0	0.282562	9.7	0.9	0.81	788	9

Table B.2 (continued)

Sample/spot number	$^{176}\text{Yb}/^{177}\text{Hf}$ a	$\pm 2\sigma$	$^{176}\text{Lu}/^{177}\text{Hf}$ a	$\pm 2\sigma$	$^{179}\text{Hf}/^{177}\text{Hf}$	$^{180}\text{Hf}/^{177}\text{Hf}$	Sig <sub>b</sub> $^{176}\text{Hf}/^{177}\text{Hf}$ (V)	$\pm 2\sigma^c$	$^{176}\text{Hf}/^{177}\text{Hf}$	$\pm 2\sigma^c$	$^{176}\text{Hf}/^{177}\text{Hf}_{(0)}$	$\epsilon\text{Hf}(t)$ d	$\pm 2\sigma^c$	$T_{\text{DM}}$ e (Ga)	age <sup>f</sup> (Ma)	$\pm 2\sigma$
331_99	0.0	0	0.00068	0	0.00125	0.00337	13	0.281031	0	0.280999	-6.1	1.0	3.09	2516	9	
331_111	0.0	0	0.00073	0	0.00145	0.00337	12	0.281221	0	0.281184	3.9	0.8	2.66	2659	9	
331_114	0.0	0	0.00035	0	0.00155	0.00453	12	0.281977	0	0.281973	-14.2	0.6	2.01	650	9	
331_115	0.0	0	0.00097	0	0.00100	0.00290	15	0.281146	0	0.281098	-0.9	0.7	2.87	2585	9	
331_118	0.0	0	0.00018	0	0.00146	0.00322	18	0.281219	0	0.281212	-10.0	0.8	2.91	2020	9	
331_120	0.1	0	0.00167	0	0.00099	0.00362	16	0.282368	0	0.282354	-5.2	0.8	1.36	449	9	
331_old122	0.1	0	0.00191	0	0.00143	0.00377	13	0.281842	0	0.281822	-21.9	0.8	2.34	547	9	
331_old124	0.0	0	0.00106	0	0.00164	0.00327	11	0.282353	0	0.282346	-7.0	0.8	1.40	384	9	
331_old126	0.0	0	0.00094	0	0.00112	0.00252	13	0.282413	0	0.282406	-4.5	0.7	1.27	402	9	
331_old140	0.0	0	0.00099	0	0.00150	0.00260	12	0.282411	0	0.282403	-4.9	0.6	1.29	386	9	
331_old142	0.1	0	0.00163	0	0.00144	0.00430	14	0.282434	0	0.282422	-3.6	0.8	1.24	415	9	
331_old148	0.0	0	0.00156	0	0.00126	0.00355	13	0.282424	0	0.282413	-4.4	0.9	1.26	394	9	
331_old149	0.0	0	0.00039	0	0.00167	0.00441	13	0.282245	0	0.282241	-6.3	0.7	1.52	580	9	
331_old153	0.0	0	0.00086	0	0.00153	0.00405	16	0.281746	0	0.281737	-23.6	1.0	2.48	604	9	
331_old156	0.1	0	0.00215	0	0.00147	0.00355	13	0.282436	0	0.282419	-3.8	0.8	1.24	412	9	
331_old158	0.0	0	0.00127	0	0.00153	0.00349	14	0.282395	0	0.282384	-3.8	0.8	1.29	467	9	
331_old160	0.1	0	0.00196	0	0.00154	0.00414	12	0.282391	0	0.282374	-4.2	0.9	1.31	466	9	
331_old161	0.0	0	0.00095	0	0.00156	0.00385	12	0.282374	0	0.282367	-5.3	1.0	1.34	427	9	
331_old162	0.0	0	0.00068	0	0.00167	0.00321	9	0.282265	0	0.282255	-1.7	0.8	1.42	763	9	
331_old163	0.0	0	0.00138	0	0.00191	0.00389	14	0.282397	0	0.282348	27.2	0.9	0.72	1885	9	
331_old165	0.1	0	0.00220	0	0.00170	0.00360	11	0.282275	0	0.282239	-0.3	0.8	1.41	850	9	

Table B.2 (continued)

Sample/spot number	$^{176}\text{Yb}/^{177}\text{Hf}$ <sub>a</sub>	$\pm 2\sigma$	$^{176}\text{Lu}/^{177}\text{Hf}$ <sub>a</sub>	$\pm 2\sigma$	$^{176}\text{Hf}/^{177}\text{Hf}$	$^{180}\text{Hf}/^{177}\text{Hf}$	$\text{Sig}_{\text{b}}^{\text{Hf}}$ (V)	$^{176}\text{Hf}/^{177}\text{Hf}$	$\pm 2\sigma^c$	$^{176}\text{Hf}/^{177}\text{Hf}_{(t)}$	$\epsilon\text{Hf}(t)$	$\pm 2\sigma^c$	$T_{\text{DM}_e}$ (Ga)	age <sup>f</sup> (Ma)	$\pm 2\sigma$
331_old167	0.1	0	0.00164	0	0.00181	0.00527	12	0.282147	0	0.282138	-16.7	1.1	1.84	279	9
331_old169	0.0	0	0.00023	0	0.00164	0.00326	12	0.282191	0	0.282188	-5.6	0.7	1.58	693	9
331_old170	0.0	0	0.00138	0	0.00123	0.00312	14	0.282261	0	0.282243	-3.0	0.8	1.46	725	9
331_old171	0.0	0	0.00069	0	0.00191	0.00495	11	0.281092	0	0.281060	-5.5	0.9	3.01	2448	9
331_old174	0.1	0	0.00188	0	0.00190	0.00295	12	0.282677	0	0.282657	8.3	0.9	0.71	575	9
331_old181	0.1	0	0.00151	0	0.00175	0.00382	11	0.282470	0	0.282461	-4.7	0.9	1.21	303	9
333B_old165	0.0	0	0.00143	0	0.00124	0.00363	13	0.282356	0	0.282340	-2.3	0.7	1.32	600	9
331_old187	0.0	0	0.00136	0	0.00239	0.00678	13	0.282247	0	0.282207	14.4	0.8	1.17	1546	9
331_old187	0.0	0	0.00029	0	0.00206	0.00344	11	0.281252	0	0.281249	-41.0	0.8	3.41	600	9
331_old193	0.0	0	0.00077	0	0.00142	0.00454	11	0.281025	0	0.280985	-2.3	0.9	3.04	2696	9
331_old198	0.0	0	0.00071	0	0.00187	0.00428	9	0.282491	0	0.282483	1.2	0.9	1.07	532	9
331_old199	0.0	0	0.00073	0	0.00122	0.00290	17	0.281635	0	0.281630	-32.2	0.8	2.77	388	9
331_old200	0.0	0	0.00092	0	0.00247	0.00680	12	0.282323	0	0.282317	-8.1	1.0	1.46	381	9
331_old203	0.1	0	0.00166	0	0.00158	0.00394	12	0.282443	0	0.282430	-3.5	0.8	1.23	405	9
331_old204	0.0	0	0.00105	0	0.00143	0.00323	12	0.282363	0	0.282355	-6.5	0.8	1.38	389	9
332_6	0.1	0	0.00228	0	0.00151	0.00280	12	0.282410	0	0.282390	-3.5	0.9	1.28	472	9
332_8	0.1	0	0.00172	0	0.00147	0.00302	13	0.282424	0	0.282410	-3.6	0.9	1.25	433	9
332_9	0.0	0	0.00102	0	0.00117	0.00275	10	0.281797	0	0.281779	-15.0	0.8	2.28	923	9
332_10	0.0	0	0.00059	0	0.00160	0.00270	9	0.281503	0	0.281492	-23.9	0.8	2.81	975	9
332_11	0.1	0	0.00153	0	0.00122	0.00371	13	0.282304	0	0.282288	-5.0	0.8	1.44	565	9

Table B.2 (continued)

Sample/spot number	$^{176}\text{Yb}/^{177}\text{Hf}$ <sub>a</sub>	$\pm 2\sigma$	$^{176}\text{Lu}/^{177}\text{Hf}$ <sub>a</sub>	$\pm 2\sigma$	$^{178}\text{Hf}/^{177}\text{Hf}$	$\pm 2\sigma$	$^{180}\text{Hf}/^{177}\text{Hf}$	$\text{Sig}_b^{\text{Hf}}$	$^{176}\text{Hf}/^{177}\text{Hf}$	$\pm 2\sigma^c$	$^{176}\text{Hf}/^{177}\text{Hf}_{(t)}$	$\epsilon\text{Hf}(t)$	$\pm 2\sigma^c$	$T_{\text{DM}}$ <sub>e</sub>	age <sup>f</sup>	$\pm 2\sigma$
								(V)						(Ga)	(Ma)	
332_12	0.1	0	0.00215	0	0.00130	0.00336	13	0.282314	0	0.282295	-7.2	0.8	0.8	1.47	453	9
332_13	0.0	0	0.00054	0	0.00160	0.00342	12	0.281769	0	0.281748	10.3	0.8	0.8	1.83	2076	9
332_15	0.0	0	0.00040	0	0.00135	0.00312	11	0.281500	0	0.281484	1.6	0.9	0.9	2.34	2103	9
332_16	0.0	0	0.00114	0	0.00180	0.00441	10	0.282385	0	0.282375	-4.2	0.8	0.8	1.31	461	9
332_17	0.0	0	0.00109	0	0.00148	0.00459	10	0.282367	0	0.282357	-4.5	1.0	1.0	1.34	476	9
332_18	0.1	0	0.00194	0	0.00137	0.00320	11	0.282415	0	0.282398	-3.2	0.7	0.7	1.26	470	9
332_19	0.0	0	0.00076	0	0.00162	0.00433	10	0.282437	0	0.282428	1.6	0.8	0.8	1.13	638	9
332_20	0.0	0	0.00105	0	0.00144	0.00366	13	0.282386	0	0.282377	-4.3	0.7	0.7	1.31	457	9
332_21	0.0	0	0.00102	0	0.00159	0.00372	11	0.281172	0	0.281160	-43.7	1.0	1.0	3.57	618	9
332_22	0.0	0	0.00145	0	0.00152	0.00343	12	0.282417	0	0.282406	-3.8	0.9	0.9	1.26	434	9
332_23	0.1	0	0.00198	0	0.00183	0.00381	11	0.282395	0	0.282377	-3.4	0.9	0.9	1.29	497	9
332_24	0.0	0	0.00123	0	0.00130	0.00412	11	0.282593	0	0.282581	3.8	0.9	0.9	0.89	494	9
332_26	0.0	0	0.00070	0	0.00180	0.00383	10	0.282489	0	0.282478	7.2	0.7	0.7	0.96	806	9
332_27	0.0	0	0.00097	0	0.00168	0.00437	9	0.281722	0	0.281703	-15.0	1.0	1.0	2.38	1038	9
332_29	0.0	0	0.00109	0	0.00164	0.00375	12	0.282455	0	0.282446	-1.9	0.7	0.7	1.18	451	9
332_30	0.0	0	0.00124	0	0.00139	0.00310	11	0.282505	0	0.282486	6.9	1.0	1.0	0.96	781	9
332_31	0.0	0	0.00057	0	0.00172	0.00388	10	0.281330	0	0.281309	-7.7	1.0	1.0	2.74	1970	9
332_39	0.1	0	0.00174	0	0.00163	0.00370	10	0.282415	0	0.282350	29.8	1.0	1.0	0.66	1992	9
332_41	0.0	0	0.00083	0	0.00200	0.00447	10	0.282440	0	0.282430	1.8	0.8	0.8	1.13	642	9
332_44	0.1	0	0.00152	0	0.00152	0.00430	8	0.282097	0	0.282081	-12.8	0.7	0.7	1.85	545	9

Table B.2 (continued)

Sample/spot number	$^{176}\text{Yb}/^{177}\text{Hf}$ <sub>a</sub>	$\pm 2\sigma$	$^{176}\text{Lu}/^{177}\text{Hf}$ <sub>a</sub>	$\pm 2\sigma$	$^{178}\text{Hf}/^{177}\text{Hf}$	$^{180}\text{Hf}/^{177}\text{Hf}$	$^{176}\text{Hf}/^{177}\text{Hf}$	Sig <sub>b</sub> <sup>Hf</sup>	$\pm 2\sigma^c$	$^{176}\text{Hf}/^{177}\text{Hf}$ <sub>(t)</sub>	$\epsilon\text{Hf}(t)$ <sub>d</sub>	$T_{\text{DM}}$ <sub>e</sub>	age <sup>f</sup>	$\pm 2\sigma$
							(V)			(Ga)	(Ma)	(Ga)	(Ma)	
332_45	0.0	0	0.00089	0	0.00130	0.00363	12	0.281994	0	0.281977	-6.9	1.87	970	9
332_46	0.0	0	0.00126	0	0.00140	0.00319	11	0.282386	0	0.282375	-3.9	1.30	477	9
332_47	0.0	0	0.00098	0	0.00141	0.00320	14	0.282386	0	0.282378	-4.6	1.31	439	9
332_48	0.0	0	0.00095	0	0.00165	0.00406	9	0.282282	0	0.282271	-4.2	1.44	626	9
332_50	0.1	0	0.00231	0	0.00138	0.00276	14	0.282474	0	0.282454	-1.4	1.16	463	9
332_52	0.0	0	0.00077	0	0.00113	0.00363	14	0.282416	0	0.282404	4.5	1.11	802	9
332_53	0.1	0	0.00191	0	0.00154	0.00380	13	0.282357	0	0.282341	-5.6	1.38	452	9
332_54	0.0	0	0.00068	0	0.00101	0.00320	15	0.282285	0	0.282278	-4.7	1.45	592	9
332_55	0.0	0	0.00028	0	0.00163	0.00397	12	0.281143	0	0.281129	-0.5	2.82	2557	9
332_57	0.0	0	0.00083	0	0.00133	0.00404	13	0.282219	0	0.282209	-6.4	1.56	627	9
332_58	0.0	0	0.00084	0	0.00130	0.00386	11	0.282143	0	0.282127	-0.7	1.57	1006	9
332_59	0.0	0	0.00070	0	0.00116	0.00319	13	0.281464	0	0.281441	-8.8	2.59	1720	9
332_60	0.0	0	0.00088	0	0.00171	0.00424	10	0.282456	0	0.282449	-2.5	1.18	420	9
332_61	0.0	0	0.00053	0	0.00146	0.00365	12	0.280783	0	0.280758	-15.4	3.58	2483	9
332_62	0.0	0	0.00116	0	0.00212	0.00604	13	0.282369	0	0.282352	1.3	1.24	744	9
332_72	0.0	0	0.00124	0	0.00125	0.00278	15	0.282394	0	0.282383	-3.6	1.29	476	9
332_74	0.1	0	0.00160	0	0.00137	0.00271	13	0.282409	0	0.282396	-3.7	1.27	451	9
333B_old152	0.1	0	0.00275	0	0.00158	0.00379	10	0.282470	0	0.282439	1.1	1.13	600	9
333_172	0.0	0	0.00058	0	0.00121	0.00274	15	0.282572	0	0.282563	10.0	0.7	800	9
333_176	0.0	0	0.00116	0	0.00181	0.00370	18	0.282234	0	0.282218	-4.5	1.52	697	9

Table B.2 (continued)

Sample/spot number	$^{176}\text{Yb}/^{177}\text{Hf}$ <sub>a</sub>	$\pm 2\sigma$	$^{176}\text{Lu}/^{177}\text{Hf}$ <sub>a</sub>	$\pm 2\sigma$	$^{176}\text{Hf}/^{177}\text{Hf}$	$^{180}\text{Hf}/^{177}\text{Hf}$	Sig <sub>b</sub> <sup>Hf</sup>	$^{176}\text{Hf}/^{177}\text{Hf}$	$\pm 2\sigma^c$	$^{176}\text{Hf}/^{177}\text{Hf}_0^d$	$\epsilon\text{Hf}(t)$ <sub>d</sub>	$\pm 2\sigma^c$	$T_{\text{DM}}$ <sub>e</sub>	age <sup>f</sup>	$\pm 2\sigma$
							(V)						(Ga)	(Ma)	
333_182	0.0	0	0.00083	0	0.00430	0.01000	14	0.281528	0	0.281496	-0.8	1.1	2.37	1981	9
333_182	0.0	0	0.00060	0	0.00140	0.00224	14	0.281067	0	0.281037	-1.8	0.9	2.96	2638	9
333_183	0.1	0	0.00179	0	0.00146	0.00317	15	0.282409	0	0.282394	-4.1	0.8	1.28	439	9
333_188	0.0	0	0.00083	0	0.00151	0.00376	10	0.282488	0	0.282479	3.1	0.9	1.04	624	9
333_189	0.0	0	0.00055	0	0.00143	0.00345	12	0.282513	0	0.282504	8.1	0.9	0.91	807	9
333_190	0.0	0	0.00048	0	0.00154	0.00308	10	0.281152	0	0.281127	4.0	0.9	2.73	2753	9
333_193	0.0	0	0.00067	0	0.00143	0.00372	11	0.282341	0	0.282335	-5.7	0.9	1.39	460	9
333_199	0.0	0	0.00079	0	0.00149	0.00432	13	0.281546	0	0.281532	-23.1	0.8	2.74	948	9
333_201	0.0	0	0.00092	0	0.00163	0.00548	15	0.282214	0	0.282166	40.7	1.2	0.64	2738	9
333_205	0.0	0	0.00061	0	0.00143	0.00379	11	0.281583	0	0.281566	-8.3	0.7	2.43	1549	9
333_206	0.0	0	0.00111	0	0.00144	0.00313	12	0.282170	0	0.282149	0.4	0.9	1.52	1023	9
333_207	0.0	0	0.00093	0	0.00138	0.00312	13	0.281333	0	0.281299	-9.2	0.8	2.78	1922	9
333_209	0.1	0	0.00241	0	0.02033	0.03881	3	0.281856	0	0.281834	-22.6	0.9	2.34	498	9
333_211	0.1	0	0.00155	0	0.00175	0.00347	11	0.282187	0	0.282164	-4.3	0.8	1.58	791	9
333_212	0.0	0	0.00034	0	0.00146	0.00487	13	0.281380	0	0.281365	-0.6	1.0	2.53	2190	9
333_215	0.1	0	0.00189	0	0.00115	0.00301	15	0.282424	0	0.282408	-3.4	0.7	1.25	446	9
333_216	0.0	0	0.00160	0	0.00158	0.00293	14	0.282390	0	0.282365	3.7	0.8	1.18	831	9
333_olc78	0.0	0	0.00154	0	0.00159	0.00357	12	0.282449	0	0.282432	0.9	0.9	1.14	600	9
333_olc81	0.1	0	0.00168	0	0.00129	0.00338	15	0.282417	0	0.282398	-0.3	0.7	1.21	600	9
333_olc83	0.1	0	0.00197	0	0.00167	0.00355	14	0.282410	0	0.282388	-0.6	0.8	1.23	600	9

Table B.2 (continued)

Sample/spot number	$^{176}\text{Yb}/^{177}\text{Hf}$ $\pm 2\sigma$	$^{176}\text{Lu}/^{177}\text{Hf}$ $\pm 2\sigma$	$^{176}\text{Hf}/^{177}\text{Hf}$ $\pm 2\sigma$	$^{180}\text{Hf}/^{177}\text{Hf}$	$\text{Sig}_{\text{Hf}}^{\text{Hf}}$ (V)	$^{176}\text{Hf}/^{177}\text{Hf}$ $\pm 2\sigma$	$^{176}\text{Hf}/^{177}\text{Hf}$ $\pm 2\sigma$	$\epsilon_{\text{Hf}}^{\text{Hf}}(t)$ $\pm 2\sigma$	$T_{\text{DM}}$ $\epsilon$ (Ga)	age <sup>f</sup> (Ma)	$\pm 2\sigma$		
333_old86	0.0	0.00084	0	0.00134	0.00404	12	0.282394	0	0.282383	0.8	1.21	674	9
333_old91	0.1	0.00200	0	0.00165	0.00506	18	0.282437	0	0.282422	-4.0	1.24	398	9
333_old95	0.0	0.00117	0	0.00139	0.00488	14	0.282444	0	0.282435	-3.5	1.22	397	9
333_old96	0.0	0.00159	0	0.00150	0.00268	14	0.282397	0	0.282387	-6.6	1.34	338	9
333_old97	0.0	0.00135	0	0.00137	0.00313	12	0.282334	0	0.282302	11.3	1.11	1264	9
333_old98	0.0	0.00031	0	0.00140	0.00516	14	0.282254	0	0.282251	-6.1	1.51	572	9
333_old100	0.0	0.00114	0	0.00121	0.00300	15	0.282449	0	0.282436	1.1	1.13	601	9
333_old104	0.0	0.00054	0	0.00137	0.00333	12	0.282656	0	0.282651	7.7	0.73	557	9
333_old105	0.0	0.00145	0	0.00148	0.00345	13	0.282376	0	0.282354	3.0	1.20	814	9
333_old107	0.0	0.00159	0	0.00119	0.00361	15	0.282395	0	0.282384	-5.7	1.33	380	9
333_old108	0.0	0.00099	0	0.00201	0.00431	12	0.282214	0	0.282204	-8.7	1.61	532	9
333_old110	0.0	0.00118	0	0.00134	0.00322	13	0.282279	0	0.282261	0.1	1.38	832	9
333_old112	0.0	0.00125	0	0.00181	0.00404	19	0.282268	0	0.282256	-6.8	1.51	534	9
333_old113	0.0	0.00082	0	0.00112	0.00268	18	0.282158	0	0.282148	-8.4	1.68	634	9
333_old115	0.1	0.00181	0	0.00141	0.00349	15	0.282381	0	0.282368	-6.2	1.35	386	9
333_old117	0.1	0.00202	0	0.00148	0.00324	18	0.282365	0	0.282348	-5.5	1.37	445	9
333_old118	0.0	0.00108	0	0.00124	0.00442	13	0.282006	0	0.281996	-16.2	2.02	525	9
333_old124	0.1	0.00226	0	0.00118	0.00351	16	0.282413	0	0.282398	-5.5	1.30	367	9
333_old125	0.0	0.00115	0	0.00114	0.00276	15	0.282325	0	0.282319	-11.0	1.50	246	9
333_old127	0.0	0.00133	0	0.00130	0.00311	15	0.282407	0	0.282398	-5.3	1.30	378	9

Table B.2 (continued)

Sample/spot number	$^{176}\text{Yb}/^{177}\text{Hf}$ <sub>a</sub>	$\pm 2\sigma$	$^{176}\text{Lu}/^{177}\text{Hf}$ <sub>a</sub>	$\pm 2\sigma$	$^{178}\text{Hf}/^{177}\text{Hf}$	$\pm 2\sigma$	$^{180}\text{Hf}/^{177}\text{Hf}$	$\text{Sig}_{\text{Hf}}^{\text{b}}$	$^{176}\text{Hf}/^{177}\text{Hf}$	$\pm 2\sigma^{\text{c}}$	$^{176}\text{Hf}/^{177}\text{Hf}$ <sub>(t)</sub>	$\epsilon_{\text{Hf}}^{\text{d}}$	$T_{\text{DM}}^{\text{e}}$	age <sup>f</sup>	$\pm 2\sigma$
								(V)					(Ga)	(Ma)	
333_old128	0.1	0	0.00175	0	0.00133	0.00235	16	0.282365	0	0.282352	-6.4	0.6	1.38	402	9
333_old134	0.0	0	0.00080	0	0.00146	0.00206	15	0.281078	0	0.281040	-4.7	0.9	3.02	2513	9
333_old136	0.0	0	0.00137	0	0.00156	0.00725	12	0.282366	0	0.282357	-6.9	1.1	1.38	369	9
333_old137	0.0	0	0.00144	0	0.00131	0.00294	16	0.282502	0	0.282484	3.6	0.7	1.02	636	9
333_old138	0.0	0	0.00092	0	0.00152	0.00414	16	0.282308	0	0.282302	-8.7	0.9	1.49	378	9
333_old139	0.0	0	0.00125	0	0.00145	0.00344	15	0.282358	0	0.282349	-7.5	0.9	1.40	357	9
333_old140	0.0	0	0.00068	0	0.00169	0.00335	14	0.281936	0	0.281930	-20.0	0.7	2.17	460	9
333_old142	0.1	0	0.00164	0	0.00125	0.00322	13	0.282388	0	0.282375	-5.1	0.8	1.33	423	9
333_old144	0.0	0	0.00093	0	0.00138	0.00295	14	0.282356	0	0.282340	5.3	0.7	1.18	942	9
333_old147	0.0	0	0.00040	0	0.00130	0.00396	13	0.282395	0	0.282391	-4.1	1.0	1.29	441	9
333_old152	0.1	0	0.00185	0	0.00119	0.00295	16	0.282377	0	0.282364	-6.5	0.7	1.37	375	9
333_old149	0.0	0	0.00122	0	0.00182	0.00749	14	0.282359	0	0.282324	18.3	0.9	0.94	1535	9
333B_old151	0.1	0	0.00171	0	0.00136	0.00317	13	0.282401	0	0.282390	-6.4	0.8	1.33	342	9
333B_old155	0.1	0	0.00156	0	0.00137	0.00409	13	0.282406	0	0.282396	-6.3	0.9	1.32	333	9
333B_old157	0.0	0	0.00102	0	0.00202	0.00442	10	0.282184	0	0.282170	-5.1	0.9	1.59	747	9
333B_old159	0.0	0	0.00148	0	0.00142	0.00336	13	0.282376	0	0.282367	-7.2	0.8	1.37	343	9
333B_old160	0.0	0	0.00125	0	0.00136	0.00297	12	0.282126	0	0.282109	-8.1	0.9	1.73	708	9
333B_old163	0.0	0	0.00064	0	0.00187	0.00333	10	0.281730	0	0.281720	-18.3	0.8	2.41	866	9
333B_old164	0.1	0	0.00175	0	0.00177	0.00476	12	0.282377	0	0.282357	-1.6	0.9	1.29	605	9

Table B.2 (continued)

Sample/spot number	$^{176}\text{Yb}/^{177}\text{Hf}$ $\pm 2\sigma$	$^{176}\text{Lu}/^{177}\text{Hf}$ $\pm 2\sigma$	$^{178}\text{Hf}/^{177}\text{Hf}$ $\pm 2\sigma$	$^{180}\text{Hf}/^{177}\text{Hf}$	$\text{Sig}_b^{\text{Hf}}$ (V)	$^{176}\text{Hf}/^{177}\text{Hf}$ $\pm 2\sigma$	$^{176}\text{Hf}/^{177}\text{Hf}$ $\pm 2\sigma$	$\epsilon\text{Hf}(t)$ $\pm 2\sigma$	$T_{DM}$ $\epsilon$ (Ga)	age <sup>f</sup> (Ma)	$\pm 2\sigma$				
333B_old167	0.1	0	0.00238	0	0.00184	0.00411	14	0.282407	0	0.282333	21.0	1.1	0.87	1639	9
333B_old168	0.0	0	0.00080	0	0.00131	0.00431	13	0.282186	0	0.282174	-3.7	0.8	1.56	803	9
333B_old170	0.0	0	0.00042	0	0.00159	0.00341	11	0.282557	0	0.282553	4.3	0.8	0.92	563	9
333B_old172	0.1	0	0.00209	0	0.00205	0.00505	13	0.282370	0	0.282354	-6.0	1.0	1.37	413	9
333B_old174	0.1	0	0.00200	0	0.00155	0.00402	12	0.282047	0	0.282028	-15.5	1.1	1.96	506	9
333B_old174	0.1	0	0.00210	0	0.00252	0.00915	14	0.282420	0	0.282396	-0.4	1.0	1.21	600	9
333B_old178	0.1	0	0.00172	0	0.00186	0.00375	14	0.282367	0	0.282355	-6.9	0.6	1.39	374	9
333B_old178	0.1	0	0.00168	0	0.00139	0.00327	13	0.282391	0	0.282372	-1.2	0.8	1.26	600	9
333B_old180	0.1	0	0.00178	0	0.00118	0.00318	12	0.282223	0	0.282145	29.9	0.9	0.91	2312	9
333B_old182	0.0	0	0.00104	0	0.00140	0.00246	12	0.282222	0	0.282215	-12.1	0.6	1.66	362	9
333B_old183	0.1	0	0.00214	0	0.00129	0.00380	13	0.282383	0	0.282370	-7.3	0.8	1.37	330	9
333B_old184	0.1	0	0.00185	0	0.00149	0.00310	13	0.282389	0	0.282378	-7.4	0.8	1.36	313	9
333B_old185	0.1	0	0.00195	0	0.00151	0.00440	11	0.282394	0	0.282374	-2.4	0.9	1.28	543	9
333B_old1856	0.0	0	0.00090	0	0.00161	0.00452	12	0.281768	0	0.281751	-13.9	0.9	2.29	1015	9
333B_old188	0.1	0	0.00204	0	0.00197	0.00481	14	0.282478	0	0.282450	4.3	1.0	1.05	723	9
333B_old189	0.0	0	0.00143	0	0.00146	0.00243	13	0.282384	0	0.282369	-2.7	0.8	1.29	536	9
333B_old190	0.0	0	0.00132	0	0.00152	0.00296	13	0.282346	0	0.282338	-8.9	0.9	1.44	312	9
333B_old197	0.1	0	0.00247	0	0.00141	0.00287	13	0.282426	0	0.282413	-6.8	0.9	1.31	287	9
333B_old198	0.0	0	0.00114	0	0.00145	0.00373	12	0.282433	0	0.282420	0.0	0.8	1.17	578	9
333B_old200	0.1	0	0.00167	0	0.00122	0.00372	14	0.282370	0	0.282348	0.4	0.9	1.26	712	9

Table B.2 (continued)

Sample/spot number	$^{176}\text{Yb}/^{177}\text{Hf}$ $\pm 2\sigma$	$^{176}\text{Lu}/^{177}\text{Hf}$ $\pm 2\sigma$	$^{176}\text{Hf}/^{177}\text{Hf}$ $\pm 2\sigma$	$^{180}\text{Hf}/^{177}\text{Hf}$	$\text{Sig}_{\text{b}}^{\text{Hf}}$ (V)	$^{176}\text{Hf}/^{177}\text{Hf}$ $\pm 2\sigma^{\text{c}}$	$^{176}\text{Hf}/^{177}\text{Hf}_{(0)}$ $\pm 2\sigma^{\text{c}}$	$\epsilon\text{Hf}(t)$ $\pm 2\sigma^{\text{c}}$	$T_{\text{DM}}$ $\epsilon$ (Ga)	age <sup>f</sup> (Ma)	$\pm 2\sigma$				
333B_01d202	0.0	0	0.00108	0	0.00152	0.00380	12	0.282356	0	0.282342	-0.6	1.1	1.29	675	9
333B_01d204	0.0	0	0.00084	0	0.00189	0.00361	8	0.282647	0	0.282641	4.1	1.1	0.81	415	9
333B_01d206	0.0	0	0.00086	0	0.00172	0.00328	11	0.282164	0	0.282158	-14.7	0.8	1.78	338	9
333B_01d209	0.1	0	0.00174	0	0.00124	0.00243	15	0.282382	0	0.282312	30.8	0.7	0.68	2095	9
333B_01d210	0.1	0	0.00200	0	0.00187	0.00365	9	0.282363	0	0.282343	-4.2	1.0	1.35	512	9
333B_01d211	0.0	0	0.00085	0	0.00161	0.00367	11	0.282136	0	0.282128	-12.4	1.0	1.78	487	9
333B_01d212	0.1	0	0.00155	0	0.00125	0.00287	17	0.282331	0	0.282325	-11.3	0.8	1.50	225	9
333B_01d215	0.1	0	0.00182	0	0.00138	0.00426	14	0.282360	0	0.282350	-8.6	1.0	1.42	304	9
333B_01d218	0.1	0	0.00159	0	0.00135	0.00736	12	0.282184	0	0.282161	-4.7	0.9	1.60	778	9